

Summer 8-15-2019

Siderophore-Dependent Transport Paradigms for Iron Across the Bacterial Cell Envelope in the Human Pathogen *Staphylococcus aureus*

Nathaniel Endicott

Washington University in St. Louis

Follow this and additional works at: https://openscholarship.wustl.edu/art_sci_etds

 Part of the [Biochemistry Commons](#)

Recommended Citation

Endicott, Nathaniel, "Siderophore-Dependent Transport Paradigms for Iron Across the Bacterial Cell Envelope in the Human Pathogen *Staphylococcus aureus*" (2019). *Arts & Sciences Electronic Theses and Dissertations*. 1843.
https://openscholarship.wustl.edu/art_sci_etds/1843

This Dissertation is brought to you for free and open access by the Arts & Sciences at Washington University Open Scholarship. It has been accepted for inclusion in Arts & Sciences Electronic Theses and Dissertations by an authorized administrator of Washington University Open Scholarship. For more information, please contact digital@wumail.wustl.edu.

WASHINGTON UNIVERSITY IN ST. LOUIS

Department of Chemistry

Dissertation Examination Committee:

Timothy A. Wencewicz, Chair

Jeffrey P. Henderson

Meredith Jackrel

Kevin D. Moeller

John-Stephen Taylor

Siderophore-Dependent Transport Paradigms for Iron Across the Bacterial Cell Envelope in the
Human Pathogen *Staphylococcus aureus*

by

Nathaniel P. Endicott

A dissertation presented to
The Graduate School
of Washington University in
partial fulfillment of the
requirements for the degree
of Doctor of Philosophy

August 2019
St. Louis, Missouri

© 2019, Nathaniel P. Endicott

Table of Contents

List of Figures	iv
List of Tables	vi
Acknowledgments.....	vii
Abstract of the Dissertation	1
Chapter 1: Introduction	3
1.1 Preface.....	4
1.2 The Antimicrobial Resistance Crisis.....	4
1.3 Multidrug Resistance.....	7
1.4 Virulence Factors of <i>S. aureus</i>	9
1.5 The Importance of Iron for Bacterial Virulence.....	11
1.6 Siderophore Utilization for Iron Acquisition	12
1.7 Siderophore System in <i>S. aureus</i>	13
1.8 ABC transporters.....	17
1.9 Clinical Relevance of Xenosiderophore Utilization.....	18
1.10 Mechanism of Iron Transport.....	19
1.11 Figures.....	21
1.12 References	35
Chapter 2: Structural Basis for Xenosiderophore Utilization by the Human Pathogen <i>Staphylococcus aureus</i>	44
2.1 Preface.....	44
2.2 Abstract	45
2.3 Introduction	46
2.4 Results and Discussion.....	49
2.5 Further Discussions and Conclusions	55
2.6 Materials and Methods	59
2.7 Acknowledgements	64
2.8 Tables and Figures	65
2.9 References	89
Chapter 3: Iron Exchange from <i>holo</i> -Transferrin to <i>apo</i> -Siderophores Catalyzed by a Siderophore Binding Protein.....	99
3.1 Preface.....	100
3.2 Abstract	100

3.3	Introduction	101
3.4	Results and Discussion.....	105
3.5	Further Discussions and Conclusions	110
3.6	Materials and Methods	113
3.7	Acknowledgements	118
3.8	Tables and Figures	119
3.9	References	127
Chapter 4: Conclusions and Perspectives		130
4.1	Preface.....	131
4.2	Summary of Dissertation.....	131
4.3	Future Directions and Broader Context	133
4.4	Figures.....	140
4.5	References	141
Appendix A: Synthesis and NMR Spectra for Chapter 2		142
Appendix B: NMR, Raw Curves, Protein Sequences, and Compound Data for Chapter 3		179

List of Figures

Chapter 1

Figure 1.1: Overview of the problem of bactericidal treatment.....	21
Figure 1.2: Favorable outcomes from bacteriostatic treatment.....	22
Figure 1.3: Common exotoxins of <i>S. aureus</i>	23
Figure 1.4: The adhesion protein SpA of <i>S. aureus</i>	24
Figure 1.5: Common sources of iron in the body.....	25
Figure 1.6: Overview of siderophore-mediated iron acquisition in Gram-positive bacteria.....	26
Figure 1.7: Native siderophores and metallophores of <i>S. aureus</i>	27
Figure 1.8: Gene loci important for <i>S. aureus</i> iron acquisition.....	28
Figure 1.9: Homology model of the Fhu uptake system to BtuCDF.....	29
Figure 1.10: FhuD2 binding pocket.....	30
Figure 1.11: Canonical mechanism for cell entry.....	31
Figure 1.12: Displacement mechanism for cell entry.....	32
Figure 1.13: Shuttle mechanism for cell entry.....	33
Figure 1.14: Emergence of catalysis in non-catalytic proteins.....	34

Chapter 2

Figure 2.1: Chemical structures of <i>S. aureus</i> xenosiderophores	66
Figure 2.2: Structures of benzyl protected siderophores 20–38.....	68
Figure 2.3: Structures of siderophores Dan, DFOB, SDFOB, and 1–17.....	69
Figure 2.4: Structures of siderophores Dan-Fe, FOB, SFOB, and 1-Fe–17-Fe.....	70
Scheme 2.1: Synthesis of ferrioxamine siderophores used in this study.....	70
Figure 2.5: Siderophore side chains influence the kinetic and thermodynamic stability of siderophore-Fe(III) complexes.....	71
Figure 2.6: Exponential decay plots for EDTA iron(III) binding competition assay with ferrioxamine siderophores.....	72

Figure 2.7: Iron(III) exchange half-lives ($t_{1/2}$) between ferrioxamine siderophores and EDTA in pH 7.4.....	75
Figure 2.8: SDS-PAGE analysis of purified N-His6-FhuD2.....	76
Figure 2.9: Siderophore side chains weakly influence FhuD2 binding.....	77
Figure 2.10: Summary of ferrioxamine xenosiderophore structure-function relationships.....	79
Figure 2.11: Net siderophore charge strongly influences utilization by <i>S. aureus</i> SG511.....	80
Figure 2.12: <i>S. aureus</i> ATCC 11632 growth promotion.....	81
Figure 2.13: <i>S. aureus</i> ATCC 11632 growth curves in iron restrictive TMS minimal media.....	82
Figure 2.14: Electrostatic surface models of HtsA (PDB 3LI2), SirA (PDB 3MWF), and FhuD2 (PDB 4FIL).....	83
Equations 2.1-2.11: Calculation of K_d values.....	84
Figure 2.15: Fluorescence quenching curves for titration of N-His6-FhuD2 with siderophores.....	85
Figure 2.16: <i>S. aureus</i> ATCC 11632 growth curves in iron restrictive TMS minimal media.....	88

Chapter 3

Figure 3.1: Schematic representation of shuttle mechanism.....	119
Figure 3.2: Catalytic iron exchange of siderophore binding proteins.....	120
Figure 3.3: Siderophore competitive and reversible binding to FhuD2.....	121
Figure 3.4: Macrocyclic siderophores can accept but not donate ferric iron	122
Figure 3.5: Mutational scanning of FhuD2 active site	123
Figure 3.6: Mechanistic model for iron exchange.....	124
Figure 3.7: Model for iron exchange based on dynamic motions of FhuD2.....	125
Figure 3.8: DFO attenuation of iron exchange from FOB	126

Chapter 4

Figure 4.1: Newly presented siderophore-mediated uptake paradigm.....	140
---	-----

***Please note that all figure, scheme, table, and compound numbering is internal to each individual chapter.**

List of Tables

Chapter 2

Table 2.1: Known iron acquisition virulence factors and associated genes in <i>S. aureus</i> pathogens.....	65
Table 2.2: Net charge, apparent $\log K_{Fe}$ values, MIC values for siderophore-sideromycin competition, and apparent FhuD2 K_d values for ferrioxamine siderophores.....	67
Table 2.3: Primary protein sequences of wild type FhuD2.....	78
Table 2.4: Codon optimized nucleotide sequence of FhuD2- <i>N</i> -His ₆ from <i>S. aureus</i>	78
Table 2.5: Strains and plasmids used in this work.....	83

Chapter 3

Table 3.1: Apparent binding affinities and kinetic parameters for FhuD2 mutants.....	126
--	-----

***Please note that all figure, scheme, table, and compound numbering is internal to each individual chapter.**

Acknowledgments

My advisor, Dr. Tim Wencewicz, has been instrumental in providing guidance and support throughout my years at WashU. His mentorship has allowed me to flourish as a scientist and develop higher level experimental and theoretical knowledge. His encouragement of me attending many conferences gave me the opportunity to network with other scientists, both in academia and industry, and he was supportive when I had opportunities to pursue additional teaching and mentorship experiences outside of lab. My traveling and teaching experiences with my fellow graduate students were some of my most memorable at WashU and have prepared me well for a career moving forward.

My thesis committee of Drs. John-Stephen Taylor, Jeffrey Henderson, Meredith Jackrel and Kevin Moeller provided useful scientific and teaching input to push my research and this dissertation in the right direction. Dr. Taylor was particularly instrumental to my graduate school success by generously allowing me to use his fluorimeter and giving me an entire bench space in his lab for myself. Dr. Moeller's willingness to provide a letter of recommendation within the same day I notified him was hugely beneficial in the placement for my next position.

The support of my friends and family has made everything I've done possible, I cannot thank all of you enough. I would finally like to thank the WUSTL chemistry department and NSF for making this work possible through funding the project (fund number 1654611).

Nathaniel P. Endicott

Washington University in St. Louis

August 2019

Dedicated to my sister.

ABSTRACT OF THE DISSERTATION

Siderophore-Dependent Transport Paradigms for Iron Across the Bacterial Cell Envelope in the
Human Pathogen *Staphylococcus aureus*

by

Nathaniel P. Endicott

Doctor of Philosophy in Chemistry

Washington University in St. Louis, 2019

Professor Timothy A. Wencewicz, Chair

This work is focused on iron trafficking through ABC transporters in *Staphylococcus aureus* and combatting the growing antimicrobial resistance crisis by exploiting virulence factors as therapeutic targets. Specifically, the goal was to understand the role of a siderophore-binding lipoprotein FhuD2 in *S. aureus* iron trafficking. While *S. aureus* endogenously produces three metallophores for metal sequestration from the host, FhuD2 is thought to scavenge metals from hydroxamate-based xenosiderophores encountered in the host environment. FhuD2 is a critical virulence factor and vaccine candidate (Novartis) for MRSA. Since xenosiderophore scavenging systems are often dispensable, it was hypothesized that FhuD2 must be playing another role to enhance pathogen virulence. Through careful investigations using a fluorescent siderophore probe, this work has revealed a new role for FhuD2 in the *S. aureus* iron trafficking pathway. FhuD2 does tightly bind hydroxamate xenosiderophores, but it does not immediately use the siderophore as a transport substrate. Instead, the siderophore serves as a cofactor for a newly proposed enzymatic function of FhuD2 in iron trafficking from human holo-transferrin. Using a “turn-off” fluorescent

siderophore probe it was shown that the FhuD2 apo-siderophore complex is capable of catalyzing iron extraction from transferrin. The interaction of FhuD2 with transferrin better explains its role as a virulence factor and establishes a new paradigm for iron trafficking in bacteria with broad relevance. This same phenomenon was confirmed another human pathogen, *Bacillus subtilis*. Structure-activity relationship analysis of siderophores governing cell entry revealed a charge-based preference for whole cell uptake in *S. aureus*.

Chapter 1: Introduction

1.1 Preface

This chapter was written by Nathaniel Endicott (NPE) with feedback provided by Dr. Tim Wencewicz (TAW).

1.2 The Antimicrobial Resistance Crisis

Antimicrobial resistance is one of the most pressing problems facing modern society. It is projected to eclipse cancer in yearly annual death globally by 2050 if not addressed. The history of antibiotic development originated with the discovery of penicillin by Alexander Fleming in 1928.¹ Penicillin was one of the most successful antibiotics in history and was heavily used in World War II.² Resistance to penicillin became an increasing problem throughout the 1950s, but new antibiotics were developed which temporarily solved the penicillin resistance problem in what is coined the Golden Age of antibiotic discovery. However, resistance began growing in multiple areas until resistance was seen in nearly every class of antibiotics, while simultaneously fewer new classes of drugs were discovered.^{3,4}

There are multiple underlying causes of the spread of antibiotic resistance. The overuse of antibiotics is a major contributing factor, due to horizontal gene transfer allowing resistance to rapidly spread between different species of bacteria. Resistance spontaneously occurs through mutation, and the use of antibiotics directly fuels the natural selection of drug-resistance strains and leaves enriched pools of resistant pathogens to survive at an infection site.⁵ Overuse of antibiotics often results from inadequate stewardship including prescription practices. About 30% to 50% of the time, the choice of antibiotic, duration of administration or treatment indication are inappropriate for a given indication.⁶ Unnecessary durations of treatment results in extended

evolutionary pressure for drug resistant strains to survive, and subtherapeutic concentrations promote this process further. Use of antibiotics in agriculture is another factor, as they are widely used for livestock growth supplements.⁷ It is financially profitable for the agricultural industry to use copious amounts of antibiotics because of the positive effect in animal health leading to higher yields and product quality. This practice makes agricultural settings reservoirs of antibiotic resistant bacteria, including some human pathogenic strains. Unfortunately, when the animals are eaten the antibiotics and antibiotic resistance genes harbored within them are transferred to humans after consumption, resulting in enhanced exposure of human commensals to antibiotics and associated resistance that can be accommodated long-term by the gut microbiome of an individual.⁸ Agricultural antibiotic use can disrupt the balance of native microbiomes and excreted antibiotics in urine or stool of ingesting animals spreads throughout soil and is widely distributed by groundwater, fertilizer and surface runoff.⁷

Adding to the resistance problem is the glaring lack of new antibiotic development by the pharmaceutical industry. Regulatory and economic issues are the main barriers preventing development of new antibiotics.⁷ From an economic standpoint, antibiotics pose a problem due to them often completely curing an infection while only being needed for short periods of time. Chronic illnesses requiring continual treatment are much more desirable research targets in this regard. The current estimated market value of net present value of new developed antibiotics is \$50 million, only 5% of the estimated value of a drug used to treat a neuromuscular disease.⁷ Antibiotics cost consumers relatively less than other types of treatments, one notable example being the high cost of cancer treatment. Another way in which antibiotic development is not profitable lies in their common use as treatments of last resort, due to infectious-disease specialist recommendations of limiting antibiotic use.⁹ Resistance emerging from the use of new antibiotics

is inevitable, but the timeline dissemination is often unpredictable, making newly discovered antibiotics at risk for quickly becoming obsolete. Additionally, because many antibiotics are now off-patent, they are supplied by generic drug manufacturers, resulting in both effective and cheap drugs for common ailments. This results in a public expectation that new antibiotics might be priced similarly, posing the problem of potential backlash for companies in antibiotic development.¹ Few antibacterial drugs have reached phase 2 or 3 in development as of 2013, especially those that could deal with some of the ESKAPE pathogens, such as *Pseudomonas aeruginosa*, *Acinetobacter baumannii*, and Enterobacteriaceae.¹⁰

Regulatory barriers represent an obstacle in the development of new antibiotics due to issues such as changes in licensing and other regulation rules, bureaucracy, and ranging amounts of clinical trial requirements for different countries. The U.S. Food and Drug Administration has raised the standard for clinical trial quality over the past several years, resulting in high cost and high populations required for new drug trials. Many smaller companies cannot afford the cost of phase 3 trials.¹¹ There is hope on the horizon for more efficient regulatory practices, however, as the Infectious Diseases Society of America has proposed a novel regulatory pathway based on smaller population sizes, resulting in a much faster and cheaper pathway to navigate clinical trials. The downside of this approach is new antibiotics would be designed to specifically treat only high-risk patients who could afford to take on the potential side effects of the specific drug. Limiting the exposure of new drugs to smaller populations does have the advantage of minimizing the spread of resistance, but lacks the profitability needed to drive discovery in the private sector and poses the risk for high compensatory prescription costs that limit use to privileged populations.⁷

1.3 Multidrug Resistance

The antimicrobial resistance landscape is dominated by multidrug resistant strains of bacteria, notable examples being vancomycin-resistant Enterococci, carbapenem-resistant Enterobacteriaceae, multidrug resistant *Pseudomonas aeruginosa*, and methicillin-resistant *Staphylococcus aureus* (MRSA). Enterococci present a problem due to their role in a variety of illnesses, affecting areas such as the urinary tract and the bloodstream. Around 30% of enterococcal infections are vancomycin-resistant, which leads to around 1,300 deaths per year in the United States. Although some antibiotic options, such as linezolid, are available to treat vancomycin-resistant strains, the total number of vancomycin-resistant infections has reached over 20,000 per year necessitating the discovery of new drugs in this area.³ Carbapenem-resistant Enterobacteriaceae are considered resistant against nearly all available antibiotics. Almost 600 deaths per year result from infections caused by carbapenem-resistant Enterobacteriaceae, fueled by the presence of an enzyme called NDM-1 that confers this high resistance to beta-lactam antibiotics.^{2,3} Multidrug-resistant *Pseudomonas aeruginosa* occur primarily in the urinary tract and surgical sites and pose a major problem for cystic fibrosis patients in the form of pulmonary infections. 6,000 cases per year of *P. aeruginosa* are multidrug-resistant, and around 400 deaths per year are caused by these resistant strains, some of which have shown resistance to almost all known antibiotics.³

Methicillin-resistant *Staphylococcus aureus* (MRSA) represents one of the most serious antibiotic-resistant threats known, resulting in over 11,000 deaths per year in the U.S. alone.¹² First discovered almost 50 years ago, MRSA is highly resistant to beta-lactam antibiotics and several other drug classes.^{2,4} Although many drugs retain activity against MRSA, such as linezolid,

tigecycline, and ceftobiprole, MRSA has shown insidious ability to spread and thrive in various different types of epidemiological settings, ranging from animals, hospitals and communities.¹³ Thus, a focus on healthcare associated infections is not enough when studying and managing MRSA. Many of the endogenous resistance mechanisms in MRSA are transferable on plasmids including resistance to glycopeptides and linezolid, drugs of last resort.¹³ There has been some progress addressing the issue of healthcare associated MRSA, primarily through improvement of hygiene practices in hospital settings, but community-associated infection rates caused by MRSA have been on the rise, likely due to the difficulties of controlling hygiene in public settings compared to hospitals.^{3,13}

An important technique in researching solutions to the antimicrobial resistance problem is to focus on bacterial virulence as potentially underexplored targets to develop bacteriostatic antibiotics. While bactericidal antibiotics outright kill an infection of interest, bacteriostatic antibiotics only stagnate growth. Although *a priori* bacteriostatic treatments seem like an inferior approach, they have several advantages. Firstly, they create less evolutionary pressure on bacteria to develop resistance. Bactericidal treatments leave only resistant strains remaining, meaning once the resistant strains multiply, they represent a much a higher percentage of the given population (**Figure 1.1**). Secondly, bacteriostatic treatments place a greater burden on the body's own defense systems to rid the body of the infection, having a similar effect as that of a vaccine, leaving the body better able to handle future infections (**Figure 1.2**).¹⁴

1.4 Virulence Factors of *S. aureus*

S. aureus possesses several key virulence factors allowing it to invade and circumvent protections by the innate immune system.¹⁶ Exoproteins are present in almost all types of *S. aureus* strains, ranging from exotoxins to multiple kinds of enzymes, such as proteases, lipases, and collagenase. Using these proteins, local host tissue can often be converted into nutrients allowing for bacterial growth.¹⁷ Some of the exotoxins produced by *S. aureus* are cytolytic, forming β -barrel plasma membrane pores which results in lysis of the targeted cell.¹⁸ Some examples of these cytolytic toxins produced by *S. aureus* are the hemolysins and leukocidins.¹⁹ α -hemolysin is especially cytolytic toward monocytes and human platelets. This toxin is a pore former, which can often result in changes of iron gradients, activation of signaling pathways for stress, and membrane integrity loss.²⁰ Panton-Valentine leukocidin targets leukocytes, and γ -hemolysin targets erythrocytes, and is a known necrotizing disease virulence factor.¹⁸ Two aspects of the toxin are each important in pore formation, LukS-PV and LukF-PV, which work together to form an octameric β -barrel complex which lies perpendicular to the cell membrane plane.¹⁹ Another type of exotoxins produced by *S. aureus* are the staphylococcal enterotoxins, the exfoliative toxins, and the toxic shock syndrome toxin-1, which is considered a pyrogenic toxin superantigen.²² Superantigenicity refers to the toxin's ability to spur propagation of T-lymphocytes, which cause food poisoning and shock syndrome (**Figure 1.3**).²³ Exfoliative toxins have also been implicated in T lymphocyte proliferation.²⁴ *S. aureus* produces other proteins which affect the immune system, such as the staphylococcal complement inhibitor, which blocks C3b formation on the bacterium surface, interfering with phagocytosis of *S. aureus* cells by human neutrophils.²⁵ The chemotaxis inhibitory protein extracellular fibrinogen binding protein both function to block neutrophil receptors from chemoattractants.²⁶ A formyl peptide receptor-like-1 inhibitory protein

blocks neutrophil migration to tissue from blood vessels.²⁷ Staphylokinase binds to α -defensins to eliminate their bactericidal activity.²⁸

Adhesion proteins play an important role in the ability of *S. aureus* to initiate the colonization process on host cells. The microbial surface component recognizing adhesive matrix molecules are comprised of covalently anchored proteins to cell peptidoglycans which attach to the extracellular matrix.²⁹ Perhaps the most notable protein in this family is SpA, which has been shown to be vital in inducing pneumonia.³⁰ Mice models have confirmed that the lack of SpA reduces rates of pneumonia and mortality. SpA is 42-kDa in size and covalently anchors to the bacterial cell wall, and it binds a large glycoprotein called the von Willebrand factor that participates in healing endothelial damage through platelet adhesion.³¹ The five repeated domains of SpA all bind with high affinity to immunoglobulin G in the Fc region.³² The binding to the Fc region of immunoglobulin G triggers a conformational shift that causes the bacteria not to be recognized by polymorphonuclear leukocytes (**Figure 1.4**).³³

Virulence factors in *S. aureus* are highly regulated by a variety of environmental cues. Temperature, osmolarity, pH, oxygen tension and nutrient availability all influence virulence factor expression.³⁴ Production of virulence factors is controlled by multiple global regulatory loci, such as the staphylococcal accessory regulators and ferric uptake regulators (Fur).^{34,35} These kinds of regulators are part of an intricate network that modulates expression of virulence genes. A specific target virulence gene has the ability to be influenced by many different regulators that can “cross talk” to make sure that the gene is only expressed in favorable conditions. For example, *agr* has been shown to negatively regulate *spa* expression, which encodes for SpA production.³⁶ On the other hand, SarS binding to the *spa* promoter activates SpA expression.³⁷ Intriguingly, *agr* also downregulates *sarS* expression.³⁵ It therefore appears that the mechanism by which *agr*

downregulates expression of *spa* is through suppression of *sarS*.³⁷ Virulence gene regulators can therefore affect target gene expression by directly binding to promoters or they can play an indirect role via other regulators.

1.5 The Importance of Iron in Bacterial Virulence

Regulation of iron uptake through the ferric uptake regulators is imperative for any invading pathogen such as *S. aureus* to survive. Iron acquisition plays a crucial role in bacterial virulence. Iron is vital for the survival of nearly all organisms, as processes such as electron transport, nitrogen fixation, DNA replication, photosynthesis, amino acid biosynthesis and tricarboxylic acid cycle all require iron.³⁸ Other processes such as virulence factor expression, symbiosis and host colonization all are highly relevant to the iron problem.³⁹ One reason why iron uptake is highly regulated is not just because of its beneficial nature, as excess iron can also be detrimental, leading to hydroxyl radical, superoxide and hydrogen peroxide generation.^{40,41} Reactive oxygen species result in DNA damage, membrane dysfunction, protein damage, and lipid peroxidation.^{42,43}

Iron exists either as ferric Fe(III) in its oxidized form or ferrous Fe(II) in its reduced form. Bacteria require approximately 10^{-6} M iron to survive, but ferric iron is highly restricted down to 10^{-24} M levels in biological settings, sequestered into iron-sulfur proteins, heme, and iron storage proteins such as transferrin (**Figure 1.5**).⁴⁴ For many bacteria such as *S. aureus*, ferric uptake regulators act as a global sensor of iron in the intracellular environment by coordinating transcription of genes responsive to iron with the available iron.⁴⁵ Iron acquisition in *S. aureus* is illustrated by the reduced virulence in animal models when iron acquisition is disrupted.⁴⁶ Staphylococcal strains which are defective in heme uptake, however, are not significantly affected

in virulence for murine pneumonia models, indicating heme iron alone is not necessary for *S. aureus* proliferation in murine lungs.⁴⁷ Fur-mediated iron availability sensing is conserved across many different strains of Gram-negative and Gram-positive bacteria such as *S. aureus*.⁴⁸ In iron rich environments, Fur generally functions as a repressor with the ability to bind DNA, inhibiting expression of select genes important for iron uptake. In iron-limited environments, such as an infection site, this Fur repression is attenuated, and the same genes are then expressed.^{49,50} Fur regulates not only genes encoding systems for iron acquisition, but also influences many cytoplasmic proteins, plays a role in the expression of stress proteins with antioxidative properties, and is involved in the formation of biofilms.^{51,52,53}

1.6 Siderophore Utilization for Iron Acquisition

The relevance of iron acquisition necessitates multiple avenues of iron transport for bacteria. The production of siderophores represents one of the most relevant virulence factors in this area. Siderophores are small molecules with high iron affinity, produced additionally by plants and fungi but not mammals.^{54,55,56} Siderophores commonly bind iron through bidentate chelating motifs such as catecholates, phenolate oxazolines, α -hydroxycarboxylic acids, and hydroxamates, where the hard oxygen donors match well to hard ferric iron.⁵⁷ Combinations of bidentate metal-chelating groups in a siderophore scaffold facilitates the hexadentate coordination to the metal center necessary for achieving the desired octahedral geometry. Often the ligands are preorganized around the metal on macrocyclic siderophore scaffolds.⁵⁷ Many bacteria can produce and utilize multiple different siderophores. In *E. coli*, for example, can utilize ferric complexes of rhodotorulate, coprogen, ferrichrome, citrate, enterobactin, and linearized enterobactin.⁵⁸ Interestingly, rhodotorulate, coprogen and ferrichrome are not produced by *E. coli* itself. This use

of xenosiderophores is a common strategy by bacteria in order to lessen metabolic burden.⁵⁹ Other notable examples of xenosiderophores are enterobactin uptake in *Pseudomonas aeruginosa* and ferrioxamine in *Yersinia enterocolitica* and *S. aureus*.^{60,61} Biosynthesized within the cell, siderophores are sent into the extracellular environment via efflux pumps, where they return back through the cell membrane through the use of membrane-anchored ABC transporters (**Figure 1.6**).⁵⁷

The logic behind bacteria being able to utilize multiple different siderophores can be explained in that different siderophores can have specific advantages to unique environmental conditions.⁶² In *Salmonella enterica*, for example, enterobactin is produced to satisfy nutritional requirements, but the human body has evolved a defense system against this route for iron acquisition. The defense protein lipocalin-2 binds and directly sequesters ferric enterobactin.⁵⁷ *Salmonella* counteracts this by producing salmochelins, glucosylated enterobactin derivatives that are unable to be captured by lipocalin-2.^{63,64} Salmochelin production has also been observed in various strains of *E. coli*.⁶⁴ In the case of *P. aeruginosa*, the two siderophores it produces, pyoverdine and pyochelin have orders of magnitude difference in their ability to coordinate Fe(III).^{65,66} Mathematical simulations illustrate the ability of *P. aeruginosa* to switch between producing each of these siderophores in response to varying iron conditions gives it a fitness advantage over strains that do not have this functionality.⁶⁷

1.7 Siderophore System in *S. aureus*

The iron uptake system in *S. aureus* specifically is like many other bacteria in terms of regulation and strategies to acquire iron. The mechanism of Fur binding to the *fur* box on DNA in iron-rich conditions followed by the release of Fur from DNA in iron depleted conditions holds

true for *S. aureus*, resulting in transcriptional repression of the regulon for Fur when iron is bountiful and de-repression when iron is scarce.^{68,69} *S. aureus* strains deficient in *fur* exhibit a profile of gene expression mirroring an iron starved organism. Mice infected with *S. aureus* have been imaged for gene transcription revealing that Fur-regulated genes become expressed in kidney and heart abscesses, indicating the bacteria has iron starved in these locations.^{70,71} Cytoplasmic protein profiles for wild type *S. aureus* have been compared to an isogenic *fur* mutant and it was found that there are twenty different staphylococcal proteins that are at a higher abundance without the presence of Fur, indicating they are negatively regulated by Fur.⁷² A further analysis indicated increased levels in fermentative and glycolytic enzymes, pointing toward the ability of *S. aureus* to modulate its metabolism to adapt to iron-starved host environments.⁶⁹ For iron-limited conditions, an increase in fermentative metabolism causes an increase in lactate production, which lowers the environmental pH to therefore negatively affect the affinity for transferrin to bind iron. In *S. aureus*, Fur regulates multiple virulence factors specifically, such as the expression of its immunomodulatory and cytolytic toxins and siderophores.⁶⁹

The native *S. aureus* siderophore system constitutes of two different siderophores, staphyloferrin A and staphyloferrin B (**Figure 1.7**). The genes important for the biosynthesis of staphyloferrin A and B are directly regulated by Fur and are highly expressed in iron-deficient conditions.⁷² Synthesized forms of each of these siderophores have shown the ability to restore the defects of staphylococcal mutants unable to produce each respective siderophore.⁶⁹ Although a third siderophore in *S. aureus* has been implicated as existing, aureochelin, the molecule has not been fully characterized.⁷⁴ Mutants unable to synthesize staphyloferrin A and B in isolated supernatants cannot support wild type growth of *S. aureus* with no iron present, indicating aureochelin, if present, does not play a significant role in iron acquisition on its own.⁷⁵

Additionally, iron acquisition from sources such as transferrin has been implicated to be related to siderophores, though *S. aureus* does not produce a direct transferrin receptor.⁵⁸

Staphyloferrin A on its own has shown relevance in iron acquisition. Mutants lacking the ability to produce staphyloferrin B have shown capability to sustain some growth in serum.⁷⁵ The *sfnABCD* operon encodes for staphyloferrin A production, which was found through bioinformatic screening and confirmed by biochemical and genetic approaches (**Figure 1.8**).⁷⁷ Although *sfnABCD* inactivation fails to attenuate growth of *S. aureus* growth in serum, its inactivation in a mutant without the capability to produce staphyloferrin B results in greatly impaired *S. aureus* growth.⁷⁵ ABC transporters often are present close to the genes required for siderophore production. Genes encoding for HtsABC, the transporter involved in uptake of staphyloferrin A, are located adjacent to the *sfn* operon. HtsABC has also been linked to heme binding, indicating that its role might be promiscuous and relevant in multiple types of iron uptake.⁷⁵ The crystal structure of HtsA was the first siderophore receptor of its kind to be characterized from a Gram-positive bacterium, and this structure directly supports the involvement of HtsA in siderophore utilization, which occurs through a conformational change of HtsA upon staphyloferrin A binding which entraps the siderophore substrate.⁷⁸ One noteworthy aspect of the crystal structure is the likelihood that HtsA does not directly bind heme, implicating the possibility of another lipoprotein acting as a conduit for heme transport.⁶⁹

Staphyloferrin B synthesis is encoded by the *sbnABCDEFGHI* operon (**Figure 1.8**).⁷⁹ Its import through the membrane occurs by *sirABC*, with SirBC as the membrane permease component of staphyloferrin B import to the cytoplasm and SirA as the lipoprotein receptor involved in binding staphyloferrin B from the extracellular environment.⁸⁰ The conformational change in SirA encloses staphyloferrin B in the binding pocket, analogous to HtsA.⁸¹ Both HtsA

and SirA bind their respective substrates with low nanomolar association constants, illustrating the tailored evolution of *S. aureus* to acquire iron in an infection setting.⁶⁹ The presence of both staphyloferrin A and B in *S. aureus* indicates each siderophore possibly performing unique roles, such as scavenging iron from different host proteins or performing more efficiently in different infection settings.

Many transition metals other than iron, such as copper, nickel, zinc and cobalt are crucial to biological processes, having relevance in areas such as enzymatic reactions, signaling agents and protein stability. *S. aureus* possesses several transition-metal transport systems, such as NixA, Nik, Adc, and Cnt.⁸² The Nik system is an ATP-binding cassette (ABC) transporter important for nickel acquisition, composed of the solute-binding protein (SBP) portion NikA and NikBCDE to form the rest of the transport channel. The Nik system takes advantage of L-histidine and other small-molecule chelators to determine urease activity, transport nickel, and colonize the urinary tract in mice.⁸³⁻⁸⁵ The NixA system has similar functions, such as impacting urease activity and playing a role in kidney colonization.⁸³ Adc, composed of the metal-binding component AdcA and the ABC transporter AdcBC, is involved in zinc acquisition.⁸⁶ Cnt, while originally shown as a nickel and cobalt acquisition system, has been shown to transport additional metals, such as zinc, iron, manganese, and copper depending on environmental conditions.^{87,88} The substrate for the Cnt system is the general metallophore staphylopine, representing an additional native metal binder in *S. aureus* (**Figure 1.7**).⁸²

1.8 ABC Transporters

The ABC transports involved in the uptake of staphyloferrin A, B, and staphylopin are part of the family ATP-powered pumps. The pumps use energy from ATP hydrolysis to move the specific substrate across membranes or into cellular vesicles against the electrochemical gradient of the environment.⁸⁹ ABC pumps constitute a large, diverse superfamily, and most of the *ABC* genes encode membrane-anchored proteins participating directly in molecular membrane transport.⁹⁰ Depending on the directionality of cytoplasmic transport, these transporters can be characterized as importers or exporters.⁹¹ The ABC proteins are constituted of the nucleotide binding domain (NBD), which contains several conserved motifs such as the Walker A and B sequences, the ABC signature motif, and Q loop and the H loop. Also present are the transmembrane domains (TMDs), which are composed of multiple hydrophobic α -helices. Overall the core unit of the ABC transporter contains two NBDs along with two TMDs. The two NBDs bind together and function to hydrolyze ATP, providing the transportation driving force, and the TMDs are important in substrate recognition as well as translocation through the lipid membrane.⁹⁰ ABC transporters often contain a membrane-bound substrate-binding protein (SBP) portion relevant for delivering the substrate to the importer complex (**Figure 1.9**). ABCC transporters are a subfamily of the ABC transporters relevant in *S. aureus*. One of the activities relevant to the ABCC transporters includes toxin excretion, involving several fungal and bacterial toxins.⁹³ Another important aspect is xenosiderophore utilization as seen in the Fhu system (**Figure 1.9**).⁹⁴

ABC transporters are associated with an ATPase, but *sirABC* and *htsABC* operons both do not encode a putative ATPase.⁹⁵ The *fur* operon in *S. aureus*, *fhuCBG*, however, does encode a

putative ATPase, *fhuC*, which is necessary for the transport of staphyloferrin A and B.⁷⁵ A *fhuCBG* mutant showed inhibited growth in iron-deficient conditions that is not recovered by the addition of staphyloferrin A or B on their own, but the presence of *fhuC* in addition to staphyloferrin A or B does recover growth, indicating FhuC is highly relevant in *S. aureus* iron acquisition.⁷⁵ Hydroxamate siderophores not directly produced by *S. aureus* can be utilized by *S. aureus* to help establish residency in the microbiome (**Figure 1.7**).⁶⁹ *fhuCBG* is directly related to the uptake of xenosiderophores in *S. aureus*, along with the lipoprotein receptors FhuD1 and FhuD2, located at distinct loci in the *S. aureus* genome (**Figure 1.8**).⁹⁶ FhuD1 and FhuD2 only undergo moderate conformational changes upon binding their siderophore substrate, unlike SirA and HtsA.^{97,98} Less conformational change naturally leads to less affinity for any one specific siderophore, but it creates promiscuity for multiple kinds of siderophores, allowing *S. aureus* to run a separate xenosiderophore stealing platform in addition to its uptake of staphyloferrin A and B (**Figure 1.10**).

1.9 Clinical Relevance of Xenosiderophore Utilization

Utilization of xenosiderophores by *S. aureus* has consequences on clinical use of the siderophore desferrioxamine B (DFO) as a first line therapeutic in treating iron overload disease. The large dose of DFO provides an easy source of iron for a local *S. aureus* infection to flourish. *S. aureus* is the most common infection for thalassemic patients treated with DFO in order to reduce blood iron levels after blood transfusions which are a necessary form of treatment.⁹⁹ Even as other types of iron overload treatments have grown in popularity, combination therapy with DFO and other iron chelators has shown promise in circumstances in which monotherapy is not adequate, assuring the clinical importance of DFO in the near future.¹⁰⁰ In addition to its use in

treating iron overload, DFO has shown promise as a delivery vector for antibiotics and other types of molecular cargo with potential applications for infection imaging, cancer, Parkinson's, Alzheimer's, and COPD.¹⁰¹⁻¹⁰⁶

Elucidation of the membrane transport paradigms for siderophores such as DFO at the ABC transporter level is critical for intelligent design of future siderophore-based therapeutics. Reducing infection risk and increasing efficacy of siderophore therapeutics are directly linked to understanding cell entry. In this dissertation, the different mechanistic possibilities of a *holo*-siderophore approaching Gram-positive cell membrane will be discussed in the context of the DFO and FhuD2 system in *S. aureus*. Molecular mechanisms for siderophore recognition, transport, and utilization as an iron source were explored through a fluorescence quenching assay using a siderophore probe molecule to monitor iron exchange processes, resin-immobilized FhuD2 to evaluate the reversibility of siderophore binding, and a rationally designed panel of DFO analogs to probe structural elements that influence cell entry in *S. aureus*.

1.10 Mechanism of Iron Transport

The answer to the question of determining cell entry revolves around understanding the possible mechanisms by which cell entry can occur. Once a siderophore has acquired iron in the extracellular environment and returns to the cell membrane, it has three options. In the first option, it can directly bind to the SBP and then pass through the ABC transporter in order to gain access to the interior of the cell. This is the currently accepted model for vitamin B₁₂ transport in bacteria and is conceptually the simplest option for cell entry (**Figure 1.11**).¹⁰⁷ One noteworthy aspect of bacterial ABC transporters, however, is the presence of *apo*-siderophores commonly bound to the surface of the SBP. This is the most likely state for an SBP dictated by the concentration gradient

of *apo*-siderophores being excreted from the interior of the cell. The second option for membrane transport involves an *apo*-siderophore bound to the SBP as a *holo*-siderophore approaches the cell. In this mechanism, the *holo*-siderophore competitively displaces the *apo*-siderophore at the SBP active site.¹⁰⁸ The *holo*-siderophore then gains cell entry. The third mechanism involves the same situation, an *apo*-siderophore bound to the SBP and an approaching *holo*-siderophore. Instead of displacement at the SBP, though, the incoming *holo*-siderophore non-reductively shuttles its iron to the SBP-bound *apo*-siderophore. The new *holo*-siderophore then enters the cell.¹⁰⁹ Several unanswered big picture questions remain surrounding these membrane transport paradigms and were recently defined by the work of Professor Ken Raymond.¹⁰⁸ Notably, the conditions favoring the shuttle or displacement mechanism are unknown. The biological reason behind having multiple different mechanistic pathways was also unclear. The specific mechanistic detail behind the shuttle mechanism was additionally left in the dark. The non-reductive shuttle of iron would logically be a kinetically slow process, pointing to the possible role of the SBP as a catalyst in this exchange. There is precedent for the evolution of catalytic effects originating from initially non-catalytic proteins, and FhuD2 showing potential as a vaccine candidate points to its significance in *S. aureus* virulence (**Figure 1.14**).¹¹⁰ In chapter 2, the structure-activity relationship rules for cell entry in a panel of DFO analogs was analyzed in detail, and negative charge ultimately dictated the ability for *S. aureus* to acquire *holo*-siderophores from the environment. In chapter 3, the mechanistic details of the shuttle and displacement mechanism were studied and a new paradigm for siderophore-mediated iron acquisition is proposed involving siderophores as cofactors in the enzymatic transfer of iron from human defense proteins such as transferrin. The logic used in the experimental design and execution proves insight on the siderophore system and iron acquisition in *S. aureus* and likely has widespread applications to many other relevant bacterial pathogens.

1.11 Figures

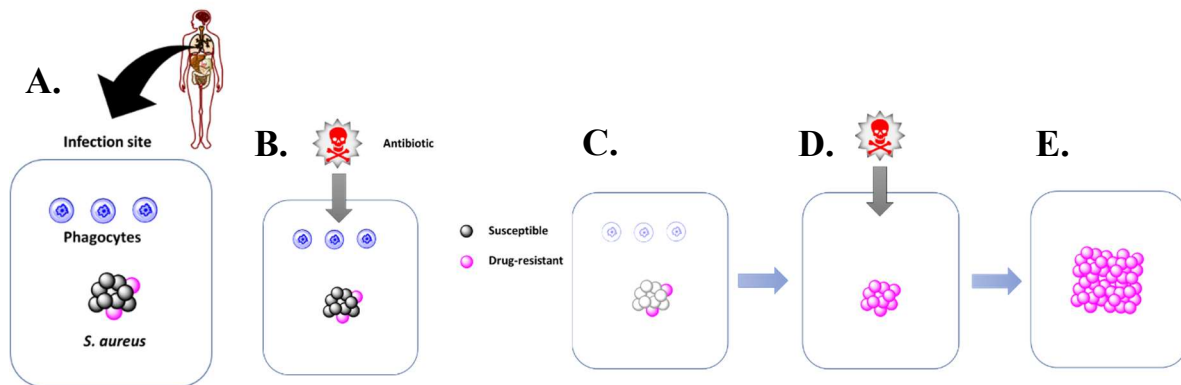


Figure 1.1. Overview of the problem of bactericidal treatment. Bactericidal antibiotic treatment leaving only drug-resistant strains behind results in high evolutionary pressure for only the drug-resistant strains to survive. (A) An infection site is a complex equilibrium of invading bacteria and body defense cells such as phagocytes. (B) Administration of a bactericidal antibiotic kills of susceptible bacteria leaving behind a small population of resistant cells that can evade host defense cells (C) Resistant cells can dominate the population and the body's immune system has not responded to the pathogen. (D) Administration of the same antibiotic becomes less effective once the population of drug-resistant strains becomes much higher. (E) Left without an effective answer, drug-resistant strains are free to propagate.

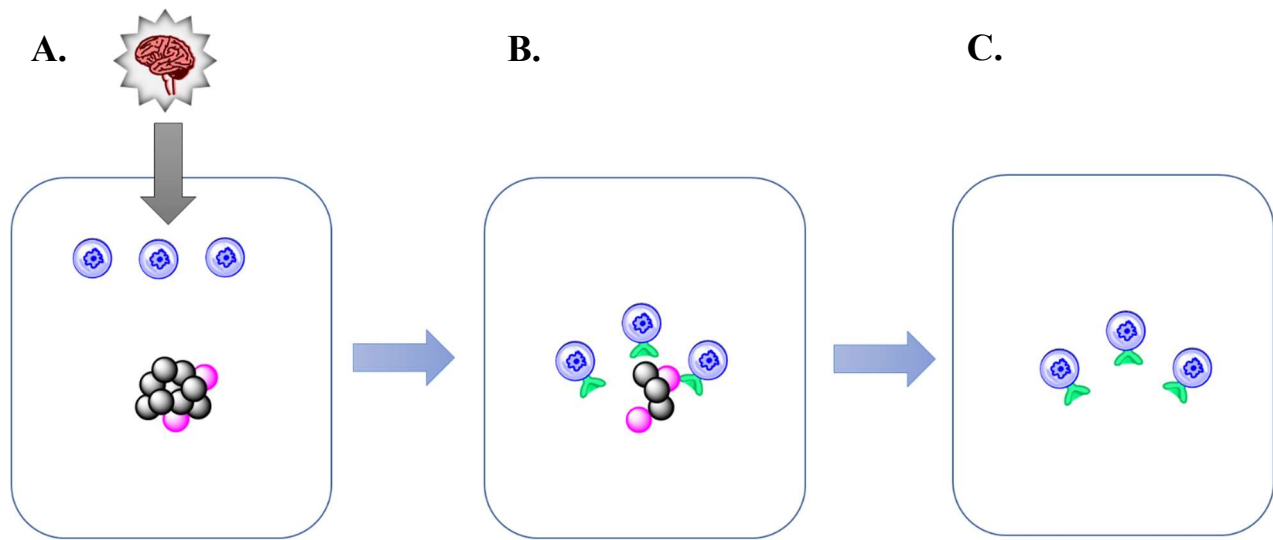


Figure 1.2. Favorable outcomes from bacteriostatic treatment. If an antibiotic only exhibits bacteriostatic effects, it can allow the body's own immune system to deal with the infection by halting pathogen growth and allowing for an innate and adaptive immune response. This applies less evolutionary pressure on drug-resistant strains to survive as well as leaving the body's own immune system better adapted to handle future infections, like a vaccine. (A) Administration of a bacteriostatic antibiotic has the benefit of often being useful for a specific bacterial target, leaving the host defense cells free to recognize the pathogen. (B) If the bacterial infection has been stagnated after bacteriostatic treatment, the innate immune system can clear the infection. (C) The immune system is left better able to handle future infections after being adapted to deal with the most recent one.

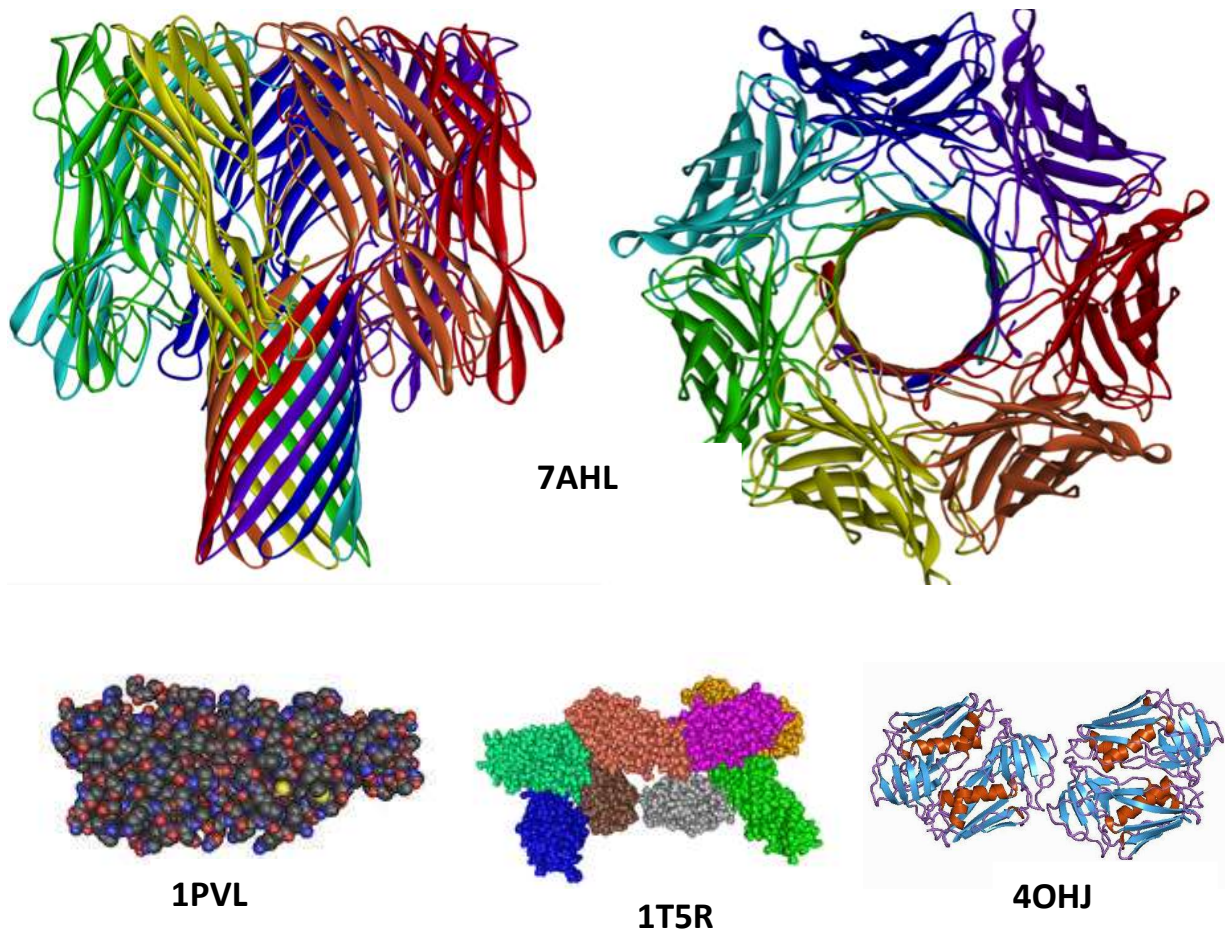


Figure 1.3. Common exotoxins of *S. aureus*. Pictured above is α -hemolysin, a pore former that is cytolytic. Pore formation has several potentially negative effects on cells, notably loss of membrane integrity. Pictured below is Pantone-Valentine leukocidin, LukS-PV on the left and LukF-PV in the middle. Each work in concert to form an octameric β -barrel complex lying on the cell membrane. Pictured on the lower right is toxic shock syndrome toxin-1, which can encourage propagation of T-lymphocytes. PDB entry numbers are provided. Image was generated using PyMOL.

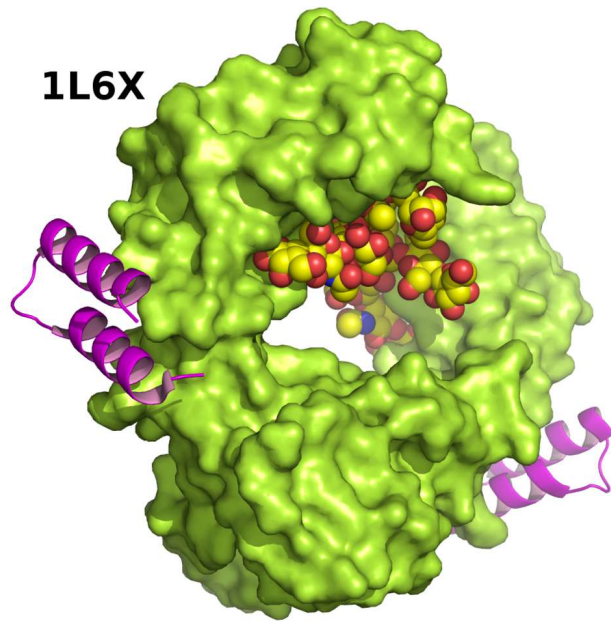


Figure 1.4. The adhesion protein SpA of *S. aureus*. SpA (purple) bound to the Fc region of immunoglobulin G. The conformational shift triggered by this binding event safeguards *S. aureus* from recognition by polymorphonuclear leukocytes. PDB entry number is provided. Image was generated using PyMOL.

1A8E

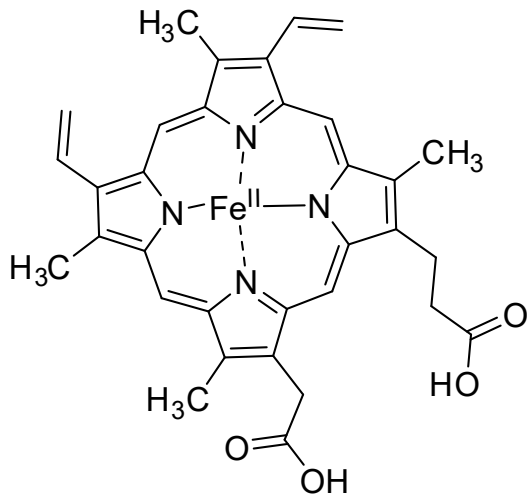
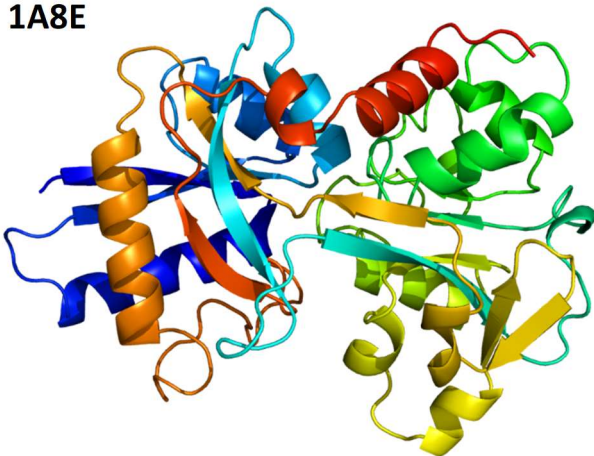


Figure 1.5. Common sources of iron in the body. Transferrin (left) is a human defense protein specializing in iron sequestration. Heme (right, pictured in its form heme B) is most common source of iron in the bloodstream, often bound hemoglobin.

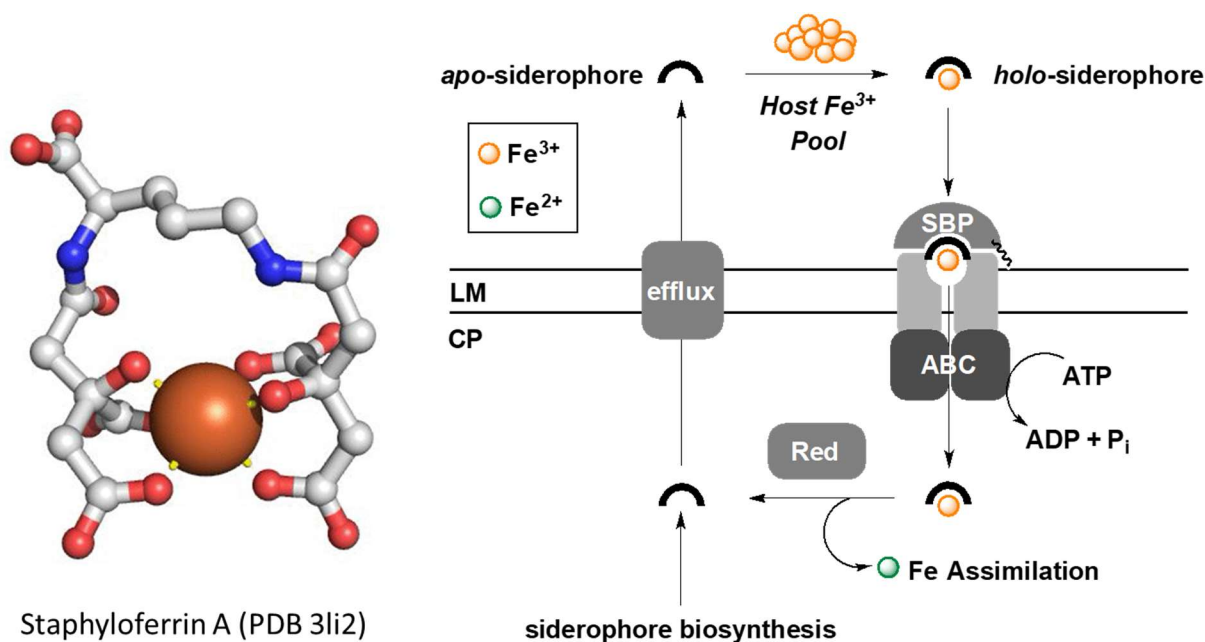


Figure 1.6. Overview of siderophore-mediated iron acquisition in Gram-positive bacteria. Shown is an example of hexadentate chelation of Fe(III) in the siderophore staphyloferrin A, a binding mode shared by ferrioxamine B. On the right the general pathway of siderophores is illustrated. Siderophores are biosynthesized intracellular before being sent into the extracellular environment via efflux pumps. Iron-bound siderophores then return to the interior of the cell by membrane-bound ABC transporter systems.

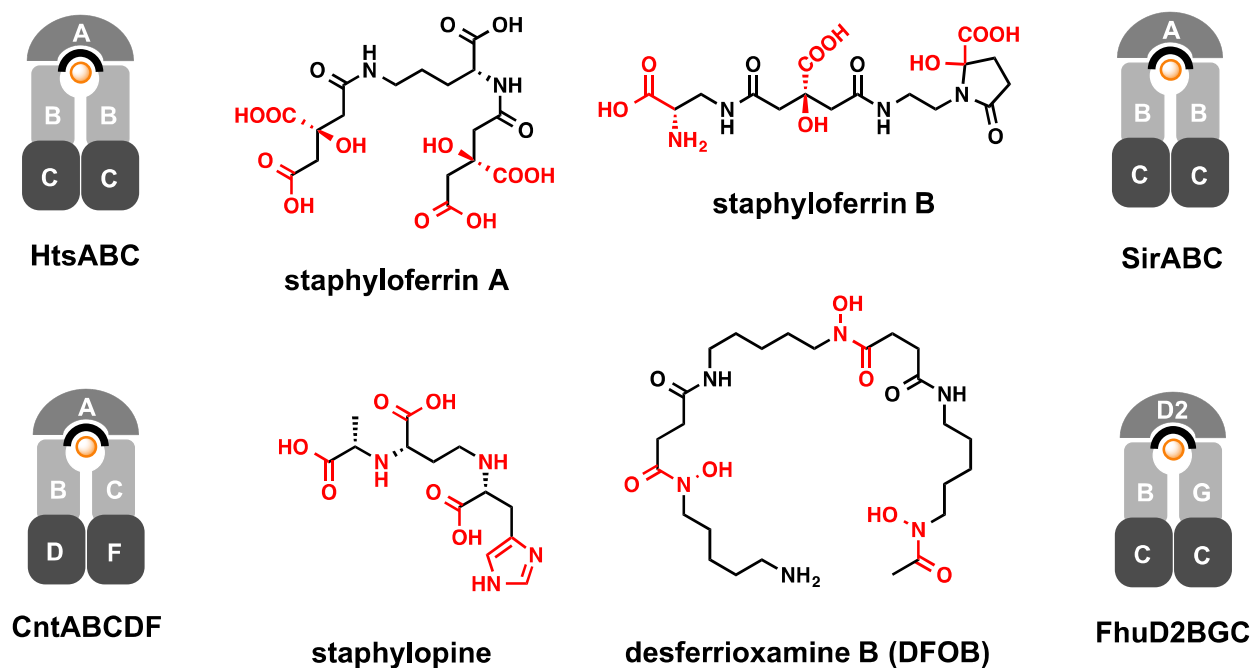


Figure 1.7. Native siderophores and metallophores of *S. aureus* with their corresponding membrane transporter systems. *S. aureus* can notably utilize hydroxamate siderophores such as DFO in addition to its native siderophores, staphyloferrin A and B, as well as its general metallophore, staphylopine.

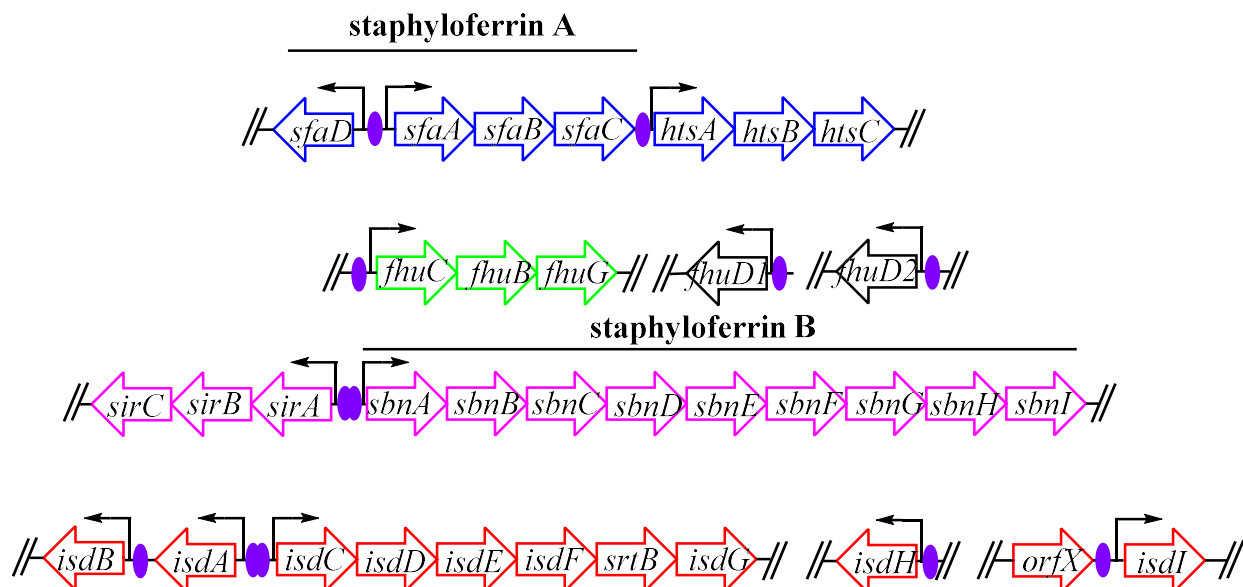


Figure 1.8. Gene loci important for *S. aureus* iron acquisition. For staphyloferrin A biosynthesis, the genes required are encoded by the *sfa* operon. The *sbn* operon genes encode staphyloferrin B biosynthesis. Purple ovals indicate promotor regions that contain a consensus *fur* box. Genes are not to scale.

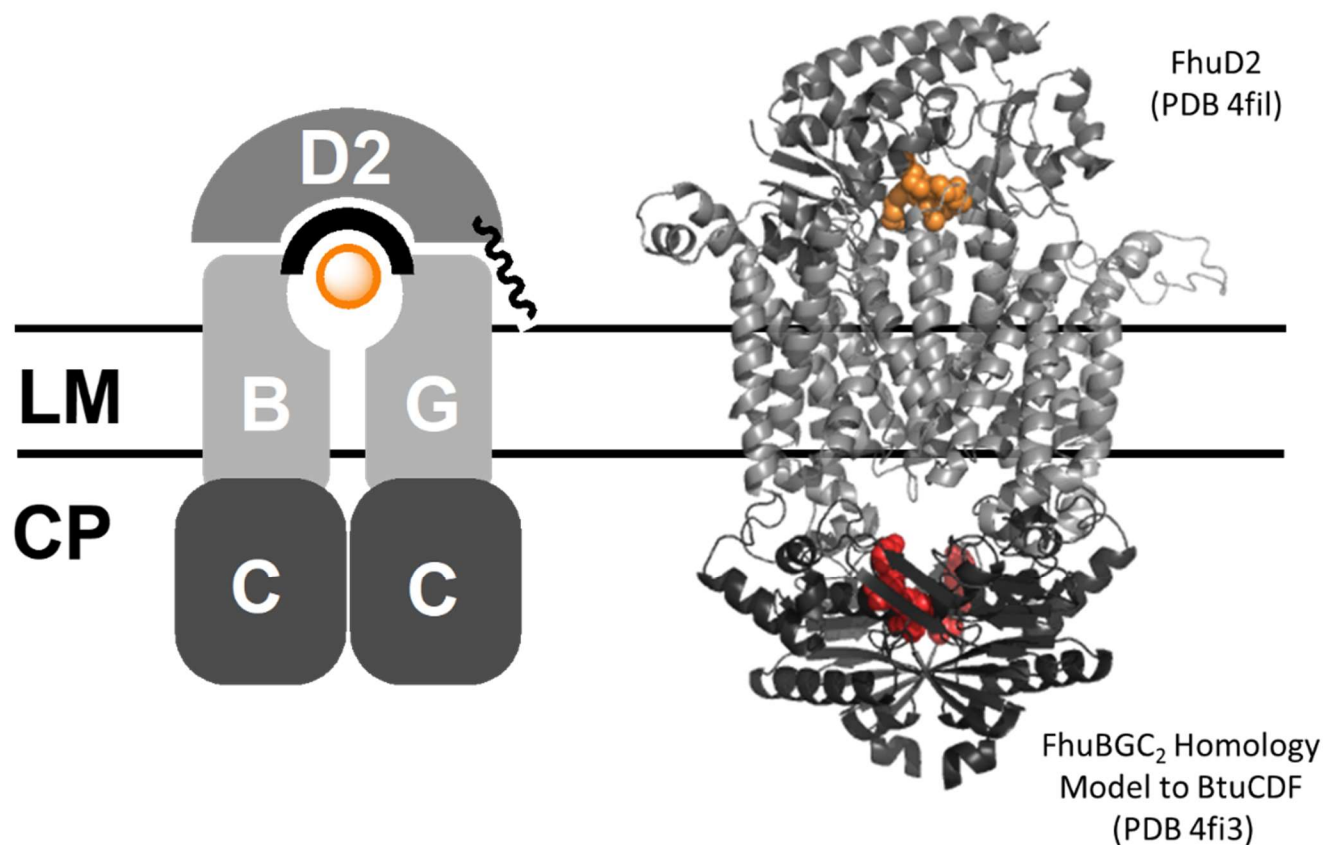


Figure 1.9. Homology model of the Fhu uptake system to BtuCDF. BtuCDF is the bacterial importer of vitamin B₁₂. The molecular dynamics of the NBDs (black, bottom) and the TMDs (light gray, middle) along with the SBP region (dark gray, top) are thought to be highly conserved between the two systems.

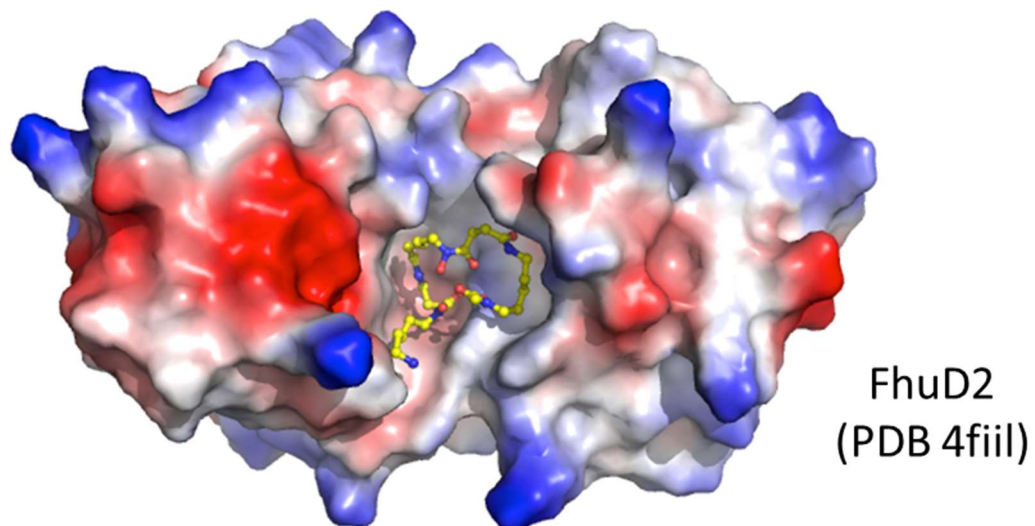


Figure 1.10. FhuD2 binding pocket. The binding pocket of FhuD2 is charge-neutral, allowing for the promiscuous binding of many different siderophore substrates. There only appears to be a single distinct location for siderophore binding. Minimal conformational change occurs when the siderophore is bound.

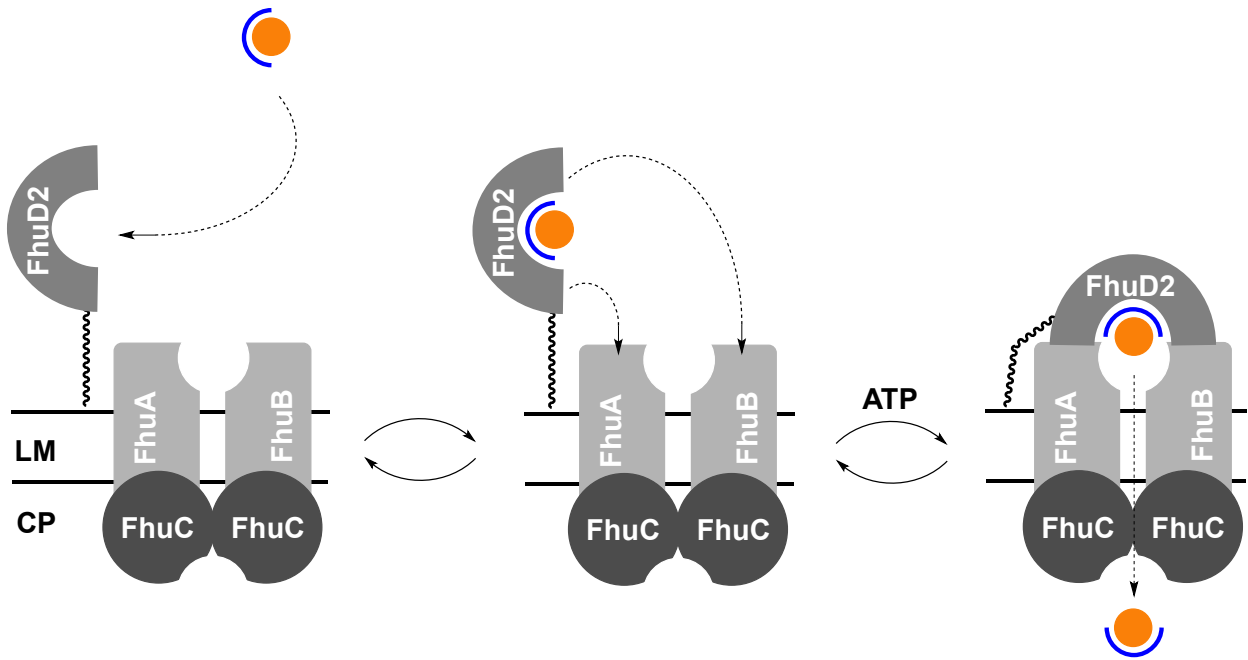


Figure 1.11. Canonical mechanism for cell entry. Seen in the case of the bacterial import of vitamin B₁₂, the canonical pathway only involves a single substrate, pictured here as a *holo*-siderophore, directly binding the SBP and then entering the cell through the ABC transporter.

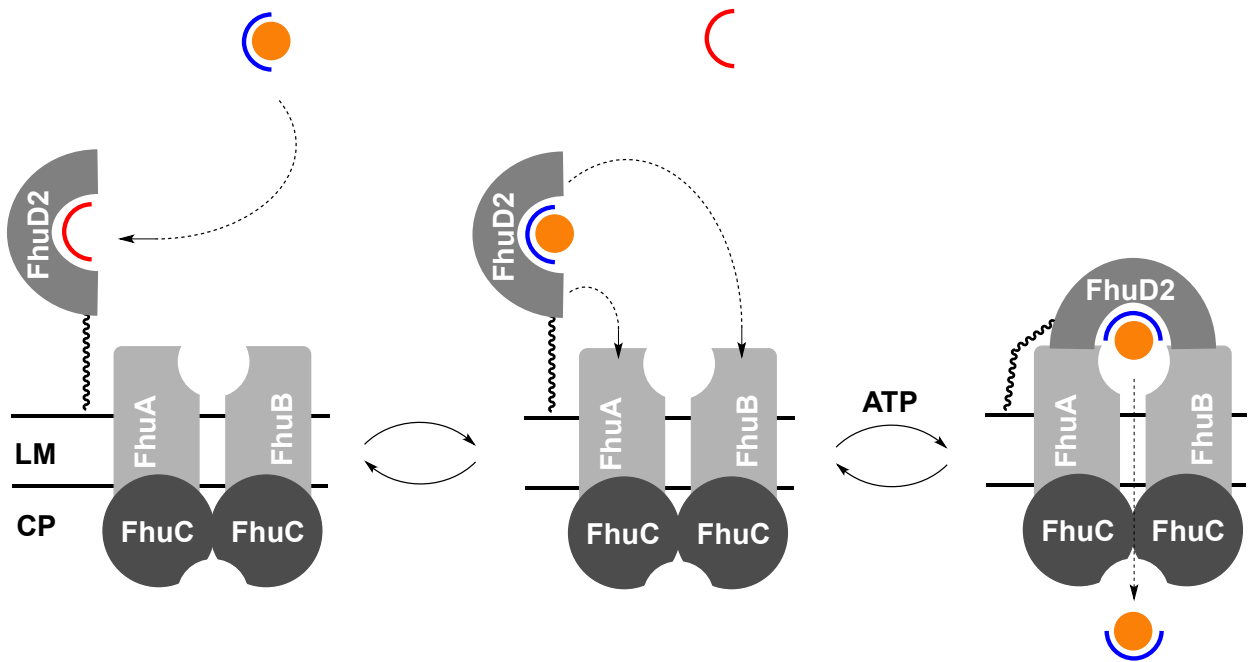


Figure 1.12. Displacement mechanism for cell entry. Unlike the canonical pathway, the displacement mechanism involves two substrates for the system. An incoming *holo*-siderophore displaces an *apo*-siderophore already bound to the SBP, then the *holo*-siderophore that has completed the displacement gains entry into the cell.

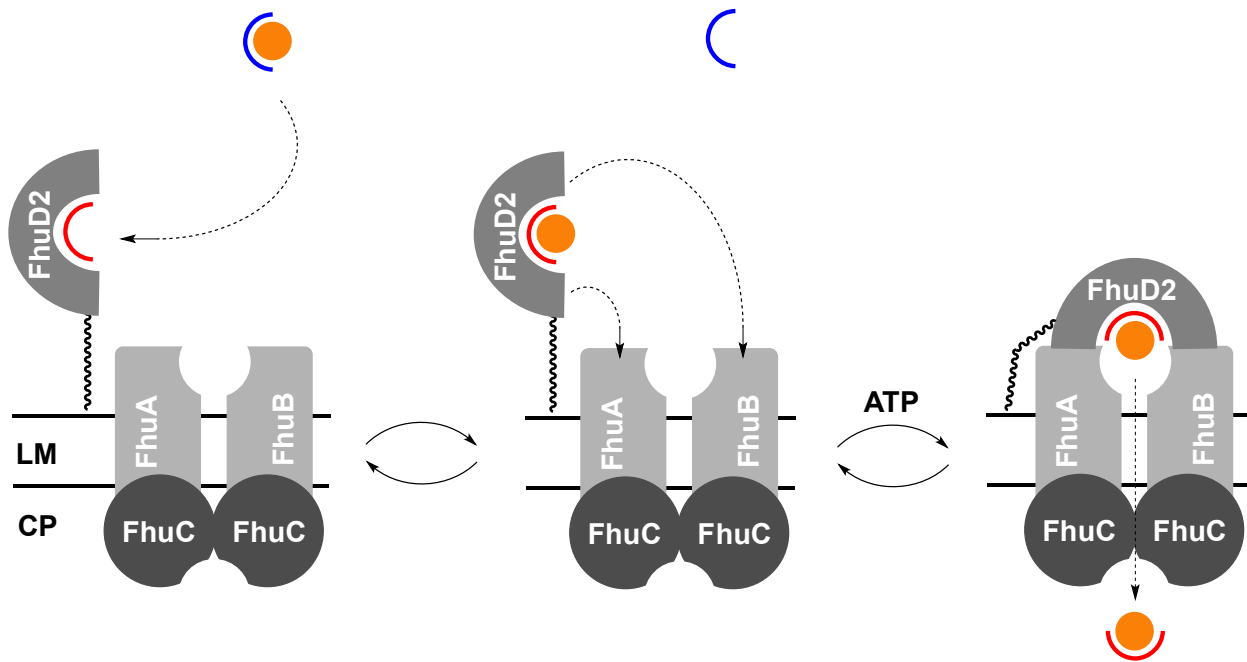


Figure 1.13. Shuttle mechanism for cell entry. The setup for the shuttle mechanism is the same as the displacement mechanism, in which a *holo*-siderophore approaches an *apo*-siderophore already bound to the SBP. Instead of displacing the *apo*-siderophore, the *holo*-siderophore non-reductively transfers its iron to the SBP-bound siderophore, which then enters the cell once it has received the iron.

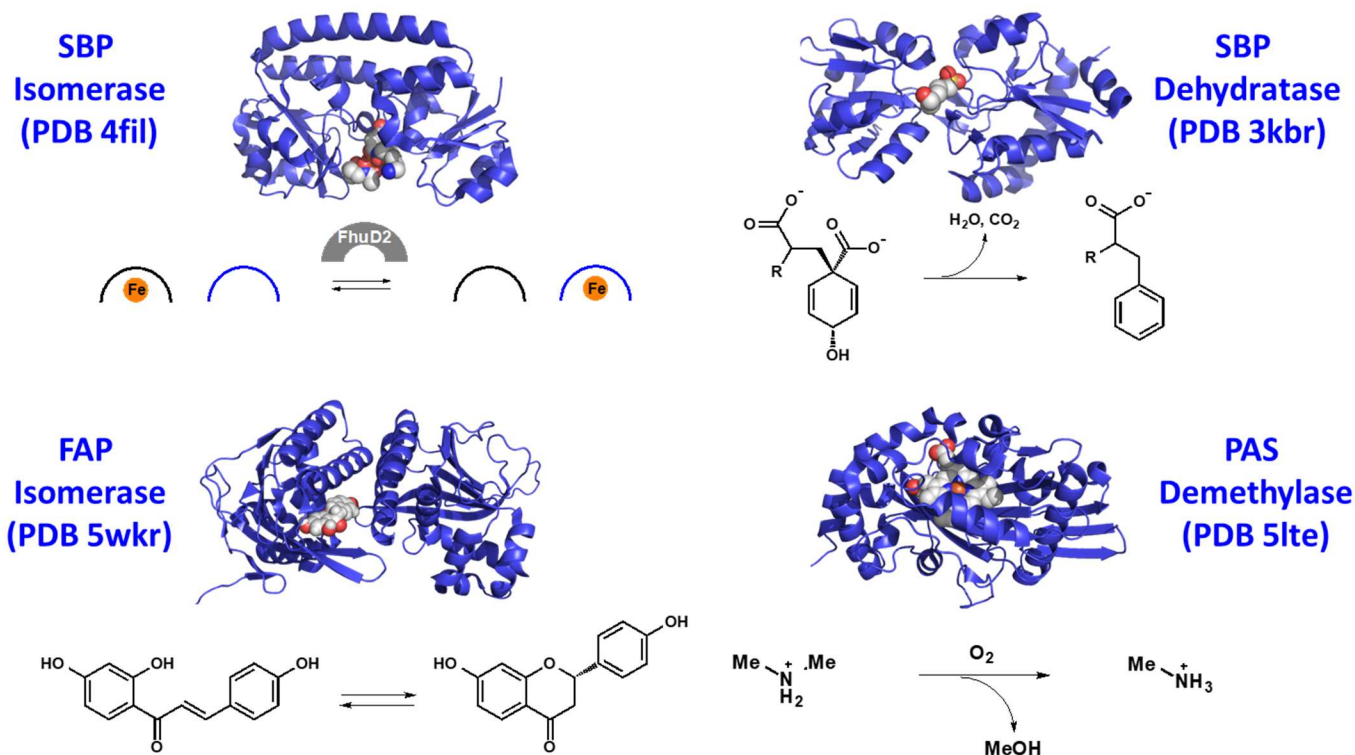


Figure 1.14. Emergence of catalysis in non-catalytic proteins. The shuttle iron mechanism (top left) points to the possibility that FhuD2 plays an enzymatic role in the iron transfer, similar to how catalysis has occurred in other proteins including prephenate dehydrogenase (PDB 3KBR), flavone isomerase (PDB 5WKR), and PAS demethylase (PDB 5LTE).

1.12 References

- [1] Wright GD. (2014) Something new: revisiting natural products in antibiotic drug discovery. *Can J Microbiol.* 60(3):147–154.
- [2] Sengupta S, Chattopadhyay MK, Grossart HP. (2013) The multifaceted roles of antibiotics and antibiotic resistance in nature. *Front Microbiol.* 4:47
- [3] Centers for Disease Control and Prevention, Office of Infectious Disease Antibiotic resistance threats in the United States, (2013) Available at: <http://www.cdc.gov/drugresistance/threat-report-2013>. Accessed February 28, 2019
- [4] Spellberg B, Gilbert DN. (2014) The future of antibiotics and resistance: a tribute to a career of leadership by John Bartlett. *Clin Infect Dis.* 59 (suppl 2):S71–S75.
- [5] Read AF, Woods RJ. (2014) Antibiotic resistance management. *Evol Med Public Health.* 2014(1):147.
- [6] Luyt CE, Bréchet N, Trouillet JL, Chastre J. (2014) Antibiotic stewardship in the intensive care unit. *Crit Care.* 18(5):480.
- [7] Bartlett JG, Gilbert DN, Spellberg B. (2013) Seven ways to preserve the miracle of antibiotics. *Clin Infect Dis.* 56(10):1445–1450.
- [8] Michael CA, Dominey-Howes D, Labbate M. (2014) The antibiotic resistance crisis: causes, consequences, and management. *Front Public Health.* 2:145.
- [9] Golkar Z, Bagasra O, Pace DG. (2014) J Bacteriophage therapy: a potential solution for the antibiotic resistance crisis. *Infect Dev C.* 8(2):129-36.
- [10] Lushniak BD. (2014) Antibiotic resistance: a public health crisis. *Public Health Rep.* 129(4):314-6.
- [11] Piddock LJ Lancet. (2012) The crisis of no new antibiotics--what is the way forward? *Infect Dis.* 12(3):249-53).
- [12] Gross M. (2013) Antibiotics in crisis. *Curr Biol.* 23(24):R1063-5
- [13] Rossolini GM, Arena F, Pecile P, Pollini S. (2014) Update on the antibiotic resistance crisis. *Curr. Opin. Pharmacol.* 18():56-60.
- [14] Pankey GA, Sabath LD. (2004) Clinical relevance of bacteriostatic versus bactericidal mechanisms of action in the treatment of Gram-positive bacterial infections. *Clin Infect Dis.* 38(6), 864-70.
- [15] Bien J, Sokolova O, and Bozko P. J Pathog. (2011) Characterization of virulence factors of *Staphylococcus aureus*: novel function of known virulence factors that are implicated in activation of airway epithelial proinflammatory response. *J Pathog.* 601905.

- [16] Lowy FD. (1998) Staphylococcus aureus infections. *N Engl J Med.* 339(8):520-32.
- [17] Dinges MM, Orwin PM, Schlievert PM. (2000) Exotoxins of Staphylococcus aureus. *Clin Microbiol Rev.* 13(1):16-34.
- [18] Foster TJ. (2005) Immune evasion by staphylococci. *Nat Rev Microbiol.* 3(12):948-58.
- [19] Miles G, Movileanu L, Bayley H. (2002) Subunit composition of a bicomponent toxin: staphylococcal leukocidin forms an octameric transmembrane pore. *Protein Sci.* 11(4):894-902.
- [20] Kaneko J, Kamio Y. (2004) Bacterial two-component and hetero-heptameric pore-forming cytolytic toxins: structures, pore-forming mechanism, and organization of the genes. *Biosci. Biotechnol. Biochem.* 68(5):981-1003.
- [21] Menestrina G, Serra MD, Prévost G. Toxicon. (2001) Mode of action of beta-barrel pore-forming toxins of the staphylococcal alpha-hemolysin family. 39(11):1661-72.
- [22] Holtfreter S, Bröker BM. (2005) Staphylococcal superantigens: do they play a role in sepsis? *Arch Immunol Ther Exp (Warsz).* 53(1):13-27.
- [23] Melish ME, Glasgow LA. (1970) The staphylococcal scalded-skin syndrome. *N Engl J Med.* 282(20):1114-9.
- [24] Morlock BA, Spero L, Johnson AD. (1980) Mitogenic activity of staphylococcal exfoliative toxin. *Infect Immun.* 30(2):381-4.
- [25] Rooijackers SH, Ruyken M, Roos A, Daha MR, Presanis JS, Sim RB, van Wamel WJ, van Kessel KP, van Strijp JA. (2005) Immune evasion by a staphylococcal complement inhibitor that acts on C3 convertases. *Nat Immunol.* 6(9):920-7.
- [26] de Haas CJ, Veldkamp KE, Peschel A, Weerkamp F, Van Wamel WJ, Heezius EC, Poppelier MJ, Van Kessel KP, van Strijp JA. (2004) Chemotaxis inhibitory protein of Staphylococcus aureus, a bacterial antiinflammatory agent. *J Exp Med.* 199(5):687-95.
- [27] Chavakis T, Hussain M, Kanse SM, Peters G, Bretzel RG, Flock JI, Herrmann M, Preissner KT. (2002) Staphylococcus aureus extracellular adherence protein serves as anti-inflammatory factor by inhibiting the recruitment of host leukocytes. *Nat Med.* 8(7):687-93.
- [28] Bokarewa MI, Jin T, Tarkowski A. (2006) Staphylococcus aureus: Staphylokinase. *Int J Biochem Cell Biol.* 38(4):504-9.
- [29] Speziale P, Pietrocola G, Rindi S, Provenzano M, Provenza G, Di Poto A, Visai L, Arciola CR. (2009) Structural and functional role of Staphylococcus aureus surface components recognizing adhesive matrix molecules of the host. *Future Microbiol.* 4(10):1337-52.
- [30] Gómez MI, Lee A, Reddy B, Muir A, Soong G, Pitt A, Cheung A, Prince A. (2004) Staphylococcus aureus protein A induces airway epithelial inflammatory responses by activating TNFR1. *Nat Med.* 10(8):842-8.

- [31] Cheung AL, Projan SJ, Gresham H. (2002) The Genomic Aspect of Virulence, Sepsis, and Resistance to Killing Mechanisms in *Staphylococcus aureus*. *Curr. Infect. Dis. Rep.* 4(5):400-410.
- [32] Roben PW, Salem AN, Silverman GJ. (1995) VH3 family antibodies bind domain D of staphylococcal protein A. *J Immunol.* 154(12):6437-45.
- [33] Foster TJ. (2005) Immune evasion by staphylococci. *Nat Rev Microbiol.* 3(12):948-58.
- [34] Torres VJ, Attia AS, Mason WJ, Hood MI, Corbin BD, Beasley FC, Anderson KL, Stauff DL, McDonald WH, Zimmerman LJ, Friedman DB, Heinrichs DE, Dunman PM, Skaar EP. (2010) *Staphylococcus aureus* fur regulates the expression of virulence factors that contribute to the pathogenesis of pneumonia. *Infect Immun.* 78(4):1618-28.
- [35] Cheung AL, Schmidt K, Bateman B, Manna AC. (2001) SarS, a SarA homolog repressible by agr, is an activator of protein A synthesis in *Staphylococcus aureus*. *Infect Immun.* 69(4):2448-55.
- [36] Projan S, Novick R. (1997) The molecular basis of pathogenicity. In: Archer G, Crossley K, editors. *Staphylococci in Human Diseases*. New York, NY, USA: Churchill Livingstone; pp. 55–81.
- [37] Tegmark K, Karlsson A, Arvidson. (2000) Identification and characterization of SarH1, a new global regulator of virulence gene expression in *Staphylococcus aureus*. *Mol Microbiol.* 37(2):398-409.
- [38] Jin CW, Ye YQ, Zheng SJ. (2014) An underground tale: contribution of microbial activity to plant iron acquisition via ecological processes. *Ann. Bot.* 113(1):7-18.
- [39] Sheldon JR, Heinrichs DE. (2015) Recent developments in understanding the iron acquisition strategies of Gram-positive pathogens. *FEMS Microbiol Rev.* 39(4):592-630.
- [40] Fenton HJH. (1894) Oxidation of tartaric acid in the presence of iron. *J Chem Soc.* 65:899–910.
- [41] Haber F, Weiss H. (1932) On the catalysis of hydroperoxide. *Naturwissenschaften* 20:948–950.
- [42] Imlay JA. (2002) How oxygen damages microbes: oxygen tolerance and obligate anaerobiosis. *Adv Microb Physiol.* 46:111-53.
- [43] Farr SB, Touati D, Kogoma T. (1988) Effects of oxygen stress on membrane functions in *Escherichia coli*: role of HPI catalase. *J Bacteriol.* 170(4):1837-42.
- [44] Drechsel H, Winkelmann G. (1997) Iron chelation and siderophores, p 1–49. In Winkelmann G, Carrano CJ. (ed), *Transition metals in microbial metabolism*. Harwood Academic Publishers, Amsterdam, the Netherlands.

- [45] Roy EM, Griffith KL. (2017) Characterization of novel iron acquisition activity that coordinates the iron response with population density under iron-replete conditions in *Bacillus subtilis*. *J Bacteriol.* 199(1): e00487-16.
- [46] Skaar EP, Humayun M, Bae T, DeBord KL, Schneewind O. (2004) Iron-source preference of *Staphylococcus aureus* infections. *Science.* 305(5690):1626-8.
- [47] Mason WJ, Skaar EP. (2009) Assessing the contribution of heme-iron acquisition to *Staphylococcus aureus* pneumonia using computed tomography. *PLoS One.* 4(8):e6668.
- [48] Lee JW, Helmann. Functional specialization within the Fur family of metalloregulators. (2007) *Biometals.* (3-4):485-99.
- [49] Beasley FC, Vinés ED, Grigg JC, Zheng Q, Liu S, Lajoie GA, Murphy ME, Heinrichs DE. (2009) Characterization of staphyloferrin A biosynthetic and transport mutants in *Staphylococcus aureus*. *Mol Microbiol.* 72(4):947-63.
- [50] Torres VJ, Pishchany G, Humayun M, Schneewind O, Skaar EP. (2006) *Staphylococcus aureus* IsdB is a hemoglobin receptor required for heme iron utilization. *J Bacteriol.* 188(24):8421-9.
- [51] Friedman DB, Stauff DL, Pishchany G, Whitwell CW, Torres VJ, Skaar EP. (2006) *Staphylococcus aureus* redirects central metabolism to increase iron availability. *PLoS Pathog.* 2(8):e87.
- [52] Johnson M, Cockayne A, Williams PH, Morrissey JA. (2005) Iron-responsive regulation of biofilm formation in *Staphylococcus aureus* involves fur-dependent and fur-independent mechanisms. *J Bacteriol.* 187(23):8211-5.
- [53] Horsburgh MJ, Ingham E, Foster SJ. (2001) In *Staphylococcus aureus*, fur is an interactive regulator with PerR, contributes to virulence, and is necessary for oxidative stress resistance through positive regulation of catalase and iron homeostasis. *J Bacteriol.* 183(2):468-75.
- [54] Lankford CE. (1973) Bacterial assimilation of iron. *Crit Rev Microbiol.* 2:273–331.
- [55] Haas H, Eisendle M, Turgeon BG. (2008) Siderophores in fungal physiology and virulence. *Annu Rev Phytopathol.* 46:149-87.
- [56] Kloepper JW, Leong J, Teintze M, Schroth MN. (1980) Enhanced plant growth by siderophores produced by plant growth-promoting rhizobacteria. *Nature.* 286:885–886.
- [57] Johnstone TC, Nolan EM. (2015) Beyond Iron: Non-classical biological functions of bacterial siderophores. *Dalton Trans.* 44(14): 6320-6339.
- [58] Miethke M, Marahiel MA. (2007) Siderophore-based iron acquisition and pathogen control. *Microbiol Mol Biol Rev.* 71(3):413-51.
- [59] Hantke K. (1983) Identification of an iron uptake system specific for coprogen and rhodotorulic acid in *Escherichia coli* K12. *Mol Gen Genet.* 191(2):301-6.

- [60] Bäumler AJ, Hantke K. (1992) Ferrioxamine uptake in *Yersinia enterocolitica*: characterization of the receptor protein FoxA. *Mol Microbiol.* 6(10):1309-21.
- [61] Ghysels B, Ochsner U, Möllman U, Heinisch L, Vasil M, Cornelis P, Matthijs S. (2005) The *Pseudomonas aeruginosa* *pirA* gene encodes a second receptor for ferrienterobactin and synthetic catecholate analogues. *FEMS Microbiol Lett.* 15; 246(2):167-74.
- [62] Valdebenito M, Crumbliss AL, Winkelmann G, Hantke K. (2006) Environmental factors influence the production of enterobactin, salmochelin, aerobactin, and yersiniabactin in *Escherichia coli* strain Nissle 1917. *Int J Med Microbiol.* 296(8):513-20.
- [63] Fischbach MA, Lin H, Liu DR, Walsh CT. (2006) How pathogenic bacteria evade mammalian sabotage in the battle for iron. *Nat Chem Biol.* 2(3):132-8.
- [64] Hantke K, Nicholson G, Rabsch W, Winkelmann G. (2003) Salmochelins, siderophores of *Salmonella enterica* and uropathogenic *Escherichia coli* strains, are recognized by the outer membrane receptor Iron. *Proc Natl Acad Sci U S A.* 100(7):3677-82.
- [65] Ravel J, Cornelis P. (2003) Genomics of pyoverdine-mediated iron uptake in pseudomonads. *Trends Microbiol.* 11(5):195-200.
- [66] Albrecht-Gary AM, Blanc S, Rochel N, Ocaktan AZ, Abdallah MA. (1994) Chemical aspects of siderophore mediated iron transport. *Inorg Chem.* 33:6391–6402.
- [67] Dumas Z, Ross-Gillespie A, Kümmerli R. (2013) Switching between apparently redundant iron-uptake mechanisms benefits bacteria in changeable environments. *Proc Biol Sci.* 280(1764):20131055.
- [68] Baichoo N, Wang T, Ye R, Helmann JD. (2002) Global analysis of the *Bacillus subtilis* Fur regulon and the iron starvation stimulon. *Mol Microbiol.* 45(6):1613-29.
- [69] Hammer ND, Skaar EP. (2011) Molecular mechanisms of *Staphylococcus aureus* iron acquisition. *Annu Rev Microbiol.* 65:129-47.
- [70] Pishchany G, Dickey SE, Skaar EP. (2009) Subcellular localization of the *Staphylococcus aureus* heme iron transport components IsdA and IsdB. *Infect Immun.* 77(7):2624-34.
- [71] Reniere ML, Skaar EP. (2008) *Staphylococcus aureus* haem oxygenases are differentially regulated by iron and haem. *Mol Microbiol.* 69(5):1304-15.
- [72] Friedman DB, Stauff DL, Pishchany G, Whitwell CW, Torres VJ, Skaar EP. (2006) *Staphylococcus aureus* redirects central metabolism to increase iron availability. *PLoS Pathog.* 2(8):e87.
- [73] Friedman DB, Stauff DL, Pishchany G, Whitwell CW, Torres VJ, Skaar EP. (2006) *Staphylococcus aureus* redirects central metabolism to increase iron availability. *PLoS Pathog.* 2(8):e87.

- [74] Courcol RJ, Trivier D, Bissinger MC, Martin GR, Brown MR. (1997) Siderophore production by *Staphylococcus aureus* and identification of iron-regulated proteins. *Infect Immun.* 65(5):1944-8.
- [75] Beasley FC, Vinés ED, Grigg JC, Zheng Q, Liu S, Lajoie GA, Murphy ME, Heinrichs DE. (2009) Characterization of staphyloferrin A biosynthetic and transport mutants in *Staphylococcus aureus*. *Mol Microbiol.* 72(4):947-63.
- [76] Park RY, Sun HY, Choi MH, Bai YH, Shin SH. (2005) *Staphylococcus aureus* siderophore-mediated iron-acquisition system plays a dominant and essential role in the utilization of transferrin-bound iron. *J Microbiol.* 43(2):183-90.
- [77] Cotton JL, Tao J, Balibar CJ. (2009) Identification and characterization of the *Staphylococcus aureus* gene cluster coding for staphyloferrin A. *Biochemistry* 48(5):1025-35.
- [78] Grigg JC, Cooper JD, Cheung J, Heinrichs DE, Murphy ME. (2010) The *Staphylococcus aureus* siderophore receptor HtsA undergoes localized conformational changes to enclose staphyloferrin A in an arginine-rich binding pocket. *J Biol Chem.* 285(15):11162-71.
- [79] Cheung J, Beasley FC, Liu S, Lajoie GA, Heinrichs DE. (2009) Molecular characterization of staphyloferrin B biosynthesis in *Staphylococcus aureus*. *Mol Microbiol.* 74(3):594-608.
- [80] Dale SE, Doherty-Kirby A, Lajoie G, Heinrichs DE. (2004) Role of siderophore biosynthesis in virulence of *Staphylococcus aureus*: identification and characterization of genes involved in production of a siderophore. *Infect Immun.* 72(1):29-37.
- [81] Grigg JC, Cheung J, Heinrichs DE, Murphy ME. (2010) Specificity of Staphyloferrin B recognition by the SirA receptor from *Staphylococcus aureus*. *J Biol Chem.* 285(45):34579-88.
- [82] Song L, Zhang Y, Chen W, Gu T, Zhang SY, Ji Q. (2018) Mechanistic insights into staphylopine-mediated metal acquisition. *PNAS.* 115(15):3942-47.
- [83] Hiron A, et al. (2010) A nickel ABC-transporter of *Staphylococcus aureus* is involved in urinary tract infection. *Mol Microbiol.* 77:1246–1260.
- [84] Lebrette H, et al. (2014) Promiscuous nickel import in human pathogens: Structure, thermodynamics, and evolution of extracytoplasmic nickel-binding proteins. *Structure* 22:1421–1432.
- [85] Lebrette H, et al. (2015) Novel insights into nickel import in *Staphylococcus aureus*: The positive role of free histidine and structural characterization of a new thiazolidine-type nickel chelator. *Metallomics* 7:613–621.
- [86] Grim KP, et al. (2017) The metallophore staphylopine enables *Staphylococcus aureus* to compete with the host for zinc and overcome nutritional immunity. *MBio* 8:e01281-17.

- [87] Remy L, et al. (2013) The *Staphylococcus aureus* Opp1 ABC transporter imports nickel and cobalt in zinc-depleted conditions and contributes to virulence. *Mol Microbiol.* 87:730–743.
- [88] Ghssein G, et al. (2016) Biosynthesis of a broad-spectrum nicotianamine-like metallophore in *Staphylococcus aureus*. *Science* 352:1105–1109.
- [89] Vasiliou V, Vasiliou K, Nebert D. (2009) Human ATP-binding cassette (ABC) transporter family. *Human Genomics.* 3(3): 281-290.
- [90] Verrier PJ, Bird D, Burla B, Dassa E, Forestier C, Geisler M, Klein M, Kolukisaoglu U, Lee Y, Martinoia E, Murphy A, Rea PA, Samuels L, Schulz B, Spalding EJ, Yazaki K, Theodoulou FL. (2008) Plant ABC proteins--a unified nomenclature and updated inventory. *Trends Plant Sci.* 13(4):151-9.
- [91] Dassa E, Bouige P. (2001) The ABC of ABCS: a phylogenetic and functional classification of ABC systems in living organisms. *Res Microbiol.* 152(3-4):211-29.
- [92] Rice AJ, Park A, and Pinkett H. (2014) Diversity in ABC transporters: type I, II and III importers. *Crit Rev Biochem Mol Biol.* 49(5): 426-437.
- [93] Dean M, Rzhetsky A, Allikmets R. (2011) The human ATP-binding cassette (ABC) transporter superfamily. *Genome Res.* 11(7):1156-66.
- [94] Endicott NP, Lee E, Wencewicz TA. (2017) Structural basis for xenosiderophore utilization by the human pathogen *Staphylococcus aureus*. *ACS Infect Dis.* 3(7). 542-553.
- [95] Speziali CD, Dale SE, Henderson JA, Vinés ED, Heinrichs DE. (2006) Requirement of *Staphylococcus aureus* ATP-binding cassette-ATPase FhuC for iron-restricted growth and evidence that it functions with more than one iron transporter. *J Bacteriol.* 188(6):2048-55.
- [96] Sebulskey MT, Hohnstein D, Hunter MD, Heinrichs DE. (2000) Identification and characterization of a membrane permease involved in iron-hydroxamate transport in *Staphylococcus aureus*. *J Bacteriol.* 182(16):4394-400.
- [97] Sebulskey MT, Shilton BH, Speziali CD, Heinrichs DE. (2003) The role of FhuD2 in iron(III)-hydroxamate transport in *Staphylococcus aureus*. Demonstration that FhuD2 binds iron(III)-hydroxamates but with minimal conformational change and implication of mutations on transport. *J Biol Chem.* 278(50):49890-900.
- [98] Sebulskey MT, Speziali CD, Shilton BH, Edgell DR, Heinrichs DE. (2004) FhuD1, a ferric hydroxamate-binding lipoprotein in *Staphylococcus aureus*: a case of gene duplication and lateral transfer. *J Biol Chem.* 279(51):53152-9.
- [99] Brock JH, Ng J. (1983) The Effect of Desferrioxamine on the Growth of *Staphylococcus-Aureus*, *Yersinia-Enterocolitica* and *Streptococcus-Faecalis* in Human-Serum - Uptake of Desferrioxamine-Bound Iron. *Fems Microbiology Letters.* 20:439–42.

- [100] Wu D., Wen X., Liu W., Hu H., Ye B., Zhou Y. (2018) Comparison of the effects of deferasirox, deferoxamine, and combination of deferasirox and deferoxamine on an aplastic anemia mouse model complicated with iron overload. *Drug Des. Dev. Ther.* 12:1081–1091.
- [101] Wencewicz TA, Long TE, Mollmann U, Miller MJ. (2013) Trihydroximate siderophore-fluoroquinolone conjugates are selective sideromycin antibiotics that target *Staphylococcus aureus*. *Bioconjug Chem.* 24(3): 473-486.
- [102] Vera DR, Smith CC, Bixby LM, Glatt DM, Dunn SS, Saito R, Kim WY, Serody JS, Vincent BG, Parrott MC. (2018) Immuno-PET imaging of tumor-infiltrating lymphocytes using zirconium-89 radiolabeled anti-CD3 antibody in immune-competent mice bearing syngeneic tumors. *PLoS One.* 13(3): e0193832.
- [103] You L, Wang J, Liu T, Zhang Y, Han X, Wang T, Guo S, Dong T, Xu J, Anderson G, Liu Q, Chang YZ, Lou X, Nie G. (2018) Targeted brain delivery of rabies virus glycoprotein 29-modified deferoxamine-loaded nanoparticles reverses functional deficits in parkinsonian mice. *ACS Nano.* 12(5): 4123-4139.
- [104] Guo JP, Pan JX, Xiong L, Xia WF, Cui S, Xiong WC. (2015) Iron chelation inhibits osteoclastic differentiation in vitro and in Tg2576 mouse model of Alzheimer's disease. *PLoS One.* 10(11): e0139395.
- [105] Bajbouj K, Shafarin J, Hamad M. (2018) High-dose deferoxamine treatment disrupts intracellular iron homeostasis, reduces growth, and induces apoptosis in metastatic and nonmetastatic breast cancer cell lines. *Technol Cancer Res Treat.* 17: 1-11.
- [106] Cloonan SM, Glass K, Laucho-Contreras ME, Bhashyam AR, Cervo M, Pabon MA, Konrad C, Plverino F, Siempos II, Perez E, Mizumura K, Ghosh MC, Parameswaran H, Williams NC, Rooney KT, Chen ZH, Goldklang MP, Yuan GC, Moore SC, Demeo DL, Rouault TA, D'Armiento JM, Schon EA, Manfredi G, Quackenbush J, Mahmood A, Silverman EK, Own CA, Choi AM. (2016) Mitochondrial iron chelation ameliorates cigarette smoke-induced bronchitis and emphysema in mice. *Nat Med.* 22(2): 163-74.
- [107] Min Yang, Nurit Livnat Levanon, Burçin Acar, Burcu Aykac Fas, Gal Masrati, Jessica Rose, Nir Ben-Tal, Turkan Haliloglu, Yongfang Zhao, and Oded Lewinson. (2018) Single-molecule probing of the conformational homogeneity of the ABC transporter BtuCD. *Nature Chem Biology.* 14; 715–722.
- [108] Fukushima, T.; Allred, B. E.; Sia, A. K.; Nichiporuk, R.; Andersen, U. N.; Raymond, K. N. (2013) Gram-positive siderophore-shuttle with iron-exchange from Fe-siderophore to apo-siderophore by *Bacillus cereus* YxeB. *Proc. Natl. Acad. Sci. U.S.A.* 110, 13821.
- [109] Fukushima, T.; Allred, B. E.; Raymond, K. N. (2014) Direct Evidence of iron uptake by the gram-positive siderophore-shuttle mechanism without iron reduction. *ACS Chem. Biol.* 9, 2092.

- [110] Mariotti P, Malito E, Biancucci M, Lo Surdo P, Mishra RP, Nardi-Dei V, Savino S, Nissum M, Spraggon G, Grandi G, Bagnoli F, Bottomley MJ. (2013) Structural and functional characterization of the *Staphylococcus aureus* virulence factor and vaccine candidate FhuD2. *Biochem J.* 449(3):683-93.

Chapter 2: Structural Basis for
Xenosiderophore Utilization by the Human
Pathogen *Staphylococcus aureus*

2.1 Preface

This chapter was adapted with permission from an article of the same title published in ACS Infectious Diseases by Nathaniel P. Endicott, Eries Lee and Timothy A. Wencewicz.

2.2 Abstract

Staphylococcus aureus produces a cocktail of metallophores (staphylopine, staphyloferrin A, and staphyloferrin B) to scavenge transition metals during infection of a host. In addition, *S. aureus* displays the extracellular surface lipoproteins FhuD1 and FhuD2 along with the ABC transporter complex FhuCBG to facilitate the use of hydroxamate xenosiderophores such as desferrioxamine B (**DFOB**) for iron acquisition. **DFOB** is used as a chelation therapy to treat human iron overload diseases and has been linked to an increased risk of *S. aureus* infections. We used a panel of synthetic **DFOB** analogs and a FhuD2-selective trihydroxamate sideromycin to probe xenosiderophore utilization in *S. aureus* and establish structure-activity relationships for Fe(III) binding, FhuD2 binding, *S. aureus* growth promotion, and competition for *S. aureus* cell entry. Fe(III) binding assays and FhuD2 intrinsic fluorescence quenching experiments revealed that diverse chemical modifications of the terminal ends of linear ferrioxamine siderophores influences Fe(III) affinity, but not FhuD2 binding. Siderophore-sideromycin competition assays and xenosiderophore growth promotion assays revealed that *S. aureus* SG511 and ATCC 11632 can distinguish between competing siderophores based exclusively on net charge of the siderophore-Fe(III) complex. Our work provides a roadmap for tuning hydroxamate xenosiderophore scaffolds to suppress (net negative charge) or enhance (net positive or neutral charge) uptake by *S. aureus* for applications in metal chelation therapy and siderophore-mediated antibiotic delivery, respectively.

2.1 Introduction

Staphylococcus aureus is a Gram-positive human pathogen responsible for nearly 50% of all deaths in US hospitals caused by antibiotic resistant bacteria and fungi (>11,000 deaths per year)¹. Highly virulent phenotypes of *S. aureus*, including the methicillin-resistant (MRSA) phenotype, are often multi-drug resistant (MDR) and can be community-associated²⁻⁴. MRSA pathogens rely on a variety of virulence factors to evade the host immune system and enhance fitness (**Table 2.1**)⁵. Many virulence factors are associated with nutrient acquisition, which is central to pathogen proliferation^{6,7}. Nutritional immunity is an important part of the human innate immune response to infection⁸. During an infection, the labile pool of transition metals such as Fe, Cu, Ni, Co, Mn, and Zn is restricted and bacterial pathogens must scavenge these scarce nutrients to survive⁹.

S. aureus produces a cocktail of small molecule metallophores including staphylopine^{10,11}, staphyloferrin A^{12,13}, and staphyloferrin B¹⁴⁻¹⁶ for transition metal scavenging during infection. Staphylopine is a nicotianamine-like metallophore that facilitates Cu(II), Ni(II), Co(II), Zn(II), and Fe(II) acquisition^{10,11}. Staphyloferrin A and B are polycarboxylate siderophores with a high selectivity for Fe(III)¹²⁻¹⁶. In addition to endogenous siderophore production, *S. aureus* can utilize heme and xenosiderophores, siderophores pirated from the infection environment, as bioavailable sources of Fe(III)^{6,7}. Xenosiderophore utilization by *S. aureus* confers a special fitness advantage by placing the metabolic burden of siderophore biosynthesis on neighboring organisms^{17,18}. Natural and semi-synthetic siderophores are attractive chemical scaffolds for medicinal chemistry programs aimed at developing metal chelators for treating human diseases including iron overload¹⁹, cancer^{20,21}, chronic obstructive pulmonary disease (COPD)²², malaria^{23,24}, wound

healing²⁵, and Parkinson's²⁶. Siderophores have also been explored clinically as antibiotic delivery agents for treating bacterial infections and medical imaging agents for diagnosing human diseases such as cancer and bacterial infections²⁷⁻²⁹. However, siderophore-based pharmaceutical agents have been linked to an increased risk of infection from pathogens that are capable of utilizing the siderophore active ingredients as xenosiderophores for iron acquisition in the host³⁰. Desferrioxamine B (**DFOB**), a linear trihydroxamate siderophore produced by *Streptomyces pilosus*, is FDA approved for the treatment of human iron overload diseases and is on the World Health Organization's list of essential medicines¹⁹. **DFOB** use is a predisposing factor for infection by bacterial pathogens including *S. aureus*³¹, *Yersinia enterocolitica*³², and *Salmonella enterica*³³, which is a leading cause of death in β -thalassemia patients receiving frequent blood transfusions. There is continued interest in developing new structural analogs of **DFOB** with improved pharmacological properties and *in vivo* efficacy²⁶. We suggest that investigating xenosiderophore utilization of siderophore pharmaceuticals during lead optimization might be a good strategy to minimize the risk of infection during human use.

DFOB utilization in highly virulent *S. aureus* pathogens has been linked to the *fhuBCDG* genes³⁴, which are under transcriptional regulation by ferric uptake regulator (FUR) DNA-binding sequences³⁵. Two copies of the *fhuD* gene, *fhuD1* and *fhuD2*, are present in *S. aureus* genomes. Both *fhuD1* and *fhuD2* encode for siderophore-binding surface-displayed lipoproteins³⁶. The ferric hydroxamate operon, *fhuBCG*, encodes for a membrane embedded ATP-dependent transporter complex that is required for xenosiderophore active transport³⁴. FhuBG is a permease dedicated to xenosiderophore transport, while FhuC is a multi-functional ATPase that interfaces with FhuBG and the permeases required for staphyloferrin A and B transport, HtsBC and SirBC, respectively³⁷. FhuD1 and FhuD2 bind a diverse set of hydroxamate-containing xenosiderophores including

DFOB, ferrichrome, coprogen, and aerobactin^{38,39}. FhuD1 is dispensable for *S. aureus* growth under iron limiting conditions, while FhuD2 is essential for hydroxamate xenosiderophore utilization and is a virulence factor for *S. aureus* that has been exploited for vaccine development^{40,41}. CntA¹⁰, SirA⁴², HtsA⁴³, and SstD⁴³ are also surface-displayed lipoproteins associated with *S. aureus* virulence. CntA, SirA, and HtsA bind the endogenous *S. aureus* metallophores staphylopine, staphyloferrin A, and staphyloferrin B, respectively, and SstD binds catechol-containing siderophores. *S. aureus* pathogens are well equipped to utilize hydroxamate, α -hydroxycarboxylate, and catechol structural classes of siderophores for iron acquisition by expressing FhuD1/FhuD2, SirA/HtsA, and SstD lipoproteins, respectively, along with compatible ATP-dependent permeases.

FhuD1 and FhuD2 are also involved in the transport of hydroxamate-based sideromycins, siderophore antibiotic conjugates (SACs), including salmycin, albomycin, ferrimycin, and synthetic SACs featuring ferrichrome and **DFOB**-like siderophore components^{36,39}. Adaptive resistance to the salmycins, linear trihydroxamate-aminoglycoside sideromycins produced by *Streptomyces violaceus*, occurs via mutations in *fhuD2* leading to antibiotic exclusion⁴⁴⁻⁴⁶. Such adaptive resistance is suppressed in mouse models of infection because FhuD2 is essential for virulence⁴⁶. Danoxamine-ciprofloxacin (**Dan-Cip**) is a synthetic SAC designed to mimic the natural salmycins⁴⁷. The antibiotic activity of **Dan-Cip** is strongly antagonized in the presence of competing trihydroxamate siderophores including **DFOB** and the parent siderophore danoxamine (**Dan**). FhuD2 is known to tightly bind trihydroxamate siderophores including **DFOB** and analogs thereof with nanomolar affinity suggesting that *S. aureus* utilization of these molecules as xenosiderophores might be nonspecific³⁹. However, **DFOB** and the corresponding Fe(III) complex ferrioxamine B (**FOB**) more strongly antagonize the antibacterial activity of **Dan-Cip** than **Dan**

and its Fe(III) complex **Dan-Fe** suggesting that *S. aureus* can distinguish between competing trihydroxamate siderophores despite the high promiscuity of FhuD2 siderophore binding and the structural similarity of **DFOB** and **Dan**.

In this work we systematically explored the structural basis for hydroxamate xenosiderophore utilization by human pathogenic *S. aureus* using a rationally designed panel of synthetic **DFOB** and **Dan** analogs (**SDFOB** and compounds **1–17**; **Fig. 2.1**). We utilized **Dan-Cip** as a chemical probe for xenosiderophore utilization in *S. aureus* SG511. We measured the apparent Fe(III) affinity constants (K_{Fe}), apparent FhuD2 binding constants (K_d), and *S. aureus* SG511 minimum inhibitory concentrations (MICs) in the presence of competing **Dan-Cip** for all members of the trihydroxamate siderophore panel (**Table 2.2**). We found that net siderophore charge is the most important physiochemical property for determining xenosiderophore utilization by *S. aureus* SG511 and *S. aureus* ATCC 11632. The structure-function relationships described in this work will help to guide the development of siderophore-based molecules for applications in medical imaging and the treatment of iron overload and infectious diseases⁴⁸.

2.4 Results and Discussion

Design and Synthesis of a Ferrioxamine Siderophore Library

Dozens of naturally occurring trihydroxamate ferrioxamine siderophores are reported in the chemical literature⁴⁹. Ferrioxamine siderophores are biosynthesized by a non-ribosomal peptide synthetase-independent pathway using alternating succinic acid and *N*-hydroxy-cadaverine or *N*-hydroxy-putrescine units^{50–52}. The spacing between hydroxamate metal chelating groups governed by the succinate and cadaverine units is ideal for chelating Fe(III) in a stable 1:1 siderophore:metal complex with octahedral geometry^{53,54}. Natural and synthetic structural variants

of **DFOB** are commonly modified at the amino terminus⁴⁹. Acylation of the **DFOB** primary amine decreases water solubility, slows clearance of iron from human blood, and increases intracellular iron sequestration in human cell lines^{55,56}. Microbes produce structural variants of ferrioxamine siderophores to gain an evolutionary advantage through selective siderophore uptake, quorum sensing, growth promotion, or growth suppression of neighboring microbes^{17,18,57,58}. Siderophore acylation has also been shown to promote self-assembly in aqueous environments, enhance membrane affinity, and promote surface adhesion⁵⁹⁻⁶². We synthesized a library of ferrioxamine siderophores built on repeating succinic acid and *N*-hydroxy-cadaverine units to probe the effects of polarity, net charge, and sterics on Fe(III) affinity, FhuD2 binding, and *S. aureus* utilization (Fig. 2.1 and Fig. 2.2–2.4)^{63,64}.

DFOB is a linear trihydroxamate siderophore with free amine and *N*-acetyl termini and a net charge of +1 when bound to Fe(III)⁵³. Reaction of **DFOB** with succinic anhydride gives **SDFOB** with a net charge of -1 when bound to Fe(III)⁶⁵. **Dan** also carries a net negative charge and is found as the naturally occurring siderophore portion of the salmycin sideromycins, which are biosynthesized from three units of succinate, two units of *N*-hydroxy-cadaverine, and one unit of *N*-hydroxy-5-amino-1-pentanol⁶⁶. We completed a total synthesis of **Dan** and analogs **1-16** using a previously reported benzyl protecting group strategy (Scheme 2.1)^{45,47,63,64,67,68}. **Dan** and analogs **1-4** have a hydroxyl and carboxyl termini and a predicted net charge of -1 when bound to Fe(III). We also prepared methyl esters **5-9**, amides **10** and **11**, sulfonamides **12** and **13**, acetylated analog **14**, and alcohol **15** as charge neutral variants. Analog **16** has an amine terminus and will have a net +1 charge when bound to Fe(III). We synthesized a charge neutral macrocyclic analog **17** using an Fe(III)-templated Yamaguchi macrolactonization⁶⁴.

Side Chains Influence Kinetic and Thermodynamic Fe(III) Complex Stability

We used an EDTA metal exchange assay to measure the apparent Fe(III) affinity constants (K_{Fe}) of **DFOB**, **Dan**, **SDFOB**, **Dan-Cip** and analogs **1–17** at pH 7.4 (**Fig. 2.5**; **Table 2.2**; **Fig. 2.6**)⁶⁹. All the siderophore-Fe(III) complexes were purified by recrystallization and showed a distinct λ_{max} optical absorbance between 420-430 nm with extinction coefficients of $\sim 3000 \text{ M}^{-1}\text{cm}^{-1}$. A solution of each siderophore-Fe(III) complex at 0.1 μM in pH 7.4 buffer (10 mM HEPES, 600 mM NaCl, 100 mM KCl) in a 1 cm cuvette gave a starting absorbance of 0.1-0.2 units. Solutions were treated with 1.2 equivalents of EDTA and monitored continuously by optical absorbance at 430 nm for 90 min or until equilibrium was reached. **DFOB** had the highest affinity for Fe(III), $K_{\text{Fe}} = 10^{30.3}$; a value consistent with previous literature reports^{70,71}. **SDFOB** showed a 10-fold decrease in Fe(III) affinity, $K_{\text{Fe}} = 10^{29}$, relative to **DFOB**. Changing the primary amine of **DFOB** to a primary alcohol in analog **16** resulted in a reduction of Fe(III) binding affinity by four orders of magnitude ($K_{\text{Fe}} = 10^{26.3}$). We measured K_{Fe} values ranging from 10^{26} – 10^{28} for **Dan**, **Dan-Cip**, and analogs **1–15**, which all have a primary alcohol terminus (**Fig. 2.5c**). The primary amine of **DFOB** is protonated at pH 7.4, while the primary alcohol of **Dan** and analogs **1–16** is free to interact with the oxophilic Fe(III) and might destabilize the metal complex through intramolecular ligand displacement⁷⁰. Macrocyclization of siderophores is known to increase K_{Fe} by preorganizing the ligands for metal chelation⁶⁹. The K_{Fe} value for desferrioxamine E, a macrolactam trihydroxamate siderophore, was reported to be $10^{32.5}$, which is a 100-fold increase in K_{Fe} compared to linear **DFOB**. In contrast, macrolactone **17** had ~ 100 -fold lower Fe(III) affinity, $K_{\text{Fe}} = 10^{25.4}$, than linear **Dan** suggesting that forcing ester closer the Fe(III) center through macrocyclization destabilizes the metal complex.

Siderophore side chain substituents can interact with the Fe(III) metal center. The relative rate of methyl ester hydrolysis for the Fe(III) complexes of siderophores **5–8** at pH 10 increases with proximity of the methyl ester to Fe(III) ($t_{1/2}$: **5** > **6** > **7** > **8**) suggesting that the Fe(III) interacts with the ester as a Lewis acid or participate in water activation during hydrolysis⁶⁴. The rate limiting step of Fe(III) release from a trihydroxamate siderophore-Fe(III) complex is dissociation of the first hydroxamate ligand through water displacement on the Fe(III) center⁷⁰. We found that the Fe(III) complexes of **Dan**, **Dan-Cip**, and analogs **1–17** were more kinetically labile than **FOB** in the EDTA metal exchange assay (**Fig. 2.5b**; **Fig. 2.6,2.7**). The primary alcohol might displace the first hydroxamate ligand in an intramolecular reaction to speed up dissociation of Fe(III) from the siderophore during metal exchange with EDTA⁷⁰.

Side Chains do not Influence FhuD2 Binding

We recombinantly expressed the soluble siderophore-binding domain of *S. aureus* FhuD2 with an *N*-terminal hexahistadine tag. We purified *N*-His₆-FhuD2 by Ni-NTA affinity chromatography (**Fig. 2.8**; **Tables 2.3,2.4**). We used an intrinsic fluorescence quenching assay to assess whether *N*-His₆-FhuD2 can bind **DFOB**, **FOB**, **Dan**, **Dan-Fe**, as well as the Fe(III) complexes of **SDFOB**, **Dan-Cip**, and analogs **1-17** (**Fig. 2.9a**; **Table 2.2**)⁷². FhuD2 is known to bind the iron-free, **DFOB**, and iron-bound, **FOB**, forms of trihydroxamate siderophores^{72,73}. We observed dose-dependent fluorescence quenching when treating *N*-His₆-FhuD2 with iron-free, **DFOB** and **Dan**, and iron-bound, **FOB** and **Dan-Fe**, trihydroxamate siderophores (**Fig. 2.9b**). The apparent dissociation constants for **DFOB** ($K_d = 90.7 \pm 11.9$ nM) and **Dan** ($K_d = 70.5 \pm 11.1$ nM) were ~2-fold higher than the corresponding Fe(III) complexes **FOB** ($K_d = 48.4 \pm 6.6$ nM) and **Dan-Fe** ($K_d = 39.4 \pm 2.9$ nM) (**Table 2.2**). The fluorescence of purified recombinant *N*-His₆-FhuD2 from *S. aureus* was quenched in a dose dependent manner by all of the siderophores in our panel (**Fig. 2.9c**; **Fig. 2.10**).

Apparent dissociation constants (K_d) ranged from 39–189 nM regardless of Fe(III) affinity, side chain polarity, steric bulk, or net siderophore charge. Attachment of ciprofloxacin, a fluoroquinolone antibiotic, to the succinyl terminus of **Dan** did not significantly impact FhuD2 binding (K_d for **Dan-Cip** = 93.9 ± 23.5 nM). Our results confirm that FhuD2 is a promiscuous ferrioxamine siderophore-binding protein in pathogenic *S. aureus*.

Net Siderophore Charge Influences Xenosiderophore Utilization by S. aureus

We used a siderophore-sideromycin competition assay to assess xenosiderophore utilization by *S. aureus* SG511 (**Fig. 2.11**; **Table 2.2**)⁴⁷. We used the broth microdilution method for MIC determination to quantitatively assess the ability of the iron-free and Fe(III)-bound forms of siderophores **DFOB**, **Dan**, **SDFOB**, and **1–16** to antagonize the antibacterial activity of iron-free **Dan-Cip** against *S. aureus* SG511 under iron deficient media conditions (Mueller-Hinton broth No. 2 supplemented with 2,2'-dipyridyl). **Dan-Cip** alone gave an MIC value of 1 μ M against *S. aureus* SG511. None of the iron-free or Fe(III)-bound siderophores inhibited the growth of *S. aureus* SG511. We measured MIC values for 1:1 stoichiometric ratios of **Dan-Cip**:competing siderophore. MIC values ≥ 4 μ M were judged to be a result of the competing siderophore antagonizing the active transport **Dan-Cip** to the cytoplasm of *S. aureus* SG511 where the DNA gyrase target of the fluoroquinolone antibiotic resides⁷⁴. Despite the ability of FhuD2 to bind all siderophores with nanomolar affinity, we observed that only siderophores with a net positive charge (**DFOB** and **16**) or neutral charge (**5**, **6**, and **8–14**) antagonized the growth inhibitory activity of **Dan-Cip** towards *S. aureus* SG511. Siderophores with a net negative charge (**Dan**, **SDFOB**, **1–4**) had no effect on **Dan-Cip** activity when supplemented in the iron-free and Fe(III)-bound forms. **DFOB** and siderophore **10** were the most antagonistic towards the antibacterial activity of **Dan-Cip**, giving MIC values ≥ 128 μ M in both the iron-free and Fe(III)-bound forms.

The preformed Fe(III) complexes of siderophores **5–9** and **11–16** (MIC values ≥ 64 – $128\ \mu\text{M}$) were better antagonists than the iron-free forms (MIC values ≥ 16 – $64\ \mu\text{M}$) in the **Dan-Cip** competition assay (**Table 2.2**; **Fig. 2.11b, 2.11c**). There was no apparent correlation between antagonism of **Dan-Cip** antibacterial activity and siderophore K_{Fe} , apparent K_{d} for FhuD2, or kinetic stability of the siderophore-Fe(III) complex.

We confirmed that antagonism of **Dan-Cip** antibacterial activity was a direct result of transport competition by analyzing *S. aureus* ATCC 11632 growth curves under highly growth restrictive iron limiting conditions with siderophore supplementation (**Fig. 2.12**; **Fig. 2.13**). The growth of *S. aureus* ATCC 11632 was severely halted at $37\ ^\circ\text{C}$ over an 84-hour growth period in TMS minimal media treated with $200\ \mu\text{M}$ 2,2'-dipyridyl. We evaluated the ability of **FOB** (net +1 charge), **Dan-Fe** (net -1 charge), **5-Fe** (charge neutral), and **16-Fe** (net +1 charge) to rescue the growth of *S. aureus* ATCC 11632. **FOB** boosted *S. aureus* ATCC 11632 growth starting at a concentration of $5\ \mu\text{M}$ with full growth recovery observed starting at $20\ \mu\text{M}$. Siderophores **16-Fe**, **5-Fe**, and **Dan-Fe** promoted *S. aureus* ATCC 11632 growth at $40\ \mu\text{M}$, $80\ \mu\text{M}$, and $320\ \mu\text{M}$, respectively. **Figure 5** compares growth curves for *S. aureus* ATCC 11632 in the presence of $1.28\ \text{mM}$ **FOB**, **Dan-Fe**, **5-Fe**, and **16-Fe** and highlights the preference for utilization of the positively charged siderophores **FOB** and **16-Fe** over neutral and charge negative siderophores **5-Fe** and **Dan-Fe**, respectively, which is consistent with the trend for siderophore transport observed in the **Dan-Cip** sideromycin competition assay (**Fig. 2.11**).

2.5 Further Discussion and Conclusions

X-ray crystal structures of FhuD2 and other siderophore binding proteins show that amino acid residues in the ligand binding site do not make direct contacts to the Fe(III) metal center of bound siderophore-Fe(III) complexes⁷⁵. Specificity for siderophore ligands arises from non-covalent interactions with the metal chelating groups and the siderophore backbone. Tris-catechol binding surfaces are typically rich in positively charged amino acid side chains to accommodate the net -3 charge of a tris-catecholate Fe(III) complex⁷⁶. Polycarboxylate ligand binding sites also present a positively charged platform to ensure favorable electrostatics upon siderophore binding⁷⁷. HtsA binds staphyloferrin A using nine siderophore-interacting residues including six arginines, one tyrosine, one histidine, and one lysine^{77,78}. SirA binds staphyloferrin B using similar ionic interactions⁷⁹. FhuD2 presents a charge neutral surface suitable for binding positively charged, negatively charged, and charge neutral ferrioxamine siderophores (**Fig. 2.14**)³⁸.

HtsA and SirA undergo large conformational changes upon binding the endogenous *S. aureus* siderophores staphyloferrin A and staphyloferrin B, respectively^{78,79}. Electrostatic interactions play an important role in HtsA and SirA siderophore binding⁷⁷. FhuD2 undergoes a modest conformational change upon siderophore binding that might enable broad utilization of hydroxamate-based xenosiderophores³⁸. The charge neutral siderophore binding pocket accommodates positively charged, negatively charged, and charge neutral hydroxamate siderophores. Although FhuD2 is promiscuous for binding hydroxamate siderophores, our results suggest that other cellular factors play a role in xenosiderophore utilization. *S. aureus* SG511 showed a strong preference for transporting positively charged and charge neutral trihydroxamate siderophores over negatively charged analogs in siderophore-sideromycin competition assays

(**Fig. 2.11**). The same preference for siderophore charge was also observed in growth promotion assays using *S. aureus* ATCC 11632 (**Fig. 2.12**). We propose that xenosiderophore utilization in *S. aureus* depends primarily on net siderophore charge and is not influenced by FhuD2 affinity, Fe(III) affinity, or kinetic stability of the siderophore-Fe(III) complex.

The origin of charge preference for trihydroxamate xenosiderophore utilization by *S. aureus* is unclear. One explanation could be that the *S. aureus* cell envelope carries a strong net negative charge due to the high density of phosphatidylglycerol^{80,81} and teichoic acids⁸²⁻⁸⁴. The net negative charge of the *S. aureus* cell envelope depends on the number of lysyl-phosphatidylglycerol molecules and D-Ala teichoic acid esters. Teichoic acids, phosphatidylglycerols, and cell envelope charge play roles in virulence, biofilm formation, cell adhesion, motility, antibiotic permeability, and antibiotic resistance^{85,86}. We hypothesize that the negatively charged *S. aureus* cell envelope electrostatically repels negatively charged xenosiderophores, which decreases the local concentration of xenosiderophores around the *S. aureus* lipid membrane. Adaptive resistance to the salmycins suggests that FhuD2 is the primary receptor for trihydroxamate xenosiderophores in *S. aureus*⁴⁴. Therefore, it is unlikely that an alternate siderophore-binding protein is responsible for the charge preference of xenosiderophore utilization. Results from the siderophore-sideromycin competition assay suggest that the ferrioxamine xenosiderophores used in this study were in direct competition for transport with **Dan-Cip**, which we presume depends on FhuD2 for cell entry much like the structurally related salmycins⁴⁴.

A better understanding of siderophore membrane transport paradigms is critical for rationalizing xenosiderophore utilization in *S. aureus* pathogens⁸⁷. Two membrane transport paradigms based on shuttle and displacement mechanisms have been proposed^{72,73,88}. In the

siderophore shuttle mechanism the siderophore receptor first binds to Fe-free siderophore and catalyzes iron exchange from a second siderophore-Fe(III) complex prior to influx. Direct evidence for the siderophore shuttle mechanism has been obtained using recombinant YxeB from *B. subtilis* as a catalyst for Fe(III) exchange between **DFOB** and acetylferrioxamine B^{72,73}. In the siderophore displacement mechanism metal free siderophore bound to receptor is displaced by an incoming siderophore-Fe(III) complex that gains cell entry. Our results support that the displacement mechanism is possible. FhuD2 binds negatively charged trihydroxamate siderophores with nanomolar affinity. Charge negative xenosiderophores, such as **Dan**, moderately promote *S. aureus* ATCC 11632 growth under iron restrictive conditions. However, charge negative siderophores fail to gain cell entry when in competition with **Dan-Cip**, a charge neutral sideromycin. Hence, the measured dissociation constants of FhuD2 for siderophores are not fully predictive of xenosiderophore utilization. FhuD2 complexes with negatively charged siderophores might be kinetically labile leading to a preference for displacement mechanisms when competing with positively charged or charge neutral siderophores that might have an increased dwell time on FhuD2⁸⁹.

Our work suggests that the structure of linear ferrioxamine siderophores can be optimized through modification of the termini to suppress or enhance xenosiderophore utilization by *S. aureus* and other pathogens that express FhuD2 as a virulence factor (**Fig. 2.10**). Suppression of xenosiderophore utilization by pathogenic bacteria is desirable for use of siderophores as treatments for iron overload diseases. **DFOB** and other metal chelators including deferasirox and deferiprone are widely used to treat human iron overload diseases^{19,90}. There is growing interest in developing new metal chelators, including structural variants of **DFOB**, that show improved efficacy and better patient compliance (**DFOB** is administered via infusion pump leading to low

patient compliance)²⁶. **DFOB** and related trihydroxamate siderophores also show promise as possible therapeutic agents for treating malaria^{23,24}, cancer^{20,21}, diseases associated with ferroptosis⁹¹, COPD²², renal protection⁹², and neurological disorders such as Parkinson's²⁶. **DFOB** use has been linked to an increased risk of infection, a leading cause of death in thalassemia major patients³¹⁻³³. New structural variants of **DFOB** are needed to fully explore the increasing number of new medical applications for siderophore-based chelation therapies⁴⁸. Our work serves as a starting point for optimizing the **DFOB** structure to hinder xenosiderophore utilization by potential bacterial pathogens such as *S. aureus* while maintaining a high-affinity for Fe(III). Hindering xenosiderophore utilization by human pathogens might decrease the risk of infection during administration of siderophore-based chelation therapies³⁰. Conversion of the **DFOB** primary amine to a primary alcohol results in a 100-fold decrease in K_{Fe} , which might decrease the efficiency of iron clearance during chelation therapy and still enables xenosiderophore utilization by *S. aureus*. Succinylation of the amino terminus gives **SDFOB**, which suffers a smaller 10-fold decrease in K_{Fe} and hinders xenosiderophore utilization by pathogenic *S. aureus*. Future efforts to improve ferrioxamine siderophores for medical applications in metal chelation-based therapies should focus on structural modifications that make net siderophore charge negative and avoid oxophilic terminal functional groups near the Fe(III) metal center to maintain high K_{Fe} and provide maximum kinetic stability of the siderophore-Fe(III) complex. To enhance ferrioxamine xenosiderophore utilization by *S. aureus* for potential diagnostic and antibiotic delivery applications the net siderophore charge should be neutral or positive. Steric bulk close to the Fe(III) metal center decreases K_{Fe} so linkers should be used to provide enough space between the siderophore and molecular cargo to optimize metal chelation and receptor binding.

Our results support the need for more functional xenosiderophore selection screens using bacterial pathogens to inform the use of siderophores in medical and environmental applications⁹³⁻⁹⁸. Competition with environmental xenosiderophores and endogenous siderophores produced by the pathogen of interest must be considered. To ensure efficacy and block adaptive resistance during siderophore applications in antibiotic delivery, it is imperative that the siderophore delivery vector outcompetes endogenous pathogen siderophores and that siderophore transport proteins are required for virulence^{27,99}. FhuD2 is required *S. aureus* virulence and we show that ferrioxamine siderophores can be structurally tuned for transport based on net charge. FhuD2 promiscuously binds ferrioxamine siderophores and we found that siderophore receptor binding alone is not predictive of xenosiderophore utilization and membrane transport. Here we showed that sideromycins (siderophore-antibiotic conjugates) can be used as chemical probes for evaluating xenosiderophore utilization by pathogens of interest. Siderophore-sideromycin competition assays can be used to establish structure-function relationships that will guide the design of improved siderophore-based metal chelation therapies and pathogen-targeted sideromycin antibiotics.

2.6 Materials and Methods

Strains, Materials, and Instrumentation

Siderophore-sideromycin competition assays and bacterial growth promotion studies were performed with *S. aureus* SG511 (kindly provided by Dr. Ute Möllmann) and *S. aureus* ATCC 11632, respectively (**Table 2.5**). All media and buffers were prepared using distilled deionized H₂O. All bacterial cells were stored at –80 °C as glycerol stocks and transformations were performed via electroporation using a MicroPulser Electroporator (Bio-Rad). All siderophores and sideromycins used in this study were synthesized as described previously^{47,63,64} and obtained

through a material transfer agreement with the University of Notre Dame (**Scheme 2.1**). **DFOB** was purchased from Sigma-Aldrich (St. Louis, MO). The pET28-*fhuD2* plasmid was codon optimized, sequenced, and cloned for protein expression in *E. coli* BL21 (DE3) by GenScript. *E. coli* TOP10 cells were purchased from Invitrogen and *E. coli* BL21-Gold(DE3) cells were purchased from Agilent. Nickel-nitrilotriacetic acid (Ni-NTA) agarose was purchased from Invitrogen. Any kD SDS-PAGE gels were purchased from Bio-Rad. All buffers, salts, and chemical reagents were purchased from Sigma-Aldrich, unless otherwise stated. All pH measurements were recorded on an Orion Star A111 pH meter and a PerpHecT Ross micro pH electrode from ThermoFisher. Bacterial growth curves were measured using a Molecular Devices SpectraMax Plus 384 plate reader using sterile round-bottom polystyrene 96-well plates with sterile polystyrene lids. Optical absorbance spectroscopy was performed on a Cary 50 with autosampler and water Peltier thermostat using methacrylate cuvettes.

Determination of K_{Fe}

Apparent siderophore Fe(III) affinity values (K_{Fe}) were measured using an EDTA competition experiment according to a literature protocol⁶⁹. Pure siderophore-Fe(III) complex (**Dan-Fe**, **FOB**, **SFOB**, **Dan-Cip-Fe**, **1-Fe–17-Fe**) was dissolved in pH 7.4 HEPES buffer (10 mM HEPES, 600 mM NaCl, 100 mM KCl) to a final concentration of 0.1 μ M and treated with 1.2 equivalents of EDTA to give a total volume of 1 mL. The mixture was analyzed continuously for 90 min, or until equilibrium was reached, at 1 scan/s by optical absorbance spectroscopy at 430 nm in a methacrylate cuvette. The absorbance at 430 nm decreased over time for each siderophore-Fe(III) complex with pseudo first-order kinetics. Iron(III) exchange $t_{1/2}$ values were calculated by fitting the exponential decay plots to a pseudo first-order rate equation using GraphPad Prism version 7.0b (**Fig. 2.6,2.7**). The decrease in absorbance at 430 nm correlates directly with exchange

of Fe(III) from the siderophore to EDTA. Siderophore K_{Fe} values were calculated from the difference in absorbance at 430 nm before and after addition of EDTA as described previously (**Equations 2.1–2.11**)⁶⁹. An extinction coefficient of $3000 \text{ M}^{-1} \text{ cm}^{-1}$ was used for all siderophore-Fe(III) complexes. A K_{Fe} value of $10^{25.1}$ was used for EDTA at pH 7.4 in all calculations^{49,100}. All experiments were performed in triplicate as independent trials.

Purification of N-His₆-FhuD2

A 5 mL culture of *E. coli* BL21-Gold(DE3) containing the pET28a-*fhuD2* plasmid was grown overnight in LB containing 50 µg/mL kanamycin with agitation at 37 °C. A 200 µL aliquot was used to inoculate 500 mL of terrific broth (12 g/L tryptone, 24 g/L yeast extract, 5 g/L glycerol, 17 mM KH₂PO₄, 72 mM K₂HPO₄) containing 50 µg/mL kanamycin. The culture was grown at 37 °C with shaking until the OD₆₀₀ reached ~0.4. The culture was cooled on ice and protein expression was induced by addition of 500 µL of a sterile 0.5 M aqueous solution of IPTG. The culture was shaken at 15 °C for 18 hrs and cells were isolated by centrifugation (5,000 rpm, 20 min, 4 °C). The cell pellet was washed and suspended in 40 mL of cold lysis buffer (50 mM K₂HPO₄, 500 mM NaCl, 5 mM β-mercaptoethanol, 20 mM imidazole, 10% glycerol, pH 8). The cell suspension was flash frozen, thawed, and lysed by two passages through an Emulsiflex C5 cell disruptor (Avestin). Cell lysate was clarified by ultracentrifugation (45,000 rpm, 35 min, 4 °C) and the supernatant was treated with Ni-NTA resin and rocked gently for ~30 min. The flow-through was discarded and the Ni-NTA resin was washed twice with cold lysis buffer (40 mL) and eluted five times with 10 mL aliquots of elution buffer (50 mM K₂HPO₄, 500 mM NaCl, 5 mM β-mercaptoethanol, 300 mM imidazole, 10% glycerol, pH 8). Elution fractions were analyzed by SDS-PAGE with Coomassie blue visualization (**Fig. 2.7**). Fractions containing pure N-His₆-FhuD2 were combined and dialyzed

overnight in 1.8 L phosphate buffer (50 mM K₂HPO₄, 150 mM NaCl, 1 mM DTT, pH 8) using 10,000 MWCO SnakeSkin dialysis tubing (ThermoFisher). Protein was concentrated by centrifugal filtration using a 10,000 MWCO membrane (Amicon Ultra 15 mL; EMD Millipore), flask frozen in liquid nitrogen as 50 µL aliquots and stored at -80 °C at a final concentration of 1.8 mM.

FhuD2 Binding Studies

N-His₆-FhuD2 was recovered from a -80 °C freezer stock and thawed on ice. Stock protein solutions at 5.4 µM were prepared in TBS buffer (25 mM Tris-HCl, 8 g/L NaCl, 0.2 g/L KCl, pH 7.4) and diluted 1:50 in TBS buffer to acquire ~100 nM solutions of *N*-His₆-FhuD2 for fluorescence quenching assays^{72,73}. Stock solutions of siderophores (**DFOB**, **FOB**, **SFOB**, **Dan**, **Dan-Fe**, **Dan-Cip-Fe**, and **1-Fe-17-Fe**) were prepared in H₂O at 2 mM. Increasing concentrations of siderophore (final siderophore concentrations: 0 nM, 26.7 nM, 53.2 nM, 79.5 nM, 105.6 nM, 171 nM, 299 nM, 422 nM, 881 nM) were added to a solution of *N*-His₆-FhuD2 (~100 nM final concentration) in TBS buffer (final volume was 300 µL). The maximum fluorescence of each siderophore/*N*-His₆-FhuD2 solution was measured (typically at ~340 nm) in a HellmaAnalytics High Precision Cell cuvette made of Quartz SUPRASIL (light path was 10 x 2 mm) using a PerkinElmer LS 55 Luminescence Spectrometer (emission analyzed at 300–400 nm with an excitation λ of 280 nm, emission slits set to 10 nm, and a scan speed of 400 nm/min). Fluorescence intensity versus siderophore concentration was plotted and the apparent *K*_d of *N*-His₆-FhuD2 for each siderophore was calculated by nonlinear regression using a one binding site model in GraphPad Prism v7.0b (**Fig. 2.15**). All experiments were performed in triplicate as independent trials.

Siderophore-Sideromycin Competition Assay

Assay was performed as described previously⁴⁷. Minimum inhibitory concentrations (MICs) were measured using the broth microdilution method following the Clinical and Laboratory Standards Institute (CLSI) guidelines¹⁰¹. Each well of a 96-well plate was filled with 50 μ L of sterile Mueller-Hinton No. 2 (MHII) broth made Fe-deficient with 2,2-dipyridyl (0.8 mL of a 1 mg/mL filter sterilized aqueous solution of 2,2'-dipyridyl added to 49.2 mL of sterile MHII broth). Equimolar solutions of **Dan-Cip** and each siderophore (**DFOB**, **FOB**, **SDFOB**, **SFOB**, **Dan**, **Dan-Fe**, **1-6**, **8-16**, **1-Fe-6-Fe**, and **8-Fe-16-Fe**) were prepared at 512 μ M in sterile Fe-deficient MHII broth. 50 μ L of the compound solutions were added to the first well of the 96-well plate and diluted two-fold down each row. 50 μ L of *S. aureus* SG511 inoculum (5×10^5 cfu/mL in MHII broth) was added to each well giving a final volume of 100 μ L/well and a concentration range of 128–0.0625 μ M for each test compound. Plates were covered with lids and incubated at 37 °C for 18 hrs. The MIC was judged to be the lowest concentration (μ M) of compounds inhibiting visible bacterial growth relative to a DMSO or H₂O control. Ciprofloxacin was included as a positive control at a concentration range of 32– 0.0156 μ M and gave a recorded MIC of 0.5 μ M.

S. aureus Growth Studies

A fresh overnight culture of *S. aureus* ATCC 11632 was grown in sterile LB broth at 37 °C from frozen glycerol stocks. A 0.5 McFarland standard¹⁰² (OD₆₀₀ ~0.8–1) was prepared as the plate inoculum in filter sterilized, Fe-deficient TMS media (12.1 g/L Tris-base, 16.6 g/L succinic acid, 10 g/L casamino acids, 40 mL of salt solution (14.5 g NaCl, 9.25 g KCl, 2.75 g NH₄Cl, 3.55 g cysteine, 4.23 g thiamine, 0.31 g nicotinic acid, 2.5 mg biotin, 23.9 g MgCl₂, 2.78 g CaCl₂ in 100

mL H₂O), and 200 μ M 2,2'-dipyridyl, pH 7.4)¹⁶. Each well of a sterile 96-well plate was filled with 50 μ L of TMS media. 50 μ L of siderophore (**FOB**, **Dan-Fe**, **5-Fe**, or **16-Fe**) in sterile TMS media was added to the first column of the plate at a final concentration of 2560 μ M. Siderophores were diluted two-fold down the plate and each well of the plate was then treated with 50 μ L of inoculum to give final siderophore concentrations of 1280–1.25 μ M for **FOB** and **Dan-Fe**. Siderophores **5-Fe** and **16-Fe** were analyzed at final concentrations of 1280–40 μ M. Plates were covered with sterile lids and incubated at 37 °C. The final volume of each well was 100 μ L. The OD₆₀₀ of each well was measured continuously over 90 hrs using a SpectraMax Plus 384 Microplate Reader (**Fig. 2.16**). Plates were agitated prior to measurement of OD₆₀₀ and each growth curve was generated in triplicate against a TMS media control.

2.6 Acknowledgements

We thank Dr. John-Stephen Taylor (WUSTL, Dept. of Chemistry) for assistance with fluorescence quenching assays and helpful discussion. Compounds **1-17** and **Dan-Cip** were synthesized by TAW and obtained through a material transfer agreement (MTA) with the University of Notre Dame and Prof. Marvin J. Miller.

2.6 Tables and Figures

Table 2.1. Known iron acquisition virulence factors and associated genes in *S. aureus* pathogens.¹

Iron Source	<i>S. aureus</i> Genes
Heme Binding, extraction, and import	<i>isdAB, isdH, isdCDEF, srtB, srtA</i>
Degradation	<i>isdG, isdI, iruO</i>
Sensing and export	<i>hssRS-hrtAB</i>
Endogenous siderophores	Staphyloferrin A, Staphyloferrin B
Synthesis and export	Staphyloferrin A: <i>sfaABC, sfaD</i> Staphyloferrin B: <i>sbnA-I</i>
Import and iron release	Staphyloferrin A: <i>htsABC</i> Staphyloferrin B: <i>sirABC</i>
Xenosiderophores	Desferrioxamine B, ferrichrome, aerobactin, coprogen
Hydroxamate	<i>fhuBGC₂, fhuD1, fhuD2</i>
Catecholate	<i>sstABCD</i>
Inorganic Iron (ferrous iron transport proteins)	<i>feoAB, fepABC</i>
Major transcriptional regulator	<i>fur</i>

¹Table adapted from reference 1.

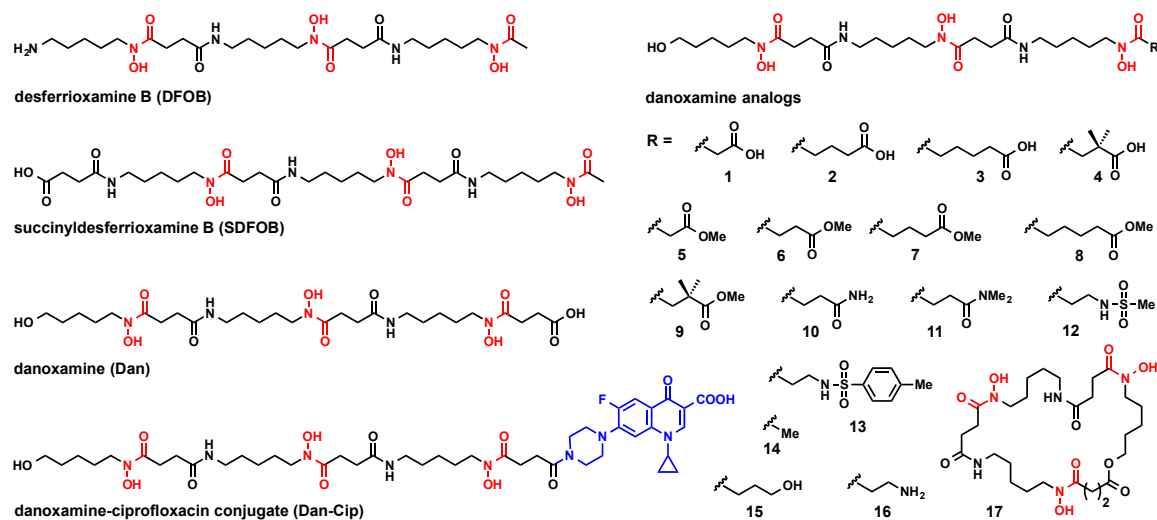


Figure 2.1. Chemical structures of *S. aureus* xenosiderophores and sideromycins utilized in this work. Siderophore backbones are shown in black, metal chelating groups are shown in red, and sideromycin antibiotic components are shown in blue.

Table 2.2. Net charge, apparent log K_{Fe} values, MIC values for siderophore-sideromycin competition, and apparent FhuD2 K_d values for ferrioxamine siderophores. ^aLog K_{Fe} values were determined by an EDTA competition assay using optical absorbance spectroscopy, and standard deviations were determined from three independent experiments. ^bMIC values were against *S. aureus* SG511 using a 1:1 molar ratio of **Dan-Cip** and the competing siderophore-Fe(III) complex (**FOB**, **Dan-Fe**, **SFOB**, or **1-Fe-17-Fe**). MICs were determined in triplicate using the broth microdilution method in MHII media containing 2,2-dipyridyl following the CLSI guidelines. ^cMIC values represent a 1:1 molar ratio of **Dan-Cip** and the competing siderophore (**DFOB**, **Dan**, **SDFOB**, or **1-17**). ^dFhuD2 K_d values were determined by fluorescence quenching, and standard deviations were determined from at least three independent experiments. K_d value is for the siderophore-Fe(III) complex. ^e K_d value is for the Fe-free siderophore.

Siderophore	Net Charge at pH 7.4	log K_{Fe} ^a	MIC w/ Fe (μ M) ^b	MIC w/o Fe (μ M) ^c	FhuD2 K_d (nM)
DFOB	+1	30.3 \pm 0.4	>128	128	48 \pm 7 ^d 91 \pm 12 ^e
Dan	-1	27.8 \pm 0.3	1	1	39 \pm 3 ^d 71 \pm 11 ^e
SDFOB	-1	29.0 \pm 0.1	0.5	0.5	67 \pm 13 ^d
Dan-Cip	0	25.6 \pm 0.1	1	N/A	94 \pm 24 ^d
1	-1	27.9 \pm 0.2	1	1	78 \pm 10 ^d
2	-1	28.0 \pm 0.1	1	1	125 \pm 43 ^d
3	-1	26.0 \pm 0.1	1	1	N/A
4	-1	25.6 \pm 0.2	2	2	152 \pm 81 ^d
5	0	27.7 \pm 0.1	128	16	193 \pm 23 ^d
6	0	26.1 \pm 0.2	128	32	46 \pm 12 ^d
7	0	27.5 \pm 0.1	N/A	N/A	46 \pm 6 ^d
8	0	28.2 \pm 0.1	128	64	114 \pm 23 ^d
9	0	28.2 \pm 0.3	128	32	102 \pm 21 ^d
10	0	27.9 \pm 0.1	128	64	55 \pm 10 ^d
11	0	27.4 \pm 0.1	64	32	70 \pm 13 ^d
12	0	27.3 \pm 0.1	64	32	65 \pm 13 ^d
13	0	28.0 \pm 0.1	128	64	49 \pm 10 ^d
14	0	26.3 \pm 0.5	128	64	71 \pm 17 ^d
15	0	25.7 \pm 0.2	64	16	189 \pm 53 ^d
16	+1	27.2 \pm 0.1	>128	128	76 \pm 11 ^d
17	0	25.4 \pm 0.1	N/A	N/A	81 \pm 21 ^d

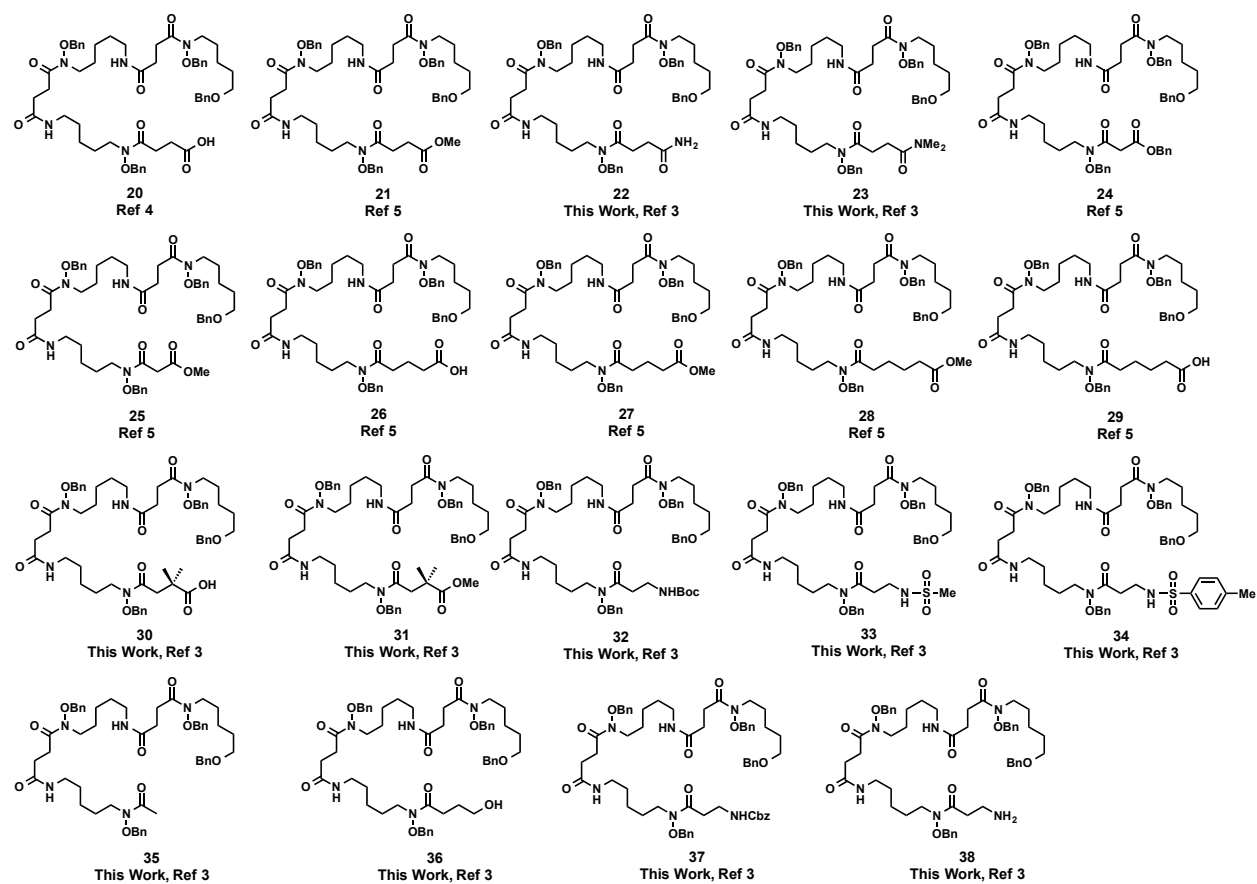


Figure 2.2. Structures of benzyl protected siderophores 20–38.

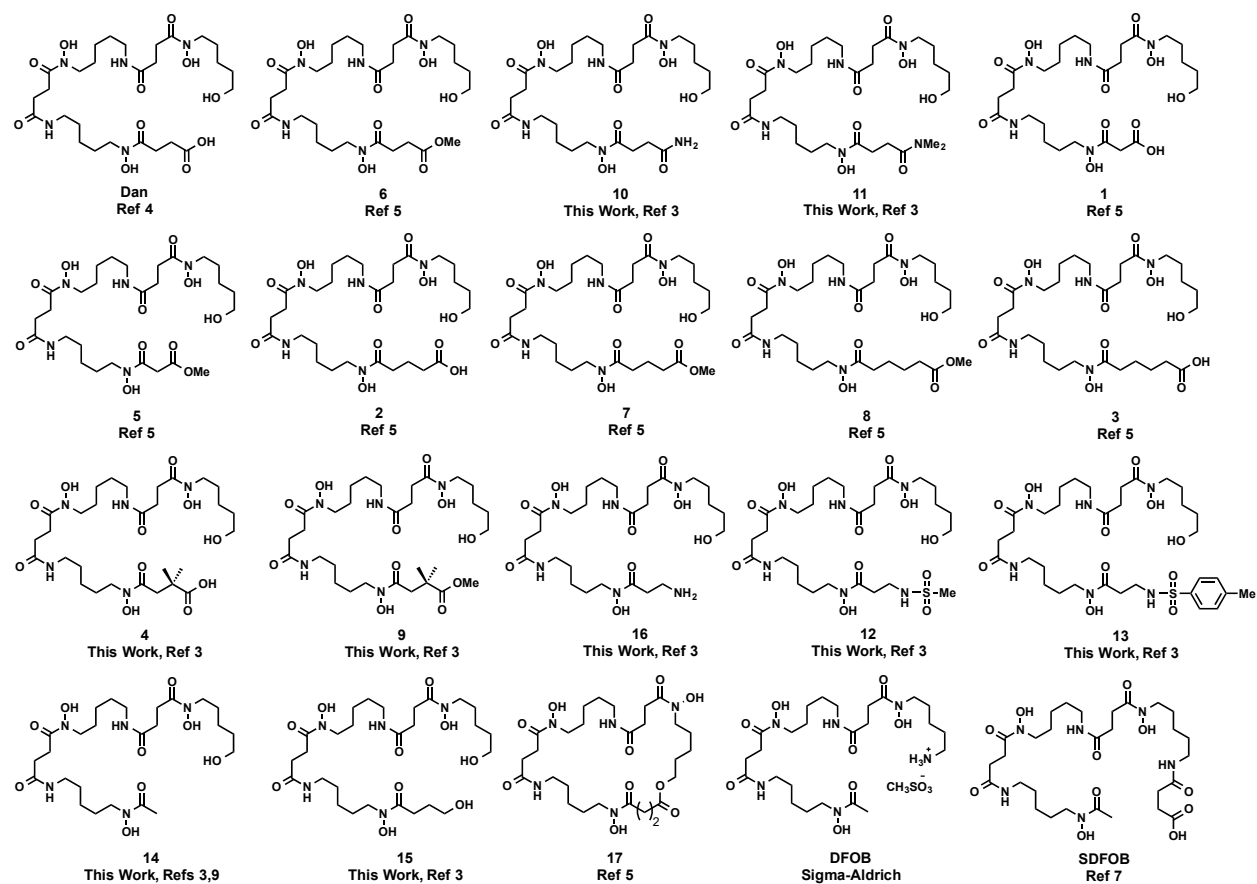


Figure 2.3. Structures of siderophores **Dan**, **DFOB**, **SDFOB**, and **1–17**.

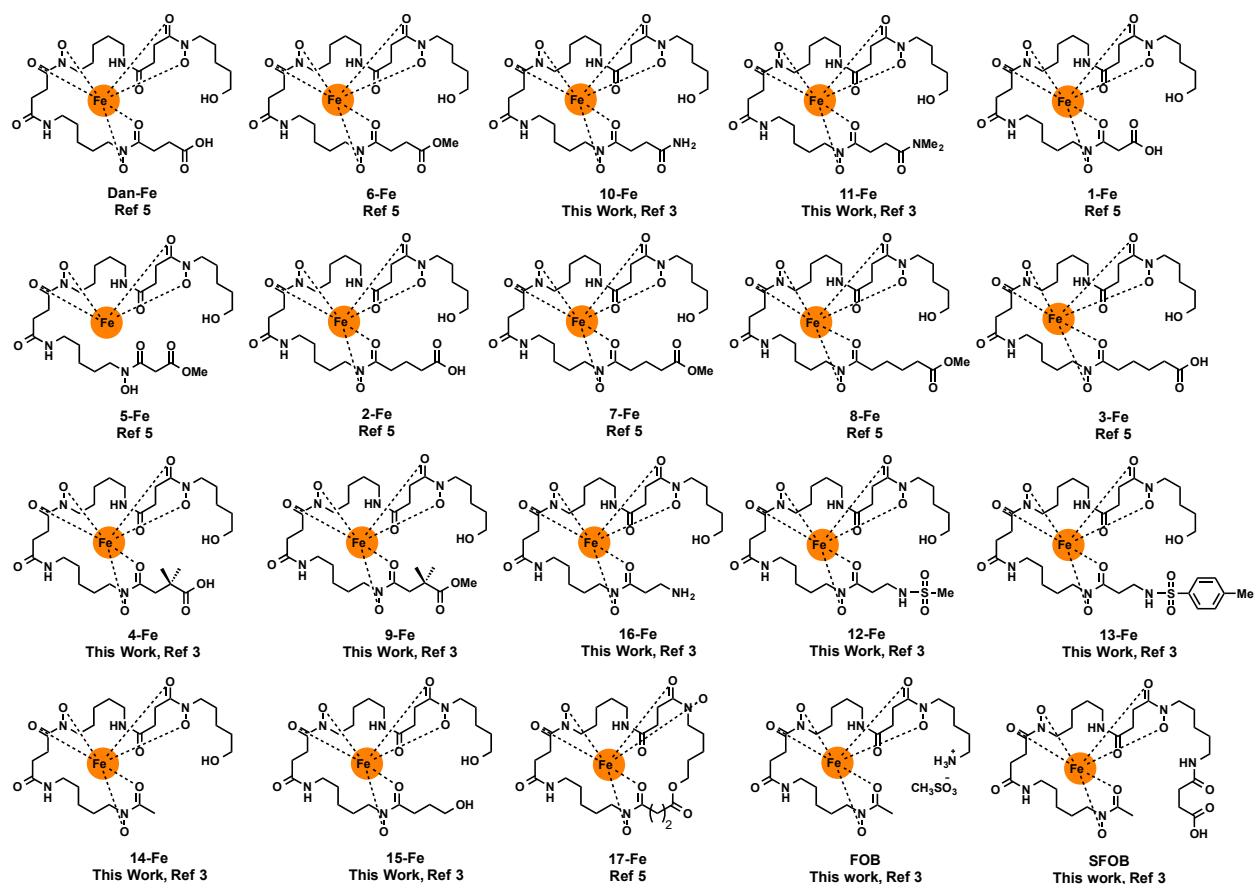
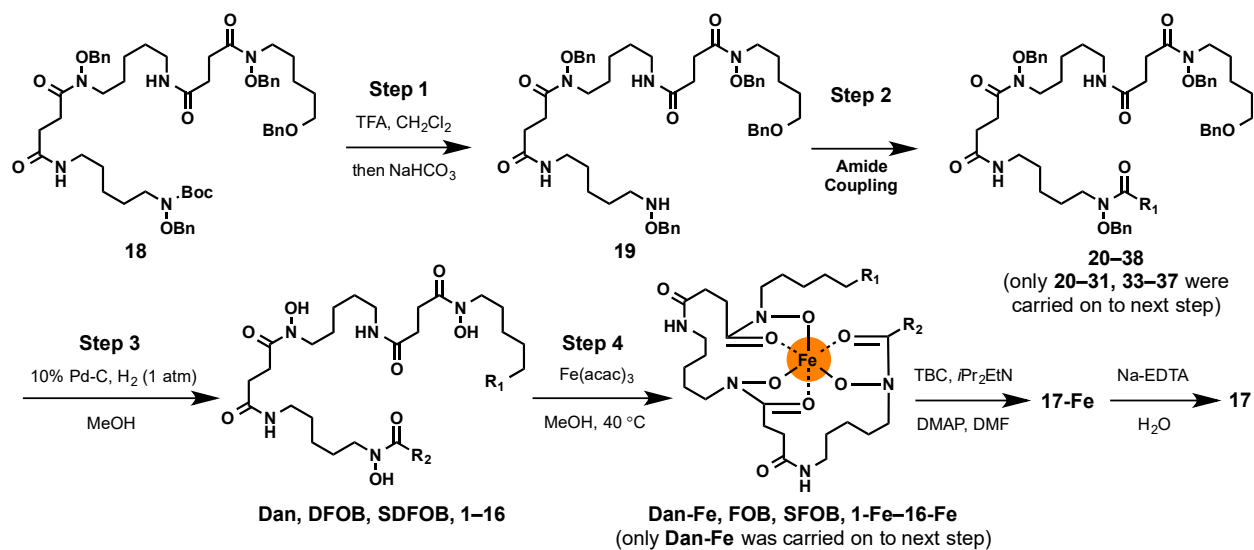


Figure 2.4. Structures of siderophores **Dan-Fe**, **FOB**, **SFOB**, and **1-Fe–17-Fe**.



Scheme 2.1. Synthesis of ferrioxamine siderophores used in this study.

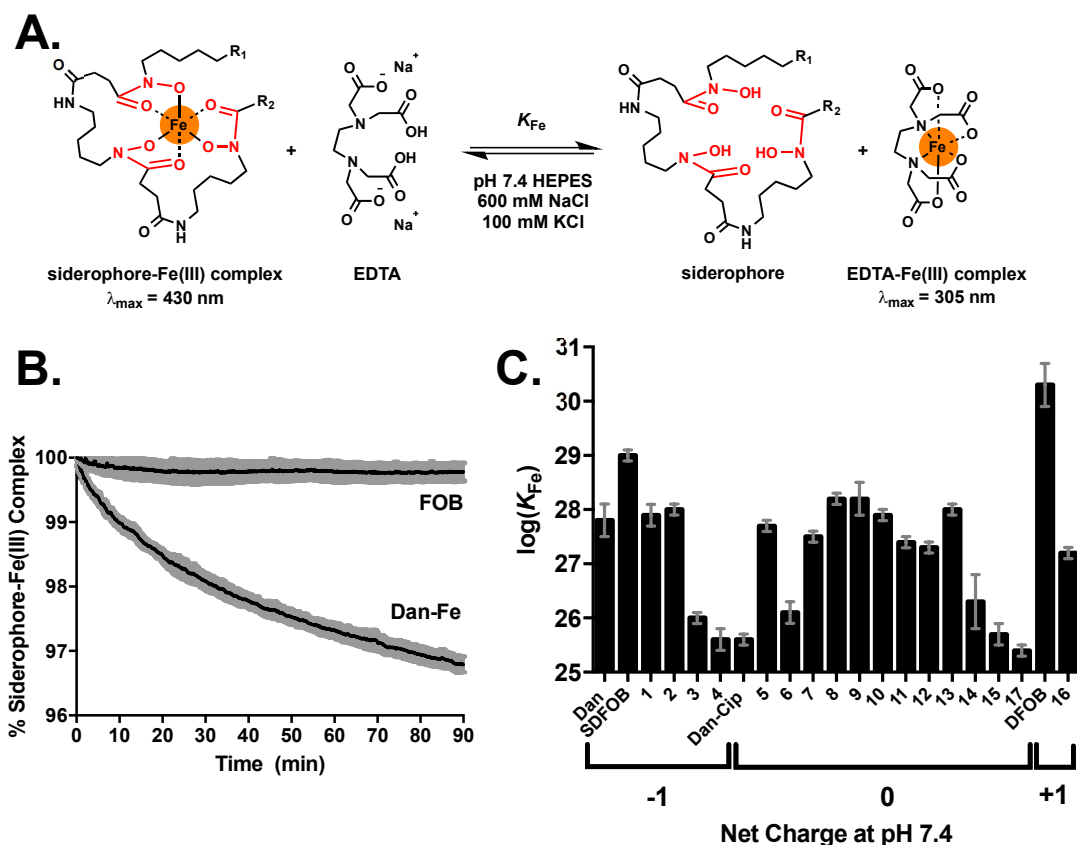


Figure 2.5. Siderophore side chains influence the kinetic and thermodynamic stability of siderophore-Fe(III) complexes. (a) Scheme depicting an EDTA competition assay for determining siderophore K_{Fe} values and Fe(III) exchange kinetics. (b) Graph depicting the percentage of siderophore-Fe(III) complex remaining as a function of time after treatment with 1.2 equivalents of EDTA at pH 7.4. The percentage of siderophore-Fe(III) complex was determined by optical absorbance spectroscopy with continuous scanning at 430 nm. The grey shaded area above and below the curve represents standard deviations for three independent experiments. (c) Bar graph depicting K_{Fe} values for all siderophores used in this study. Error bars represent standard deviations for at least three independent experiments.

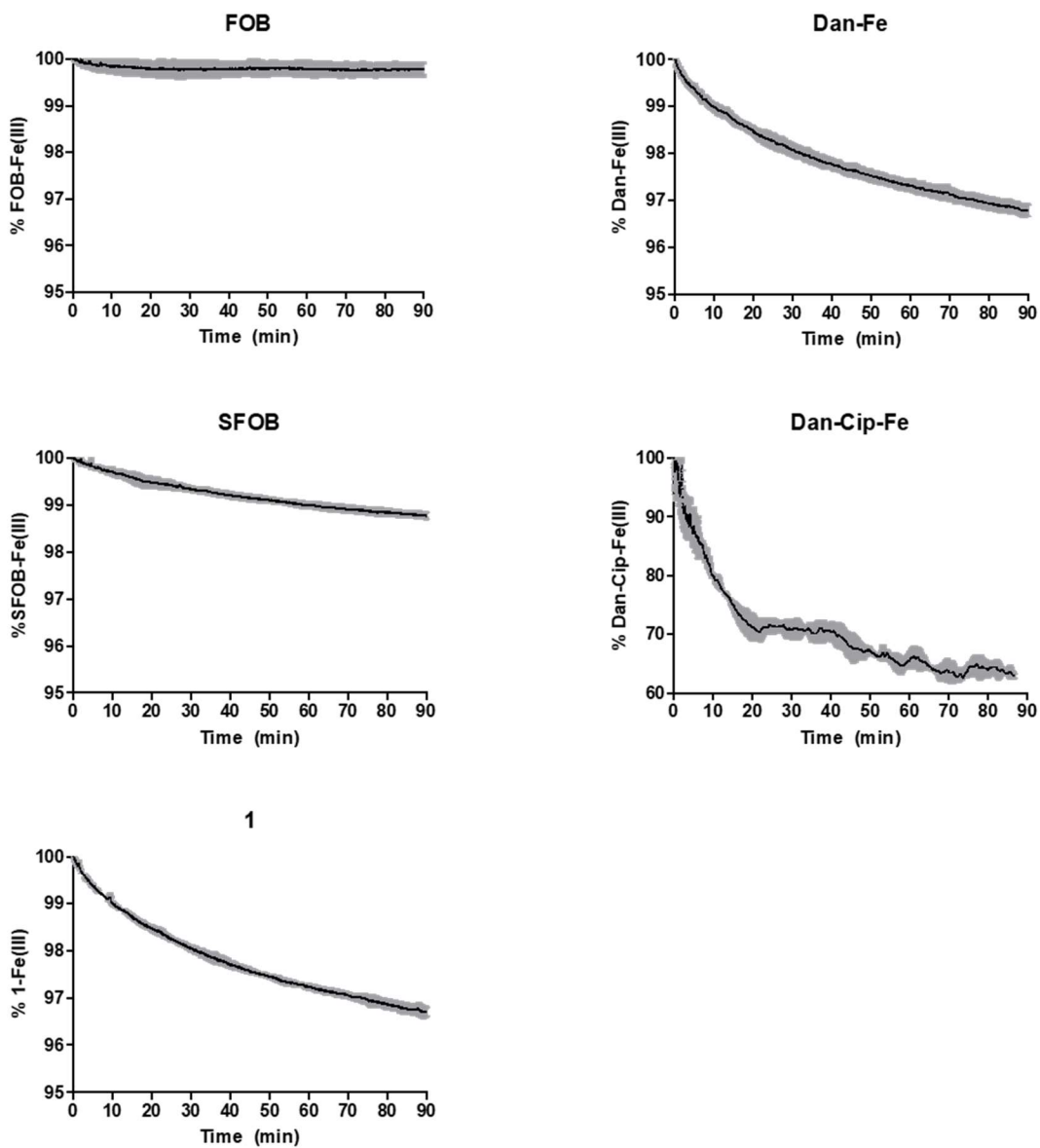


Figure 2.6a. Exponential decay plots for EDTA iron(III) binding competition assay with ferrioxamine siderophores. Error bars represent standard deviations for at least three independent trials.

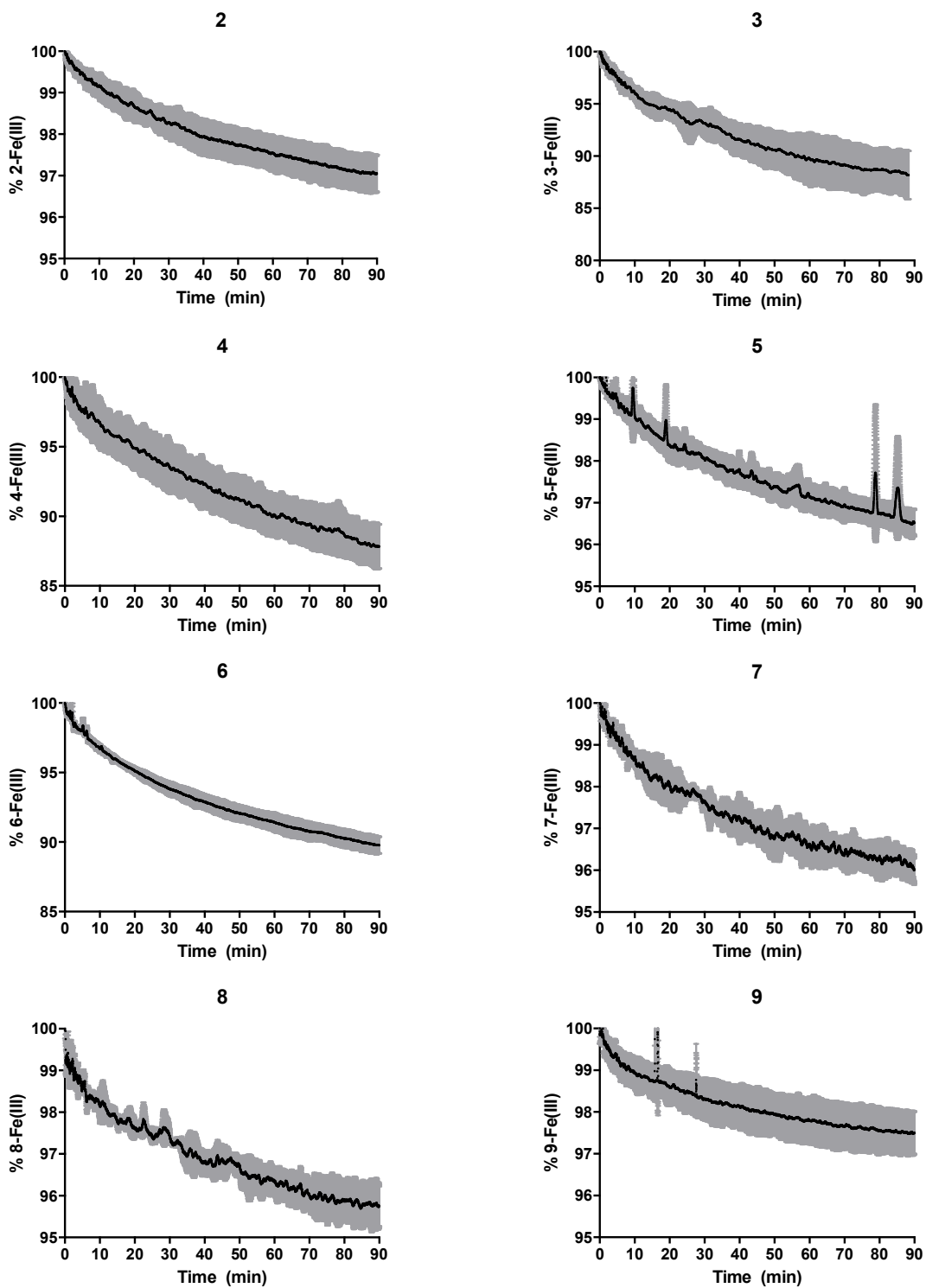


Figure 2.6b. Exponential decay plots for EDTA iron(III) binding competition assay with ferrioxamine siderophores. Error bars represent standard deviations for at least three independent trials.

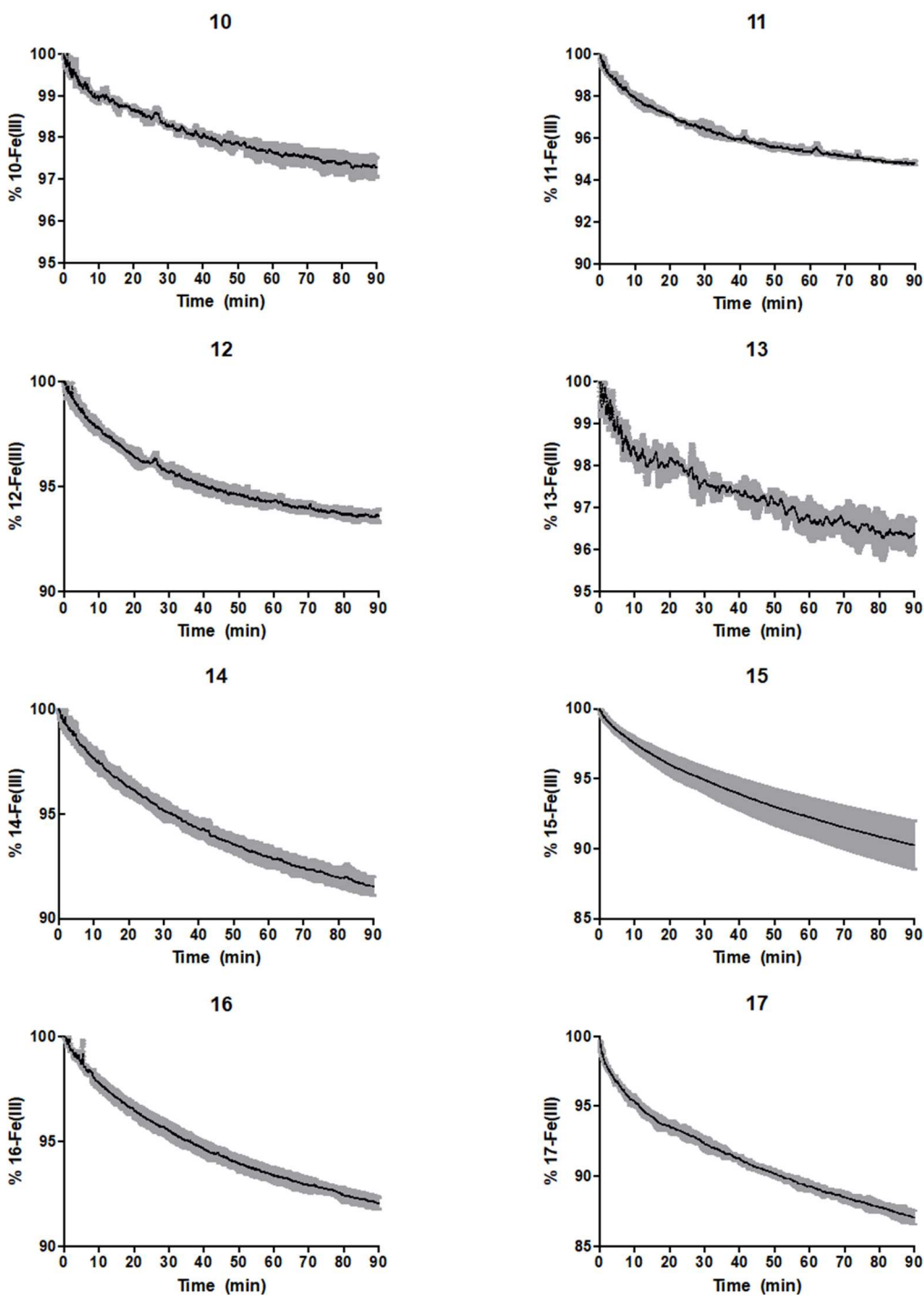


Figure 2.6c. Exponential decay plots for EDTA iron(III) binding competition assay with ferrioxamine siderophores. Error bars represent standard deviations for at least three independent trials.

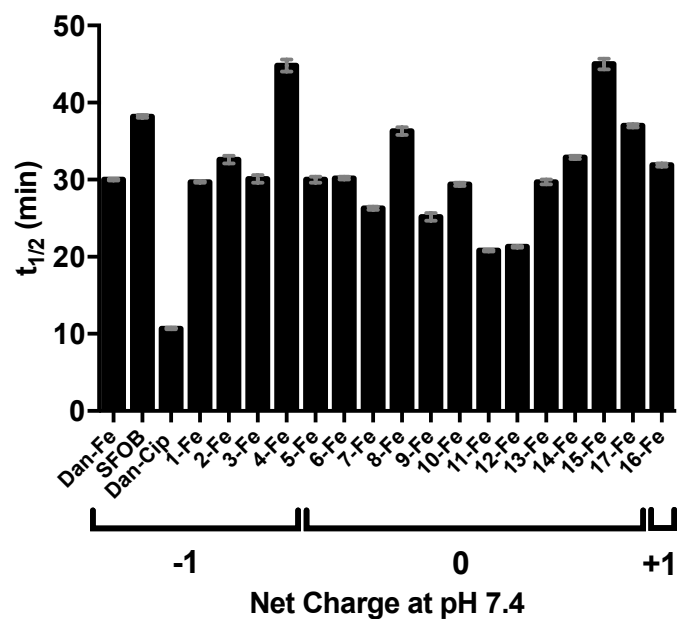


Figure 2.7. Iron(III) exchange half-lives ($t_{1/2}$) between ferrioxamine siderophores and EDTA in pH 7.4 buffer at room temperature determined from first-order rate plots. The $t_{1/2}$ for FOB was too slow to measure an accurate first-order rate. Error bars represent standard deviations from the mean for at least three independent trials.

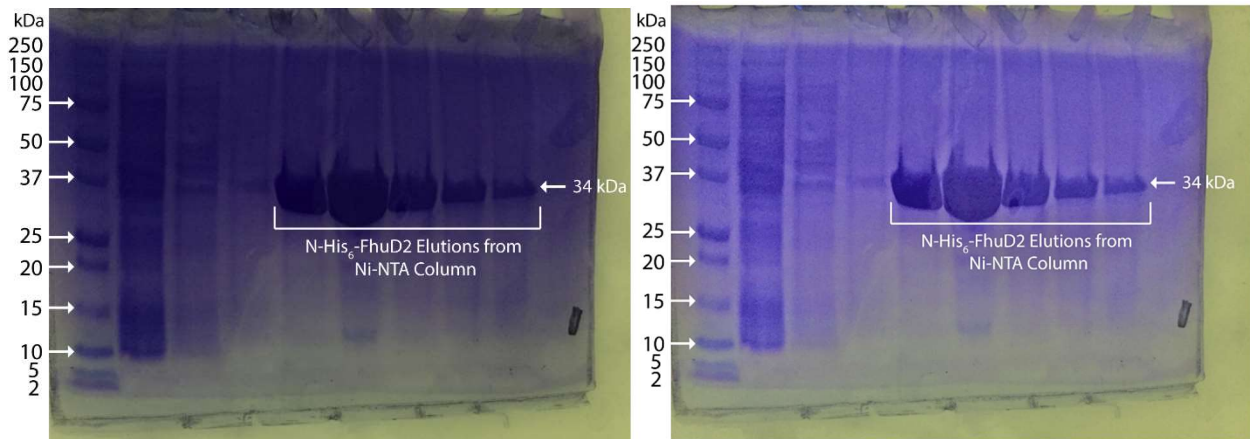


Figure 2.8. SDS-PAGE analysis of purified *N*-His₆-FhuD2. SDS-PAGE gel (Any *kD*, Bio-Rad) was loaded with protein ladder (ThermoFisher PageRuler Prestained Protein Ladder 10–180 *kDa*) in lane 1, Ni-NTA column flow through in lane 2, N-NTA column washes in lanes 3 and 4, and Ni-NTA elutions in lanes 5–9. Gels were stained with Coomassie blue and photograph. Image on left was not adjusted for contrast. Image on right was adjusted for contrast using Adobe Photoshop.

Table 2.3. Primary protein sequences of wild type FhuD2 from *S. aureus* and the truncated *N*-His₆-FhuD2 used here in fluorescence quenching assays.

<p>FhuD2-WT^a from <i>S. aureus</i> (GenBank Accession # AAK92086.1):</p> <p>MKKLLPLIIMLLVLAACGNQGEKNNKAETKSYKMDDGKTVDIPKDPKRIAVVAPTYAGGLKKLGANIVAVNQVDQSKVLKDKFKGVTKIGDGDVEKVAKEKPDLIIVYSTDKDIKKYQKVAPTVVVDYNKHKYLEQQEMLGKIVGKEDKVKA WKKDWEETTAKDGKEIKKAIGQDATVSLFDEFDKKLYTYGDNWGRGGEVLYQAFGLKMQPEQQKLTAKAGWAEVKQEEIEKYAGDYIVSTSEGKPTPGYESTNMWKNL KATKEGHIVKVDAGTYWYNDPYTLDFMRKDLKEKLIKAAK</p>
<p>FhuD2-<i>N</i>-His₆^b used in this work:</p> <p>MGSSHHHHHHSSGLVPRGSHMNNKAETKSYKMDDGKTVDIPKDPKRIAVVAPTYAGGLKKLGANIVAVNQVDQSKVLKDKFKGVTKIGDGDVEKVAKEKPDLIIVYSTDKDIKKYQKVAPTVVVDYNKHKYLEQQEMLGKIVGKEDKVKA WKKDWEETTAKDGKEIKKAIGQDATVSLFDEFDKKLYTYGDNWGRGGEVLYQAFGLKMQPEQQKLTAKAGWAEVKQEEIEKYAGDYIVSTSEGKPTPGYESTNMWKNL KATKEGHIVKVDAGTYWYNDPYTLDFMRKDLKEKLIKAAK</p>

^aPre-lipoprotein signal sequence highlighted in magenta. Soluble siderophore-binding domain

highlighted in teal. ^bHexahistidine motif with thrombin cleavage site highlighted in yellow.

Soluble siderophore-binding domain highlighted in teal.

Table 2.4. Codon optimized nucleotide sequence of FhuD2-*N*-His₆ from *S. aureus* that was cloned into a pET28 vector for protein expression in *E. coli* BL21 (DE3).

<p>ATGAACAACAAGGCGGAGACCAAAAAGCTACAAGATGGACGATGGTAAAACCGTTGACATCCCGAAAGATCCGAAGCGTATTGCGGTGGTTGCGCCGACCTATGCGGGTGCCCTGAAGAACTGGGTGCGAACATCGTTGCGGTGAACCAGCAAGTTGATCAGAGCAAGGTGCTGAAGGACAAATTCAAGGGCGTGACCAAGATTGGTGACGGCGATGTTGAGAAAGTGGCGAAAGAAAAGCCGGACCTGATCATTGTTTACAGCACCGACAAGGATATCAAGAAATATCAAAAAGTGGCGCCGACCGTGGTTGTGGATTACAACAAACACAAGTATCTGGAGCAGCAAGAAATGCTGGGCAAGATTGTTGGCAAAGAAGATAAAGTGAAGGCGTGGAAGAAAGACTGGGAGGAAACCACCGCGAAAGATGGCAAGGAGATCAAGAAAGCGATTGGCCAGGACGCGACCGTTAGCCTGTTCGACGAATTTGATAAGAAACTGTACACCTATGGTGATAACTGGGGTCGTGGTGGCGAGGTGCTGTACCAGGCGTTTCGGTCTGAAGATGCAACCGGAACAGCAAAAGCTGACCGCGAAAGCGGGTTGGGCGGAAGTGAAGCAAGAGGAAATCGAAAAATACGCGGGCGACTATATTGTGAGCACCAGCGAGGGTAAACCGACCCCGGGCTACGAAAGCACCAACATGTGGAAAAACCTGAAGGCGACCAAGAGGGTCACATCGTTAAGGTGGATGCGGGGCACCTACTGGTATAACGACCCGTATACCCTGGATTTTATGCGTAAAGACCTGAAAGAAAGCTGATTAAGGCGGCGAAATAA</p>

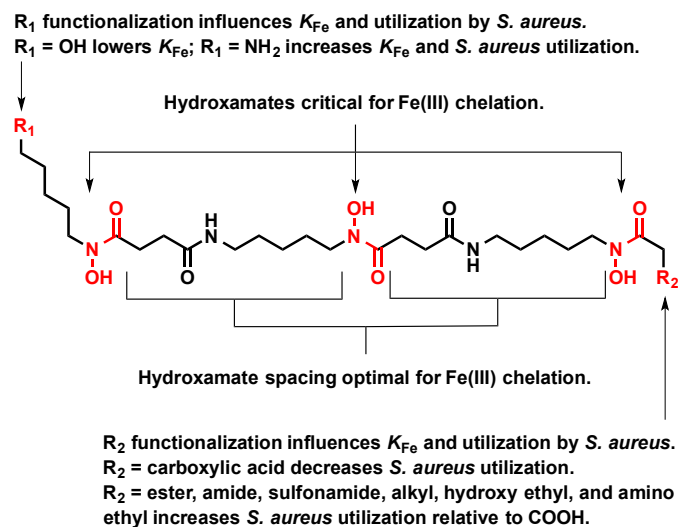


Figure 2.10. Summary of ferrioxamine xenosiderophore structure-function relationships from this work.

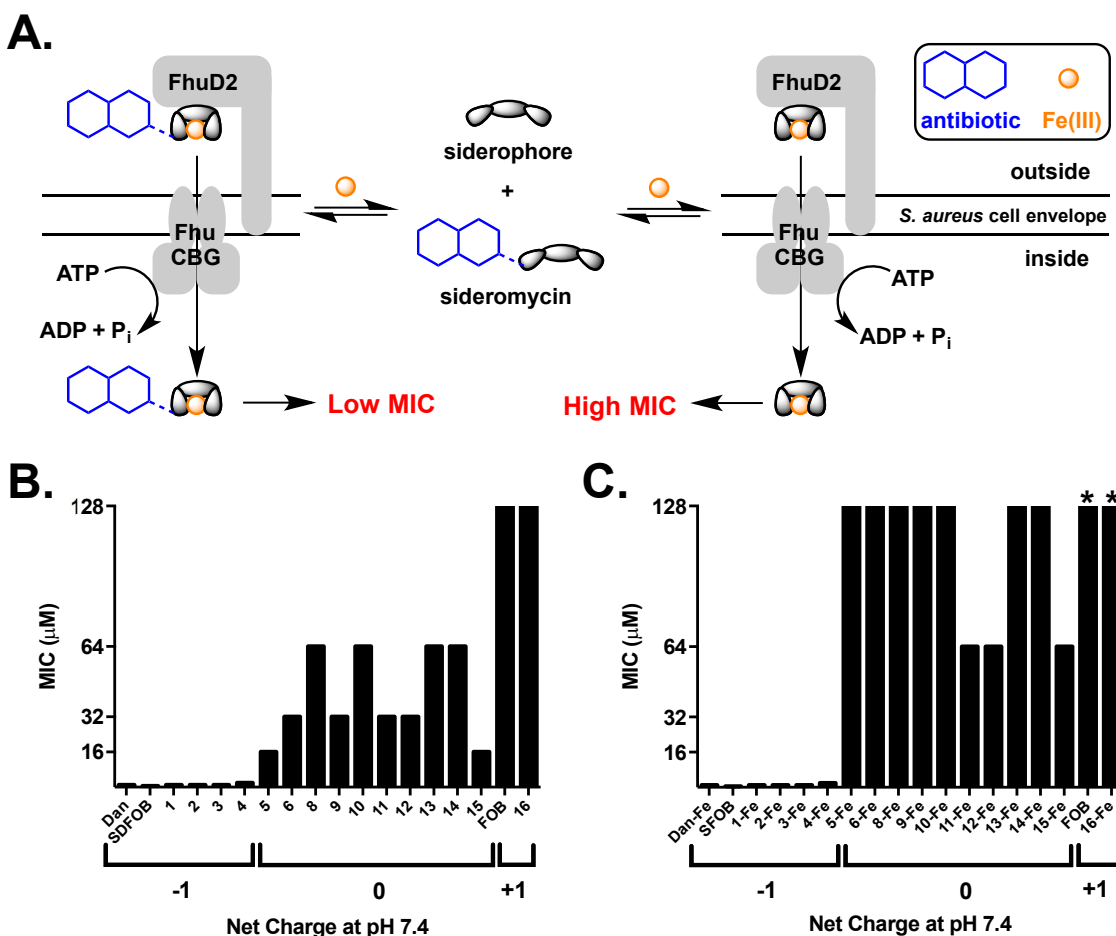


Figure 2.11. Net siderophore charge strongly influences utilization by *S. aureus* SG511. (a) Scheme depicting a siderophore-sideromycin competition MIC assay used to evaluate xenosiderophore utilization by *S. aureus* SG511. An equimolar mixture of siderophore and sideromycin are used for MIC determination. If the sideromycin is transported a low MIC value is observed. If the siderophore is transported a high MIC is observed. (b) *S. aureus* SG511 MIC values for 1:1 mixtures of iron-free siderophore and iron-free sideromycin **Dan-Cip**. (c) *S. aureus* SG511 MIC values for 1:1 mixtures of Fe(III)-bound siderophores and iron-free sideromycin **Dan-Cip**. All MICs were determined in triplicate. The standard error of an MIC assay determined using CLSI guidelines is 2-fold. *MICs for compounds **FOB** and **16-Fe** were >128 μ M.

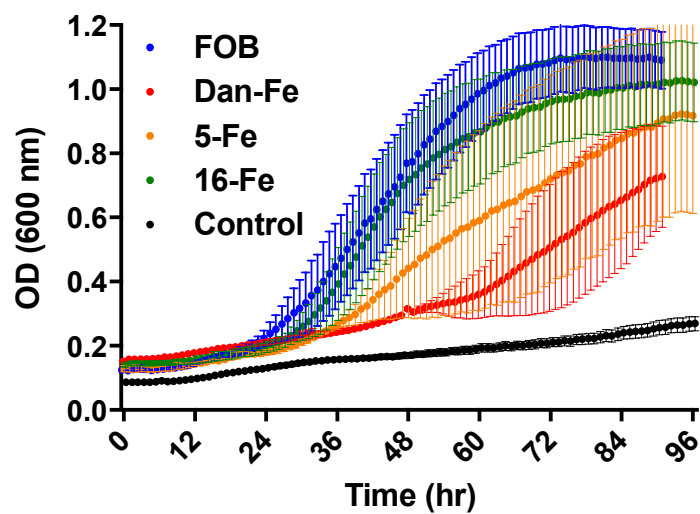


Figure 2.12. *S. aureus* ATCC 11632 growth promotion by **FOB**, **Dan-Fe**, **5-Fe**, and **16-Fe** supplemented at 1.28 mM under Fe-limiting conditions (TMS minimal media treated with 200 μ M 2,2'-dipyridyl).

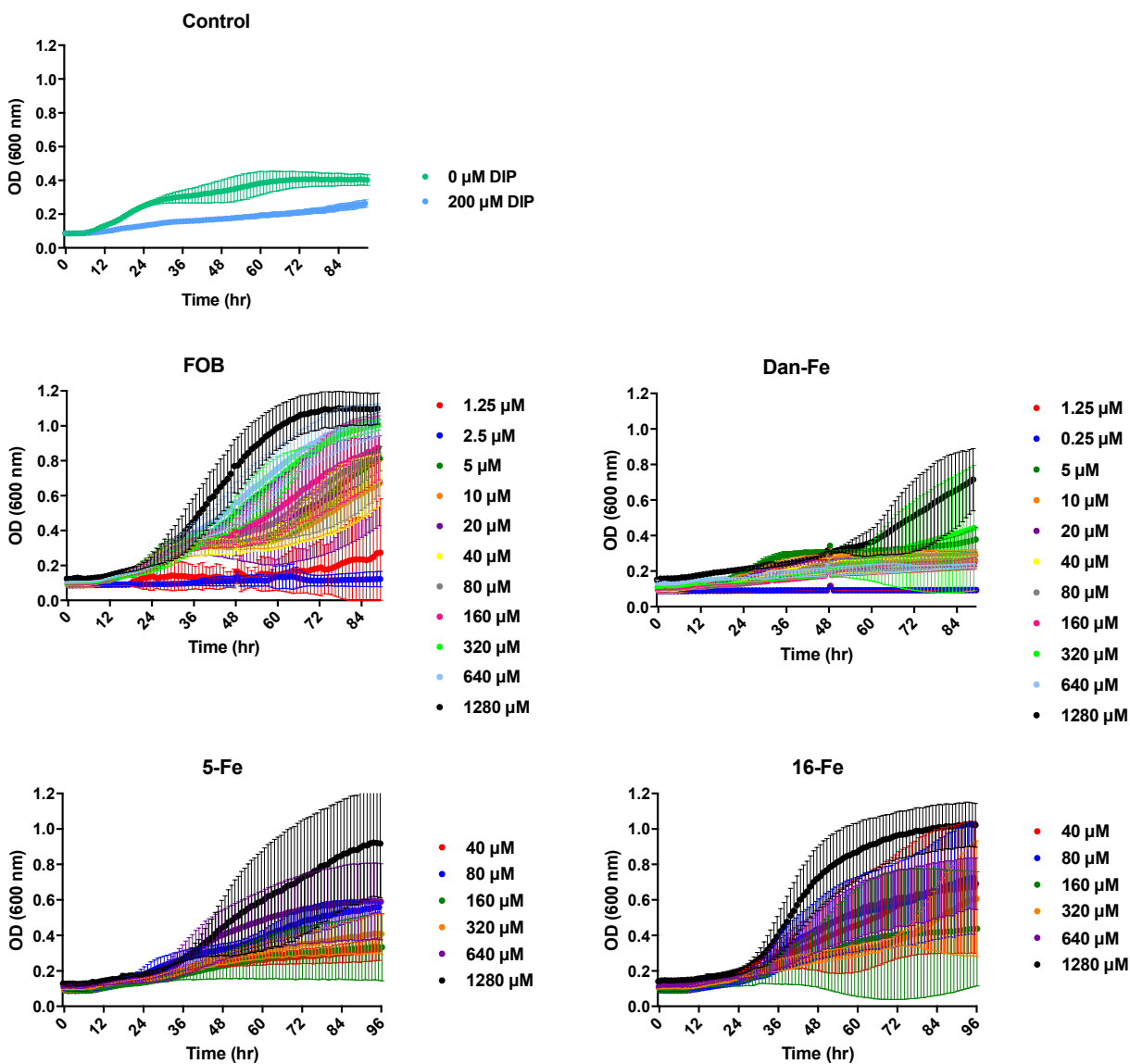


Figure 2.13. *S. aureus* ATCC 11632 growth curves in iron restrictive TMS minimal media (pH 7.4) at 37 °C with siderophore supplementation. Error bars represent standard deviations for at least three independent trials.

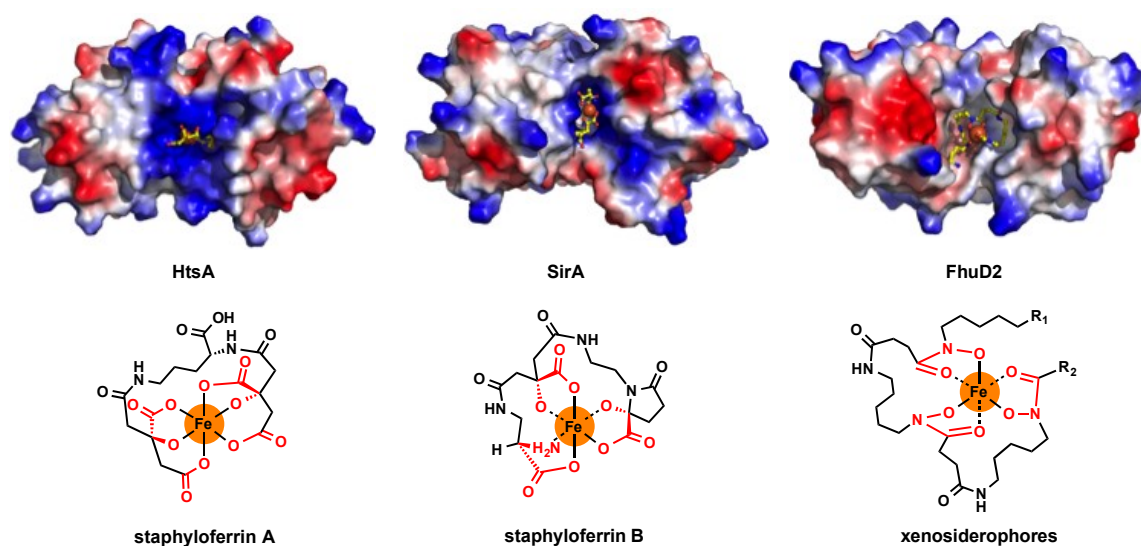


Figure 2.14. Electrostatic surface models of HtsA (PDB 3li2), SirA (PDB 3mwf), and FhuD2 (PDB 4fil) bound to ferric complexes of staphyloferrin A (net negative charge), staphyloferrin B (net negative charge), and **FOB** (net positive charge), respectively. Positively charged protein surfaces are shown in blue, negative charged protein surfaces are shown in red, and charge neutral protein surfaces are shown in light grey.

Table 2.5. Strains and plasmids used in this work.

Strain	Plasmid	Inducible Gene/Marker	Origin/Reference
<i>Staphylococcus aureus</i> SG511	None	Wild Type	Hans Knöll Institute
<i>Staphylococcus aureus</i> ATCC 11632	None	Wild Type	ATCC
<i>E. coli</i> TOP10	None	Cloning strain	Agilent
<i>E. coli</i> BL21 (DE3)	None	Protein expression strain	Agilent
<i>E. coli</i> Top10	pET28a	FhuD2	This work
<i>E. coli</i> BL21 (DE3)	pET28a	FhuD2	This work

- (1) $K_L = \frac{[FeL]}{[Fe^{3+}][L]}$ for the following equilibrium; $[Fe^{3+}] + [L] \rightleftharpoons [FeL]$
- (2) $K_{FeEDTA} = \frac{[FeEDTA]}{[Fe^{3+}][EDTA]}$ for the following equilibrium; $[Fe^{3+}] + [EDTA] \rightleftharpoons [FeEDTA]$
- (3) $K_{Exchange} = \frac{K_L}{K_{FeEDTA}}$ for the following equilibrium; $[FeEDTA] + [L] \rightleftharpoons [FeL] + [EDTA]$
- (4) $K_{Exchange} = \frac{[FeL][EDTA]}{[FeEDTA][L]}$
- (5) $\Delta = \frac{Ab_{FeL} - Abs_{FeL+EDTA}}{\varepsilon_L}$
- (6) $K_L = K_{FeEDTA} \times \frac{[FeL][EDTA]}{[FeEDTA][L]}$
- (7) $[FeL] = \frac{Abs_{FeL}}{\varepsilon_L}$
- (8) $[EDTA] = [EDTA]_T - \Delta$ where $[EDTA]_T = \text{total EDTA added}$
- (9) $[FeEDTA] = \Delta$
- (10) $[L] = \Delta$
- (11) $K_{Fe} = \text{apparent } K_L$

Equations 2.1-2.11.

Apparent siderophore Fe(III) affinity values (K_{Fe}) were determined using a well-established competition experiment with EDTA using optical absorbance spectroscopy². Equations 1–11 and equilibria reactions were used to calculate K_{Fe} . Equations 1–11 show the equilibria for a general ligand (L), which in our case is the siderophore forming a 1:1 complex with Fe(III). We assumed there is no free iron in solution. We assumed that all absorbance at 430 nm was due to the presence of siderophore-Fe(III) complex and that a loss in absorbance at 430 nm is due to transfer of Fe(III) to EDTA. By starting with recrystallized highly pure siderophore-Fe(III) complex we initiated ligand exchange by addition of 1.2 equivalents of EDTA, as described in the materials and methods section of the main text. By monitoring the absorbance at 430 nm (Abs_{FeL}) we calculated apparent K_{Fe} as shown below.

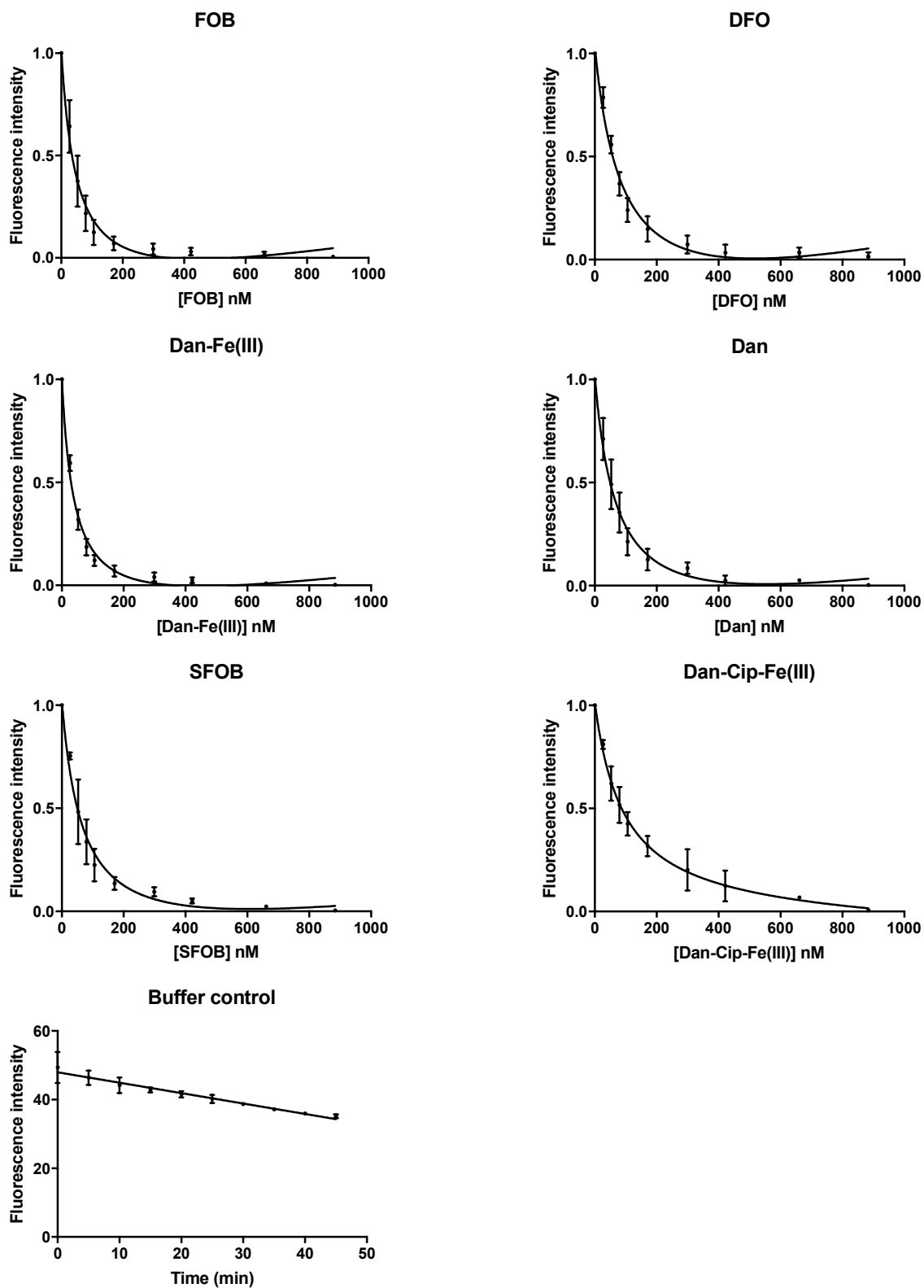


Figure 2.15a. Fluorescence quenching curves for titration of *N*-His₆-FhuD2 with siderophores.

Error bars represent standard deviations for at least three independent trials.

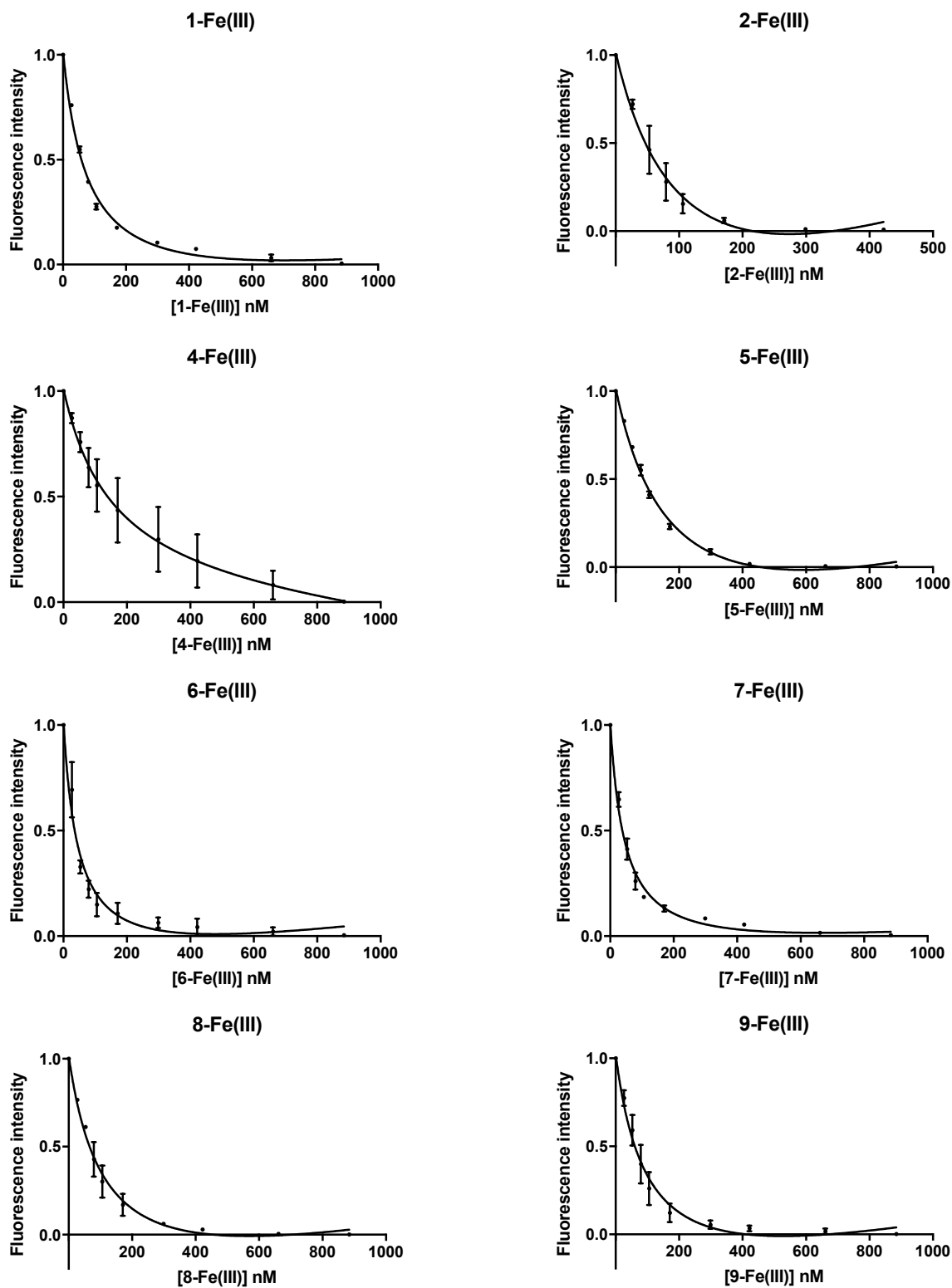


Figure 2.15b. Fluorescence quenching curves for titration of *N*-His₆-FhuD2 with siderophores.

Error bars represent standard deviations for at least three independent trials.

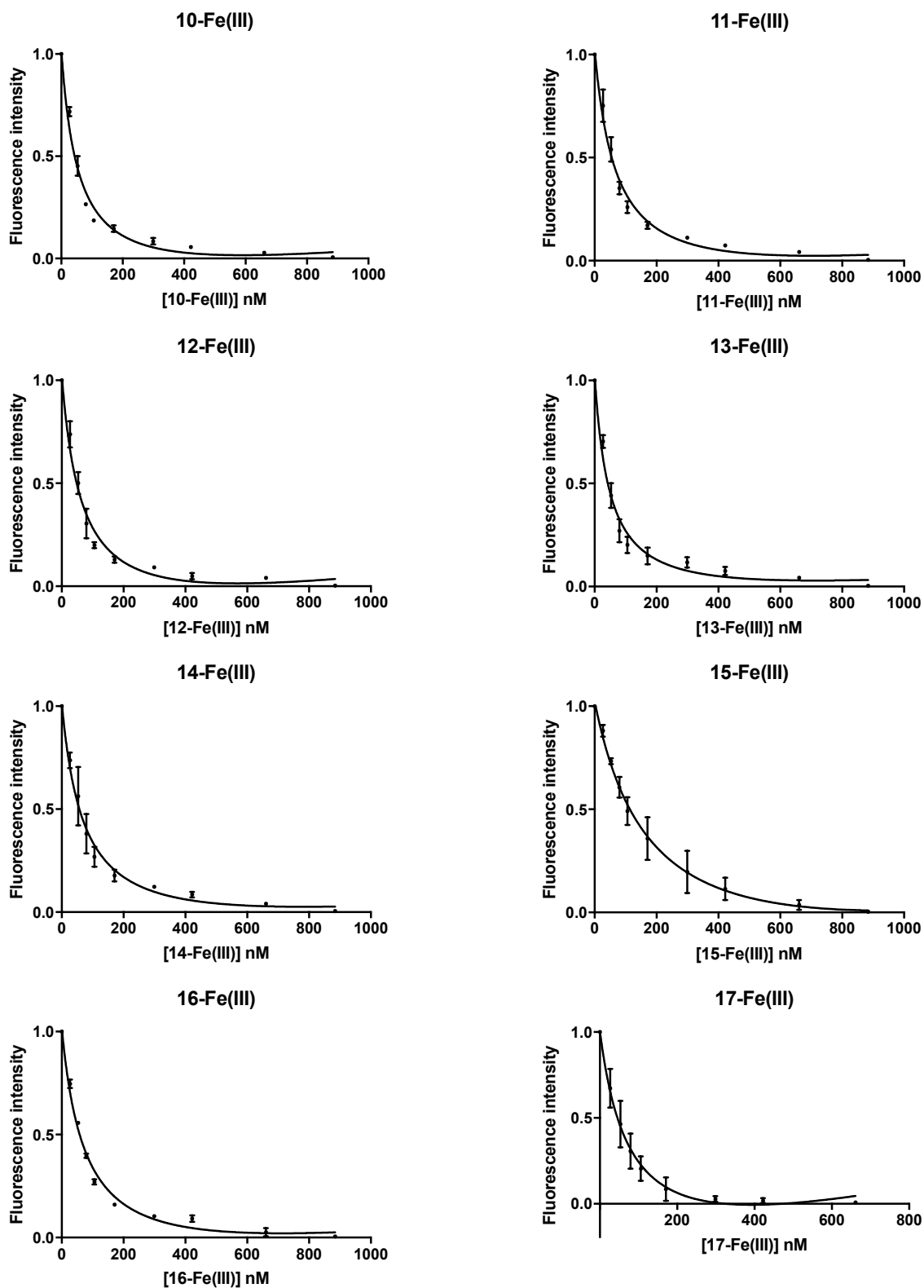


Figure 2.15c. Fluorescence quenching curves for titration of *N*-His₆-FhuD2 with siderophores.

Error bars represent standard deviations for at least three independent trials.

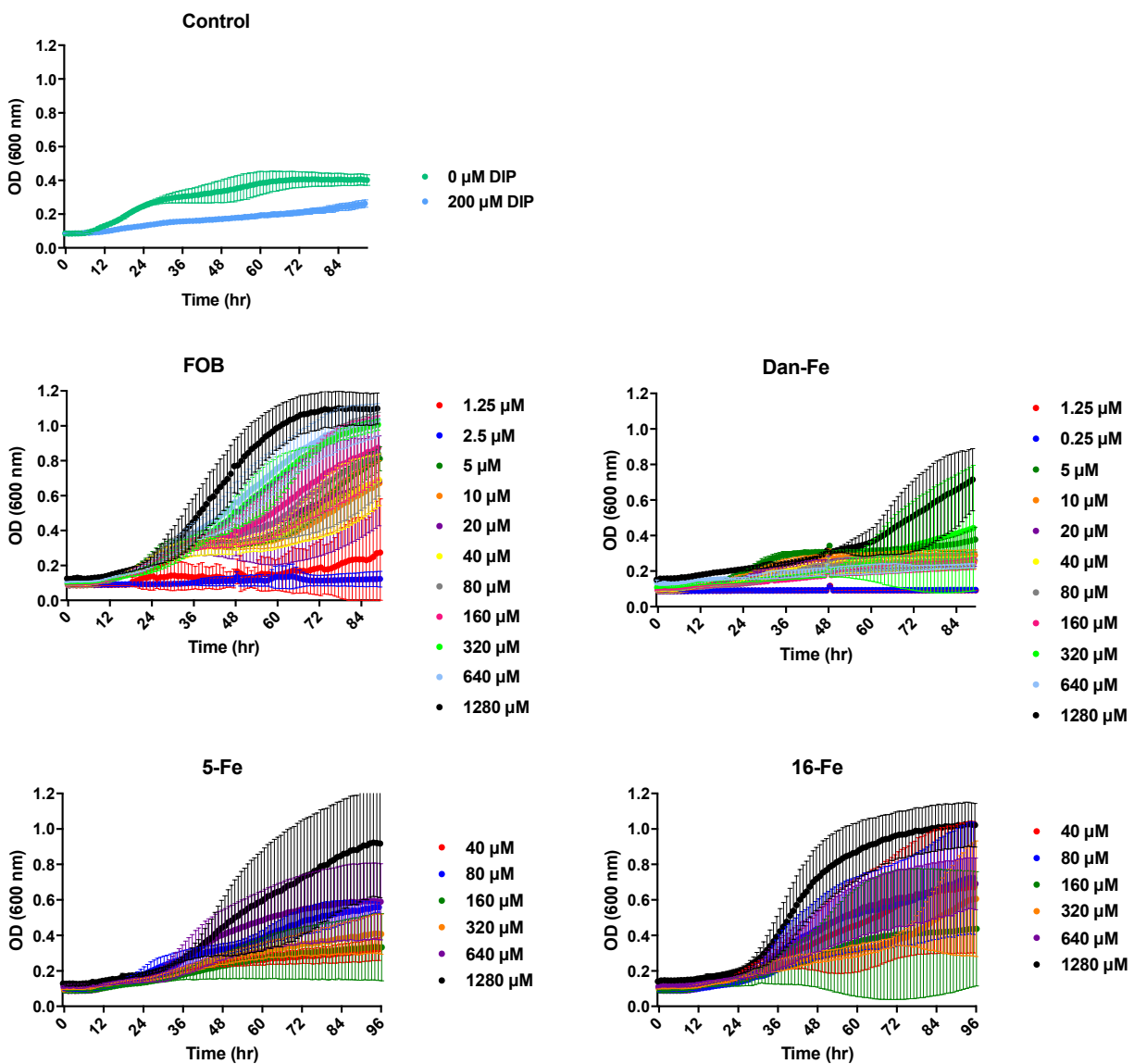


Figure 2.16. *S. aureus* ATCC 11632 growth curves in iron restrictive TMS minimal media (pH 7.4) at 37 °C with siderophore supplementation. Error bars represent standard deviations for at least three independent trials.

2.7 References

- [1] Antibiotic Resistance Threats in the United States, 2013. Center for Disease Control and Prevention, U.S. Department of Health and Human Services: Washington DC, Published Online, 2013.
- [2] Klevens, R. M.; Morrison, M. A.; Nadle, J.; Petit, S.; Gershman, K.; Ray, S.; Harrison, L. H.; Lynfield, R.; Dumyati, G.; Townes, J. M.; Craig, A. S.; Zell, E. R.; Fosheim, G. E.; McDougal, L. K.; Carey, R. B.; Fridkin, S. K. (2007) Invasive methicillin-resistant *Staphylococcus aureus* infections in the United States. *JAMA* 298, 1763. DOI: 10.1001/jama.298.15.1763.
- [3] Klein, E.; Smith, D. L.; Laxminarayan, R. (2007) Hospitalizations and deaths caused by methicillin-resistant *Staphylococcus aureus*, United States, 1999-2005. *Emerging Infectious Diseases* 13, 1840. DOI: 10.3201/eid1312.070629.
- [4] Klein, E.; Smith, D. L.; Laxminarayan, R. (2009) Community-associated methicillin-resistant *Staphylococcus aureus* in outpatients, United States, 1999-2006. *Emerging Infectious Diseases* 15, 1925. DOI: 10.3201/eid1512.081341.
- [5] Otto, M. (2010) Basis of virulence in community-associated methicillin-resistant *Staphylococcus aureus*. *Ann. Rev. Microbiol.* 64, 143. DOI: 10.1146/annurev.micro.112408.134309.
- [6] Hammer, N. D.; Skaar, E. P. (2011) Molecular mechanisms of *Staphylococcus aureus* iron acquisition. *Ann. Rev. Microbiol.* 65, 129. DOI: 10.1146/annurev-micro-090110-10285.
- [7] Sheldon, J. R.; Heinrichs, D. E. (2015) Recent developments in understanding the iron acquisition strategies of gram positive pathogens. *FEMS Microbiol. Rev.* 39, 592. DOI: 10.1093/femsre/fuv009.
- [8] Hood, M. I.; Skaar, E. P. (2012) Nutritional immunity: transition metals at the pathogen–host interface. *Nat. Rev. Microbiol.* 10, 525. DOI: 10.1038/nrmicro2836.
- [9] Palmer, L. D.; Skaar, E. P. (2016) Transition metals and virulence in bacteria. *Ann. Rev. Gen.* 50, 67. DOI: 10.1146/annurev-genet-120215-035146.
- [10] Ghssein, G.; Brutesco, C.; Ouerdane, L.; Fojeik, C.; Izaute, A.; Wang, S.; Hajjar, C.; Lobinski, R.; Lemaire, D.; Richaud, P.; Voulhoux, R.; Espaillat, A.; Cava, F.; Pignol, D.; Borezee-Durant, E.; Arnoux, P. (2016) Biosynthesis of a broad-spectrum nicotianamine-like metallophore in *Staphylococcus aureus*. *Science* 352, 1105. DOI: 10.1126/science.aaf1018.
- [11] Nolan, E. M. (2016) A metal shuttle keeps pathogens well fed. *Science* 352, 1055. DOI: 10.1126/science.aaf8755.

- [12] Konetschny-Rapp, S.; Jung, G.; Meiwes, J.; Zahner, H., Staphyloferrin A: a structurally new siderophore from *Staphylococci*. (1990) *Eur. J. Biochem.* 191, 65. DOI: 10.1111/j.1432-1033.1990.tb19094.x.
- [13] Meiwes, J.; Fiedler, H. P.; Haag, H.; Zahner, H.; Konetschny-Rapp, S.; Jung, G. (1990) Isolation and characterization of staphyloferrin A, a compound with siderophore activity from *Staphylococcus hyicus* DSM 20459. *FEMS Microbiol. Lett.* 55, 201. DOI: [https://doi.org/10.1016/0378-1097\(90\)90195-V](https://doi.org/10.1016/0378-1097(90)90195-V).
- [14] Drechsel, H.; Freund, S.; Nicholson, G.; Haag, H.; Jung, O.; Zahner, H.; Jung, G. (1993) Purification and chemical characterization of staphyloferrin B, a hydrophilic siderophore from *Staphylococci*. *Biometals* 6, 185. DOI: 10.1007/BF00205858.
- [15] Haag, H.; Fiedler, H. P.; Meiwes, J.; Drechsel, H.; Jung, G.; Zahner, H. (1994) Isolation and biological characterization of staphyloferrin B, a compound with siderophore activity from *Staphylococci*. *FEMS Microbiol. Lett.* 115, 125. DOI: 10.1111/j.1574-6968.1994.tb06626.x.
- [16] Madsen, J. L.; Johnstone, T. C.; Nolan, E. M. (2015) Chemical synthesis of staphyloferrin B affords insight into the molecular structure, iron chelation, and biological activity of a polycarboxylate siderophore deployed by the human pathogen *Staphylococcus aureus*. *J. Am. Chem. Soc.* 137, 9117. DOI: 10.1021/jacs.5b04557.
- [17] D'Onofrio, A.; Crawford, J. M.; Stewart, E. J.; Witt, K.; Gavrish, E.; Epstein, S.; Clardy, J.; Lewis, K. (2010) Siderophores from neighboring organisms promote the growth of uncultured bacteria. *Chem. Biol.* 17, 254. DOI: 10.1016/j.chembiol.2010.02.010.
- [18] Challis, G. L.; Hopwood, D. A. (2003) Synergy and contingency as driving forces for the evolution of multiple secondary metabolite production by *Streptomyces* species. *Proc. Natl. Acad. Sci. U.S.A.* 100, 14555. DOI: 10.1073/pnas.1934677100.
- [19] Kalinowski, D. S.; Richardson, D. R. (2005) The evolution of iron chelators for the treatment of iron overload disease and cancer. *Pharmacol. Rev.* 57, 547. DOI: 10.1124/pr.57.4.2.
- [20] Yamasaki, T.; Terai, S.; Sakaida, I. (2011) Deferoxamine for advanced hepatocellular carcinoma. *N. Engl. J. Med.* 365, 576. DOI: 10.1056/NEJMc1105726.
- [21] Konishi, H.; Fujiya, M.; Tanaka, H.; Ueno, N.; Moriichi, K.; Sasajima, J.; Ikuta, K.; Akutsu, H.; Tanabe, H.; Kohgo, Y. (2016) Probiotic-derived ferrichrome inhibits colon cancer progression via JNK-mediated apoptosis. *Nat. Comm.* 7, 12365. DOI: 10.1038/ncomms12365.

- [22] Cloonan, S. M.; Glass, K.; Laucho-Contreras, M. E.; Bhashyam, A. R.; Cervo, M.; Pabon, M. A.; Konrad, C.; Polverino, F.; Siempos, II; Perez, E.; Mizumura, K.; Ghosh, M. C.; Parameswaran, H.; Williams, N. C.; Rooney, K. T.; Chen, Z. H.; Goldklang, M. P.; Yuan, G. C.; Moore, S. C.; Demeo, D. L.; Rouault, T. A.; D'Armiento, J. M.; Schon, E. A.; Manfredi, G.; Quackenbush, J.; Mahmood, A.; Silverman, E. K.; Owen, C. A.; Choi, A. M. (2016) Mitochondrial iron chelation ameliorates cigarette smoke-induced bronchitis and emphysema in mice. *Nat. Med.* 22, 163. DOI: 10.1038/nm.4021.
- [23] Shanzer, A.; Libman, J.; Lytton, S. D.; Glickstein, H.; Cabantchik, Z. I. (1991) Reversed siderophores act as antimalarial agents. *Proc. Natl. Acad. Sci. U.S.A.* 88, 6585. DOI: 10.1073/pnas.88.15.6585.
- [24] Loyevsky, M.; Lytton, S. D.; Mester, B.; Libman, J.; Shanzer, A.; Cabantchik, Z. I. (1993) The antimalarial action of desferal involves a direct access route to erythrocytic (*Plasmodium falciparum*) parasites. *J. Clin. Invest.* 91, 218. DOI: 10.1172/JCI116174.
- [25] Tchanque-Fossuo, C. N.; Dahle, S. E.; Buchman, S. R.; Rivkah Isseroff R. (2017) Deferoxamine: potential novel topical therapeutic for chronic wounds. *Br. J. Dermatol.* 176, 1056. DOI: 10.1111/bjd.14956.
- [26] Gotsbacher, M. P.; Telfer, T. J.; Witting, P. K.; Double, K. L.; Finkelstein, D. I.; Codd, R. (2017) Analogues of desferrioxamine B designed to attenuate iron-mediated neurodegeneration: synthesis, characterisation and activity in the MPTP-mouse model of Parkinson's disease. *Metallomics* [Online early access]. DOI: 10.1039/C7MT00039A.
- [27] Wencewicz, T. A.; Miller, M. J. (2017) Sideromycins as pathogen-targeted antibiotics. *Top. Med. Chem.* [Online early access]. DOI: 10.1007/7355_2017_19.
- [28] Zheng, T.; Nolan, E. M. (2012) Siderophore-based detection of Fe(III) and microbial pathogens. *Metallomics* 4, 866. DOI: 10.1039/c2mt20082a.
- [29] Tieu, W.; Lifa, T.; Katsifis, A.; Codd, R. (2017) Octadentate zirconium(IV)-loaded macrocycles with varied stoichiometry assembled from hydroxamic acid monomers using metal-templated synthesis. *Inorg. Chem.* 56, 3719. DOI: 10.1021/acs.inorgchem.7b00362.
- [30] Kontoghiorghes, G. J.; Kolnagou, A.; Skiada, A.; Petrikkos, G. (2010) The role of iron and chelators on infections in iron overload and non iron loaded conditions: prospects for the design of new antimicrobial therapies. *Hemoglobin* 34, 227. DOI: 10.3109/03630269.2010.483662.
- [31] Arifin, A. J.; Hannauer, M.; Welch, I.; Heinrichs, D. E. (2014) Deferoxamine mesylate enhances virulence of community-associated methicillin resistant *Staphylococcus aureus*. *Microbes and Infection* 16, 967. DOI: 10.1016/j.micinf.2014.09.003.
- [32] Robins-Browne, R. M.; Prpic, J. K. (1983) Desferrioxamine and systemic yersiniosis. *Lancet* 2, 1372. DOI: 10.1016/j.micinf.2014.09.003.

- [33] Collins, H. L.; Kaufmann, S. H. E.; Schaible, U. E. (2002) Iron chelation via deferoxamine exacerbates experimental Salmonellosis via inhibition of the nicotinamide adenine dinucleotide phosphate oxidase-dependent respiratory burst. *J. Immunol.* 168, 3458. DOI: <https://doi.org/10.4049/jimmunol.168.7.3458>.
- [34] Sebulsky, M. T.; Hohnstein, D.; Hunter, M. D.; Heinrichs, D. E. (2000) Identification and characterization of a membrane permease involved in iron-hydroxamate transport in *Staphylococcus aureus*. *J. Bacteriol.* 182, 4394. DOI: 10.1128/JB.182.16.4394-4400.2000.
- [35] Troxell, B.; Hassan, H. M. (2013) Transcriptional regulation by ferric uptake regulator (Fur) in pathogenic bacteria. *Front. Cell. Infect. Microbiol.* 3, article 59. DOI: 10.3389/fcimb.2013.00059.
- [36] Sebulsky, M. T.; Heinrichs, D. E. (2001) Identification and characterization of *fhuD1* and *fhuD2*, two genes involved in iron-hydroxamate uptake in *Staphylococcus aureus*. *J. Bacteriol.* 183, 4994. DOI: 10.1128/JB.183.17.4994-5000.2001.
- [37] Speziali, C. D.; Dale, S. E.; Henderson, J. A.; Vinés, E. D.; Heinrichs, D. E. Requirement of *Staphylococcus aureus* ATP-binding cassette-ATPase FhuC for iron-restricted growth and evidence that it functions with more than one iron transporter. *J. Bacteriol.* 188, 2048. DOI: 10.1128/JB.188.6.2048-2055.2006.
- [38] Podkova, K. J.; Briere, L. A.; Heinrichs, D. E.; Shilton, B. H. (2014) Crystal and solution structure analysis of FhuD2 from *Staphylococcus aureus* in multiple unliganded conformations and bound to ferrioxamine-B. *Biochemistry* 53, 2017. DOI: 10.1021/bi401349d.
- [39] Sebulsky, M. T.; Shilton, B. H.; Speziali, C. D.; Heinrichs, D. E. (2003) The role of FhuD2 in iron(III)-hydroxamate transport in *Staphylococcus aureus*. Demonstration that FhuD2 binds iron(III)-hydroxamates but with minimal conformational change and implication of mutations on transport. *J. Biol. Chem.* 278, 49890. DOI: 10.1074/jbc.M305073200.
- [40] Mariotti, P.; Malito, E.; Biancucci, M.; Lo Surdo, P.; Mishra, R. P.; Nardi-Dei, V.; Savino, S.; Nissum, M.; Spraggon, G.; Grandi, G.; Bagnoli, F.; Bottomley, M. J. (2013) Structural and functional characterization of the *Staphylococcus aureus* virulence factor and vaccine candidate FhuD2. *Biochem. J.* 449, 683. DOI: 10.1042/BJ20121426.
- [41] Mishra, R. P.; Mariotti, P.; Fiaschi, L.; Nosari, S.; Maccari, S.; Liberatori, S.; Fontana, M. R.; Pezzicoli, A.; De Falco, M. G.; Falugi, F.; Altindis, E.; Serruto, D.; Grandi, G.; Bagnoli, F. (2012) *Staphylococcus aureus* FhuD2 is involved in the early phase of staphylococcal dissemination and generates protective immunity in mice. *J. Infect. Dis.* 206, 1041. DOI: <https://doi.org/10.1093/infdis/jis463>.

- [42] Heinrichs, J. H.; Gatlin, L. E.; Kunsch, C.; Choi, G. H.; Hanson, M. S. (1999) Identification and characterization of SirA, an iron-regulated protein from *Staphylococcus aureus*. *J. Bacteriol.* *181*, 1436.
- [43] Beasley, F. C.; Marolda, C. L.; Cheung, J.; Buac, S.; Heinrichs, D. E. (2011) *Staphylococcus aureus* transporters Hts, Sir, and Sst capture iron liberated from human transferrin by staphyloferrin A, staphyloferrin B, and catecholamine stress hormones, respectively, and contribute to virulence. *Infect. Immun.* *79*, 2345. DOI: 10.1128/IAI.00117-11.
- [44] Gwinner, T. (2008) Das Siderophore-Antibiotikum Salmycin. Eberhard Karls Universitat Tübingen, Tübingen, Germany.
- [45] Wencewicz, T. A.; Mollmann, U.; Long, T. E.; Miller, M. J. (2009) Is drug release necessary for antimicrobial activity of siderophore-drug conjugates? Syntheses and biological studies of the naturally occurring salmycin "Trojan Horse" antibiotics and synthetic desferri-danoxamine-antibiotic conjugates. *Biometals* *22*, 633. DOI: 10.1007/s10534-009-9218-3.
- [46] Braun, V.; Pramanik, A.; Gwinner, T.; Koberle, M.; Bohn, E. (2009) Sideromycins: tools and antibiotics. *Biometals* *22*, 3. DOI: 10.1007/s10534-008-9199-7.
- [47] Wencewicz, T. A.; Long, T. E.; Mollmann, U.; Miller, M. J. (2013) Trihydroxamate siderophore-fluoroquinolone conjugates are selective sideromycin antibiotics that target *Staphylococcus aureus*. *Bioconjugate Chem.* *24*, 473. DOI: 10.1021/bc300610f.
- [48] Kurth, C.; Kage, H.; Nett, M. (2016) Siderophores as molecular tools in medical and environmental applications. *Org. Biomol. Chem.* *14*, 8212. DOI: 10.1039/C6OB01400C.
- [49] Hider, R. C.; Kong, X. (2010) Chemistry and biology of siderophores. *Nat. Prod. Rep.* *27*, 637. DOI: 10.1039/B906679A.
- [50] Challis, G. L. (2005) A widely distributed bacterial pathway for siderophore biosynthesis independent of nonribosomal peptide synthetases. *ChemBioChem* *6*, 601. DOI: 10.1002/cbic.200400283.
- [51] Telfer, T. J.; Gotsbacher, M. P.; Soe, C. Z.; Codd, R. (2016) Mixing up the pieces of the desferrioxamine B jigsaw defines the biosynthetic sequence catalyzed by DesD. *ACS Chem. Biol.* *11*, 1452. DOI: 10.1021/acscchembio.6b00056.
- [52] Richardson-Sanchez, T.; Tieu, W.; Codd, R. (2017) Reverse biosynthesis: generating combinatorial pools of drug leads from enzyme-mediated fragmentation of natural products. *ChemBioChem* *18*, 368. DOI: 10.1002/cbic.201600636.
- [53] Dhungana, S.; White, P. S.; Crumbliss, A. L. (2001) Crystal structure of ferrioxamine B: a comparative analysis and implications for molecular recognition. *J. Biol. Inorg. Chem.* *6*, 810. DOI: 10.1007/s007750100259.

- [54] Poreddy, A. R.; Schall, O. F.; Osiek, T. A.; Wheatley, J. R.; Beusen, D. D.; Marshall, G. R.; Slomczynska, U. (2004) Hydroxamate-based iron chelators: combinatorial syntheses of desferrioxamine B analogues and evaluation of binding affinities. *J. Comb. Chem.* 6, 239. DOI: 10.1021/cc030039a.
- [55] Ihnat, P. M.; Vennerstrom, J. L.; Robinson, D. H. (2000) Synthesis and solution properties of deferoxamine amides. *J. Pharm. Sci.* 89, 1525. DOI: 10.1002/1520-6017(200012)89:12<1525::AID-JPS3>3.0.CO;2-T.
- [56] Liu, J.; Obando, D.; Schipanski, L. G.; Groebler, L. K.; Witting, P. K.; Kalinowski, D. S.; Richardson, D. R.; Codd, R. (2010) Conjugates of desferrioxamine B (DFOB) with derivatives of adamantane or with orally available chelators as potential agents for treating iron overload. *J. Med. Chem.* 53, 1370. DOI: 10.1021/jm9016703.
- [57] Traxler, M. F.; Seyedsayamdost, M. R.; Clardy, J.; Kolter, R. (2012) Interspecies modulation of bacterial development through iron competition and siderophore piracy. *Mol. Microbiol.* 86, 628. DOI: 10.1111/mmi.12008.
- [58] Ishida, S.; Arai, M.; Niikawa, H.; Kobayashi, M. (2011) Inhibitory effect of cyclic trihydroxamate siderophore, desferrioxamine E, on the biofilm formation of Mycobacterium species. *Biol. Pharm. Bull.* 34, 917. DOI: 10.1248/bpb.34.917.
- [59] Zane, H. K.; Naka, H.; Rosconi, F.; Sandy, M.; Haygood, M. G.; Butler, A. (2014) Biosynthesis of amphi-enterobactin siderophores by *Vibrio harveyi* BAA-1116: identification of a bifunctional nonribosomal peptide synthetase condensation domain. *J. Am. Chem. Soc.* 136, 5615. DOI: 10.1021/ja5019942.
- [60] Maier, G. P.; Rapp, M. V.; Waite, J. H.; Israelachvili, J. N.; Butler, A. (2015) Adaptive synergy between catechol and lysine promotes wet adhesion by surface salt displacement. *Science* 349, 628. DOI: 10.1126/science.aab0556.
- [61] Martinez, J. S.; Carter-Franklin, J. N.; Mann, E. L.; Martin, J. D.; Haygood, M. G.; Butler, A. (2003) Structure and membrane affinity of a suite of amphiphilic siderophores produced by a marine bacterium. *Proc. Natl. Acad. Sci. U.S.A.* 100, 3754. DOI: 10.1073/pnas.0637444100.
- [62] Martinez, J. S.; Zhang, G. P.; Holt, P. D.; Jung, H. T.; Carrano, C. J.; Haygood, M. G.; Butler, A. (2000) Self-assembling amphiphilic siderophores from marine bacteria. *Science* 287, 1245. DOI: 10.1126/science.287.5456.
- [63] Wencewicz, T. A. (2011) Development of microbe-selective antibacterial agents: From small molecules to siderophores. University of Notre Dame, Notre Dame, IN.
- [64] Wencewicz, T. A.; Oliver, A. G.; Miller, M. J. (2012) Iron(III)-templated macrolactonization of trihydroxamate siderophores. *Org. Lett.* 14, 4390. DOI: 10.1021/ol301869x.

- [65] Liu, X. S.; Patterson, L. D.; Miller, M. J.; Theil, E. C. (2007) Peptides selected for the protein nanocage pores change the rate of iron recovery from the ferritin mineral. *J. Biol. Chem.* 282, 31821. DOI: 10.1074/jbc.C700153200.
- [66] Vértessy, L.; Aretz, W.; Fehlhäber, H.-W.; Kogler, H. (1995) Salmycin A–D, antibiotika aus *Streptomyces violaceus*, DSM 8286, mit siderophor-aminoglycosid-struktur. *Helv. Chim. Acta* 78, 46. DOI: 10.1002/hlca.19950780105.
- [67] Roosenberg, J. M., 2nd; Miller, M. J. (2000) Total synthesis of the siderophore danoxamine. *J. Org. Chem.* 65, 4833. DOI: 10.1021/jo000050m.
- [68] Dong, L.; Roosenberg, J. M.; Miller, M. J. (2002) Total synthesis of desferrisalmycin B. *J. Am. Chem. Soc.* 124, 15001. DOI: 10.1021/ja028386w.
- [69] Crumbliss, A. L., Aqueous solution equilibrium and kinetic studies of iron siderophore and model siderophore complexes. In *Handbook of Microbial Iron Chelates*, Winkelmann, G., Ed. CRC Press: Boca Raton, FL, 1991; pp 177-233.
- [70] Monzyk, B.; Crumbliss, A. L. (1982) Kinetics and mechanism of the stepwise dissociation of iron(III) from ferrioxamine B in aqueous acid. *J. Am. Chem. Soc.* 104, 4921. DOI: 10.1021/ja00382a031.
- [71] Anderegg, G.; L'Eplattenier, F.; Schwarzenbach, G. (1963) Hydroxamatkomplexe III. Eisen(III)-austausch zwischen sideraminen und komplexonen. Diskussion der bildungskonstanten der hydroxamatkomplexe. *Helv. Chim. Acta* 46, 1409. DOI: 10.1002/hlca.19630460436.
- [72] Fukushima, T.; Allred, B. E.; Sia, A. K.; Nichiporuk, R.; Andersen, U. N.; Raymond, K. N. (2013) Gram-positive siderophore-shuttle with iron-exchange from Fe-siderophore to apo-siderophore by *Bacillus cereus* YxeB. *Proc. Natl. Acad. Sci. U.S.A.* 110, 13821. DOI: 10.1073/pnas.1304235110.
- [73] Fukushima, T.; Allred, B. E.; Raymond, K. N. (2014) Direct Evidence of iron uptake by the gram-positive siderophore-shuttle mechanism without iron reduction. *ACS Chem. Biol.* 9, 2092. DOI: 10.1021/cb500319n.
- [74] Collin, F.; Karkare, S.; Maxwell, A. (2011) Exploiting bacterial DNA gyrase as a drug target: current state and perspectives. *App. Microbiol. Biotechnol.* 92, 479. DOI: 10.1007/s00253-011-3557-z.
- [75] Chu, B. C.; Vogel, H. J. (2011) A structural and functional analysis of type III periplasmic and substrate binding proteins: their role in bacterial siderophore and heme transport. *Biol. Chem.* 392, 39. DOI: 10.1515/BC.2011.012.

- [76] Liu, X.; Du, Q.; Wang, Z.; Liu, S.; Li, N.; Chen, Y.; Zhu, C.; Zhu, D.; Wei, T.; Huang, Y.; Xu, S.; Gu, L. (2012) Crystal structure of periplasmic catecholate-siderophore binding protein VctP from *Vibrio cholerae* at 1.7 Å resolution. *FEBS Lett.* 586, 1240. DOI: 10.1016/j.febslet.2012.03.043.
- [77] Cooper, J. D.; Hannauer, M.; Marolda, C. L.; Briere, L. A.; Heinrichs, D. E. (2014) Identification of a positively charged platform in *Staphylococcus aureus* HtsA that is essential for ferric staphyloferrin A transport. *Biochemistry* 53, 5060. DOI: 10.1021/bi500729h.
- [78] Grigg, J. C.; Cooper, J. D.; Cheung, J.; Heinrichs, D. E.; Murphy, M. E. P. (2010) The *Staphylococcus aureus* siderophore receptor HtsA undergoes localized conformational changes to enclose staphyloferrin A in an arginine-rich binding pocket. *J. Biol. Chem.* 285, 11162. DOI: 10.1074/jbc.M109.097865.
- [79] Grigg, J. C.; Cheung, J.; Heinrichs, D. E.; Murphy, M. E. P. (2010) Specificity of staphyloferrin B recognition by the SirA receptor from *Staphylococcus aureus*. *J. Biol. Chem.* 285, 34579. DOI: 10.1074/jbc.M110.172924.
- [80] Jones, T.; Yeaman, M. R.; Sakoulas, G.; Yang, S.-J.; Proctor, R. A.; Sahl, H.-G.; Schrenzel, J.; Xiong, Y. Q.; Bayer, A. S. (2008) Failures in clinical treatment of *Staphylococcus aureus* infection with daptomycin are associated with alterations in surface charge, membrane phospholipid asymmetry, and drug binding. *Antimicrob. Agents Chemother.* 52, 269. DOI: 10.1128/AAC.00719-07.
- [81] Yang, S. J.; Xiong, Y. Q.; Dunman, P. M.; Schrenzel, J.; Francois, P.; Peschel, A.; Bayer, A. S. (2009) Regulation of *mprF* in daptomycin-nonsusceptible *Staphylococcus aureus* strains. *Antimicrob. Agents Chemother.* 53, 2636. DOI: 10.1128/AAC.01415-08.
- [82] Peschel, A.; Vuong, C.; Otto, M.; Götz, F. (2000) The D-alanine residues of *Staphylococcus aureus* teichoic acids alter the susceptibility to vancomycin and the activity of autolytic enzymes. *Antimicrob. Agents Chemother.* 44, 2845. DOI: 10.1128/AAC.44.10.2845-2847.2000.
- [83] Kovacs, M.; Halfmann, A.; Fedtke, I.; Heintz, M.; Peschel, A.; Vollmer, W.; Hakenbeck, R.; Bruckner, R. (2006) A functional *dlt* operon, encoding proteins required for incorporation of D-alanine in teichoic acids in gram-positive bacteria, confers resistance to cationic antimicrobial peptides in *Streptococcus pneumoniae*. *J. Bacteriol.* 188, 5797. DOI: 10.1128/JB.00336-06.
- [84] Saar-Dover, R.; Bitler, A.; Nezer, R.; Shmuel-Galia, L.; Firon, A.; Shimoni, E.; Trieu-Cuot, P.; Shai, Y. (2012) D-Alanylation of lipoteichoic acids confers resistance to cationic peptides in group B *Streptococcus* by increasing the cell wall density. *PLOS Path.* 8, e1002891. DOI: 10.1128/JB.00336-06.

- [85] Halder, S.; Yadav, K. K.; Sarkar, R.; Mukherjee, S.; Saha, P.; Halder, S.; Karmakar, S.; Sen, T. (2015) Alteration of Zeta potential and membrane permeability in bacteria: a study with cationic agents. *SpringerPlus* 4, 672. DOI: 10.1186/s40064-015-1476-7.
- [86] Wanner, S.; Schade, J.; Keinhörster, D.; Weller, N.; George, S. E.; Kull, L.; Bauer, J.; Grau, T.; Winstel, V.; Stoy, H.; Kretschmer, D.; Kolata, J.; Wolz, C.; Bröker, B. M.; Weidenmaier, C. (2017) Wall teichoic acids mediate increased virulence in *Staphylococcus aureus*. *Nat. Microbiol.* 2, 16257. DOI: 10.1038/nmicrobiol.2016.257.
- [87] Schalk, I. J.; Guillon, L. (2013) Fate of ferrisiderophores after import across bacterial outer membranes: different iron release strategies are observed in the cytoplasm or periplasm depending on the siderophore pathways. *Amino Acids* 44, 1267. DOI: 10.1007/s00726-013-1468-.
- [88] Stintzi, A.; Barnes, C.; Xu, J.; Raymond, K. N. (2000) Microbial iron transport via a siderophore shuttle: A membrane ion transport paradigm. *Proc. Natl. Acad. Sci. U.S.A.* 97, 10691. DOI: 10.1073/pnas.200318797.
- [89] Zawadzka, A. M.; Abergel, R. J.; Nichiporuk, R.; Andersen, U. N.; Raymond, K. N. (2009) Siderophore-mediated iron acquisition systems in *Bacillus cereus*: Identification of receptors for anthrax virulence-associated petrobactin. *Biochemistry* 48, 3645. DOI: 10.1021/bi8018674.
- [90] Hatcher, H. C.; Singh, R. N.; Torti, F. M.; Torti, S. V. (2009) Synthetic and natural iron chelators: therapeutic potential and clinical use. *Future Med. Chem.* 1, 1643. DOI: 10.4155/fmc.09.121.
- [91] Xie, Y.; Hou, W.; Song, X.; Yu, Y.; Huang, J.; Sun, X.; Kang, R.; Tang, D. (2016) Ferroptosis: process and function. *Cell Death Differ.* 23, 369. DOI: 10.1038/cdd.2015.158.
- [92] Groebler, L. K.; Liu, J.; Shanu, A.; Codd, R.; Witting, P. K. (2011) Comparing the potential renal protective activity of desferrioxamine B and the novel chelator desferrioxamine B-N-(3-hydroxyadamant-1-yl)carboxamide in a cell model of myoglobinuria. *Biochem. J.* 435, 669. DOI: 10.1042/BJ20101728.
- [93] Deiss, K.; Hantke, K.; Winkelmann, G. (1998) Molecular recognition of siderophores: a study with cloned ferrioxamine receptors (FoxA) from *Erwinia herbicola* and *Yersinia enterocolitica*. *Biometals* 11, 131. DOI: 10.1023/A:1009230012577.
- [94] Bugdahn, N.; Peuckert, F.; Albrecht, A. G.; Miethke, M.; Marahiel, M. A.; Oberthür, M. (2010) Direct identification of a siderophore import protein using synthetic petrobactin ligands. *Ang. Chem. Int. Ed.* 49, 10210. DOI: 10.1002/anie.201005527.

- [95] Funahashi, T.; Tanabe, T.; Mihara, K.; Miyamoto, K.; Tsujibo, H.; Yamamoto, S. (2012) Identification and characterization of an outer membrane receptor gene in *Acinetobacter baumannii* required for utilization of desferricoprogen, rhodotorulic acid, and desferrioxamine B as xenosiderophores. *Biol. Pharm. Bull.* 35, 753. DOI: 10.1007/s10534-011-9488-4.
- [96] Miethke, M.; Kraushaar, T.; Marahiel, M. A. (2013) Uptake of xenosiderophores in *Bacillus subtilis* occurs with high affinity and enhances the folding stabilities of substrate binding proteins. *FEBS Lett.* 587, 206. DOI: 10.1016/j.febslet.2012.11.027.
- [97] Shapiro, J. A.; Wencewicz, T. A. (2016) Acinetobactin isomerization enables adaptive iron acquisition in *Acinetobacter baumannii* through pH-triggered siderophore swapping. *ACS Infect. Dis.* 2, 157. DOI: 10.1021/acsinfecdis.5b00145.
- [98] Shapiro, J. A.; Wencewicz, T. A. (2017) Structure-function studies of acinetobactin analogs. *Metallomics* [Online early access]. DOI: 10.1039/c7mt00064b.
- [99] Tomaras, A. P.; Crandon, J. L.; McPherson, C. J.; Banevicius, M. A.; Finegan, S. M.; Irvine, R. L.; Brown, M. F.; O'Donnell, J. P.; Nicolau, D. P. (2013) Adaptation-based resistance to siderophore-conjugated antibacterial agents by *Pseudomonas aeruginosa*. *Antimicrob. Agents Chemother.* 57, 4197. DOI: 10.1128/AAC.00629-13.
- [100] Martell, A. E.; Smith, R. M. (1974) *Critical stability constants*, vol. 1, Plenum Press, New York, NY.
- [101] CLSI (2009) *Methods for dilution antimicrobial susceptibility tests for bacteria that grow aerobically*, 8th ed, Villanova, PA.
- [102] Murray, P. R.; Baron, E. J.; Pfaller, M. A.; Tenover, F. C.; Tenover, R. H. (1999) *Manual of clinical microbiology*, 7th ed, American Society for Microbiology, Washington, DC.

**Chapter 3: Iron Exchange from *holo*-
Transferrin to *apo*-Siderophores Catalyzed
by a Siderophore Binding Protein**

3.1 Preface

This chapter was adapted with permission from an article of the same title to be submitted for publication by Nathaniel P. Endicott, Gerry-Sann Rivera and Timothy A. Wencewicz.

3.2 Abstract

Iron transport in microbes has been the focus of intense study for decades. Tremendous insight has been gained on the regulation, structure, and function of microbial iron transport systems, but we still lack a clear mechanistic understanding of the fundamental chemical steps that take place during the passage of extracellular iron through the microbial cell envelope. Siderophore-mediated iron acquisition has been particularly well studied in microbes and much is known about how these small molecules are biosynthesized and excreted to scavenge iron(III) from biological sources through formation of high affinity complexes that are imported via dedicated membrane transport pathways. Two siderophore-dependent membrane transport paradigms for iron have been proposed in bacteria; namely, the “iron shuttle” and “siderophore displacement” paradigms. We have developed a kinetic fluorescence quenching assay using a fluorescent siderophore probe molecule, DFO-NBD, and a siderophore binding assay using resin-immobilized siderophore-binding protein, FhuD2, to test the “iron shuttle” and “siderophore displacement” paradigms, respectively, at play for trihydroxamate ferrioxamine siderophores utilized by the human pathogen *Staphylococcus aureus*. We have shown that both membrane transport paradigms are operational and provide a refined mechanism for FhuD2-catalyzed iron exchange whereby FhuD2 transfers its conformational flexibility to displace hydroxamate coordinate bonds from the iron(III) metal center using highly conserved Trp197 and Arg199

residues that accelerate ligand exchange through hydrogen bonding interactions with hydroxamate oxygen atoms. Our study revealed that the predominating transport mechanism depends on concentration, siderophore type (linear or macrocyclic), and the biological source of the iron. Linear *holo*-siderophores readily undergo iron exchange as the metal donor, while macrocyclic siderophores can only serve as metal acceptors in the *apo* form due to the rigidified macrocyclic framework resisting the conformational plasticity of the siderophore-binding protein required for catalyzing iron exchange from the *holo*-siderophore. We discovered that FhuD2 can recognize human transferrin as a substrate and efficiently catalyzes iron exchange from *holo*-transferrin to *apo*-siderophores revealing a new paradigm for FhuD2-mediated iron acquisition during *S. aureus* infection that sheds new light on the value of surface exposed FhuD2 lipoprotein as a virulence factor and viable vaccine target. We hope that our updated mechanistic model of siderophore-mediated iron acquisition will serve as a useful guide for studying metal trafficking in cells and designing next generation siderophore-based therapeutics to combat infectious disease.

3.3 Introduction

The spread of antimicrobial resistance is rapidly accelerating and poses a monstrous threat to society if left unchecked.¹ Overall overuse of antibiotics, incorrect prescriptions, and agricultural demand have all contributed to this problem.²⁻⁵ The pharmaceutical industry has performed poorly in developing new antibiotics. Regulatory barriers and economics are two relevant factors, as the economic cost to develop new antibiotics is vastly greater than other kinds of diseases.⁴ Even if new antibiotics are successfully developed, quick spreading of resistance often renders new drugs ineffective. The net result of these effects is that very few antibiotics have reached phase 2 development in recent years, particularly ones that combat the ESKAPE

pathogens.⁶ The ESKAPE pathogens are a group of bacteria especially notorious for their ability to evade traditional antibiotic techniques. Many of these bacteria have developed extensive drug resistance, such as multidrug resistant multidrug resistant *Pseudomonas aeruginosa* and methicillin-resistant *Staphylococcus aureus* (MRSA).¹ MRSA in particular is resistant to beta-lactam antibiotics and is responsible for some of the biggest death tolls in the bacterial pathogen landscape, being the infection which has caused the most death annually in the U.S.⁷ Rates of death in community settings, especially countries with poor hygiene practices, is projected to continue to rise.⁸ It is therefore imperative to develop a more complete understanding of bacterial virulence pathways in order to more intelligently tailor the future generation of antibiotic compounds.

S. aureus possesses several key virulence factors which aid its ability to thrive in an infection setting. These virulence factors are regulated by multiple environmental cues, such as temperature, pH, and nutrient availability.⁹ Regulatory loci are key in the controlling of these virulence factors, and the ferric uptake regulators (Fur) are highly involved in the acquisition of iron.¹⁰ Iron is important for the survival of almost every organism on earth due to its key role in processes such as nitrogen fixation, DNA replication, amino acid biosynthesis, oxygen binding and catalysis.¹¹ In its ferric Fe(III) form bacteria need much higher concentrations of iron (10^{-6} M) than is available in an infection setting (10^{-24}).¹² Like other bacteria, *S. aureus* exhibits noticeable growth inhibition if iron uptake is blocked.¹³ The primary way *S. aureus* addresses the problem of iron acquisition is through the use of siderophores, small secondary metabolites which chelate iron at high affinity.¹⁴⁻¹⁶ Siderophores are biosynthesized intracellularly before excreted to gather iron in the extracellular environment, where they return through the cell membrane through ABC transporters anchored to the cell membrane in Gram positive bacteria.¹⁷ Fur in *S. aureus* directly regulates its siderophore system.¹⁸ *S. aureus* primarily produces two siderophores, staphyloferrin

A and B.¹⁹ It possesses two unique ABC transporters for Staphyloferrin A and B, HtsABC and SirABC, respectively.^{20,21}

One noteworthy phenomenon in bacteria is the acquisition of siderophores produced by other bacteria, called xenosiderophores, as a method of reducing metabolic burden.²² *S. aureus* is no exception to this, and has shown the ability to uptake ferrioxamine xenosiderophores through its FhuCBG system.²³ Desferrioxamine B (DFOB) is a trihydroxamate siderophore most notable for its role as a first line choice in treating iron overload disease. DFOB also has shown promise in the areas of infection imaging, drug delivery, burn recovery, wound healing, and as therapy for cancer, Parkinson's, Alzheimer's and COPD.²⁴⁻²⁹ The growing threat of antimicrobial resistance and use of DFOB makes understanding the iron uptake pathway in FhuD2 vitally important to allow for rational design of siderophore therapeutics.

Long recognized for their role in the uptake of iron-bound siderophores, high iron affinity virulence factors which allow pathogenic bacteria to combat nutritional immunity in the host, we propose the siderophore-binding protein component of the ABC transporter system (SBP) serves an additional purpose as an enzyme catalyzing the nonreductive removal of iron from human defense proteins such as transferrin (**Figure 3.1**). In this work we show *apo*-siderophores pre-bound to the SBP serve as cofactors in this iron acquisition process. Traditional dogma for siderophore-mediated iron acquisition involves siderophore biosynthesis within the cell followed by efflux into the extracellular environment.³⁰⁻³⁵ Iron-bound siderophores then return to the cell where SBPs facilitate cellular re-entry before the iron is released for use in the cell. This siderophore system has been considered to function separately from the pathogenic strategy of directly binding host iron transporters, as seen in bacterial heme-transport proteins. These methods

of iron acquisition are both genetically linked to Fur proteins and must no longer be considered independent of each other.

The capability of non-reductive iron shuttling between siderophores has been implicated in studies of YxeB, a siderophore binding protein (SBP) from *Bacillus cereus* that is homologous to FhuD2, by Raymond and coworkers.³⁰ In this shuttle mechanism, an approaching *holo*-siderophore to the SBP transfers its iron to an *apo*-siderophore already bound to the protein. The siderophore that has newly received the iron then enters the cell. In an alternative mechanism, the incoming *holo*-siderophore could displace the *apo*-siderophore on the active site of the protein. We utilized a siderophore-fluorescent probe previously designed for use in observing iron uptake in plants, 7-nitrobenz-2 Oxa-1,3-diazole-desferrioxamine (DFONBD) as a turn-off probe when bound to iron to examine the role of shuttling vs. displacement in *S. aureus*. A resin-immobilized FhuD2 assay was used to qualitatively analyze displacement of multiple siderophores at the SBP binding pocket.

Kinetic rates of iron exchange between DFONBD and a select panel iron-bound siderophores were measured by fluorescence quenching both in the presence and absence of FhuD2. We found that FhuD2 catalyzed the exchange of iron and lowered apparent iron affinity for linear siderophores. These effects were not observed in equivalent cyclic siderophores. To examine the biological implications of iron shuttling transferrin was introduced as an iron source. Transferrin is one of the most relevant iron transporters in humans and plays a vital role in iron sequestration from invading pathogens. DFOB by itself is unable to access transferrin-bound iron. Fluorescence quenching revealed DFONBD poorly acquires iron from *holo*-transferrin, but rapidly does so when FhuD2 is present. LC-MS experiments provided additional evidence that FhuD2

facilitates iron removal from transferrin with apo-siderophores (**Figure 3.1**). A series of active site mutants were tested for their ability to catalyze iron exchange and it was found that These findings give new meaning to the shuttle mechanism and provide an updated understanding of the siderophore paradigm in pathogenic bacteria.

The exchange of iron between biological sources and high-affinity siderophores is thermodynamically favorable, but exceedingly slow kinetically. We present a revised model for this iron exchange where the extracellular siderophore-binding proteins play an active role in catalyzing this process to provide a meaningful kinetic advantage for iron acquisition in siderophore-utilizing bacteria. In our model, the siderophore-binding proteins are not innocent bystanders waiting for the diffusion-controlled chance opportunity to snatch a specific *holo*-siderophore from the environment, but instead serve as broad catalyst for iron exchange between iron-sequestering host proteins and *apo*-siderophore cofactors localized at the cell surface in the binding calyx of surface-displayed siderophore-binding proteins such as FhuD2 in *S. aureus* and YxeB in *B. cereus*.

3.4 Results and Discussion

Development of a Kinetic Fluorescence Quenching Assay for Iron Exchange Between Siderophores.

DFONBD is a turn off fluorescence probe which loses its diagnostic fluorescence emission peak at ~550 nm when bound to iron. Monitoring of maximum fluorescence over time represents DFO-NBD being converted to FONBD as fluorescence decreases. The viability of the fluorescence quenching assay was tested by titrating FeCl₃ as an iron source, and the corresponding fluorescence

quenching confirmed literature results when different concentrations of FeCl_3 were allowed to equilibrate with DFO-NBD for 1 h. Each individual experimental condition can be analyzed over time in a fluorescence decay plot normalized to the maximum fluorescence of DFO-NBD at 0 min. As an iron source FeCl_3 was replaced by iron-bound siderophores, revealing a stronger preference for iron exchange between linear siderophores. Cyclic siderophores exhibited minimal iron exchange with DFO-NBD. LC-MS experiments verify a direct connection between decreased fluorescence and exchange of iron between DFO-NBD and an iron source over time (**Figure 3.2**).

Competitive Displacement for Many Siderophores Occurs in the SBP Active Site

While the shuttle mechanism could be tested using the fluorescent DFO-NBD probe, the displacement mechanism was tested using a resin-immobilized FhuD2 system previously developed for purifying siderophore natural products from complex *Streptomyces* fermentations.³⁶ In this assay, purified *N*-His₆ FhuD2 is bound to a Ni-NTA resin and is first loaded with a single siderophore or a mixture of siderophores depending on the nature of the desired competition study. The column is washed with buffer until the siderophores added are no longer detected by LC-MS. Afterward, a separate siderophore is added to the column in an elution step, which displaces the initially bound siderophore that is detectable by LC-MS in the elution buffer, confirming displacement of siderophores has occurred from FhuD2 (**Figure 3.3**). All of the siderophores used in this study were confirmed to competitively displace each other on resin-immobilized FhuD2 and YxeB, including the DFO-NBD fluorescent probe, linear ferrioxamine siderophores, and macrocyclic ferrioxamine siderophores.

FhuD2 Catalyzes Iron Exchange Between Linear Siderophores.

The fluorescence quenching assay for measuring iron exchange between an iron-bound siderophores was repeated in the presence of FhuD2. Low concentrations of FhuD2 was pre-complexed with the iron-bound siderophore before mixing with DFO-NBD. A big difference in iron exchange was observed when linear iron-bound siderophores first bound to FhuD2 were mixed with DFO-NBD. This large drop in fluorescence quenching caused by FhuD2 was not observed for cyclic siderophores serving as the ferric iron source. We found that macrocyclic siderophores can only serve as metal acceptors, not donors during redox neutral SBP-catalyzed iron exchange. (**Figure 3.4**). LC-MS was used to confirm iron exchange was occurring in the fluorescence quenching assay conditions.

Iron Exchange from holo-Transferrin.

Fluorescence quenching of DFO-NBD in the presence of *holo*-transferrin as an iron source was tested. Very little iron exchange occurred without FhuD2 present in the reaction *holo*-transferrin appeared to bind FhuD2 at nanomolar affinity when using an intrinsic tryptophan fluorescence quenching experiment. Using *holo*-transferrin as the source of ferric iron in the FhuD2-catalyzed iron exchange experiment with DFONBD revealed a profound degree of fluorescence quenching indicating a large degree of iron exchange from transferrin to DFONBD. This was confirmed by LCMS using DFOB and DFOE as siderophore cofactors for FhuD2. We evaluated the effect of time and transferrin concentration on the iron exchange using steady-state Michaelis-Menten studies. Human transferrin proved to be an efficient substrate for FhuD2 and apparent K_m values correlated with the nanomolar binding affinities measured in the intrinsic Trp

fluorescence quenching studies, which further supports a catalytically productive interaction between FhuD2 bound to DFONBD and iron donating substrate transferrin.

Iron Exchange from holo-Transferrin from FhuD2 active site mutants

A series of active site mutants of FhuD2 was analyzed for their ability to catalyze iron exchange between a siderophore and *holo*-transferrin in the DFO-NBD fluorescence quenching assays. The FhuD2 mutants were also evaluated in the immobilized FhuD2 siderophore displacement assay. Collectively these studies revealed active site residues important for siderophore binding and catalysis of iron exchange. A total of eight active site mutants were prepared (Y256F, Y106F, R175A, W255A, Y254F, Y167F, Y169F, W173A) guided by the crystal structure of FhuD2 bound to FOB (PDB 4FIL) (**Table 3.1, Figure 3.5**). We identified several active site residues that impact substrate binding and iron exchange. R175 and W173 are the only two residues that make direct contact with the bound siderophore cofactor. Mutation of these residues to Ala resulting in at least an 8-fold drop in catalytic efficiency. For the R175A mutant, this drop in catalytic efficiency was attributed to decreased affinity for substrate. However, for the W173A mutant, the drop in catalytic efficiency was attributed to a significant drop in k_{cat} suggesting a role for W173A in the iron exchange mechanism (see below). Several of the Tyr mutants exhibited enhanced substrate binding affinity, but a loss in catalytic efficiency associated with impaired iron exchange. Specifically, Tyr167 and Tyr169 showed a significant drop in catalytic efficiency compared to WT FhuD2 (~4-fold), which led us to propose a key role in iron exchange via ligand displacement and metal chelation. Displacement studies using immobilized FhuD2 mutants corroborated the binding data from the steady state Michaelis-Menten studies and supported impaired siderophore-binding capability of some mutants.

Mechanism for FhuD2-Catalyzed Iron Exchange.

We propose a mechanistic solution to FhuD2 catalysis of linear iron exchange based on dynamic motion of FhuD2. The binding pocket of FhuD2 does not come in contact with iron, so natural dynamics function to peel linear siderophores away from the metal utilizing certain key residues in the active site (**Figure 3.6**). Comparison of the “closed” (PDB 4FIL) and “open” (PDB 4FNA) forms of FhuD2 using the PyMOL Morph function revealed dynamic motions of several key active site residues indicated in substrate binding and catalysis by our functional studies (**Figure 3.5**). We propose a mechanism for iron exchange where the bound siderophore acts as a cofactor and acceptor of ferric iron from a variety of biological sources including transferrin (**Figure 3.6**). A linear siderophore cofactor such as DFOB can move with the dynamic motions of FhuD2 due to the inherent conformational flexibility. Macrocyclic siderophores are more rigid and thus resist conformational dynamics of the SBP. We reached this conclusion by measuring apparent iron affinities of stoichiometric ferric siderophore-FhuD2 complexes using an EDTA competition experiment. We found that complexation to FhuD2 lowered the apparent K_{Fe} values for linear, but not macrocyclic siderophores, suggesting that FhuD2 does promote a more kinetically and thermodynamically more labile ferric iron metal center consistent with the proposed role as an iron exchange catalyst.

As outlined in **Figure 3.6**, we propose an initial binding interaction between an iron-free siderophore-FhuD2 complex and ferric transferrin. For related substrate binding proteins such as maltose binding protein, the effect of molecular crowding by hydrophobic proteins has been demonstrated to promote transition from an “open” to “closed” conformation.³⁷ The transition from “open” to “closed” promotes movement of key residues (**Figure 3.5**), including Tyr167 and

Tyr169 that we propose to displace mobile ligands from the transferrin ferric iron center to form an intermediate FhuD2-transferrin co-complex of ferric iron. The nearby hydroxamate ligands of the bound siderophore cofactor are now positioned to displace the remaining transferrin ligands giving apo-transferrin and a bound ferric siderophore iron complex in the “closed” FhuD2 active site. Dissociation of transferrin enables the ferric SBP to interact with this FhuABC permease to facilitate import of the ferric siderophore iron complex.

DFO attenuates fluorescence quenching of DFO-NBD.

We obtained an additional supportive piece of experimental evidence to demonstrate that the iron exchange process observed via LCMS and fluorescence quenching was indeed siderophore and FhuD2-dependent. In the DFO-NBD iron exchange assay, we included increasing concentrations of DFO as a competing iron acceptor siderophore cofactor (**Figure 3.8**). The addition of increasing amounts of DFO led to a reduced amount of fluorescence quenching, indicating DFO-NBD fluorescence quenching was a direct result of acquiring iron from a specific iron source. DFO and DFO-NBD possess similar iron binding affinities and should therefore function similarly as substrates for iron from a source such as *holo*-transferrin. This result suggests that developing structurally optimized ferrioxamine siderophores with enhanced binding and improved iron affinity might enable inhibition of the iron exchange step in siderophore utilization by the Fhu system in *S. aureus* as a novel antivirulence therapeutic strategy.

3.5 Further Discussions and Conclusions

The proposed mechanism for SBP iron acquisition through *apo*-siderophores has several biological advantages. Notably, the concentration gradient of iron-free siderophores is greatest

immediately near the cell membrane, resulting in promiscuous binders such as FhuD2 being mostly in the state of being bound to *apo*-siderophores. Binding *apo*-siderophores to SBPs on the cell surface additionally prevents loss of the cell's own siderophores through surface localization. Relying on the return of produced siderophores in an environment with many competing cells would likely be energetically unfavorable and fights the principles of passive diffusion. Utilizing a cell's own siderophores as an iron transport cofactor while minimizing the risk of another bacterial cell stealing siderophores provides bacteria with a distinct competitive advantage in an infection environment. A further advantage is the utilization of macrocyclic siderophores to as iron receivers when bound to the protein, perhaps more reliably delivering iron into the cell since conformational dynamics result in loss of iron from a macrocyclic siderophore being less likely when bound to a SBP such as FhuD2 (**Figure 3.8**).

The fluorescence quenching assay with FhuD2 does present complications to consider. All that is being measured in the fluorescence decay assay is the conversion of DFO-NBD to FO-NBD. After initial catalysis of this conversion by FhuD2, multiple competing equilibria results in the rate of fluorescence decay becoming similar to the non-enzymatic rate after several minutes. As more FO-NBD forms in solution, it becomes more likely to self-exchange with other DFO-NBD molecules, resulting in a net zero in fluorescence quenching. Additionally, FO-NBD becomes more likely to exchange back to DFO-NBD as time increases, resulting in a fluorescence recovery affect. The order of addition of FhuD2 was explored. FhuD2 was found to increase intrinsic fluorescence of DFO-NBD. FhuD2 pre-bound to DFO-NBD drowned out the initial signal, giving the illusion of no iron exchange. Therefore, FhuD2 pre-bound to the iron source was the standard order of addition in all assays.

The quantitative rates of displacement were not measured but showed noticeable difference across many of the active site mutants tested. This points to the idea that the rate of displacement vs. shuttle could be governed by affinity for the active site. Iron sources with similar or much higher affinity for the active site than the bound *apo*-siderophore would be more likely to undergo displacement than shuttle. Likewise, iron sources with much lower affinity for the binding site or sources too large to access the site at all, as is the case of *holo*-transferrin, would be pushed toward the shuttle mechanism. Additional studies with mutants and developing a better structural understanding of what constitutes high affinity binding would be an intriguing avenue to pursue going forward. A siderophore with too high of binding to the SBP could actually show growth inhibition for the system if the siderophore sticks to the SBP and is not able to be pushed into the cell or displaced off the protein.

Antimicrobial resistance is one of the most pressing problems in modern medicine. Bettering our understanding of bacterial iron acquisition is one step in combating antimicrobial resistance. FhuD2 catalyzed iron acquisition sheds light on why FhuD2 has shown promise as a vaccination target even though it was previously understood to play a secondary role in iron-bound siderophore uptake. The extent to which this FhuD2-mediated iron acquisition mechanism occurs in other bacterial systems could be explored to discover new SBP vaccination targets. *S. aureus* has a myriad of ways to sequester iron from its environment. Staphyloferrin A has been linked to the ability to pull iron directly from human transferrin. Thus, the FhuD2 mechanism for iron acquisition from transferrin appears somewhat redundant on the surface. This indicates the possibility of additional yet discovered functions of FhuD2.

3.6 Materials and Methods

Synthesis of DFO-NBD.

DFO-NBD was synthesized as described previously in Chapter 2. 656 mg of desferrioxamine B mesylate was dissolved in 10 mL methanol. 200 mg of NBD-Cl was dissolved in 7.5 mL methanol. Both these solutions were added to 20 mL of 0.1 N NaHCO_3 and the entire mixture was heated in an oil bath for 1 h. The mixture was concentrated under reduced pressure and purified via prep HPLC. FO-NBD was formed by adding 1.1 equivalents of $\text{Fe}(\text{acac})_3$ to DFO-NBD and letting mix for 1 hour.

K_{Fe} determination.

Apparent iron affinity of siderophores and siderophore-FhuD2 complexes were measured as described previously. 0.12 mM EDTA was added to 0.1 mM siderophore-Fe(III) in HEPES (10 mM HEPES, 100 mM KCl 600 mM NaCl, pH 7.4) to give a final volume of 1 mL. For the FhuD2 assay 0.1 mM siderophore-Fe(III) was mixed with 0.1 mM FhuD2 in HEPES for 15 min before 0.12 mM EDTA was added to give a final volume of 1 mL. The mixture was continuously analyzed for 90 min at 1 scan/s (480 nm for DFONBD, 430 nm for other siderophores) by optical absorbance spectroscopy using a methacrylate cuvette. The analyzed absorbance correlating to a given siderophore-Fe(III) complex decreased by pseudo first-order kinetics. The minimum absorbance as a thermodynamic endpoint was used to calculate apparent K_{Fe} using an extinction coefficient of $3000 \text{ M}^{-1} \text{ cm}^{-1}$ and a K_{Fe} value of $10^{25.1}$ for EDTA. Experiments were done at least in duplicate.

FhuD2 determination of K_d .

FhuD2 was prepared as described previously. N-His6-FhuD2 was thawed on ice from a -80°C freezer stock. 5.4 μM stock solutions were made in TBS buffer (25 mM TrisHCl, 0.2 g/L KCl, 8 g/L NaCl, pH 7.4) and diluted 1:50 to obtain ~ 100 nM solutions of N-His6-FhuD2 for the following assay. 4 μM solutions of FOE or transferrin were prepared in H_2O . Increasing concentrations of FOE (final concentration range: 0, 26.7, 53.2, 79.5, 105.6, 171, 299, 422, and 881 nM) were added to a solution of N-His6-FhuD2 at 100 nM final concentration in TBS buffer at a final volume of 300 μL . A PerkinElmer LS 55 Luminescence Spectrometer was used to analyze maximum fluorescence at ~ 340 nm over time at emission range 300-400 nm and 280 nm excitation and a scan speed of 400 nm/min. Emission slits were set to 10 nm and a HellmaAnalytics High Precision Cell cuvette made of Quartz SUPRASIL was used with a light path of 10×2 mm. Fluorescence intensity versus concentration of FOE was plotted, and Graphpad Prism v7.0b was used to calculate apparent K_d using a one site binding model by nonlinear regression. The above was repeated for holo-transferrin in place of FOE. All experiments were performed at least in duplicate.

Intrinsic Trp fluorescence quenching.

0.5 μM FeCl_3 was added to 2 μM DFO-NBD in HEPES at a final volume of 200 μL . A PerkinElmer LS 55 Luminescence Spectrometer analyzed maximum fluorescence at ~ 540 nm over time at emission range 500-600 nm and 475 nm excitation with a scan speed of 100 nm/min. Emission slits were set to 10 nm and a HellmaAnalytics High Precision Cell cuvette made of Quartz SUPRASIL with a light path of 10×2 mm was used. Scans were taken periodically out to 3 h. Each point of maximum fluorescence at a given time was normalized relative to the maximum

fluorescence at 0 min. The maximum fluorescence at 0 min represents 100% DFONBD. These experiments were repeated at 1, 1.5, 2, 4, and 8 μM FeCl_3 . The concentration of FeCl_3 vs. relative fluorescence at 60 min for each different concentration of FeCl_3 was plotted using Graphpad Prism v7.0b. All experiments were performed at least in duplicate.

Fluorescence-based kinetic assay for iron exchange.

A set concentration (usually 2 μM) of DFO-NBD was mixed with 0.5 μM of an iron source (iron-bound siderophore or holo-Tf) at a final volume of 200 μL and maximum fluorescence at ~ 540 nm was monitored over time, once per minute for the first 15 min, then at 30 min and finally at 60 min. The same fluorimeter setup as the FeCl_3 experiment was used. Relative fluorescence intensity to the maximum fluorescence intensity at 0 min was plotted against time using Graphpad Prism v7.0b. These experiments were repeated at 1, 1.5, 2, and 4 μM of an iron source. The above was then repeated at a constant concentration of the iron source and variable DFO-NBD. Finally, every reaction condition was repeated in the presence of 100 nm FhuD2 which was first allowed to mix with the iron source for 15 min before DFO-NBD was added. All experiments were completed at least in duplicate.

Siderophore displacement from immobilized FhuD2.

This procedure is adapted from a procedure reported in Rivera, G. S. M.; Beamish, C. R.; Wencewicz, T. A. ACS Infectious Diseases 2018, 4, 845-859. A fritted glass column was loaded with fresh Ni-NTA agarose resin in 1:1 EtOH:H₂O to give a working resin volume of 2.3 cm x 1 cm. The resin was washed with H₂O and equilibrated with SBP buffer (50 mM K₂HPO₄, 150 mM NaCl, 1 mM DTT, pH 8) at 4 °C. N-His₆-FhuD2 was thawed from a frozen stock (100 μL of 3.8 mM in SBP buffer; this is enough protein to fully saturate the Ni-NTA agarose resin), diluted to 3

mL final volume with SBP buffer, and added to the Ni-NTA agarose resin. After rocking at 4 °C for 30 min excess SBP buffer was eluted and the column was washed with SBP buffer until no *N*-His₆-FhuD2 was detected by SDS-PAGE analysis. The *N*-His₆-FhuD2-saturated Ni-NTA agarose resin is referred to as SBP-resin. Five siderophores (**FO-B, FO-NBD, FO-E, and Dan**) were used in pairs as the siderophore of interest (S₁) or sacrificial siderophore (S₂). Siderophore S₁ is first loaded to the SBP-resin by addition of 5 mL of a 0.02 mg/mL solution of S₁ in SBP buffer followed by 20 min of rocking at 4 °C. Excess SBP buffer is eluted and the SBP resin is washed five times with 15 mL of SBP buffer until LC-MS analysis shows no detectable ions for siderophore S₁. Next, 5 mL of a 0.02 mg/mL solution siderophore S₂ in SBP buffer is added and the SBP resin is rocked at 4 °C for 20 min. The column eluent is analyzed by LC-MS for the presence of siderophore S₁ ions to confirm displacement from the SBP resin by competitive binding of excess siderophore S₂. The SBP resin can now be used in a second cycle using the now resin bound siderophore S₂ as the siderophore of interest S₁. For LC-MS analysis of samples a gradient was formed from 5% B to 95% B over 20 min, followed by a 3 min hold at 100% B, and re-equilibration to 5% B over 2 min. Caution: using DTT in SBP buffer can lead to reduced Ni-NTA resin as indicated by a blue to orange color change during the procedure. BME can be used as an alternative to DTT to prevent this from taking place. Each experiment was performed in duplicate as independent trials.

Siderophore mix displacement with SBP-resin.

This procedure is adapted from a procedure reported in Rivera, G. S. M.; Beamish, C. R.; Wencewicz, T. A. ACS Infectious Diseases 2018, 4, 845-859. A fritted glass column was loaded with fresh Ni-NTA agarose resin in 1:1 EtOH:H₂O to give a working resin volume of 2.3 cm x 1 cm. The resin was washed with H₂O and equilibrated with SBP buffer (50 mM K₂HPO₄, 150 mM NaCl, 1 mM DTT, pH 8) at 4 °C. *N*-His₆-FhuD2 was thawed from a frozen stock (100 µL of 3.8

mM in SBP buffer; this is enough protein to fully saturate the Ni-NTA agarose resin), diluted to 3 mL final volume with SBP buffer, and added to the Ni-NTA agarose resin. After rocking at 4 °C for 30 min excess SBP buffer was eluted and the column was washed with SBP buffer until no *N*-His₆-FhuD2 was detected by SDS-PAGE analysis. The *N*-His₆-FhuD2-saturated Ni-NTA agarose resin is referred to as SBP-resin. A mixture of five siderophores (**FO-B**, **FO-NBD**, **FO-E**, and **Dan**) were used as the siderophores of interest, with the sixth siderophore (**SFO**) as the sacrificial siderophore. The mixture of five siderophores is first loaded to the SBP-resin by addition of 5 mL of a 0.005 mg/mL solution of each siderophore in SBP buffer followed by 20 min of rocking at 4 °C. Excess SBP buffer is eluted and the SBP resin is washed five times with 15 mL of SBP buffer until LC-MS analysis shows no detectable ions for siderophore S₁. Next, 5 mL of a 0.02 mg/mL solution **SFO** in SBP buffer is added and the SBP resin is rocked at 4 °C for 20 min. The column eluent is analyzed by LC-MS for the presence of each siderophore in the mixture (**FO-B**, **FO-NBD**, **FO-E**, and **Dan**) ions to confirm displacement from the SBP resin by competitive binding of excess siderophore **SFO**. For LC-MS analysis of samples a gradient was formed from 5% B to 95% B over 20 min, followed by a 3 min hold at 100% B, and re-equilibration to 5% B over 2 min. Caution: using DTT in SBP buffer can lead to reduced Ni-NTA resin as indicated by a blue to orange color change during the procedure. BME can be used as an alternative to DTT to prevent this from taking place. Each experiment was performed in duplicate as independent trials.

LC-MS confirmation of iron exchange.

50 uM of an iron source (iron-bound siderophore or holo-Tf) was mixed with 50 uM of iron-free siderophore in HEPES at a final volume of 200 uL and analyzed by relative % formation of the new iron-bound siderophore over time by LC-MS. An Agilent 6130 quadrupole with G1313 autosampler, 1200 series solvent module, and G1315 diode array detector was used in LC-MS

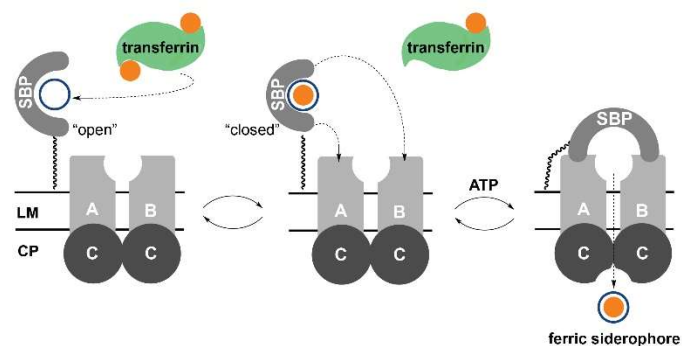
analysis. The experiment was repeated except in the presence of 10 μ M FhuD2 that is allowed to equilibrate with the iron source for 15 min before the iron-free siderophore is added. All experiments were performed at least in duplicate.

3.7 Acknowledgements

We thank Dr. Brad Evans at the Proteomics & Mass Spectrometry Facility at the Donald Danforth Plant Science Center, St. Louis, MO for assistance with the acquisition of the QTRAP LC-MS/MS spectra (supported by the National Science Foundation under Grant No. DBI-0521250). We thank Prof. John-Stephen Taylor (WUSTL, Dept. of Chemistry) for assistance with fluorescence quenching studies. We thank the NSF for funding through an NSF CAREER award to Prof. Timothy Wencewicz (grant 1654611).

3.8 Tables and Figures

a. Iron Shuttle



b. Siderophore Shuttle

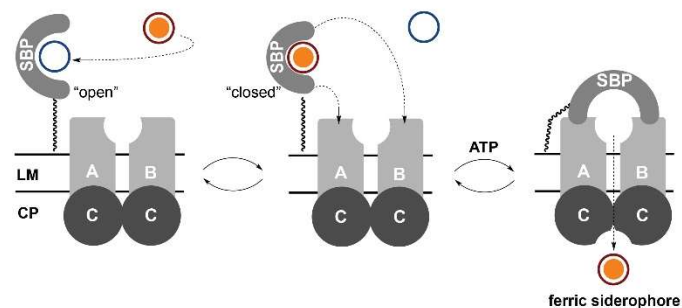


Figure 3.1. Schematic representation of the (a) “iron shuttle” and (b) “siderophore shuttle” membrane transport paradigms proposed by Raymond. In this work, we show that SBPs catalyze the exchange of iron from human transferrin to a bound siderophore cofactor.

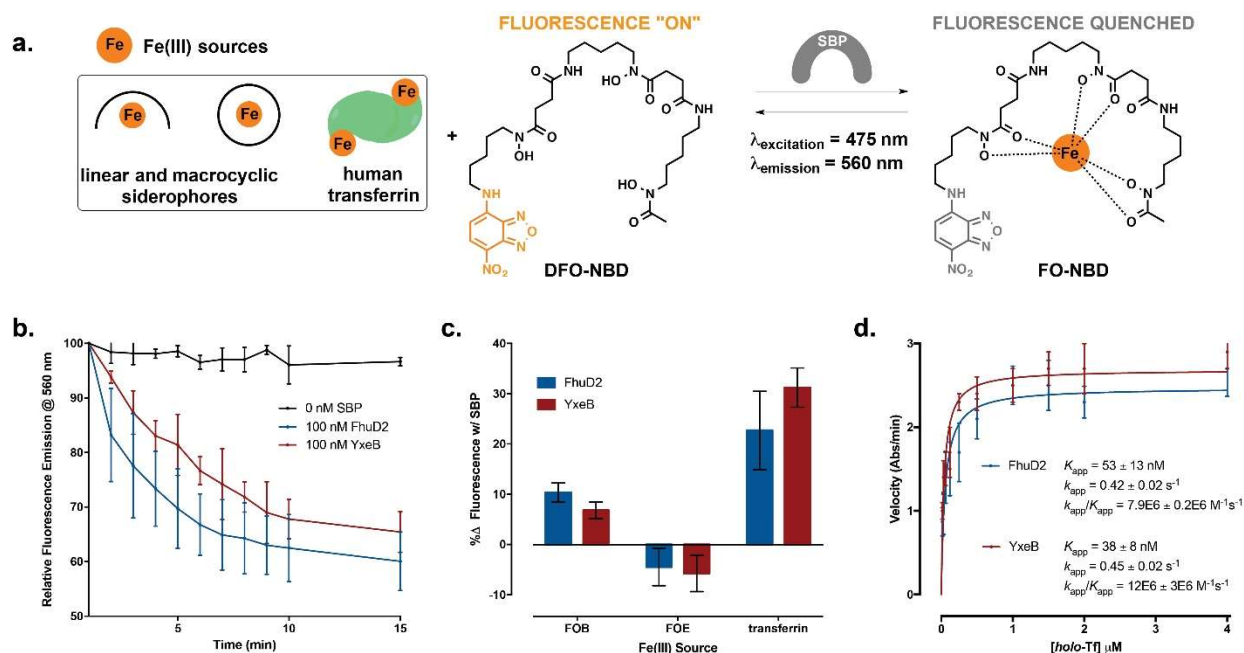


Figure 3.2. Siderophore-binding proteins (SBPs) catalyze the exchange of ferric iron from human transferrin to a siderophore cofactor. **(a)** General reaction scheme for the use of desferrioxamine-2-(4-nitro-2,1,3-benzoxadiazol-7-yl) conjugate (DFO-NBD) as a “turn off” fluorescent iron sensing probe that quenches upon chelation of iron(III). **(b)** Graph depicting relative fluorescence emission quenching of 2 μM DFO-NBD ($\lambda_{\text{excitation}} = 475 \text{ nm}$; $\lambda_{\text{emission}} = 565 \text{ nm}$) in the time domain using no SBP, 100 nM FhuD2, or 100 nM YxeB and 4 μM ferric human transferrin as the iron source. **(c)** Graph depicting the percentage change in the relative fluorescence emission of DFO-NBD ($\lambda_{\text{excitation}} = 475 \text{ nm}$; $\lambda_{\text{emission}} = 565 \text{ nm}$) after 15 minutes of incubation with 100 nM SBP (FhuD2 or YxeB) and 4 μM ferric iron source (FOB, FOE, or transferrin) relative to a control reaction with no added SBP. **(d)** Michaelis-Menten plot with apparent steady-state kinetic parameters for the exchange of ferric iron from variable transferrin to constant DFO-NBD (2 μM) catalyzed by 100 nM SBP (FhuD2 or YxeB). Error bars in all panels represent standard deviations for at least two independent trials.

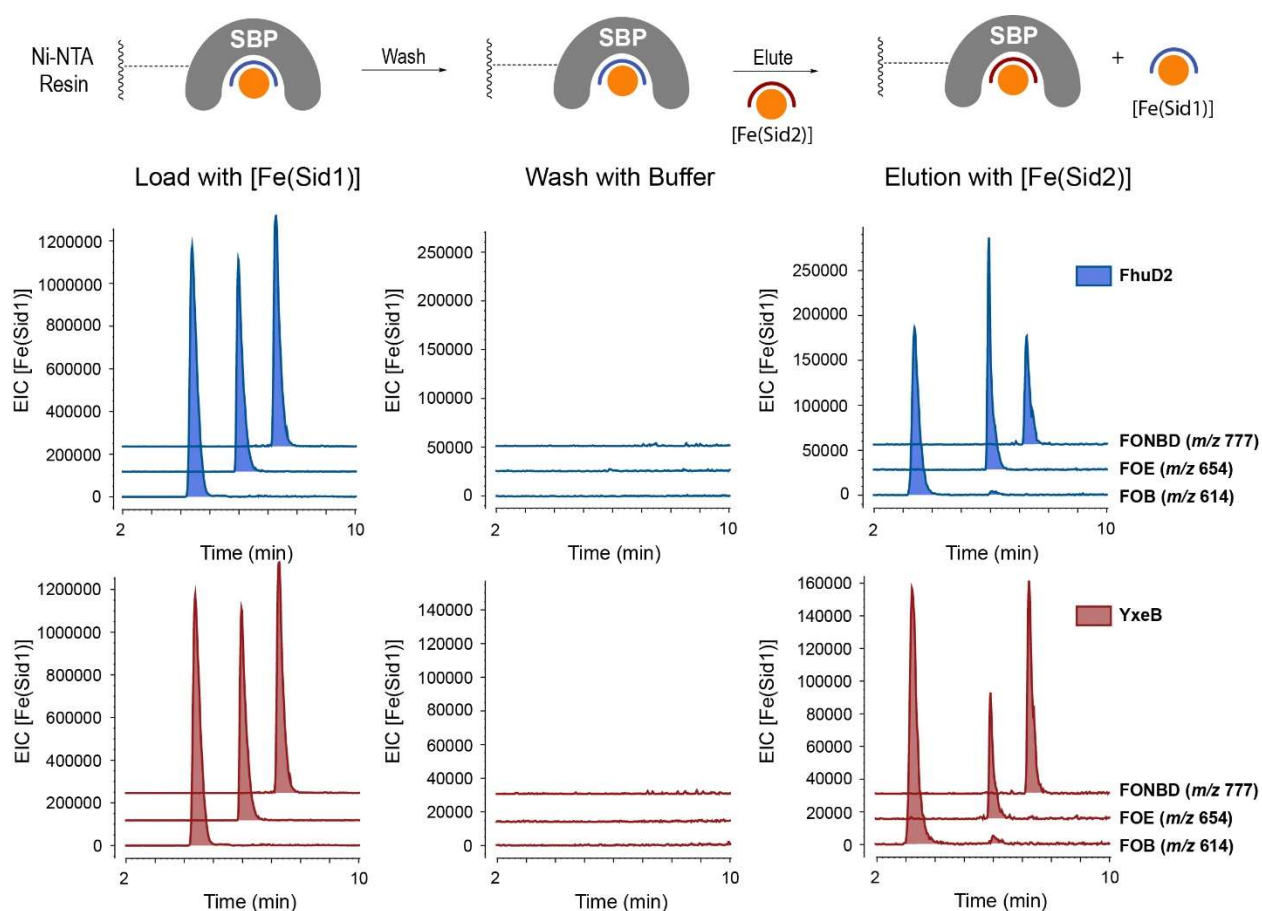


Figure 3.3. Ferrioxamine siderophores (FOB, FOE, and FONBD) bind reversibly and competitively to resin-immobilized FhuD2 and YxeB Siderophore binding proteins from *S. aureus* and *B. subtilis*, respectively. *N*-His₆-FhuD2 (**a**) or *N*-His₆-YxeB (**b**) was immobilized on Ni-NTA resin and loaded with a mixture of siderophores [Fe(Sid1)] (FOB, FOE, and FONBD), washed with phosphate buffer, and eluted with [Fe(Sid2)] (SFO). Column elutions were analyzed by LC-MS for each siderophore component in the load [Fe(Sid1)] (m/z = 614, 654, and 777 for FOB, FOE, and FONBD $[M+H]^+$ ions, respectively). Extracted ion chromatograms (EIC) are shown for FOB, FOE, and FONBD. EICs are representative for at least two independent trials.

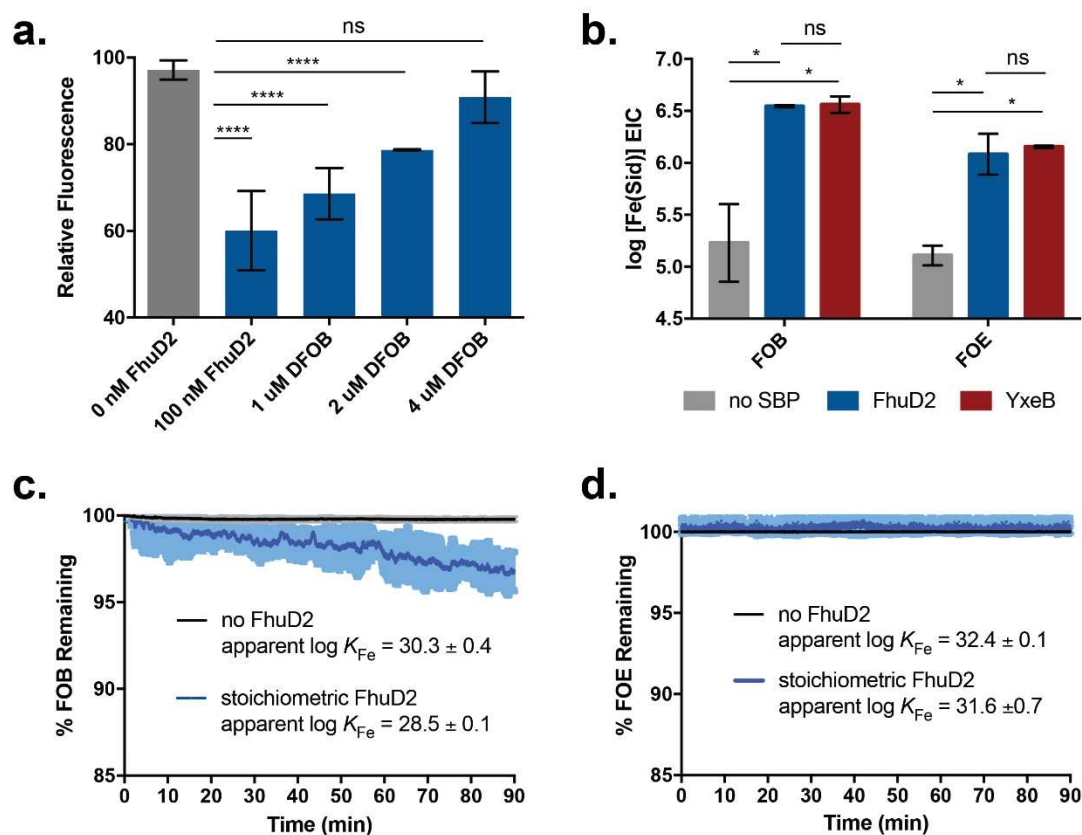


Figure 3.4. Macrocyclic siderophores can accept, but not donate, ferric iron during SBP-catalyzed exchanges. **(a)** Graph depicts the relative fluorescence emission quenching of 2 μ M DFO-NBD ($\lambda_{excitation} = 475$ nm; $\lambda_{emission} = 565$ nm) after 60 minutes of incubation with 100 nM FhuD2, 2 μ M ferric transferrin, and variable concentrations of competing DFOB (0–4 μ M). **(b)** Graph depicts the log of extracted ion counts (EICs) for [Fe(Sid)] complexes, FOB or FOE, after treatment of 50 μ M DFOB or FOE, respectively, with 50 μ M ferric transferrin without or with 10 μ M SBP (FhuD2 or YxeB). All EICs were normalized to a quinoline internal standard. The graphs in panels **(c)** and **(d)** depict the relative percentage of **(c)** FOB or **(d)** FOE remaining after treatment with 1.2 equivalents of EDTA in the presence or absence of stoichiometric FhuD2. Siderophore concentrations were determined by optical absorbance at 427 nm. The apparent ferric iron affinity (log K_{Fe}) was calculated from the decay plots. Error bars in all panels represent standard deviations for at least two independent trials. The shaded regions above the curve in panels **(c)** and **(d)** represent the error bars for every single data point along the continuously recorded data set; **** $p < 0.001$; * $p < 0.05$; ns = not significant.

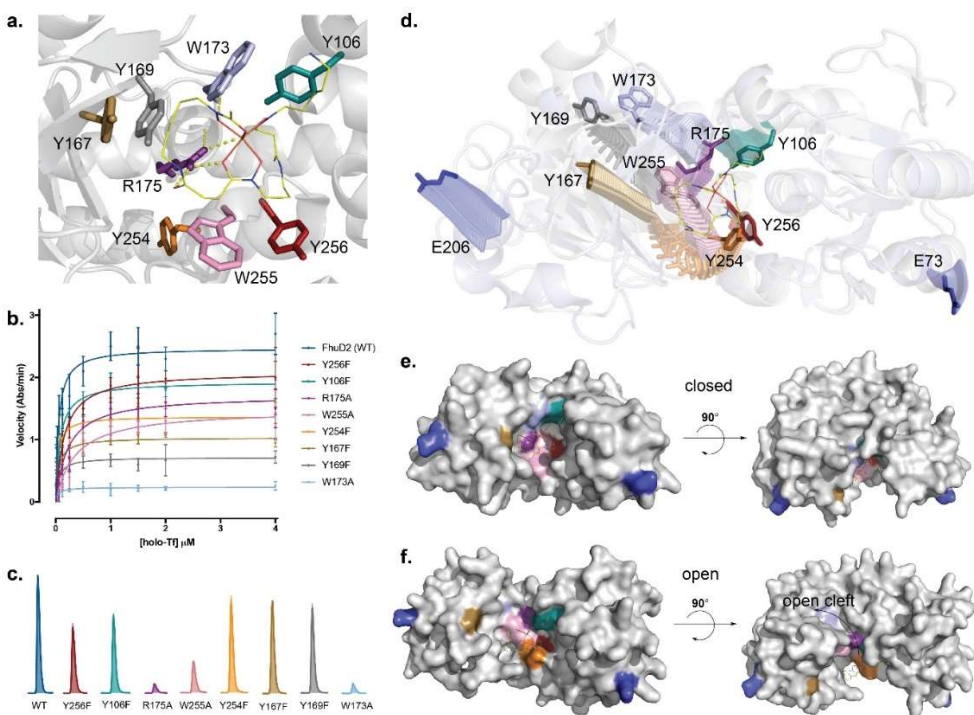


Figure 3.5. Mutational scanning of FhuD2 reveals active site residues involved in substrate binding and catalysis. **(a)** Active site residues in FhuD2 that were mutated. Color-coding of residues matches data sets in all panels. **(b)** Michaelis-Menten plot for wild-type and mutant FhuD2 variants (100 nM) reveals saturation kinetics for ferric transferrin and apparent changes in v_{\max} for the exchange of ferric iron to 2 μM DFO-NBD. **(c)** Relative binding and displacement of FOB to wild type and mutant FhuD2 variants. *N*-His₆-FhuD2 variant was immobilized on Ni-NTA resin and loaded with FOB, washed with phosphate buffer, and eluted with SFO. Column elutions were analyzed by LC-MS for FOB ($m/z = 614$ for $[M+H]^+$). Extracted ion chromatograms (EIC) are shown for FOB and were normalized to a quinoline internal standard. EICs are representative for at least two independent trials. **(d)** Stacked state model of the transition from “open” (dark, opaque residues) to “closed” (transparent residues) for FhuD2 highlighting residue dynamics. Panels **(e)** and **(f)** show surface models for FhuD2 in the **(e)** “closed” and **(f)** “open” states revealing a cleft from the movement of Y167, Y169, and W173. Images in panels **(a)**, and **(d)–(f)** were generated using PyMOL v2.2 (Schrödinger, Inc.). The stacked state model in panel **(d)** was generated using the morph function in PyMOL. The “closed” and “open” states of FhuD2 were generated from PDB entries 4fil and 4fna, respectively. Error bars in panel **(b)** represent standard deviations for at least two independent trials.

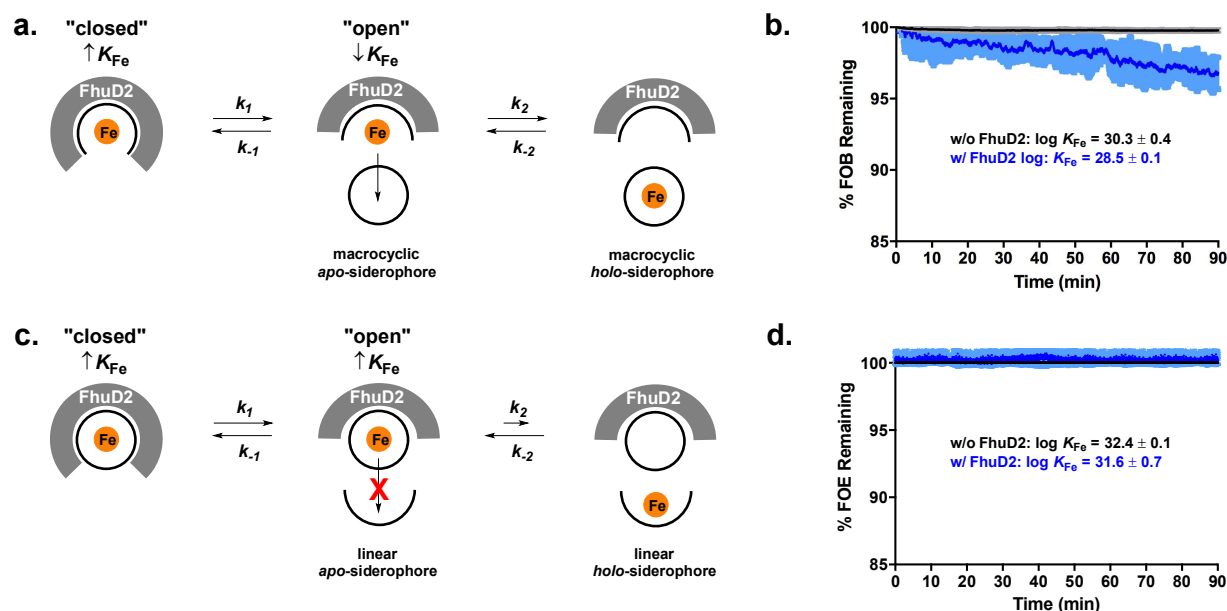


Figure 3.7. Model for iron exchange based on dynamic motions of FhuD2 causing disorder of the bound siderophore-Fe complex. FhuD2 can adopt “closed” and “open” forms in solution and solid state. This model suggests that the dynamic motion of FhuD2 can lower the siderophore iron affinity (K_{Fe}) of (a) linear siderophores to make iron exchange to a diffuse siderophore both kinetically and thermodynamically favorable. (b) EDTA competition assay shows that stoichiometric FhuD2 lowers the apparent iron affinity of the linear siderophore FOB. (c) Macrocyclic siderophores are more rigid and less responsive to the dynamic motions of FhuD2. (d) EDTA competition assays shows that stoichiometric FhuD2 has no effect on the apparent iron affinity of the macrocyclic siderophore FOE. (d) Overlay of liganded (blue; PDB 4FIL) and unliganded (salmon; PDB 4FNA) FhuD2 in “closed” and “open” conformations, respectively, highlighting the spatial orientation of conserved residues E97, W197, R199, and E231. For panels (b) and (d) the shaded region above and below the curve represents standard deviation for two independent trials. EDTA competition reactions were carried out in HEPES buffer at pH 7 at room temperature in the presence (w/) or absence (w/o) of stoichiometric FhuD2 using 1.2 equivalents of EDTA with continuous monitoring of optical absorbance at 427 nm, the characteristic absorbance for trihydroxamate iron(III) complexes.

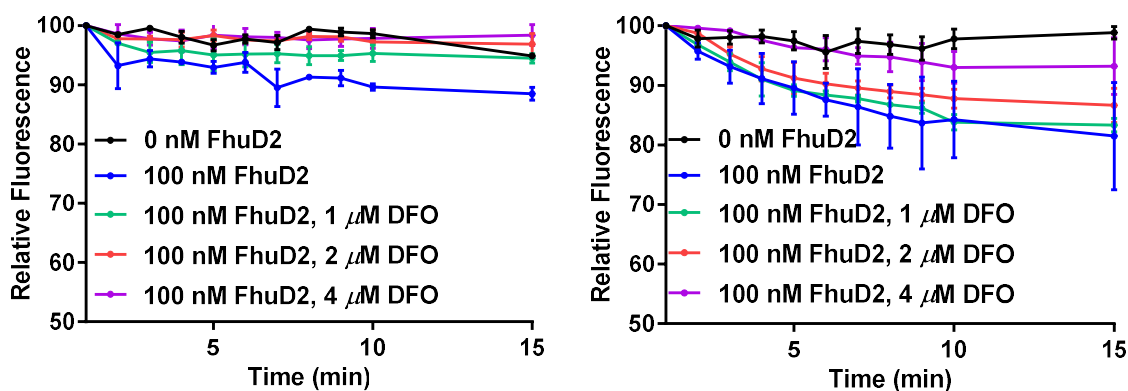


Figure 3.8. DFO attenuation of iron exchange from FOB (right) and *holo*-transferrin (left) to DFO-NBD. DFO directly competes with DFO-NBD for the iron, thus the fluorescence quenching of DFO-NBD is less pronounced at higher concentrations of DFO.

Table 3.1. Apparent binding affinities and kinetic parameters for FhuD2 mutants.

SBP	app. K_m (nM)	app. k_{cat} (s ⁻¹)	app. k_{cat}/K_m (x10 ⁶ M ⁻¹ s ⁻¹)	app. K_d (nM)			
				transferrin	DFOB	FOB	FOE
YxeB	40 ± 10 ^a	0.5 ± 0.02	10 ± 3	100 ± 40	30 ± 20	50 ± 30	30 ± 9
FhuD2	50 ± 10	0.4 ± 0.02	8 ± 0.2	70 ± 30	90 ± 10	30 ± 6	50 ± 6
Y256F	150 ± 30	0.4 ± 0.01	2 ± 0.5	70 ± 9	80 ± 30	60 ± 10	40 ± 20
Y106F	80 ± 10	0.3 ± 0.01	4 ± 0.5	100 ± 10	80 ± 20	40 ± 8	80 ± 10
R175A	220 ± 50	0.3 ± 0.02	1 ± 0.3	110 ± 30	40 ± 9	30 ± 9	50 ± 20
W255A	350 ± 110	0.3 ± 0.02	0.6 ± 0.2	110 ± 80	60 ± 20	60 ± 50	30 ± 9
Y254F	40 ± 10	0.2 ± 0.01	6 ± 0.8	90 ± 20	50 ± 10	10 ± 2	20 ± 3
Y167F	50 ± 20	0.2 ± 0.01	3 ± 1	80 ± 20	60 ± 9	40 ± 6	30 ± 3
Y169F	50 ± 20	0.1 ± 0.01	2 ± 1	110 ± 20	70 ± 10	40 ± 9	20 ± 2
W173A	50 ± 10	0.03 ± 0.002	0.9 ± 0.1	140 ± 30	100 ± 50	60 ± 8	90 ± 30

^aAll error values represent standard deviations for at least two independent trials.

3.9 References

- [1] Centers for Disease Control and Prevention, Office of Infectious Disease Antibiotic resistance threats in the United States (2013) Available at: <http://www.cdc.gov/drugresistance/threat-report-2013>. Accessed February 28, 2019.
- [2] Read AF, Woods RJ. (2014) Antibiotic resistance management. *Evol Med Public Health*. 2014(1):147.
- [3] Luyt CE, Bréchet N, Trouillet JL, Chastre. (2014) Antibiotic stewardship in the intensive care unit. *J Crit Care*. 18(5):480.
- [4] Bartlett JG, Gilbert DN, Spellberg B. (2013) Seven ways to preserve the miracle of antibiotics. *Clin Infect Dis*. 56(10):1445–1450.
- [5] Michael CA, Dominey-Howes D, Labbate M. (2014) The antibiotic resistance crisis: causes, consequences, and management. *Front Public Health*. 2:145.
- [6] Lushniak BD. (2014) Antibiotic resistance: a public health crisis. *Public Health Rep*. 129(4):314-6.
- [7] Gross M. (2013) Antibiotics in crisis. *Curr Biol*. 23(24):1063-5.
- [8] Rossolini GM, Arena F, Pecile P, Pollini. (2014) Update on the antibiotic resistance crisis. *Curr Opin Pharmacol*. 18: 56-60.
- [9] Torres VJ, Attia AS, Mason WJ, Hood MI, Corbin BD, Beasley FC, Anderson KL, Stauff DL, McDonald WH, Zimmerman LJ, Friedman DB, Heinrichs DE, Dunman PM, Skaar EP. (2010) Staphylococcus aureus fur regulates the expression of virulence factors that contribute to the pathogenesis of pneumonia. *Infect Immun*. 78(4):1618-28.
- [10] Cheung AL, Schmidt K, Bateman B, Manna AC. (2001) SarS, a SarA homolog repressible by agr, is an activator of protein A synthesis in Staphylococcus aureus. *Infect Immun*. 69(4):2448-55.
- [11] Jin CW, Ye YQ, Zheng SJ. (2014) An underground tale: contribution of microbial activity to plant iron acquisition via ecological processes. *Ann Bot*. 113(1):7-18.
- [12] Drechsel H, Winkelmann G. (1997) Iron chelation and siderophores, p 1–49. In Winkelmann G, Carrano CJ. (ed), Transition metals in microbial metabolism. Harwood Academic Publishers, Amsterdam, the Netherlands.
- [13] Skaar EP, Humayun M, Bae T, DeBord KL, Schneewind O. (2004) Iron-source preference of Staphylococcus aureus infections. *Science*. 305(5690):1626-8.
- [14] Lankford CE. (1973) Bacterial assimilation of iron. *Crit Rev Microbiol*. 2:273–331.
- [15] Haas H, Eisendle M, Turgeon BG. (2008) Siderophores in fungal physiology and virulence. *Annu Rev Phytopathol*. 46:149-87.

- [16] Kloepper JW, Leong J, Teintze M, Schroth MN. (1980) Enhanced plant growth by siderophores produced by plant growth-promoting rhizobacteria. *Nature*. 286:885–886.
- [17] Johnstone TC, Nolan EM. (2015) Beyond Iron: Non-classical biological functions of bacterial siderophores. *Dalton Trans.* 44(14): 6320-6339.
- [18] Pishchany G, Dickey SE, Skaar EP. (2009) Subcellular localization of the *Staphylococcus aureus* heme iron transport components IsdA and IsdB. *Infect Immun.* 77(7):2624-34.
- [19] Friedman DB, Stauff DL, Pishchany G, Whitwell CW, Torres VJ, Skaar EP. (2006) *Staphylococcus aureus* redirects central metabolism to increase iron availability. *PLoS Pathog.* 2(8):e87.
- [20] Beasley FC, Vinés ED, Grigg JC, Zheng Q, Liu S, Lajoie GA, Murphy ME, Heinrichs DE. (2009) Characterization of staphyloferrin A biosynthetic and transport mutants in *Staphylococcus aureus*. *Mol Microbiol.* (4):947-63.
- [21] Dale SE, Doherty-Kirby A, Lajoie G, Heinrichs DE. (2004) Role of siderophore biosynthesis in virulence of *Staphylococcus aureus*: identification and characterization of genes involved in production of a siderophore. *Infect Immun.* 72(1):29-37.
- [22] Hantke K. *Mol Gen Genet.* (1983) Identification of an iron uptake system specific for coprogen and rhodotorulic acid in *Escherichia coli* K12. *Mol Gen Genet.* 191(2):301-6.
- [23] Sebulsky MT, Hohnstein D, Hunter MD, Heinrichs DE. (2000) Identification and characterization of a membrane permease involved in iron-hydroxamate transport in *Staphylococcus aureus*. *J Bacteriol.* 182(16):4394-400.
- [24] Fukushima, T.; Allred, B. E.; Sia, A. K.; Nichiporuk, R.; Andersen, U. N.; Raymond, K. N. (2013) Gram-positive siderophore-shuttle with iron-exchange from Fe-siderophore to apo-siderophore by *Bacillus cereus* YxeB. *Proc. Natl. Acad. Sci. U.S.A.* 110, 13821.
- [25] Wencewicz TA, Long TE, Mollmann U, Miller MJ. (2013) Trihydroximate siderophore-fluoroquinolone conjugates are selective sideromycin antibiotics that target *Staphylococcus aureus*. *Bioconjug Chem.* 24(3): 473-486.
- [26] Vera DR, Smith CC, Bixby LM, Glatt DM, Dunn SS, Saito R, Kim WY, Serody JS, Vincent BG, Parrott MC. (2018) Immuno-PET imaging of tumor-infiltrating lymphocytes using zirconium-89 radiolabeled anti-CD3 antibody in immune-competent mice bearing syngeneic tumors. *PLoS One.* 13(3): e0193832.
- [27] You L, Wang J, Liu T, Zhang Y, Han X, Wang T, Guo S, Dong T, Xu J, Anderson G, Liu Q, Chang YZ, Lou X, Nie G. (2018) Targeted brain delivery of rabies virus glycoprotein 29-modified deferoxamine-loaded nanoparticles reverses functional deficits in parkinsonian mice. *ACS Nano.* 12(5): 4123-4139.
- [28] Guo JP, Pan JX, Xiong L, Xia WF, Cui S, Xiong WC. Iron chelation inhibits osteoclastic differentiation in vitro and in Tg2576 mouse model of Alzheimer's disease. (2015) *PLoS One.* 10(11): e0139395.

- [29] Bajbouj K, Shafarin J, Hamad M. (2018) High-dose deferoxamine treatment disrupts intracellular iron homeostasis, reduces growth, and induces apoptosis in metastatic and nonmetastatic breast cancer cell lines. *Technol Cancer Res Treat.* 17: 1-11.
- [30] Cloonan SM, Glass K, Laucho-Contreras ME, Bhashyam AR, Cervo M, Pabon MA, Konrad C, Plverino F, Siempos II, Perez E, Mizumura K, Ghosh MC, Parameswaran H, Williams NC, Rooney KT, Chen ZH, Goldklang MP, Yuan GC, Moore SC, Demeo DL, Rouault TA, D'Armiento JM, Schon EA, Manfredi G, Quackenbush J, Mahmood A, Silverman EK, Own CA, Choi AM. (2016) Mitochondrial iron chelation ameliorates cigarette smoke-induced bronchitis and emphysema in mice. *Nat Med.* 22(2): 163-74.
- [31] Lankford CE. (1973) Bacterial assimilation of iron. *Crit Rev Microbiol.* 2:273–331.
- [32] Haas H, Eisendle M, Turgeon BG. (2008) Siderophores in fungal physiology and virulence. *Annu Rev Phytopathol.* 46():149-87.
- [33] Kloepper JW, Leong J, Teintze M, Schroth MN. (1980) Enhanced plant growth by siderophores produced by plant growth-promoting rhizobacteria. *Nature.* 286:885–886.
- [34] Johnstone TC, Nolan EM. (2015) Beyond Iron: Non-classical biological functions of bacterial siderophores. *Dalton Trans.* 44(14): 6320-6339.
- [35] Endicott NP, Lee E, Wencewicz TA (2017) Structural basis for xenosiderophore utilization by the human pathogen *Staphylococcus aureus*. *ACS Infect Dis.* 3(7). 542-553.
- [36] Rivera GM, Beamish CR, Wencewicz TA. (2018) Immobilized FhuD2 siderophore-binding protein enables purification of salmycin sideromycins from *Streptomyces violaceus* DSM 8286. *ACS Infect. Dis.* 4(5): 845-859.
- [37] Ghosh A, Smith PES, Qin S, Yi M, Zhou HX. (2019) Both ligands and macromolecular crowders preferentially bind to closed conformations of maltose binding protein. *Biochemistry.* 58(17): 2208-2217.

Chapter 4: Conclusions and Perspectives

4.1 Preface

This chapter was written by Nathaniel Endicott (NPE) with feedback provided by Dr. Tim Wencewicz (TAW).

4.2 Summary of Dissertation

The structural basis of xenosiderophore utilization in *S. aureus* facilitated by the surface displayed SBP FhuD2, a membrane-anchored lipoprotein, was studied at the level of the substrate through a comprehensive look at a panel of DFO analogs and chemical probes. The goal was to establish structure-function relationships for the ferrioxamine siderophores with respect to binding iron, binding FhuD2, and promoting *S. aureus* growth under iron-deficient conditions. Using a panel of synthetic ferrioxamine analogs, iron affinity and kinetic stability of the siderophore-iron(III) complexes were determined by an EDTA competition assay. FhuD2 binding was measured through intrinsic tryptophan fluorescence quenching experiments. *S. aureus* growth recovery was analyzed with an iron-deficient minimal media in which iron-bound siderophore was the only iron source. Competition for cell entry was determined with a siderophore-sideromycin competition assay using minimal inhibitory concentration (MIC) as readout. Surprisingly, siderophore uptake in *S. aureus* was determined to be primarily dependent on net siderophore charge, regardless of iron affinity, kinetic stability, and FhuD2 binding.

At this stage it was important to dig deeper into the molecular mechanisms of FhuD2-mediated siderophore transport in *S. aureus*. Specifically, distinguishing the shuttle and displacement mechanisms proposed originally by Professor Ken Raymond would provide insight into how specifically cell entry by the *holo*-siderophore occurs. The development of a siderophore

displacement assay using resin-immobilized FhuD2 and a fluorescence quenching assay for iron trafficking using a fluorophore-siderophore conjugate provided the basis for studying shuttle and displacement. FhuD2 was found to reversibly siderophores, allowing for dynamic displacement of bound siderophores. FhuD2 was also shown to catalyze the exchange of iron between two siderophores. The direct role of FhuD2 in virulence led to the pursuit of functional alternatives to xenosiderophore iron exchange in a biological setting. Thus, the ability of FhuD2 to exchange the iron from human *holo*-transferrin to a siderophore was explored with the designed fluorescent siderophore chemical probe, where FhuD2 rapidly catalyzed iron exchange from *holo*-transferrin to an *apo*-siderophore at a much higher rate than the siderophore-siderophore exchange. Notably, siderophores without FhuD2 were unable to extract iron from *holo*-transferrin on a meaningful time scale.

FhuD2 appears to be playing an iron trafficking role in *S. aureus* as an enzyme that catalyzes the transfer of iron from human *holo*-transferrin to a bound siderophore cofactor which is subsequently imported into the cytoplasm. The use of the “turn-off” siderophore fluorescent probe molecule was validated by LC-MS to detect iron exchange from *holo*-transferrin to a variety of siderophores. The fluorescence assay allowed for kinetic measurements of iron exchange to determine if FhuD2 was behaving as a true enzyme. The kinetic effect was dependent on FhuD2 concentration and fit the Michaelis-Menten model. This validates the emergence of enzyme catalysis for iron exchange in a siderophore-binding protein. To probe the molecular mechanism for FhuD2-catalyzed iron exchange, the panel of FhuD2 active site mutants was prepared using the x-ray crystal structure of FhuD2 bounds to FOB as inspiration. Several residues were identified to be critical for iron exchange and siderophore binding which sheds light on the possible underlying mechanism from ligand exchange on the metal involving tyrosine residues as iron

chelators. Some of the mutants are also compromised for the ability to undergo siderophore displacement, which begins to connect the shuttle and displacement steps in the overall membrane transport paradigm. Using this knowledge, the same activity was verified in a related SBP from *Bacillus subtilis*, YxeB, to show that catalysis of iron exchange by SBPs is likely widespread in Gram-positive bacteria. The newly proposed mechanistic model is a reimagined siderophore uptake paradigm in which siderophores function as critical cofactors in the active site of FhuD2 and other SBPs, allowing these proteins to serve vital and flexible roles in scavenging iron from biological sources such as human *holo*-transferrin using xenosiderophores present in the human microbiome (Figure 4.1).

4.2 Future Directions & Broader Context

Development of an improved fluorescent probe is one major source of improvement for this work. While the simplicity of the chosen probe is a major advantage from an experimental standpoint, the capability to only effectively measure one direction of exchange, i.e. the acceptance of iron, limits some of the probe's effective scope. Work was done with measuring loss of iron from the probe, but ultimately unsuccessful results were achieved due to the initial moments of exchange blending closely with the background signal, causing unacceptable amounts of error (likely due to low signal-to-noise ratio) in the vital early kinetic moments of the reaction. An alternate probe that might quench fluorescence when loss of iron occurs could be an interesting complement to the current system. The binding of FhuD2 to DFO-NBD exposes another potential issue with the system. Experimentally the iron source to be acquired by DFO-NBD must start bound to the protein, which is not necessarily the direction of the process believed to be dominant in a biological setting. Altering the probe to possibly not be affected as much by protein binding could be a positive improvement. The concentration gradient of *apo*-siderophores being effluxed

after biosynthesis in the intracellular space dictates surface-bound proteins such as FhuD2 should be mostly in the iron free state, due to *apo*- and *holo*-siderophores both having similar affinity to the binding pocket. Therefore, the most common exchange in nature should be the acceptance of iron by an *apo*-siderophore already about to the SBP, or displacement by an incoming *holo*-siderophore. Directly measuring iron acceptance by a probe already protein-bound would be highly desirable in the development of future probes.

Another way to better develop the fluorescent probe would center on a deeper understanding of protein binding. While the focus of the current work has only included a qualitative analysis of displacement rates and equilibrium constants of binding of siderophores to the SBP of interest, an in-depth SAR analysis of the types of residues important in protein binding would allow the development of a probe that would either be highly favored to undergo displacement or shuttle depending on the affinity difference between it and the other iron source of interest. If a probe were designed to have very low affinity for the binding pocket, then it would be reasonable to say that the shuttle mechanism would be disfavored if the probe of interest were already protein-bound. Likewise, a low affinity probe if starting in the protein-bound state would highly favor the displacement mechanism. If the probe were designed to have a high affinity for the binding site, then shuttle would be highly favored if the probe started bound to the protein, and displacement would be highly favored if the probe started unbound to the protein. One advantage of dictating which mechanism is favored would be to more directly measure the shuttle mechanism. In the current setup, displacement does play a significant role in our assay, potentially causing a large “silent” effect when attempting to directly measure iron exchange. If displacement is roughly favored compared to shuttle, then measuring Michaelis-Menten parameters becomes much more difficult due to higher error. There would be several ways to design a more tailored

fluorescent probe. The panel of analogs from the first paper would be a good starting point in combination with the series of active site mutants. A detailed analysis of binding affinity of each of the analogs to each of the mutants would in theory provide a good set of rules for important residue and functional group interactions are required for higher affinity binding. Crystallography on various siderophores bound to multiple active site mutants would be a further guide into the development of high or low affinity fluorescent siderophore probes.

Another aspect in which the fluorescent probe could be improved is in the actual fluorescence signal intensity of the compound. The fluorescent signal intensity of the DFO-NBD probe is quite low compared to that of intrinsic fluorescence intensity of the SBPs for example. The probe works because of the unique fluorescence emission wavelength of DFO-NBD, but the low signal intensity generated by the probe naturally leads to elevated error due to low signal-to-noise ratios in the measured assays. More fluorescently intense probes would also allow for lower concentrations to be used in the assays, allowing for conservation of material. Also, problems such as fluorescence increases or decreases when bound to a protein would become less impactful as the starting fluorescence intensity would be increased.

The addition of whole-cell assays would provide a useful complement to the current work. One way to do this would be to grow *S. aureus* in iron deficient conditions similar to what is seen in the first chapter. Instead of the addition of a *holo*-siderophore as the iron source, *holo*-transferrin could be used in increasing concentrations to confirm the ability of *S. aureus* to utilize iron from *holo*-transferrin. Then increasing amounts of an *apo*-siderophore could be added at a set concentration of *holo*-transferrin to hopefully be able to observe increasing capability of *S. aureus* to utilize iron from *holo*-transferrin at increasing concentrations of *apo*-siderophore. This could be done in the reverse way in which increased concentrations of *holo*-transferrin could then be added

to a set concentration of *apo*-siderophore. Ultimately the results of this experiment would theoretically support the idea of *apo*-siderophore cofactors as important in the acquisition of iron from sources such as human *holo*-transferrin. Coupled to this idea would be testing *S. aureus* FhuD2-knockout strains and FhuD2-mutant strains by the same experimental setup. Presumably, *S. aureus* might be able to increasingly utilize *holo*-transferrin iron from its other siderophore uptake sources but increasing amounts of *apo*-siderophore specific to the FhuD2 system would ideally not have the same impact on growth recovery at a set concentration of *holo*-transferrin. The FhuD2 knockout strains separately isolated could be added back into the system at set concentrations of *holo*-transferrin and *apo*-siderophore, and growth recovery would ideally be observed. The *S. aureus* strains expressing mutated FhuD2 would provide a good comparison for the in vitro evaluation of FhuD2 mutants described in Chapter 3 to extend the findings to the more complex cellular context.

The substrate scope of FhuD2 and YxeB could be expanded to additional biologically relevant iron sources. Heme is one example that has been tied to utilization by *S. aureus*, and acquisition of its iron has directly been tied to the native *S. aureus* siderophores.¹ Lactoferrin and calprotectin are additional potential iron sources for invading pathogens since these are expressed as innate immune proteins that limit the concentration of free metal ions.⁹ Fluorescence quenching assays in the presence of these iron sources could be easily done using DFO-NBD and our established assay to determine the extent of SBPs to utilize different types of iron in an infection environment.

Crystallographic work in the future through collaboration would be a useful way to provide insight on the shuttle mechanism. While two binding sites appear highly unlikely, the possibility does exist and capturing multiple siderophores bound to the protein would be invaluable in piecing

together specific mechanistic detail of the shuttle mechanism. The other aspect of the shuttle mechanism, the acquisition of iron from host defense proteins such as transferrin, would also greatly be aided by crystallographic insight. Due to transferrin's size compared to FhuD2, it seems highly unlikely that transferrin would necessarily directly compete with siderophores for access to the binding pocket. Rather, protein-protein interaction inducing allosteric effects and placing the iron in *holo*-transferrin in close proximity to a bound *apo*-siderophore is needed. Observing a crystal structure of transferrin's interaction with FhuD2 would provide possible confirmation of the legitimacy of this argument and reveal if this is an interaction specific to transferrin or general to many types of metalloproteins.

One of the drawbacks of the current work is utilizing only the soluble SBP portion of the ABC transporter. Certain interactions with the SBP anchored to the membrane could end up affecting aspects of the shuttle or displacement mechanism in unknown ways. Nanodisc technology would allow for the observation of iron exchange or substrate displacement at the SBP in the context of the cellular membrane. Study of nanodisc or other lipid-based reconstitution of fully functional SBP and associated ATP-dependent permeases by native spray mass spectrometry or even crystallography would be especially insightful.

The idea of refining a treatment for iron overload disease has additional room for exploration. The ability for a negatively charged siderophore such as danoxamine to be effective at treating iron overload while being much less easily utilized by a pathogen such as *S. aureus* could be explored through collaboration with labs equipped with mouse models of pathogen infection and iron overload disease. The iron affinity of danoxamine could be tuned to be higher in order to maintain similar treatment efficacy as desferrioxamine. Other factors important in the treatment of iron overload, such as ability to efficiently cycle out of the body, could be examined

in the case of danoxamine. Testing coadministration with some other popular iron overload treatments, such as deferasirox and deferiprone, would be another way to probe the potential of danoxamine as an iron overload treatment. The extent of mobilization intracellularly could be tested in a similar way as has been done with DFO with adamantane derivatives.²

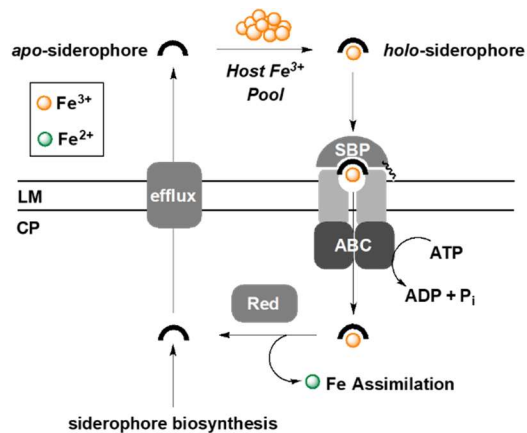
Multiple big picture questions about the nature of FhuD2 transport remain to be answered. Its role as a vaccine candidate cannot be ignored and points to its highly relevant role in *S. aureus* virulence.³ The precise nature of the interaction between FhuD2 and *holo*-transferrin could be hypothesized to be acting similar to macromolecular crowding, in which proteins interact not only with their specific substrate but also with bystander macromolecules, called molecular crowding agents. These nonspecific interactions are primarily facilitated via hydrophobic interactions of protein surfaces and can modulate protein activity and conformation.⁴ The stoichiometry of FhuD2's shuttling function is unknown. The seeming lack of a second binding site on the protein points to the potential of a dimeric interaction with another SBP in order to shuttle iron from one siderophore to another. This dimeric interaction might not be necessary when acquiring iron from a source such as transferrin, but there is literature evidence that such dimeric interactions can occur.⁵ The possibility of direct iron binding to FhuD2 cannot be ignored. Direct metal binding is observed in a variety of SBPs, including CeuE.^{6,10} Perhaps part of the way it extracts iron from *holo*-transferrin is through direct coordination to the metal. Transport of iron from a *holo*-siderophore already bound to the SBP could occur through binding to the iron and directly transporting it through the ABC transporter. There is literature evidence of direct iron chelation by SBPs and work here has shown direct fluorescence quenching of FhuD2 by FeCl₃, so this remains a possibility to explore further.⁶

The development of a more complete picture of siderophore-mediated iron acquisition necessitates studying systems outside of the siderophore uptake portion. Siderophore efflux is one area that is would make a promising therapeutic target. The efflux transporter of staphyloferrin A, SfaA, has directly been linked to *S. aureus* proliferation in epithelial cells and abscesses, as mutants lacking SfaA exhibited noticeable growth defects.⁷ The specific mechanism of how efflux occurs, however, remains largely unknown. Iron release is another highly relevant portion of the siderophore iron acquisition pathway. While it typically occurs via a reductive mechanism, the mechanism of action of iron reduction, though linked to several proteins, has not been fully elucidated.⁸

Additional SBPs could be explored to test the generality of the findings of enzymatic activity illustrated in this work, which are likely to be relevant for many SBPs in diverse pathogens beyond FhuD2 and YxeB in *S. aureus* and *B. cereus*, respectively. A multitude of different combinations of SBPs, iron sources, and apo-siderophore combinations could be analyzed for interplay of both the siderophore displacement and iron shuttle mechanisms. Different fluorescent probes may be necessary if DFO-NBD does not function as an adequate substrate for a SBP of interest, but there is vast room for expansion of these ideas into other systems. Knowledge about siderophore uptake in SBPs native to other types of bacteria could lay the groundwork for expanding the relevance of siderophore-mediated iron transport paradigms beyond *S. aureus* and provide an evolutionary context (at the residue level) for the emergence of catalysis (iron exchange) in siderophore-binding proteins.

4.4 Figures

Old paradigm



New paradigm

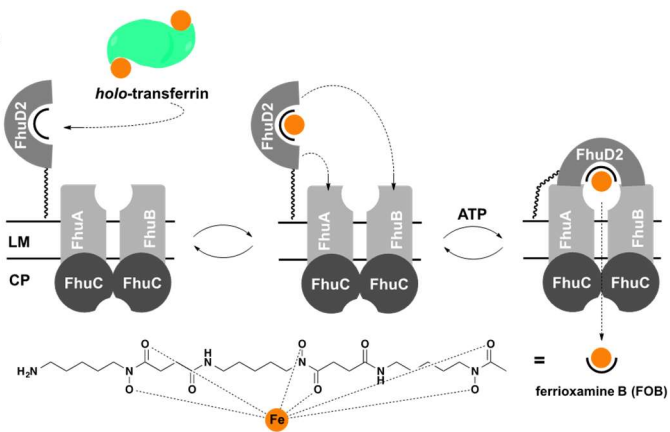


Figure 4.1. Newly presented siderophore-mediated uptake paradigm. Shown above is the previously understood system of siderophore function where the siderophore, after being effluxed from the cell, travels into the extracellular environment before eventually returning once bound to iron. In the revised paradigm, as shown below, the siderophore is effluxed from the cell but quickly binds a SBP anchored to the cell membrane. The *apo*-siderophore then serves as a cofactor to acquire iron from many different sources that may be available at an infection site, such as human *holo*-transferrin.

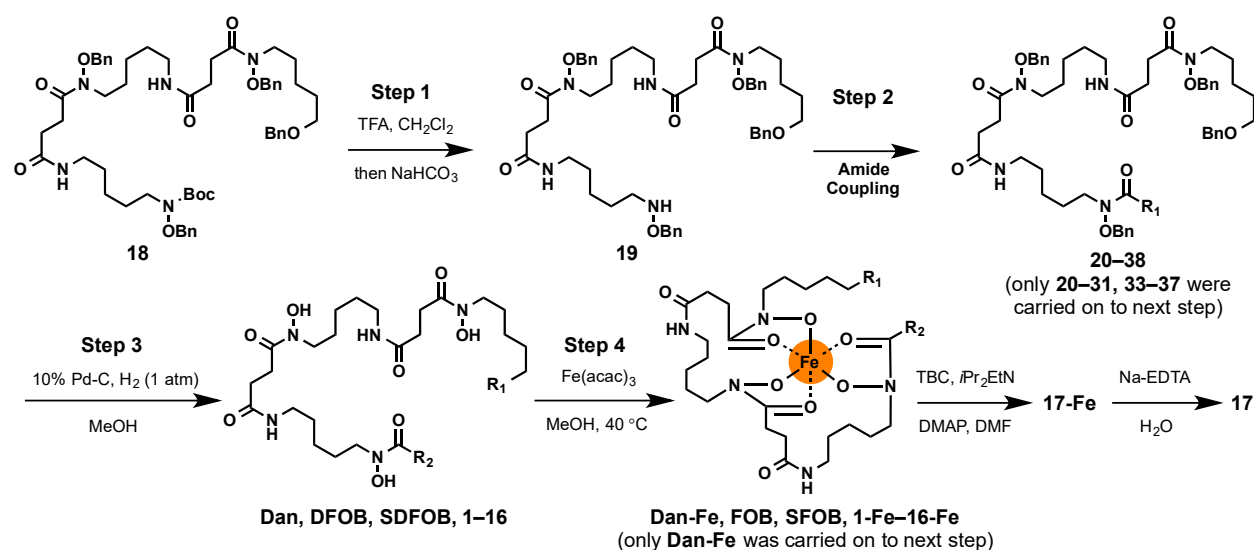
4.5 References

- [1] Conroy BS, Grigg JC, Kolesnikov M, Morales LD, Murphy MEP. (2019) Staphylococcus aureus heme and siderophore-iron acquisition pathways. *Biometals*, epub ahead of print. DOI: 10.1007/s10534-019-00188-2.
- [2] Liu J, Obando D, Schipanski LG, Groebler LK, Witting PK, Kalinowski DS, Richardson DR, Codd R. J. (2010) Conjugates of desferrioxamine B (DFOB) with derivatives of adamantane or with orally available chelators as potential agents for treating iron overload. *J. Med Chem.* 53, 1370-1382.
- [3] Mariotti P, Malito E, Biancucci M, Lo Surdo P, Mishra RP, Nardi-Dei V, Savino S, Nissum M, Spraggon G, Grandi G, Bagnoli F, Bottomley MJ. (2013) Structural and functional characterization of the Staphylococcus aureus virulence factor and vaccine candidate FhuD2. *Biochem J.* 449(3):683-93.
- [4] Ghosh A, Smith PES, Qin S, Yi M, Zhou HX. (2019) Both Ligands and Macromolecular Crowders Preferentially Bind to Closed Conformations of Maltose Binding Protein. *Biochemistry.* 58(17):2208-2217
- [5] Brillet K, Ruffenach F, Adams H, Journet L, Gasser V, Hoegy F, Guillon L, Hannauer M, Page A, Schalk IJ. (2012) An ABC transporter with two periplasmic binding proteins involved in iron acquisition in Pseudomonas aeruginosa. *ACS Chem Biol.* 7(12):2036-45.
- [6] Banerjee S, Weerasinghe AJ, Parker Siburt CJ, Kreulen RT, Armstrong SK, Brickman TJ, Lambert LA, Crumbliss AL. (2014) Bordetella pertussis FbpA binds both unchelated iron and iron siderophore complexes. *Biochemistry.* 54(24): 3952-60.
- [7] Nakaminami H, Chen C, Truong-Bolduc QC, Kim ES, Wang Y, Hooper DC. (2017) Efflux Transporter of Siderophore Staphyloferrin A in Staphylococcus aureus Contributes to Bacterial Fitness in Abscesses and Epithelial Cells. *Infect Immun.* 85(8).
- [8] Ganne G, Brillet K, Basta B, Roche B, Hoegy F, Gasser V, Schalk IJ. (2017) Iron release from the siderophore pyoverdine in Pseudomonas aeruginosa involves three new actors: FpvC, FpvG, and FpvH. *ACS Chem Biol.* 12(4): 1056-1065.
- [9] Zygiel EM, Nolan EM. (2018) Transition metal sequestration by the host-defense protein calprotectin. *Annu Rev Biochem.* 20 (87): 621-643.
- [10] Shaik MM, Cendron L, Slamina M, Ruzzene M, Zanotti G. (2014) Helicobacter pylori periplasmic receptor CeuE (HP1561) modulates its nickel affinity via organic metallophores. *Mol Microbiol.* 91(4): 724-35.

Appendix A: Synthesis and NMR Spectra for **Chapter 2**

A.1 Synthesis of the Ferrioxamine Library

General materials and methods. The trihydroxamate siderophores **1–17** and the corresponding 1:1 iron(III) complexes **1-Fe–17-Fe** were synthesized as shown in **Scheme 2.1**.³ All reactions were carried out under a dry argon atmosphere unless otherwise stated. Dichloromethane (CH_2Cl_2) was distilled from calcium hydride. Tetrahydrofuran was distilled from Na/benzophenone. Dimethylformamide (DMF), diisopropylamine ($i\text{Pr}_2\text{EtN}$), and acetonitrile (CH_3CN) were used from sealed anhydrous bottles purchased from Acros. Silica gel chromatography was performed using Sorbent Technologies silica gel 60 (32–63 μm). ^1H -NMR and ^{13}C -NMR spectra were recorded on a 600 MHz Varian DirectDrive spectrometer and FIDs were processed using ACD/ChemSketch version 10.04. Chemical shifts (δ) are given in parts per million (ppm) and are referenced to non-deuterated residual solvent. Coupling constants (J) are reported in hertz (Hz). High-resolution mass spectrometry measurements were obtained on a Bruker micrOTOF II using electrospray ionization (ESI) in positive ion mode. Sample was introduced via flow injection at 4 $\mu\text{L}/\text{min}$ and mass spectra were recorded from 50–3000 m/z for two min. HPLC was performed on a Waters 1525 binary pump instrument with a Waters 2487 dual λ absorbance detector set at 427 nm and 254 nm. The operating software for the HPLC was Breeze version 3.30. The HPLC column was a YMC Pro C18 reverse phase (3.0 x 50 mm) fit with a guard column (2.0 x 10 mm) of the same composition. Mobile phases were 10 mM ammonium acetate in H_2O (A) and 10 mM ammonium acetate in CH_3CN (B). A gradient was formed from 5%–80% (B) over 10 min, then 80%–95% (B) over 2 min, and then 95%–5% (B) over 3 min at a flow rate of 0.7 mL/min. Thin layer chromatography (TLC) was performed with aluminum-backed Merck RP-C18 F₂₅₆ silica gel plates using a 254 nm lamp or aqueous FeCl_3 stain for visualization. IR spectra were recorded on a Bruker Tensor series FT-IR spectrometer using a diamond ATR accessory or as a thin film on NaCl disks. Melting points were determined in capillary tubes using a Thomas Hoover melting point apparatus and are uncorrected. The purity of compounds tested in biological assays was evaluated by analytical HPLC and verified to be $\geq 95\%$ pure.

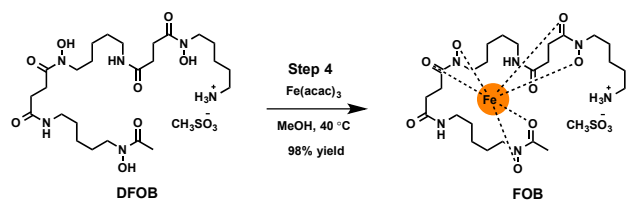


Supplementary Scheme 1. Synthesis of ferrioxamine siderophores used in this study.

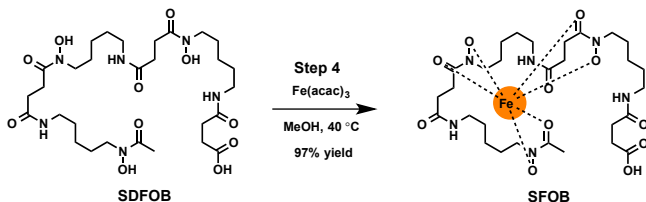
Synthesis of siderophores. The *N*-Boc-tetra-*O*-benzylated precursor **18** was prepared according to well established a literature protocol.⁴ Treatment of **18** with TFA followed by an aqueous NaHCO₃ quench gave amine **19** according to a literature protocol (**Step 1**).⁴ Amine **19** is the precursor for benzyl protected siderophores **20–38** (**Fig. 2.15**) and deprotected siderophores **1–17**, **Dan**, and **Dan-Cip**. The synthesis and full characterization of siderophores **1**, **2**, **3**, **5**, **6**, **7**, **8**, and **17** and corresponding iron(III) complexes was reported previously.⁵ The synthesis and full characterization of **Dan**, **Dan-Fe**, and **Dan-Cip** was reported previously.^{4,6} **DFOB** was purchased from Sigma-Aldrich (St. Louis, MO). **SDFOB** was synthesized from **DFOB** as reported previously.⁷ General procedures for **steps 3** and **4** are provided below along with detailed procedures for the synthesis of all new siderophores including benzyl protected precursors **22**, **23**, and **30–38**, deprotected siderophores **4** and **9–16**, and siderophore iron(III) complexes **FOB**, **SFOB**, and **4-Fe** and **9-Fe–16-Fe**. Siderophores were synthesized by Wenciewicz at the University of Notre Dame and transferred to his laboratory at Washington University in St. Louis via a material transfer agreement.

General procedure for step 3. Benzyl protected siderophore (**22**, **23**, **30**, **31**, **33–37**) was dissolved in MeOH (~0.01 M) in an HCl-washed flask with a magnetic stir bar. The flask was flushed with argon, charged with 10% Pd-C (~10% w/w), and flushed with H₂ gas several times with intermediate vacuum evacuation. The mixture was left stirring under positive pressure from a H₂ balloon. Reaction progress was monitored by RP-C18 TLC (1.5:1 CH₃CN:H₂O; FeCl₃ stain). Once complete as judged by TLC the flask was flushed with argon and the mixture was vacuum filtered through a pad of celite and concentrated under reduced pressure. Crude product was dissolved in a minimal amount of MeOH and precipitated by adding Et₂O. The siderophore (**4**, **9–16**) was isolated as a white solid after trituration with Et₂O and drying under vacuum.

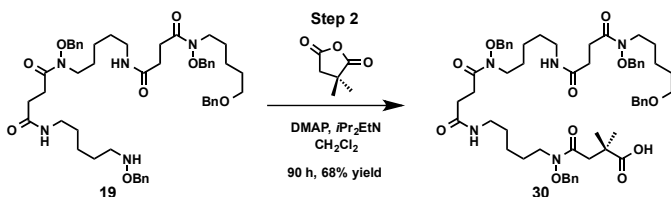
General procedure for step 4. The siderophore (**DFOB**, **SDFOB**, **4**, **9–16**) was dissolved in MeOH (0.002 M) at 40 °C (oil bath temp). Fe(acac)₃ (1.1 equiv) was added to give a clear, orange solution that was stirred for 2 hr. The MeOH was removed under reduced pressure using rotary evaporation to give the siderophore-iron(III) complex as an orange film. The crude product was dissolved in a minimal amount of MeOH and precipitated by addition of Et₂O, triturated with Et₂O, and dried under vacuum to give the pure siderophore-iron(III) complex (**FOB**, **SFOB**, **4-Fe**, **9-Fe–16-Fe**) as an orange powder.



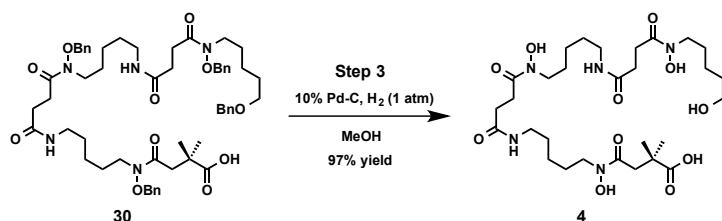
FOB (mesylate salt). Desferrioxamine B mesylate (**DFOB**; 47.5 mg, 0.072 mmol) was complexed to Fe(III) according to the general procedure for **step 4** to give siderophore-Fe(III) complex **FOB** in 98% yield as an orange powder (50.5 mg, 0.071 mmol). Mp 174–178 °C (dec.); HPLC retention time 2.06 min.



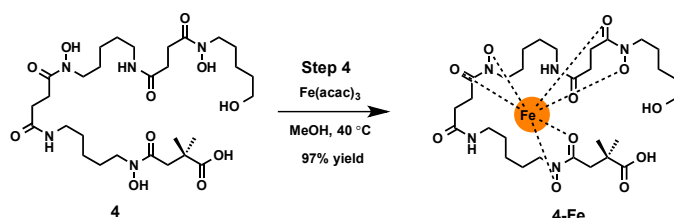
SFOB. Succinyl-desferrioxamine B (**SDFOB**; 51 mg, 0.077 mmol) was complexed to Fe(III) according to the general procedure for **step 4** to give siderophore-Fe(III) complex **SFOB** in 97% yield as an orange powder (53.2 mg, 0.075 mmol). Mp 143–148 °C; HPLC retention time 2.37 min.



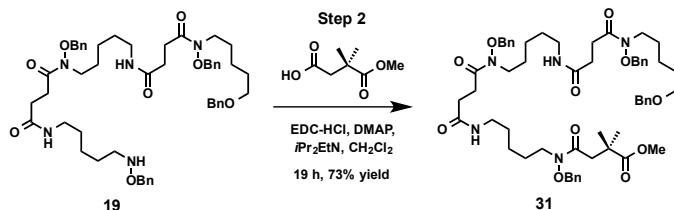
Benzyl protected siderophore 30. Hydroxylamine **19** (457.7 mg, 0.52 mmol), 2,2-dimethylsuccinic anhydride (150.0 mg, 0.71 mmol), *i*Pr₂EtN (0.1 mL, 0.71 mmol), and catalytic DMAP (31 mg, 0.25 mmol) were dissolved in 8 mL of CH₂Cl₂, respectively. After 24 h, TLC (6% MeOH in CH₂Cl₂; FeCl₃ stain) showed only trace remaining starting material (**19**). After 90 h, the reaction was quenched with 1 N HCl (10 mL). The aq. layer was extracted with CH₂Cl₂ (2 x 10 mL) and the combined CH₂Cl₂ layers were washed with brine (10 mL), dried over anhydrous MgSO₄, filtered, and concentrated under reduced pressure. This gave 579.6 mg of a cloudy, viscous oil that was purified by silica gel column chromatography (0.75 x 3 in silica gel; 3% MeOH in CH₂Cl₂). Pure product (**30**) was obtained in 68% yield as a clear, colorless oil (355.1 mg, 0.35 mmol). IR (thin film on NaCl plate) 3327, 2936, 2865, 1726, 1657, 1548, 1454, 1365, 1191 cm⁻¹; ¹H-NMR (600 MHz, CDCl₃) δ (ppm) 7.43–7.29 (m, 20 H), 6.81 (br s, 1 H), 6.58 (br s, 1 H), 4.85 (s, 4 H), 4.80 (s, 2 H), 4.48 (s, 2 H), 3.71–3.59 (m, 6 H), 3.44 (t, *J* = 6.5 Hz, 2 H), 3.23–3.16 (m, 4 H), 2.85 (t, *J* = 6.3 Hz, 2 H), 2.83–2.77 (m, 2 H), 2.69 (s, 2 H), 2.55 (t, *J* = 6.5 Hz, 2 H), 2.50 (t, *J* = 6.5 Hz, 2 H), 1.67–1.58 (m, 8 H), 1.52–1.42 (m, 4 H), 1.39–1.27 (m, 6 H), 1.25 (s, 6 H); ¹³C-NMR (150 MHz, CDCl₃) δ (ppm) 179.4, 174.5, 173.8, 173.2, 172.4, 172.3, 138.5, 134.3, 134.2, 129.2, 129.1, 129.0, 128.9, 128.8, 128.7, 128.6, 128.6, 128.3, 127.5, 127.4, 76.3, 76.3, 76.0, 72.8, 70.0, 45.4, 44.8, 43.9, 42.1, 39.9, 39.3, 39.2, 30.5, 30.4, 29.3, 28.6, 28.1, 28.0, 27.9, 26.6, 26.4, 26.3, 25.9, 23.6, 23.4, 23.3; HRMS–FAB (*m/z*): [*M*+H]⁺ calcd. for C₅₇H₇₈N₅O₁₁: 1008.5698, found 1008.5700.



Siderophore 4. Benzyl protected siderophore **30** (51.8 mg, 0.051 mmol) was deprotected according to the general procedure for **step 3** to give the siderophore **4** in 97% yield as a white solid (32.0 mg, 0.049 mmol). $^1\text{H-NMR}$ (600 MHz, CD_3OD) δ (ppm) 3.62–3.57 (m, 4 H), 3.55 (t, $J = 6.5$ Hz, 2 H), 3.21–3.13 (m, 6 H), 2.76 (t, $J = 7.2$ Hz, 2 H), 2.51 (s, 2 H), 2.48–2.43 (m, 6 H), 1.70–1.60 (m, 4 H), 1.59–1.47 (m, 8 H), 1.44–1.29 (m, 6 H), 1.23 (s, 6 H); HRMS–ESI (m/z): $[\text{M}+\text{Na}]^+$ calcd. For $\text{C}_{29}\text{H}_{53}\text{N}_5\text{NaO}_{11}$: 670.3634, found 670.3621.

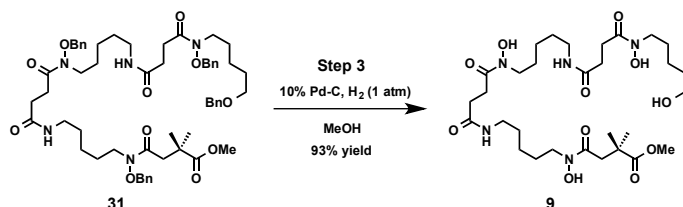


Siderophore-Fe(III) complex 4-Fe. Siderophore **4** (13.2 mg, 0.02 mmol) was complexed to Fe(III) according to the general procedure for **step 4** to give siderophore-Fe(III) complex **4-Fe** in 97% as an orange powder (13.9 mg, 0.02 mmol). Mp 130–140 °C (dec.); HRMS–ESI (m/z): $[\text{M}+\text{Na}]^+$ calcd. for $\text{C}_{29}\text{H}_{50}\text{FeN}_5\text{NaO}_{11}$: 723.2749, found 723.2742; HPLC retention time 2.80 min.

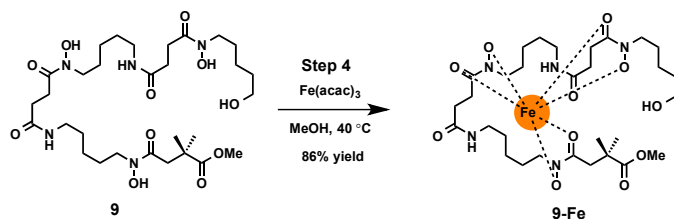


Benzyl protected siderophore 31. Hydroxylamine **19** (147.0 mg, 0.17 mmol), 3-(methoxycarbonyl)-3-methylbutanoic acid⁸ (52.0 mg, 0.32 mmol), $i\text{Pr}_2\text{EtN}$ (28.0 mg, 0.22 mmol), catalytic DMAP (5.1 mg, 0.04 mmol), and EDC-HCl (80.0 mg, 0.42 mmol) were dissolved in 10 mL of CH_2Cl_2 . After 19 h, TLC (6% MeOH in CH_2Cl_2 ; FeCl_3 stain) showed no remaining starting material (**19**). The mixture was diluted with CH_2Cl_2 (10 mL), washed with 10% aq. citric acid (2 x 10 mL), brine (10 mL), 10% aq. NaHCO_3 (10 mL), and brine (10 mL), dried over anhydrous MgSO_4 , filtered, and concentrated under reduced pressure to give 159.8 mg of a clear, colorless, viscous oil. The crude product was purified by silica gel column chromatography (1 x 3 in silica gel; 3%–6% MeOH in CH_2Cl_2). Pure product (**31**) was isolated in 73% yield as a clear, colorless, viscous oil (125.2 mg, 0.12 mmol). $^1\text{H-NMR}$ (600 MHz, CDCl_3) δ (ppm) 7.43–7.29 (m, 20 H), 6.32 (br s, 2 H), 4.85 (s, 2 H), 4.85 (s, 2 H), 4.79 (s, 2 H), 4.48 (s, 2 H), 3.66 (s, 3 H), 3.65–3.56 (m, 6 H), 3.44 (t, $J = 6.5$ Hz, 2 H), 3.22–3.17 (m, 4 H), 2.84–2.77 (m, 4 H), 2.67 (s, 2 H), 2.52–2.45 (m, 4 H), 1.67–1.59 (m, 8 H), 1.53–1.45 (m, 4 H), 1.40–1.33 (m, 2 H), 1.32–1.25 (m, 4 H), 1.22 (s, 6 H); $^{13}\text{C-NMR}$ (150 MHz, CDCl_3) δ (ppm) 177.9, 174.0, 173.8, 172.4, 172.1, 172.1, 138.5, 134.5, 134.5, 134.3, 129.1, 129.1, 128.9, 128.9, 128.8, 128.7, 128.7, 128.6, 128.3, 127.5, 127.4, 76.3, 76.3, 76.1, 72.8, 70.1, 51.9, 45.5, 44.9, 44.7, 42.4, 40.1, 39.3, 39.3, 30.7, 30.5, 29.3,

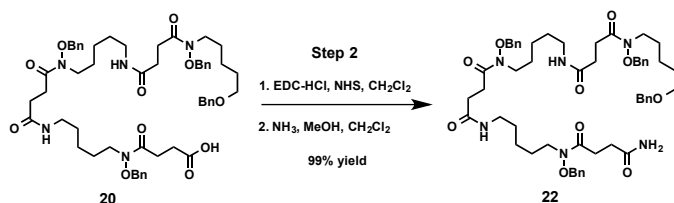
29.1, 28.4, 28.1, 28.0, 26.7, 26.4, 26.4, 25.6, 25.3, 23.9, 23.6, 23.4; HRMS–ESI (m/z): $[M+Na]^+$ calcd. for $C_{58}H_{79}N_5NaO_{11}$: 1044.5668, found 1044.5663.



Siderophore 9. Benzyl protected siderophore **31** (64.4 mg, 0.063 mmol) was deprotected according to the general procedure for **step 3** to give siderophore **9** in 93% yield as a white solid (38.7 mg, 0.058 mmol). Mp 138–140 °C; 1H -NMR (600 MHz, CD_3OD) δ (ppm) 3.65 (s, 3 H), 3.59 (t, J = 6.5 Hz, 4 H), 3.55 (t, J = 6.9 Hz, 2 H), 3.55 (t, J = 6.5 Hz, 2 H), 3.16 (t, J = 6.9 Hz, 4 H), 2.79 (s, 2 H), 2.76 (t, J = 7.2 Hz, 4 H), 2.45 (t, J = 7.2 Hz, 4 H), 1.67–1.59 (m, 6 H), 1.59–1.49 (m, 6 H), 1.40–1.29 (m, 6 H), 1.24 (s, 6 H); ^{13}C -NMR (150 MHz, CD_3OD) δ (ppm) 180.1, 175.1, 175.0, 174.6, 174.5, 173.2, 62.9, 52.5, 49.0, 48.8, 43.5, 41.4, 40.4, 33.4, 31.6, 31.6, 30.1, 30.1, 29.1, 29.1, 27.7, 27.5, 26.2, 25.1, 25.0, 24.1; HRMS–ESI (m/z): $[M+H]^+$ calcd. for $C_{30}H_{56}N_5O_{11}$: 662.3971, found 662.3971.

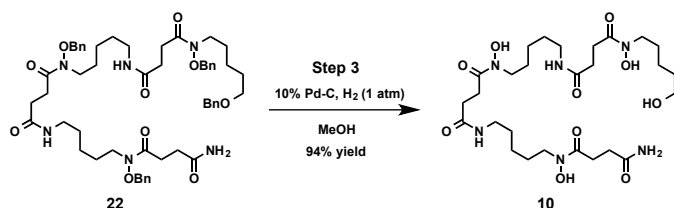


Siderophore-Fe(III) complex 9-Fe. Siderophore **9** (11.5 mg, 0.017 mmol) was complexed to Fe(III) according to the general procedure for **step 4** to give siderophore-Fe(III) complex **9-Fe** in 86% yield as an orange powder (10.6 mg, 0.015 mmol). Mp 170–173 °C; HRMS–ESI (m/z): $[M+H]^+$ calcd. for $C_{30}H_{53}FeN_5O_{11}$: 715.3086, found 715.3089; HPLC retention time 4.52 min.

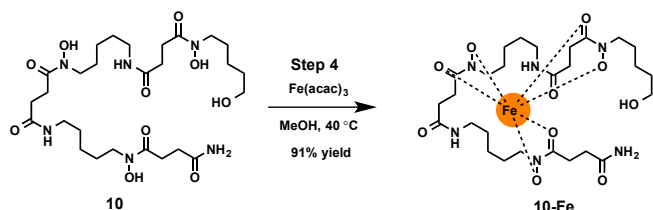


Benzyl protected siderophore 22. Benzyl protected siderophore **20** (298.2 mg, 0.30 mmol) was reacted with EDC-HCl (146.0mg, 0.76 mmol) and *N*-hydroxysuccinimide (NHS; 70.0 mg, 0.608 mmol) in 5 mL of CH_2Cl_2 for 2 h. After an aqueous work-up, the NHS activated ester of **20** was isolated in 95% yield as a clear, viscous oil (312.4 mg, 0.29 mmol). The NHS activated ester of **20** (52.1 mg, 0.048 mmol) was reacted with NH_3 in MeOH (7N, 2.0 mL, 49 mmol) in CH_2Cl_2 (2 mL) for 2.5 h. All the volatiles were removed under reduced pressure giving 66.6 mg of a clear, tan oil. The crude product was purified by silica gel column chromatography (1 x 3 in silica gel; 3%–6% MeOH in CH_2Cl_2) to give the desired product (**22**) in 99% yield as a clear, colorless, viscous oil (47.5 mg, 0.049 mmol). 1H -NMR (600 MHz, $CDCl_3$) δ (ppm) 7.41–7.29 (m, 20 H), 6.91 (br s, 1 H), 6.50 (br s, 1 H), 6.36 (br s, 1 H), 6.06 (br s, 1 H), 4.85 (s, 2 H), 4.84 (s, 2 H), 4.84 (s, 2 H), 4.48 (s, 2 H), 3.70–3.65 (m, 2 H), 3.65–3.59 (m, 4 H), 3.44 (t, J = 6.5 Hz, 2 H), 3.22–3.15 (m, 4

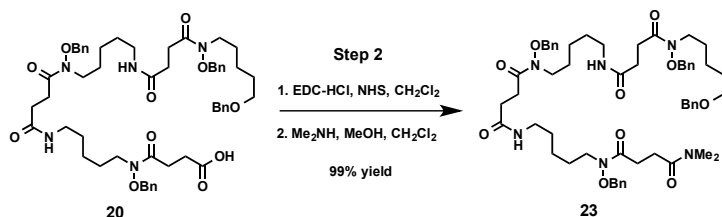
H), 2.83–2.77 (m, 4 H), 2.77–2.73 (m, 2 H), 2.57–2.50 (m, 4 H), 2.48 (t, $J = 6.5$ Hz, 2 H), 1.67–1.58 (m, 8 H), 1.51–1.44 (m, 4 H), 1.39–1.23 (m, 6 H); ^{13}C -NMR (150 MHz, CDCl_3) δ (ppm) 174.8, 174.2, 174.0, 173.8, 172.4, 172.3, 138.5, 134.4, 134.3, 129.2, 129.2, 129.1, 128.9, 128.8, 128.7, 128.3, 127.6, 127.5, 76.3, 76.1, 72.8, 70.1, 63.7, 45.5, 44.8, 44.5, 39.4, 39.2, 30.6, 30.5, 29.8, 29.6, 29.3, 28.6, 28.3, 28.1, 28.0, 27.3, 26.6, 26.4, 26.3, 23.6, 23.4; HRMS–ESI (m/z): $[\text{M}+\text{H}]^+$ calcd. for $\text{C}_{55}\text{H}_{75}\text{N}_6\text{O}_{10}$: 979.5539, found 979.5531.



Siderophore 10. Benzyl protected siderophore **22** (43.0 mg, 0.044 mmol) was deprotected according to the general procedure for **step 3** to give siderophore **10** in 94% yield as an off-white solid (25.5 mg, 0.041 mmol). Mp 152–155 °C; ^1H -NMR (600 MHz, $\text{DMSO}-d_6$) δ (ppm) 9.61 (br s, N-OH, 3 H), 7.78 (t, $J = 5.4$ Hz, 2 H), 7.28 (br s, 1 H), 6.72 (br s, 1 H), 4.35 (t, $J = 5.0$ Hz, 1 H), 3.45 (t, $J = 7.0$ Hz, 6 H), 3.39–3.34 (m, 2 H), 2.99 (q, $J = 6.7$ Hz, 4 H), 2.60–2.54 (m, 6 H), 2.26 (t, $J = 7.2$ Hz, 6 H), 1.53–1.46 (m, 6 H), 1.44–1.34 (m, 6 H), 1.27–1.17 (m, 6 H); ^{13}C -NMR (150 MHz, $\text{DMSO}-d_6$) δ (ppm) 173.6, 172.0, 171.9, 171.9, 171.3, 60.6, 47.2, 47.1, 38.4, 32.2, 29.9, 29.5, 28.8, 27.6, 27.3, 26.2, 26.0, 23.5, 22.7; HRMS–ESI (m/z): $[\text{M}+\text{H}]^+$ calcd. for $\text{C}_{27}\text{H}_{51}\text{N}_6\text{O}_{10}$: 619.3661, found 619.3654.

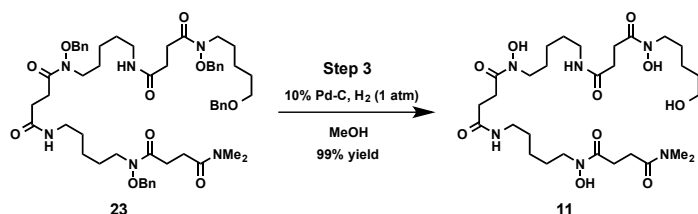


Siderophore-Fe(III) complex 10-Fe. Siderophore **10** (8.0 mg, 0.013 mmol) was complexed to Fe(III) according to the general procedure for **step 4** to give siderophore-Fe(III) complex **10-Fe** in 91% yield as an orange powder (7.9 mg, 0.012 mmol). Mp 138–144 °C (dec.); HRMS–ESI (m/z): $[\text{M}+\text{H}]^+$ calcd. for $\text{C}_{27}\text{H}_{48}\text{FeN}_6\text{O}_{10}$: 672.2776, found 672.2763; HPLC retention time 2.53 min.

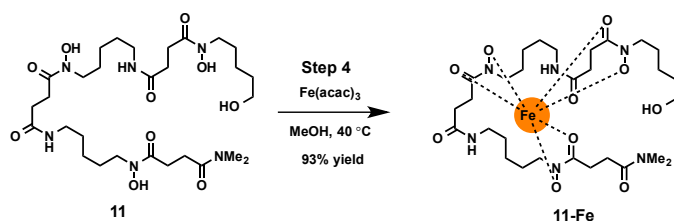


Benzyl protected siderophore 23. The NHS activated ester of **20** (52.1 mg, 0.048 mmol) was reacted with Me_2NH in MeOH (2.0 M, 2.0 mL, 4.0 mmol) in CH_2Cl_2 (2 mL) for 2.5 h. All the volatiles were removed under reduced pressure to give 61.7 mg of a clear, viscous oil. The crude product was purified by silica gel column chromatography (1 x 3 in silica gel; 3%–6% MeOH in CH_2Cl_2) to give pure product (**23**) in 99% yield as a clear, colorless, viscous oil (48.0 mg, 0.048 mmol). ^1H -NMR (600 MHz, CDCl_3) δ (ppm) 7.42–7.30 (m, 20 H), 6.56 (br s, 1 H), 6.36 (br s, 1 H), 4.90 (s, 2 H), 4.85 (s, 2 H), 4.84 (s, 2 H), 4.47 (s, 2 H), 3.68–3.59 (m, 6 H), 3.44 (t, $J = 6.5$ Hz,

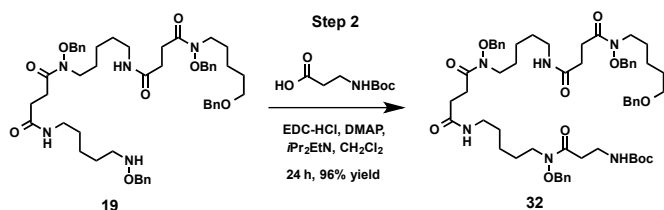
2 H), 3.22–3.16 (m, 4 H), 3.03 (s, 3 H), 2.94 (s, 3 H), 2.83–2.75 (m, 6 H), 2.65–2.60 (m, 2 H), 2.48 (t, $J = 6.6$ Hz, 4 H), 1.67–1.58 (m, 8 H), 1.52–1.45 (m, 4 H), 1.39–1.25 (m, 6 H); ^{13}C -NMR (150 MHz, CDCl_3) δ (ppm) 174.0, 173.9, 173.8, 172.2, 172.1, 171.8, 138.5, 134.6, 134.3, 129.2, 129.1, 129.1, 128.8, 128.7, 128.6, 128.6, 128.3, 127.5, 127.4, 76.3, 76.3, 76.2, 72.8, 70.1, 63.8, 45.5, 45.0, 44.8, 39.3, 39.3, 37.1, 35.5, 30.7, 30.5, 29.6, 29.3, 28.9, 28.5, 28.1, 27.9, 27.5, 27.4, 26.7, 26.4, 26.3, 25.3, 23.9, 23.6, 23.4; HRMS-ESI (m/z): $[\text{M}+\text{Na}]^+$ calcd. for $\text{C}_{57}\text{H}_{78}\text{N}_6\text{NaO}_{10}$: 1029.5672, found 1029.5674.



Siderophore 11. Benzyl protected siderophore **23** (44.5 mg, 0.044 mmol) was deprotected according to the general procedure for **step 3** to give siderophore **11** in 99% yield as a white solid (28.0 mg, 0.043 mmol). Mp 143–145 °C; ^1H -NMR (600 MHz, CD_3OD) δ (ppm) 3.60 (t, $J = 6.9$ Hz, 6 H), 3.55 (t, $J = 6.6$ Hz, 2 H), 3.16 (t, $J = 6.5$ Hz, 4 H), 3.09 (s, 3 H), 2.93 (s, 3 H), 2.80–2.73 (m, 6 H), 2.64 (t, $J = 6.6$ Hz, 2 H), 2.45 (t, $J = 7.2$ Hz, 4 H), 1.68–1.60 (m, 6 H), 1.59–1.48 (m, 6 H), 1.40–1.29 (m, 6 H); ^{13}C -NMR (150 MHz, CD_3OD) δ (ppm) 175.1, 175.1, 174.8, 174.6, 174.5, 62.9, 40.4, 37.8, 36.0, 33.4, 31.6, 30.1, 30.1, 29.1, 28.9, 28.6, 27.7, 27.5, 25.1, 25.0, 24.1; HRMS-ESI (m/z): $[\text{M}+\text{H}]^+$ calcd. for $\text{C}_{29}\text{H}_{55}\text{N}_6\text{O}_{10}$: 647.3974, found 647.3984.

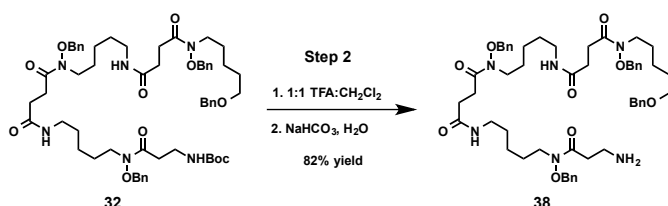


Siderophore-Fe(III) complex 11-Fe. Siderophore **11** (10.0 mg, 0.0155 mmol) was complexed to Fe(III) according to the general procedure for **step 4** to give siderophore-Fe(III) complex **11-Fe** in 93% yield as an orange powder (10.0 mg, 0.014 mmol). Mp 114–119 °C (dec.); HRMS-ESI (m/z): $[\text{M}+\text{Na}]^+$ calcd. for $\text{C}_{29}\text{H}_{51}\text{FeN}_6\text{NaO}_{10}$: 722.2908, found 722.2888; HPLC retention time 3.07 min.

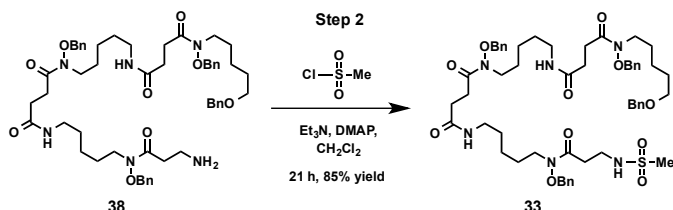


Benzyl protected siderophore 32. Hydroxylamine **19** (224.0 mg, 0.25 mmol), *N*-Boc- β -alanine (52.0 mg, 0.275 mmol), $i\text{Pr}_2\text{EtN}$ (0.05 mL, 0.29 mmol), catalytic DMAP (4.5 mg, 0.037 mmol), and EDC-HCl (125.0 mg, 0.65 mmol) were dissolved in 8 mL of CH_2Cl_2 . After 24 h, TLC (5% MeOH in CHCl_3 ; FeCl_3 stain) showed no remaining starting material (**19**). The mixture was diluted with CH_2Cl_2 (25 mL) and washed with 10% aq. citric acid (2 x 10 mL), brine (10 mL), 10% aq. NaHCO_3 (2 x 10 mL), and brine (10 mL), dried over anhydrous MgSO_4 , filtered, and concentrated under reduced pressure. This gave 263.0 mg of a cloudy, waxy oil that was purified by silica gel

column chromatography (0.5 x 4 in silica gel; 3% MeOH in CHCl₃). Pure product (**32**) was obtained in 96% yield as a waxy solid (253.6 mg, 0.24 mmol). Mp 68–70 °C; IR (thin film on NaCl plate) 3327, 2936, 2863, 1707, 1653, 1545, 1454, 1412, 1366, 1252, 1172 cm⁻¹; ¹H-NMR (600 MHz, CDCl₃) δ (ppm) 7.40–7.22 (m, 20 H), 6.41 (br s, 1 H), 6.41 (br s, 1 H), 5.29 (br s, 1 H), 4.84 (s, 4 H), 4.76 (br s, 2 H), 4.46 (s, 2 H), 3.67–3.57 (m, 6 H), 3.43 (t, *J* = 6.5 Hz, 2 H), 3.40–3.35 (m, 2 H), 3.21–3.15 (m, 4 H), 2.83–2.75 (m, 4 H), 2.64–2.58 (m, 2 H), 2.51–2.44 (m, 4 H), 1.66–1.57 (m, 8 H), 1.51–1.45 (m, 4 H), 1.42 (s, 9 H), 1.38–1.32 (m, 2 H), 1.32–1.23 (m, 4 H); ¹³C-NMR (150 MHz, CDCl₃) δ (ppm) 173.9, 173.7, 173.4, 172.0, 172.0, 155.8, 138.4, 134.2, 134.0, 129.1, 129.1, 128.9, 128.8, 128.7, 128.6, 128.5, 128.5, 128.2, 127.4, 127.3, 78.8, 76.2, 76.2, 72.7, 69.9, 45.4, 45.0, 44.6, 39.2, 35.8, 32.5, 30.5, 30.4, 29.2, 28.9, 28.3, 28.0, 27.8, 26.5, 26.3, 26.2, 23.8, 23.5, 23.3; HRMS-ESI (*m/z*): [M+Na]⁺ calcd. for C₅₉H₈₂N₆NaO₁₁: 1073.5934, found 1073.5959.

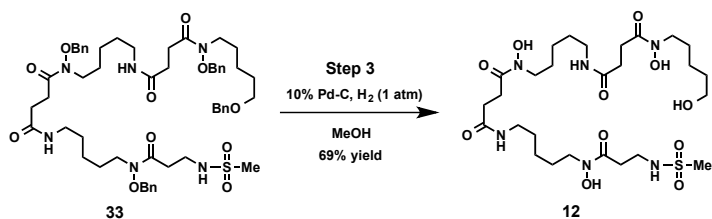


Benzyl protected siderophore 38. *N*-Boc-*O*-Benzyl protected siderophore **32** (121.0 mg, 0.115 mmol) was dissolved in a 1:1 mixture of TFA:CH₂Cl₂ (4 mL). After 1.5 h, the TFA/CH₂Cl₂ were evaporated and the resulting oil was dissolved in CHCl₃ (15 mL) and washed with satd. aq. NaHCO₃ (20 mL). The layers were separated and the CHCl₃ was dried over anhydrous MgSO₄, filtered, and concentrated under reduced pressure to give the desired siderophore amine **38** in 82% yield as a clear, colorless, viscous oil (89.4 mg, 0.094 mmol). This material was used immediately in the next reactions without purification. ¹H-NMR (500 MHz, CDCl₃) δ (ppm) 7.47–7.22 (m, 20 H), 6.41 (br s, 2 H), 4.85 (s, 4 H), 4.81 (s, 2 H), 4.47 (s, 2 H), 3.71–3.56 (m, 6 H), 3.44 (t, *J* = 6.4 Hz, 2 H), 3.24–3.15 (m, 4 H), 2.95 (t, *J* = 5.5 Hz, 2 H), 2.85–2.74 (m, 4 H), 2.59–2.52 (m, 2 H), 2.52–2.41 (m, 4 H), 1.75 (br s, 2 H), 1.69–1.56 (m, 8 H), 1.54–1.44 (m, 4 H), 1.40–1.21 (m, 6 H); ¹³C-NMR (125 MHz, CDCl₃) δ (ppm) 174.0, 173.8, 172.1, 172.1, 138.5, 134.3, 129.1, 129.1, 128.9, 128.9, 128.8, 128.7, 128.7, 128.6, 128.3, 127.5, 127.4, 76.3, 76.3, 76.2, 72.8, 70.1, 45.5, 44.9, 44.7, 39.3, 37.5, 35.7, 30.7, 30.5, 29.6, 29.3, 29.0, 28.4, 28.1, 28.0, 26.6, 26.5, 26.3, 23.9, 23.6, 23.4.

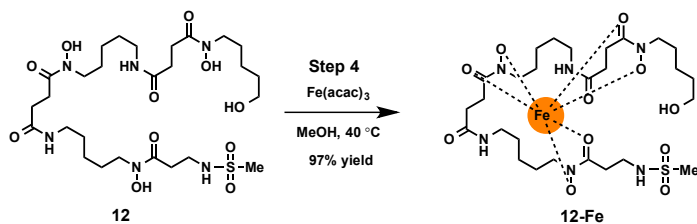


Benzyl protected siderophore 33. Amine **38** (29.8 mg, 0.313 mmol) was reacted with methanesulfonyl chloride (5.5 mg, 0.048 mmol) in the presence of Et₃N (0.013 mL, 0.093 mmol), and catalytic DMAP (1.0 mg, 0.008 mmol) in 3 mL of CH₂Cl₂. After 21 h, TLC (5% MeOH in CH₂Cl₂; FeCl₃ stain) showed no remaining starting material (**38**). The reaction mixture was diluted with CH₂Cl₂ (10 mL), washed with 10% aq. citric acid (2 x 10 mL), brine (10 mL), 10% aq. NaHCO₃ (10 mL), and brine (10 mL), dried over anhydrous MgSO₄, filtered, and concentrated to give 29 mg of a clear, colorless, viscous oil. The crude product was purified by silica gel column

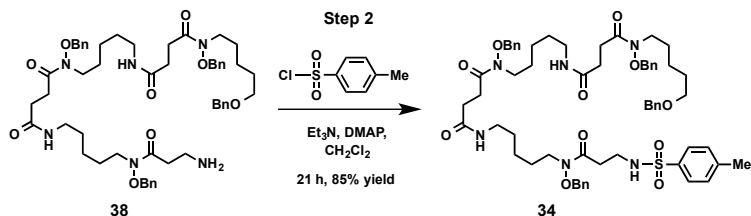
chromatography (0.5 x 4 in silica gel; 3%–5% MeOH in CH₂Cl₂) and pure product (**33**) was obtained in 85% yield as a clear, colorless, viscous oil (27.2 mg, 0.026 mmol). ¹H-NMR (600 MHz, CDCl₃) δ (ppm) 7.43–7.24 (m, 20 H), 6.40 (br s, 1 H), 6.37 (br s, 1 H), 5.50 (t, *J* = 5.9 Hz, 1 H), 4.85 (s, 6 H), 4.80 (s, 2 H), 4.48 (s, 2 H), 3.70–3.57 (m, 6 H), 3.44 (t, *J* = 6.6 Hz, 2 H), 3.38–3.29 (m, 2 H), 3.23–3.15 (m, 4 H), 2.93 (s, 3 H), 2.85–2.74 (m, 4 H), 2.68 (t, *J* = 4.8 Hz, 2 H), 2.55–2.43 (m, 4 H), 1.69–1.55 (m, 8 H), 1.54–1.44 (m, 4 H), 1.41–1.33 (m, 2 H), 1.33–1.21 (m, 4 H); ¹³C-NMR (150 MHz, CDCl₃) δ (ppm) 174.1, 173.8, 172.8, 172.2, 172.2, 138.5, 134.3, 134.0, 129.3, 129.1, 129.1, 128.9, 128.9, 128.8, 128.7, 128.6, 128.3, 127.6, 127.5, 76.3, 76.3, 76.3, 72.8, 70.1, 45.5, 44.9, 44.7, 40.0, 39.3, 38.7, 32.8, 30.7, 30.6, 29.7, 29.3, 29.0, 28.4, 28.1, 28.0, 26.7, 26.4, 26.3, 23.8, 23.6, 23.4; HRMS–ESI (*m/z*): [*M*+*H*]⁺ calcd. for C₅₅H₇₇N₆O₁₁S: 1029.5366, found 1029.5393.



Siderophore 12. Benzyl protected siderophore **33** (21.0 mg, 0.020 mmol) was deprotected according to the general procedure for **step 3** to give siderophore **12** in 69% yield as an off-white solid (9.2 mg, 0.014 mmol). Mp 120–123 °C; ¹H-NMR (600 MHz, CD₃OD) δ (ppm) 3.64–3.57 (m, 6 H), 3.55 (t, *J* = 6.6 Hz, 2 H), 3.33 (d, *J* = 7.0 Hz, 2 H), 3.17 (t, *J* = 6.7 Hz, 2 H), 3.16 (t, *J* = 6.7 Hz, 2 H), 2.95 (s, 3 H), 2.79–2.74 (m, 6 H), 2.45 (t, *J* = 7.2 Hz, 4 H), 1.68–1.60 (m, 6 H), 1.59–1.49 (m, 6 H), 1.40–1.30 (m, 6 H); ¹³C-NMR (150 MHz, CD₃OD) δ (ppm) 175.1, 62.9, 49.7, 40.4, 40.0, 33.4, 31.8, 31.7, 30.1, 30.1, 29.1, 27.7, 27.5, 25.1, 25.0, 24.1 (compound precipitated in NMR tube during FID acquisition); HRMS–ESI (*m/z*): [*M*+*H*]⁺ calcd. for C₂₇H₅₃N₆O₁₁S: 669.3488, found 669.3493.

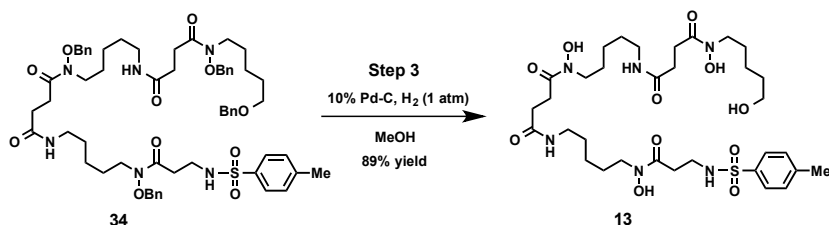


Siderophore-Fe(III) complex 12-Fe. Siderophore **12** (3.0 mg, 0.0045 mmol) was complexed to Fe(III) according to the general procedure for **step 4** to give siderophore-Fe(III) complex **12-Fe** in 97% yield as an orange powder (3.1 mg, 0.0043 mmol). Mp 147–152 °C (dec.); HRMS–ESI (*m/z*): [*M*+*H*]⁺ calcd. for C₂₇H₅₀FeN₆O₁₁S: 722.2602, found 722.2617; HPLC retention time 3.12 min.

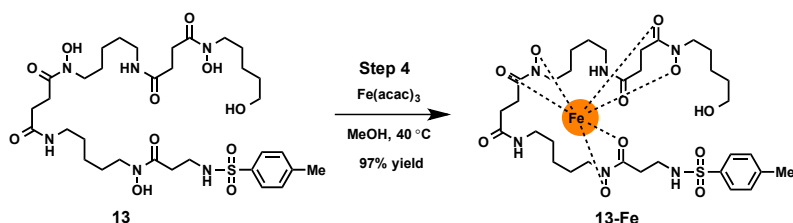


Benzyl protected siderophore 34. Amine **38** (29.8 mg, 0.31 mmol) was reacted with *p*-toluenesulfonyl chloride (9.0 mg, 0.047 mmol) in the presence of Et₃N (0.013 mL, 0.093 mmol),

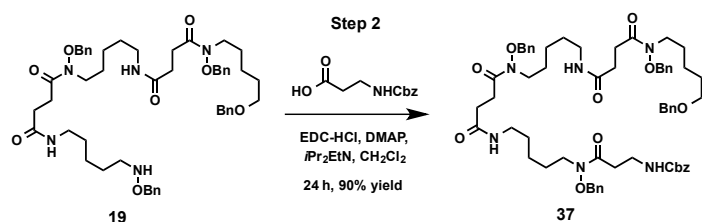
and catalytic DMAP (1.0 mg, 0.008 mmol) in 3 mL of CH₂Cl₂. After 21 h, TLC (5% MeOH in CH₂Cl₂; FeCl₃ stain) showed no remaining starting material (**38**). The reaction mixture was diluted with CH₂Cl₂ (10 mL), washed with 10% aq. citric acid (2 x 10 mL), brine (10 mL), 10% aq. NaHCO₃ (10 mL), and brine (10 mL), dried over anhydrous MgSO₄, filtered, and concentrated to give 32.0 mg of a clear, colorless, viscous oil. The crude product was purified by silica gel column chromatography (0.5 x 4 in silica gel; 3%–5% MeOH in CH₂Cl₂) and pure product (**34**) was obtained in 85% yield as a clear, colorless, viscous oil (29.3 mg, 0.0265 mmol). ¹H-NMR (600 MHz, CDCl₃) δ (ppm) 7.74 (d, *J* = 8.2 Hz, 2 H), 7.41–7.30 (m, 20 H), 7.28 (d, *J* = 7.9 Hz, 2 H), 6.37 (br s, 2 H), 5.71–5.66 (m, 1 H), 4.85 (s, 4 H), 4.74 (s, 2 H), 4.48 (s, 2 H), 3.68–3.58 (m, 6 H), 3.44 (t, *J* = 6.5 Hz, 2 H), 3.23–3.17 (m, 4 H), 3.16–3.11 (m, 2 H), 2.84–2.76 (m, 4 H), 2.62 (t, *J* = 5.3 Hz, 2 H), 2.52–2.44 (m, 4 H), 2.39 (s, 3 H), 1.68–1.56 (m, 8 H), 1.53–1.44 (m, 4 H), 1.40–1.32 (m, 2 H), 1.32–1.22 (m, 4 H); ¹³C-NMR (150 MHz, CDCl₃) δ (ppm) 174.0, 173.8, 172.8, 172.2, 143.1, 138.5, 137.1, 134.3, 134.0, 129.6, 129.2, 129.1, 129.1, 129.1, 128.9, 128.8, 128.7, 128.7, 128.6, 128.3, 127.5, 127.4, 126.9, 76.3, 76.3, 76.3, 72.8, 70.1, 45.5, 45.0, 44.7, 39.3, 38.7, 32.3, 30.7, 30.6, 29.7, 29.3, 29.0, 28.4, 28.1, 28.0, 26.7, 26.4, 26.3, 23.8, 23.6, 23.4, 21.4; HRMS–ESI (*m/z*): [*M*+*H*]⁺ calcd. for C₆₁H₈₁N₆O₁₁S: 1105.5679, found 1105.5707.



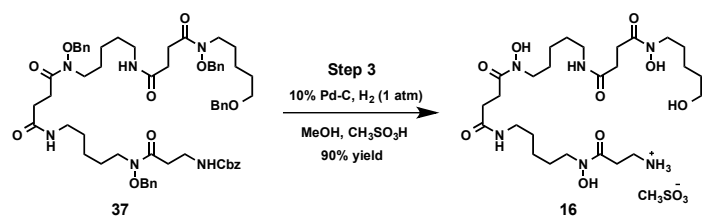
Siderophore 13. Benzyl protected siderophore **34** (22.0 mg, 0.02 mmol) was deprotected according to the general procedure for **step 3** to give siderophore **13** in 89% yield as an off-white solid (13.2 mg, 0.018 mmol). Mp 116–118 °C; ¹H-NMR (600 MHz, CD₃OD) δ (ppm) 7.74 (d, *J* = 8.5 Hz, 2 H), 7.38 (d, *J* = 8.2 Hz, 2 H), 3.59 (t, *J* = 7.0 Hz, 2 H), 3.59 (t, *J* = 6.9 Hz, 2 H), 3.56 (t, *J* = 6.9 Hz, 2 H), 3.54 (t, *J* = 6.6 Hz, 2 H), 3.16 (t, *J* = 6.9 Hz, 2 H), 3.16 (t, *J* = 6.9 Hz, 2 H), 3.09 (t, *J* = 7.2 Hz, 2 H), 2.76 (t, *J* = 7.2 Hz, 4 H), 2.66 (t, *J* = 7.2 Hz, 2 H), 2.45 (t, *J* = 7.3 Hz, 2 H), 2.45 (t, *J* = 7.0 Hz, 2 H), 2.43 (s, 3 H), 1.68–1.58 (m, 6 H), 1.58–1.48 (m, 6 H), 1.40–1.28 (m, 6 H); ¹³C-NMR (150 MHz, CD₃OD) δ (ppm) 175.1, 174.3, 174.3, 172.7, 144.8, 138.9, 130.9, 128.2, 62.9, 49.2, 49.1, 49.0, 40.4, 40.4, 40.2, 33.8, 33.4, 31.8, 31.7, 30.1, 29.1, 29.1, 27.7, 27.5, 27.5, 25.1, 25.0, 24.1, 21.6; HRMS–ESI (*m/z*): [*M*+*H*]⁺ calcd. for C₃₃H₅₇N₆O₁₁S: 745.3801, found 745.3787.



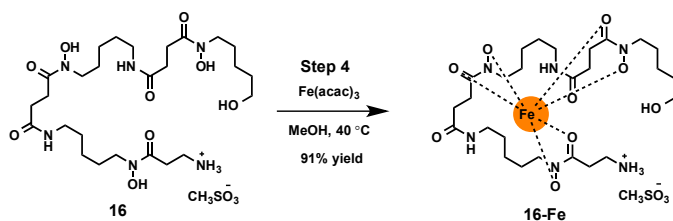
Siderophore-Fe(III) complex 13-Fe. Siderophore **13** (6.0 mg, 0.008 mmol) was complexed to Fe(III) according to the general procedure for **step 4** to give siderophore-Fe(III) complex **13-Fe** in 97% yield as an orange powder (6.2 mg, 0.008 mmol). Mp 149–154 °C (dec.); HRMS–ESI (*m/z*): [*M*+*Na*]⁺ calcd. for C₃₃H₅₃FeN₆NaO₁₁S: 820.2735, found 820.2728; HPLC retention time 4.73 min.



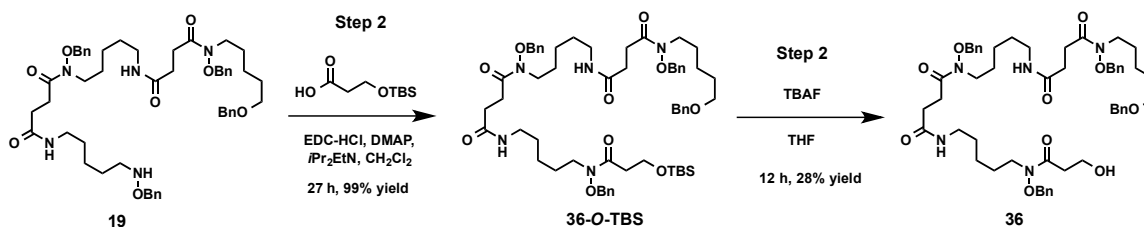
Benzyl protected siderophore 37. Hydroxylamine **19** (224.0 mg, 0.25 mmol), *N*-Cbz- β -alanine (63.0 mg, 0.28 mmol), *i*Pr₂EtN (0.05 mL, 0.29 mmol), catalytic DMAP (4.5 mg, 0.037 mmol), and EDC-HCl (125.0 mg, 0.65 mmol) were dissolved in 8 mL of CH₂Cl₂. After 24 h, TLC (5% MeOH in CHCl₃; FeCl₃ stain) showed no remaining starting material (**19**). The mixture was diluted with CH₂Cl₂ (20 mL) and washed with 10% aq. citric acid (2 x 10 mL), brine (10 mL), 10% aq. NaHCO₃ (2 x 10 mL), and brine (10 mL), dried over anhydrous MgSO₄, filtered, and concentrated under reduced pressure. This gave 301.8 mg of a cloudy oil that was purified by silica gel column chromatography (0.5 x 5 in silica gel; 3% MeOH in CHCl₃). Pure product (**37**) was obtained in 90% yield as a clear, colorless oil (242.7 mg, 0.22 mmol). ¹HNMR (600 MHz, CDCl₃) δ (ppm) 7.41–7.21 (m, 25 H), 6.44 (br s, 1 H), 6.41 (br s, 1 H), 5.64 (br s, 1 H), 5.07 (s, 2 H), 4.84 (s, 4 H), 4.75 (br s, 2 H), 4.47 (s, 2 H), 3.70–3.56 (m, 6 H), 3.47–3.41 (m, 4 H), 3.21–3.14 (m, 4 H), 2.83–2.76 (m, 4 H), 2.66–2.60 (m, 2 H), 2.51–2.43 (m, 4 H), 1.66–1.57 (m, 8 H), 1.51–1.43 (m, 4 H), 1.39–1.32 (m, 2 H), 1.31–1.23 (m, 4 H); ¹³CNMR (150 MHz, CDCl₃) δ (ppm) 173.9, 173.7, 173.2, 172.0, 172.0, 156.2, 138.4, 136.5, 134.2, 134.0, 129.1, 129.0, 128.9, 128.8, 128.7, 128.6, 128.5, 128.3, 128.2, 127.8, 127.8, 127.4, 127.3, 76.2, 76.1, 72.7, 69.9, 66.3, 45.4, 44.9, 44.6, 39.1, 36.3, 32.4, 30.5, 30.4, 29.2, 28.9, 28.3, 28.0, 27.8, 26.5, 26.3, 26.2, 23.8, 23.5, 23.3; HRMS–ESI (*m/z*): [M+Na]⁺ calcd. for C₆₂H₈₀N₆NaO₁₁: 1107.5777, found 1107.5760.



Siderophore 16. *N*-Cbz-*O*-Benzyl protected siderophore **37** (37.0 mg, 0.034 mmol) was deprotected according to the general procedure for **step 3** in the presence of methanesulfonic acid (4.0 mg, 0.042 mmol) to give the siderophore methanesulfonate salt of **16** in 90% yield as a light, pink solid (21.6 mg, 0.031 mmol). Mp 139–141 °C (dec.); ¹H-NMR (600 MHz, CD₃OD) δ (ppm) 3.62 (t, *J* = 7.0 Hz, 2 H), 3.59 (t, *J* = 7.0 Hz, 4 H), 3.54 (t, *J* = 6.5 Hz, 2 H), 3.21–3.14 (m, 6 H), 2.88 (t, *J* = 6.3 Hz, 2 H), 2.76 (t, *J* = 6.2 Hz, 4 H), 2.70 (s, 3 H), 2.45 (t, *J* = 7.0 Hz, 4 H), 1.69–1.60 (m, 6 H), 1.59–1.49 (m, 6 H), 1.40–1.30 (m, 6 H); ¹³C-NMR (150 MHz, CD₃OD) δ (ppm) 175.1, 174.6, 174.5, 172.2, 62.9, 52.3, 49.7, 49.0, 40.4, 40.4, 39.6, 36.8, 33.4, 31.6, 31.6, 30.5, 30.2, 30.1, 29.2, 29.1, 29.0, 27.7, 27.5, 27.4, 25.0, 24.1; HRMS–ESI (*m/z*): [M+H]⁺ calcd. for C₂₆H₅₁N₆O₉: 591.3712, found 591.3695.

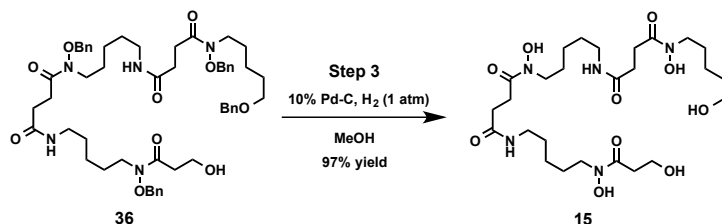


Siderophore-Fe(III) complex 16-Fe. Siderophore **16** (11.0 mg, 0.016 mmol) was complexed to Fe(III) according to the general procedure for **step 4** to give siderophore-Fe(III) complex **16-Fe** in 91% yield as an orange powder (10.5 mg, 0.014 mmol). Mp 153–158 °C (dec.); HRMS–ESI (m/z): $[M+H]^+$ calcd. for $C_{26}H_{48}FeN_6O_9$: 644.2827, found 642.2891; HPLC retention time 2.26 min.

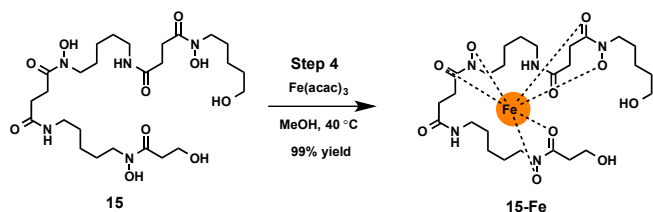


Benzyl protected siderophore 36. Hydroxylamine **19** (275.0 mg, 0.31 mmol), 4-((*tert*-butyldimethylsilyl)oxy)butanoic acid (84.0 mg, 0.41 mmol), iPr_2EtN (0.13 mL, 0.75 mmol), catalytic DMAP (11.0 mg, 0.09 mmol), and EDC-HCl (150.0 mg, 0.78 mmol) were dissolved in 8 mL of CH_2Cl_2 . After 27 h, TLC (9% MeOH in CH_2Cl_2 ; $FeCl_3$ stain) showed no remaining starting material (**19**). The mixture was diluted with CH_2Cl_2 (30 mL) and washed with 10% aq. citric acid (30 mL) and brine (50 mL), dried over anhydrous $MgSO_4$, filtered, and concentrated under reduced pressure to give 417.8 mg of a waxy solid. The crude product was purified by silica gel column chromatography (1 x 5 in silica gel; 3%–5% MeOH in CH_2Cl_2) to give pure **36-O-TBS** in 99% yield as a white, waxy solid (332.3 mg, 0.31 mmol). Mp 71–73 °C; 1H -NMR (600 MHz, $CDCl_3$) δ (ppm) 7.41–7.30 (m, 20 H), 6.32 (br s, 1 H), 6.28 (br s, 1 H), 4.85 (s, 2 H), 4.85 (s, 2 H), 4.81 (s, 2 H), 4.48 (s, 2 H), 3.68–3.59 (m, 8 H), 3.44 (t, J = 6.5 Hz, 2 H), 3.22–3.17 (m, 4 H), 2.84–2.77 (m, 4 H), 2.55–2.44 (m, 6 H), 1.86–1.80 (m, 2 H), 1.67–1.59 (m, 8 H), 1.50 (dt, J = 14.9, 7.4 Hz, 4 H), 1.36 (dt, J = 15.5, 7.7 Hz, 2 H), 1.33–1.25 (m, 4 H), 0.89 (s, 9 H), 0.04 (s, 6 H); ^{13}C -NMR (150 MHz, $CDCl_3$) δ (ppm) 174.7, 174.0, 173.8, 172.1, 172.0, 138.5, 134.5, 134.3, 129.1, 129.0, 128.9, 128.8, 128.8, 128.7, 128.6, 128.3, 127.5, 127.4, 76.3, 72.8, 70.1, 62.4, 45.5, 45.2, 44.7, 39.4, 39.3, 39.3, 30.7, 30.6, 29.3, 29.1, 28.8, 28.4, 28.1, 28.0, 27.6, 26.7, 26.5, 26.4, 25.9, 24.0, 23.6, 23.4, 18.3, -5.3; HRMS–ESI (m/z): $[M+H]^+$ calcd. for $C_{61}H_{90}N_5O_{10}Si$: 1080.6451, found 1080.6466. Purified **36-O-TBS** (224.0 mg, 0.21 mmol) was dissolved in 7 mL of anhydrous THF. TBAF (1 M in THF, 0.54 mL, 0.54 mmol) was added and the mixture was stirred at rt. After 12 h, the THF was evaporated under reduced pressure and the crude material was purified by silica gel column chromatography (1 x 6 in silica gel; 3%–7% MeOH in CH_2Cl_2) to give the desired free alcohol product **36** in 28.4% yield (47.3% yield based on recovered **36-O-TBS**) as a clear oil (56.8 mg, 0.06 mmol). 1H -NMR (600 MHz, $CDCl_3$) δ (ppm) 7.43–7.29 (m, 20 H), 6.42 (br s, 1 H), 6.18 (br s, 1 H), 4.85–4.83 (m, 4 H), 4.83–4.80 (m, 2 H), 4.47 (s, 2 H), 3.71–3.56 (m, 8 H), 3.52–3.41 (m, 4 H), 3.24–3.15 (m, 4 H), 2.84–2.75 (m, 2 H), 2.70–2.66 (m, 2 H), 2.59–2.53 (m, 2 H), 2.50–2.43 (m, 2 H), 1.91–1.83 (m, 2 H), 1.69–1.46 (m, 12 H), 1.40–1.22 (m, 6 H); ^{13}C -NMR (150 MHz, $CDCl_3$) δ (ppm) 177.3, 175.2, 173.8, 172.2, 172.1, 138.5, 134.3, 129.2, 129.1, 129.0, 128.9, 128.8, 128.7, 128.7, 128.6, 128.3, 127.6, 127.5, 76.3, 76.3, 76.2, 72.8, 70.1, 62.4, 45.5, 45.2, 44.7, 39.3,

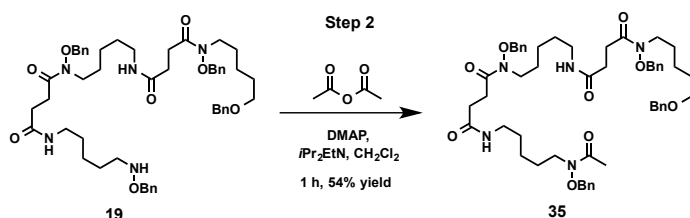
38.5, 30.8, 30.7, 30.5, 29.5, 29.3, 28.7, 28.1, 28.0, 27.3, 27.2, 26.7, 26.4, 26.3, 23.9, 23.7, 23.6, 23.4; HRMS–ESI (m/z): $[M+H]^+$ calcd. for $C_{55}H_{76}N_5O_{10}$: 966.5587, found 966.5578.



Siderophore 15. Benzyl protected siderophore **36** (38.7 mg, 0.040 mmol) was deprotected according to the general procedure for **step 3** to give siderophore **15** in 97% yield as a tan, hygroscopic solid (23.4 mg, 0.039 mmol). 1H -NMR (600 MHz, CD_3OD) δ (ppm) 3.64–3.52 (m, 8 H), 3.47 (t, $J = 7.2$ Hz, 2 H), 3.17 (t, $J = 6.7$ Hz, 4 H), 2.79–2.73 (m, 2 H), 2.71–2.66 (m, 2 H), 2.55 (t, $J = 7.5$ Hz, 2 H), 2.45 (t, $J = 7.0$ Hz, 4 H), 1.81 (quintet, $J = 7.0$ Hz, 2 H), 1.67–1.60 (m, 6 H), 1.60–1.49 (m, 6 H), 1.40–1.26 (m, 6 H); ^{13}C -NMR (150 MHz, CD_3OD) δ (ppm) 180.2, 175.7, 175.1, 174.5, 62.9, 62.6, 48.9, 40.4, 39.5, 33.4, 31.7, 30.1, 30.0, 29.2, 29.1, 28.9, 28.4, 27.6, 27.5, 27.3, 25.1, 25.0, 24.1; HRMS–ESI (m/z): $[M+H]^+$ calcd. for $C_{27}H_{52}N_5O_{10}$: 606.3709, found 606.3717.

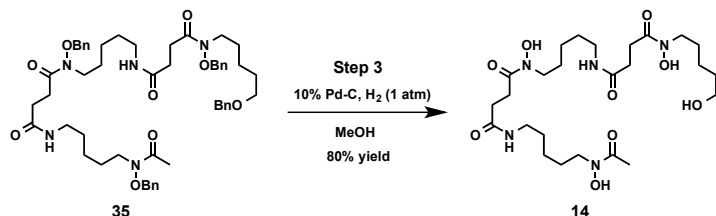


Siderophore-Fe(III) complex 15-Fe. Siderophore **15** (8.5 mg, 0.014 mmol) was complexed to $Fe(III)$ according to the general procedure for **step 4** to give siderophore- $Fe(III)$ complex **15-Fe** in 99% yield as an orange powder (9.1 mg, 0.014 mmol). Mp 192–195 °C; HRMS–ESI (m/z): $[M+H]^+$ calcd. for $C_{27}H_{49}FeN_5O_{10}$: 659.2823, found 659.2812; HPLC retention time 2.53 min.

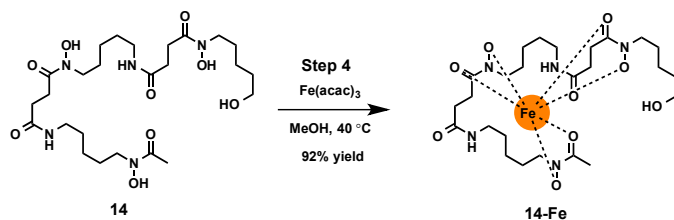


Benzyl protected siderophore 35. Hydroxylamine **19** (76.9 mg, 0.087 mmol), acetic anhydride (18 mg, 0.176 mmol), iPr_2EtN (22.0 mg, 0.17 mmol), and catalytic DMAP (1.1 mg, 0.009 mmol) were dissolved in 6.0 mL of CH_2Cl_2 . After 1 h, TLC (6% MeOH in CH_2Cl_2 ; $FeCl_3$ stain) showed no remaining starting material (**19**). The mixture was diluted with CH_2Cl_2 (15 mL) and washed with 10% aq. citric acid (10 mL), brine (10 mL), 10% aq. $NaHCO_3$ (10 mL), and brine (10 mL), dried over anhydrous $MgSO_4$, filtered, and concentrated under reduced pressure. This gave 68.5 mg of a clear, colorless oil that was purified via silica gel column chromatography (0.75 x 4 in silica gel; 3%–6% MeOH in CH_2Cl_2). Pure product (**35**) was obtained in 54% yield as a clear, colorless oil (43 mg, 0.05 mmol). All characterization data matched that previously reported in the literature.⁹ 1H -NMR (600 MHz, $CDCl_3$) δ (ppm) 7.41–7.26 (m, 20 H), 6.34 (br s, 1 H), 6.32 (br s, 1 H), 4.85 (s, 2 H), 4.84 (s, 2 H), 4.80 (s, 2 H), 4.48 (s, 2 H), 3.67–3.58 (m, 6 H), 3.44 (t, $J = 6.46$

Hz, 2 H), 3.22–3.18 (m, 4 H), 2.83–2.77 (m, 4 H), 2.50–2.47 (m, 4 H), 2.09 (s, 3 H), 1.67–1.59 (m, 8 H), 1.52–1.48 (m, 4 H), 1.39–1.35 (m, 2 H), 1.33–1.26 (m, 4 H); ^{13}C NMR (150 MHz, CDCl_3) δ (ppm) 174.0, 173.8, 172.1, 172.1, 138.5, 134.3, 129.1, 129.1, 128.9, 128.9, 128.8, 128.7, 128.7, 128.6, 128.3, 127.5, 127.4, 76.3, 76.3, 76.2, 72.8, 70.1, 45.5, 44.9, 44.7, 39.3, 39.3, 30.7, 30.6, 29.3, 29.0, 28.4, 28.1, 28.0, 26.7, 26.5, 26.4, 23.9, 23.6, 23.4, 20.5; HRMS–ESI (m/z): $[\text{M}+\text{H}]^+$ calcd. for $\text{C}_{53}\text{H}_{72}\text{N}_5\text{O}_9$: 922.5325, found 922.5362.

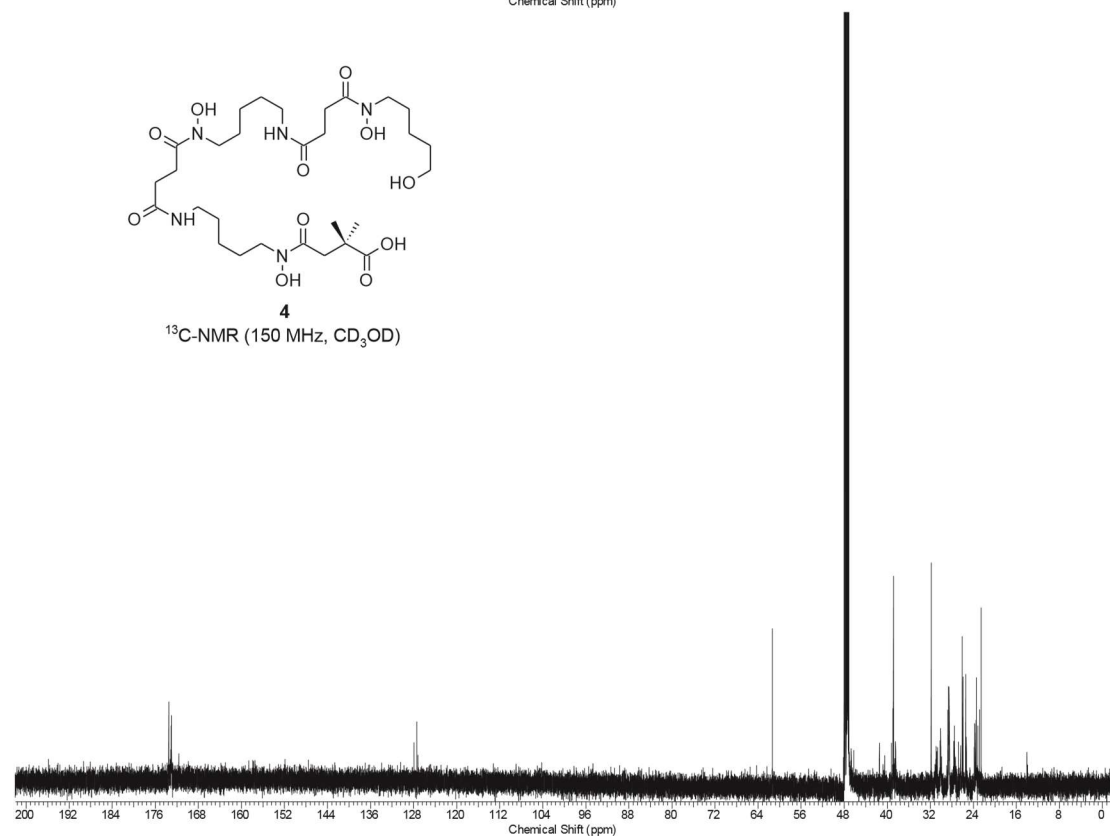
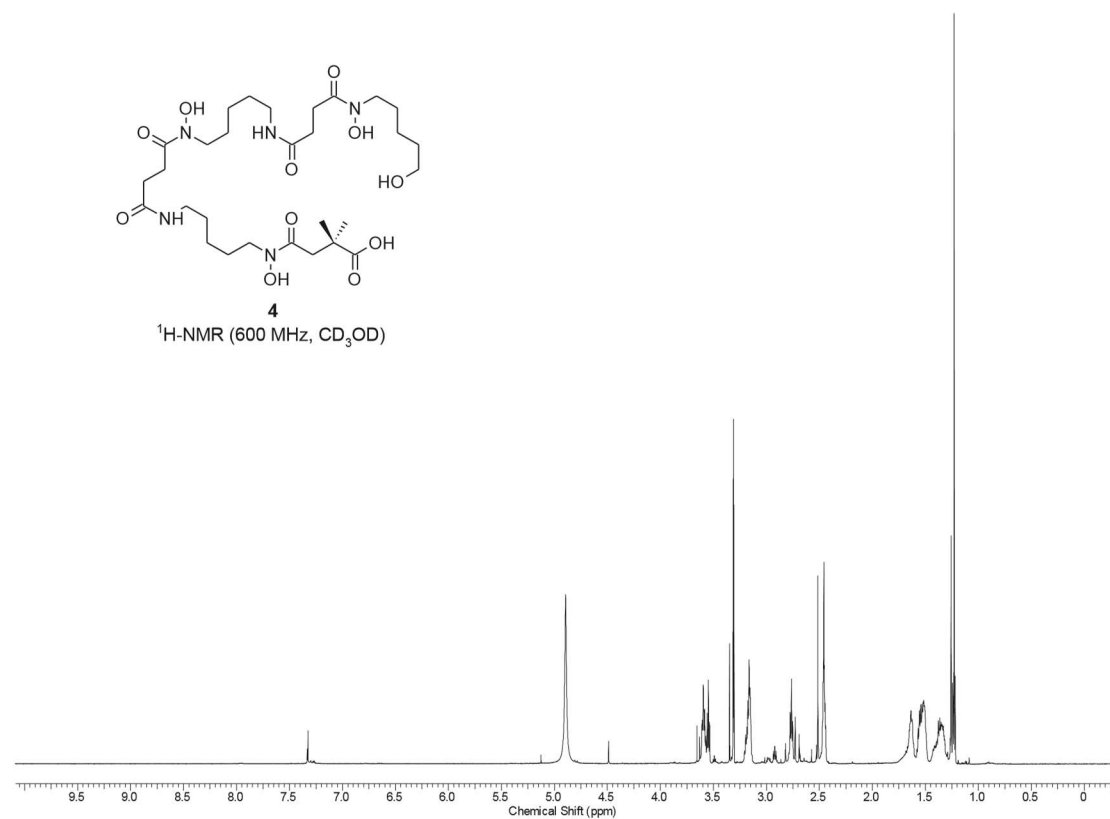


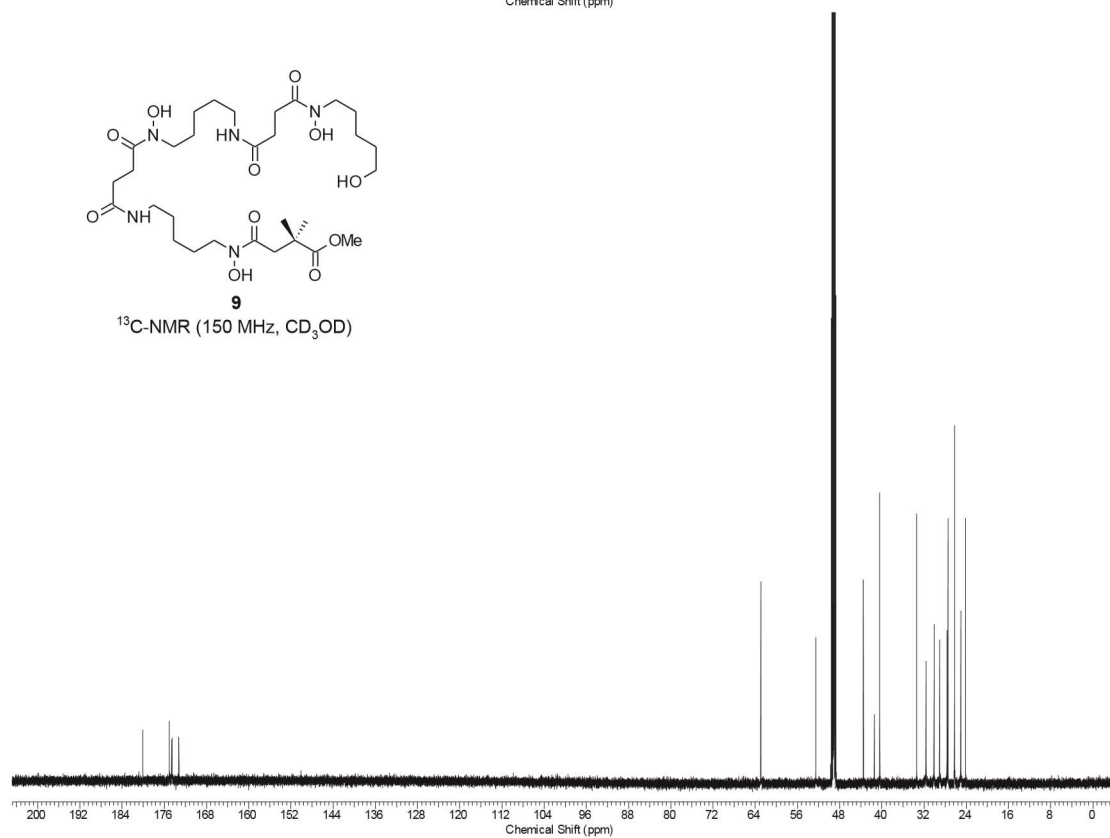
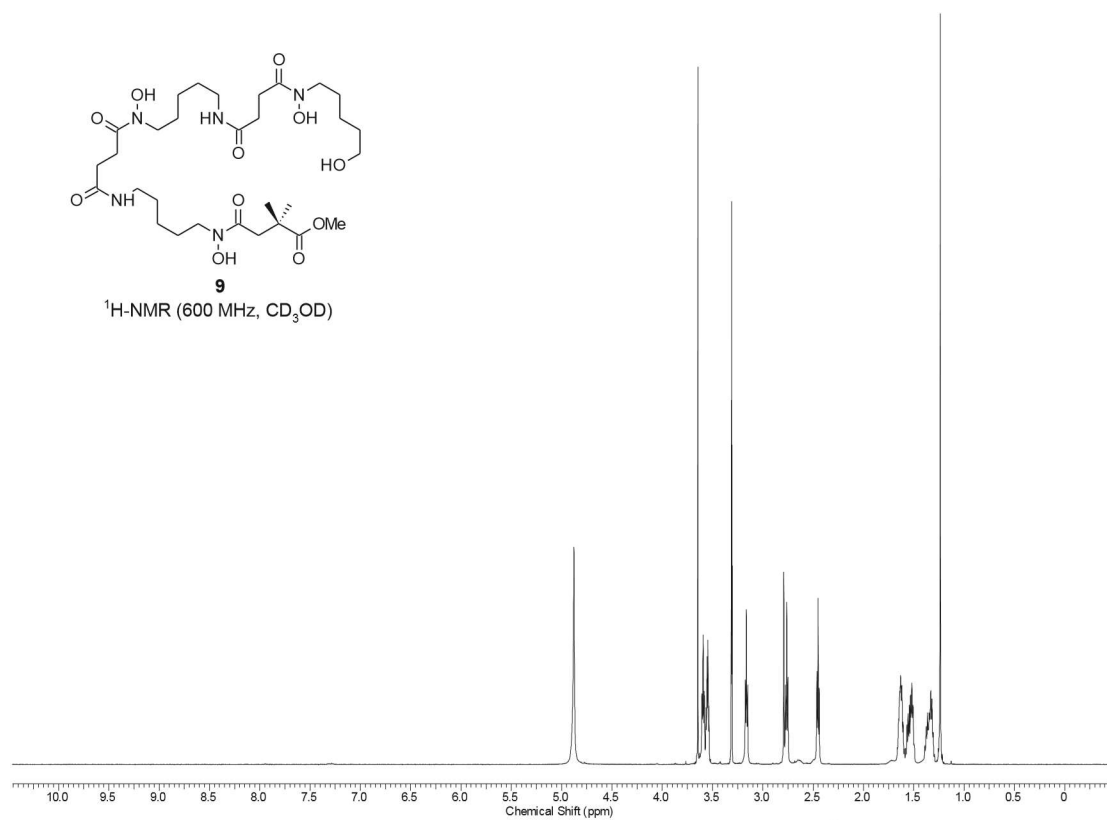
Siderophore 14. Benzyl protected siderophore **35** (34.8 mg, 0.038 mmol) was deprotected according to the general procedure for **step 3** to give siderophore **14** in 80% yield as a white solid (16.9 mg, 0.03 mmol). All characterization data matched that previously reported in the literature.⁹ Mp 123–125 °C; ^1H -NMR (600 MHz, CD_3OD) δ (ppm) 3.60 (t, $J = 6.9$ Hz, 6 H), 3.19–3.13 (m, 6 H), 2.77 (t, $J = 7.2$ Hz, 4 H), 2.48–2.43 (m, 4 H), 2.09 (s, 3 H), 1.67–1.60 (m, 4 H), 1.58–1.48 (m, 8 H), 1.41–1.30 (m, 6 H); ^{13}C -NMR (150 MHz, CD_3OD) δ (ppm) 175.1, 174.7, 174.3, 174.2, 173.2, 67.1, 62.9, 49.7, 49.2, 49.1, 48.9, 48.7, 40.5, 40.5, 40.4, 33.4, 32.5, 32.5, 32.5, 31.7, 31.7, 30.3, 30.2, 30.1, 30.1, 29.1, 27.7, 27.5, 27.5, 25.4, 25.3, 25.1, 25.0, 24.4, 24.1, 22.7, 20.3, 15.6; HRMS–ESI (m/z): $[\text{M}+\text{Na}]^+$ calcd. for $\text{C}_{25}\text{H}_{47}\text{N}_5\text{NaO}_9$: 584.3266, found 584.3291.

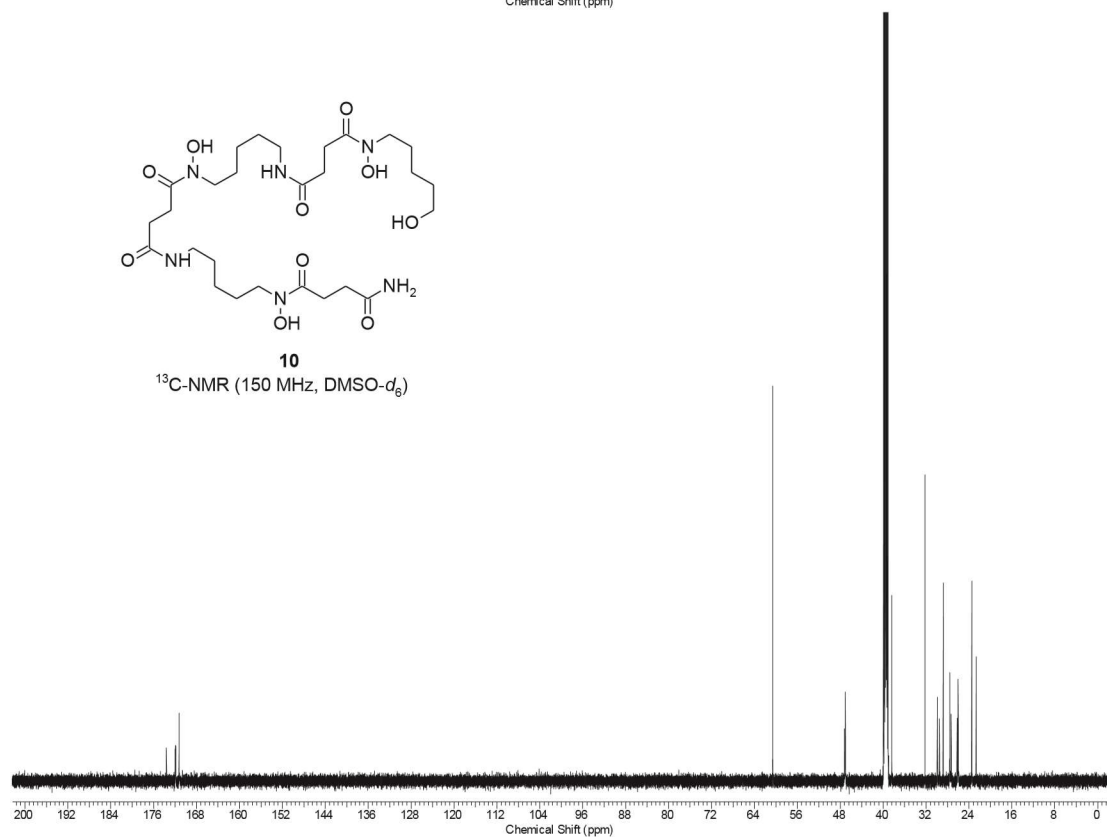
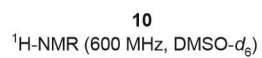


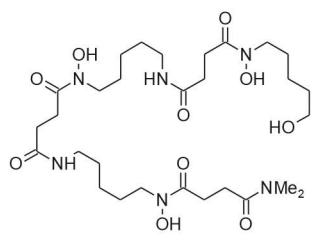
Siderophore-Fe(III) complex 14-Fe. Siderophore **14** (10.0 mg, 0.018 mmol) was complexed to Fe(III) according to the general procedure for **step 4** to give siderophore-Fe(III) complex **14-Fe** in 92% yield as an orange powder (10.0 mg, 0.016 mmol). Mp 164–167 °C; HRMS–ESI (m/z): $[\text{M}+\text{Na}]^+$ calcd. for $\text{C}_{25}\text{H}_{44}\text{FeN}_5\text{NaO}_9$: 637.2381, found 637.2403; HPLC retention time 2.75 min.

A.2 ^1H -NMR and ^{13}C -NMR Spectra of New Compounds



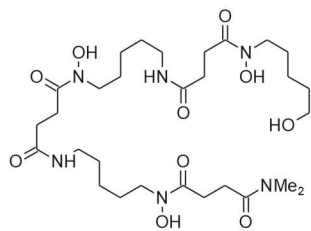
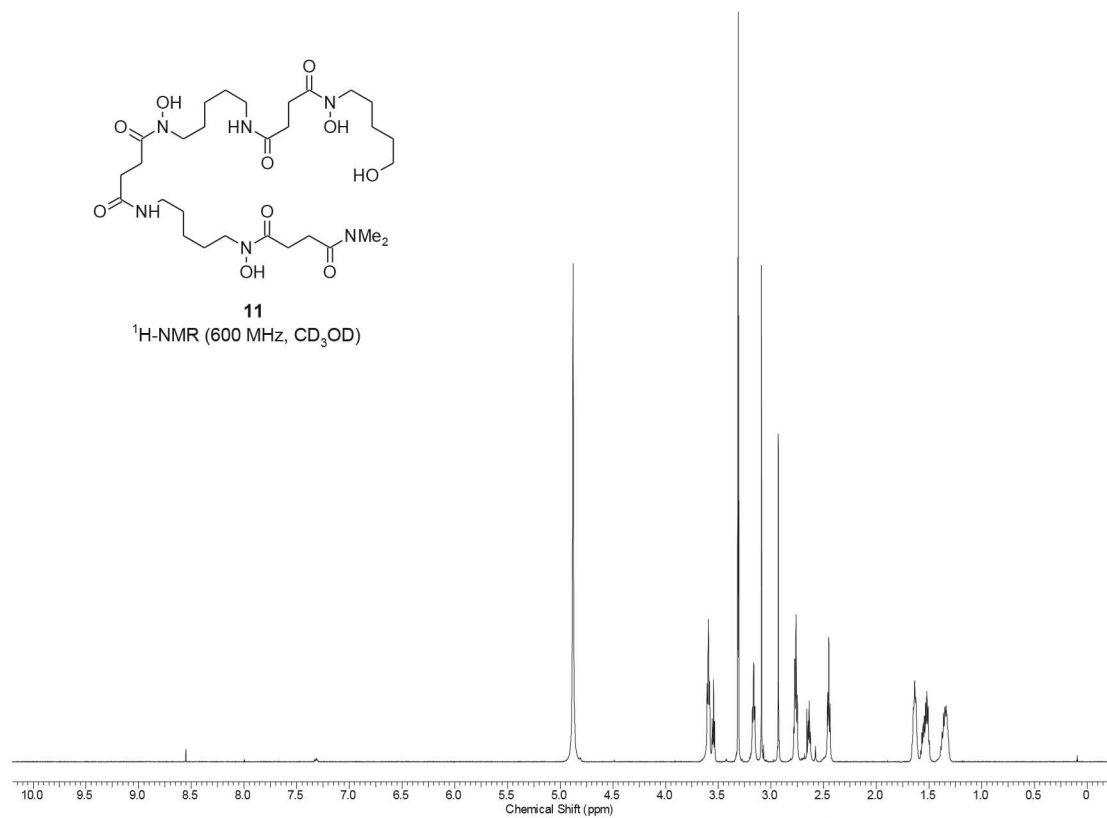






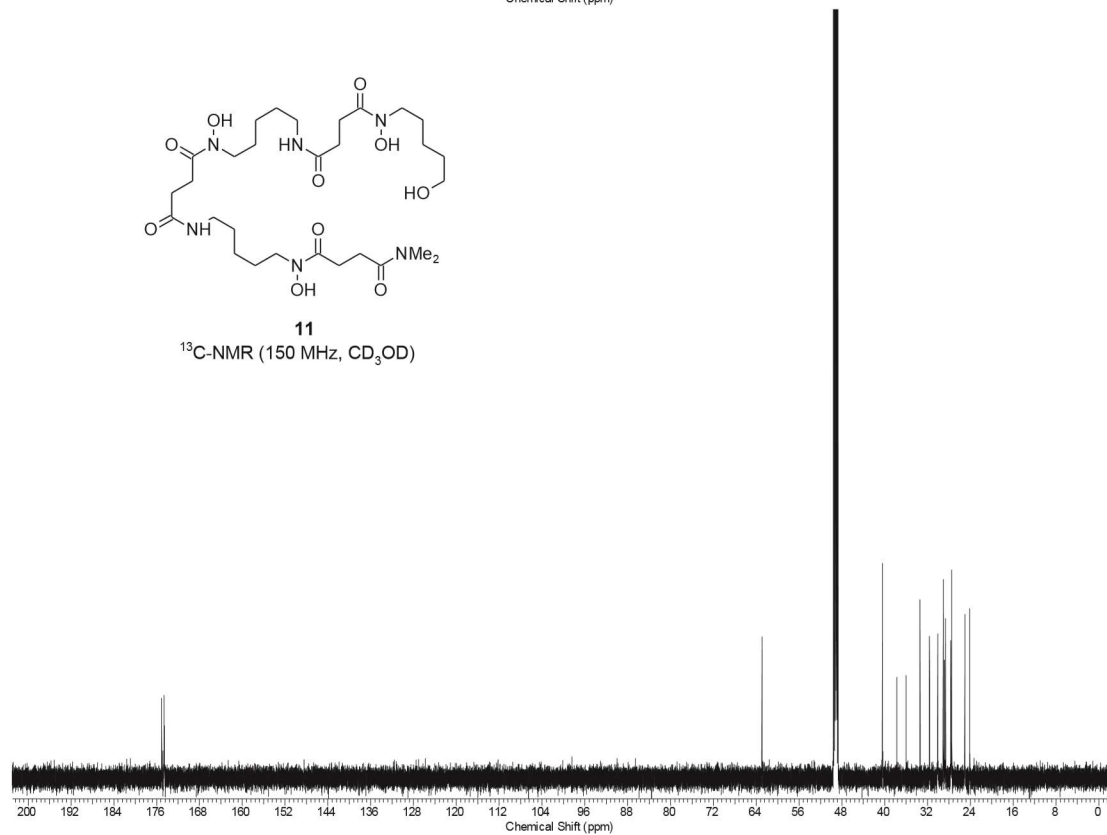
11

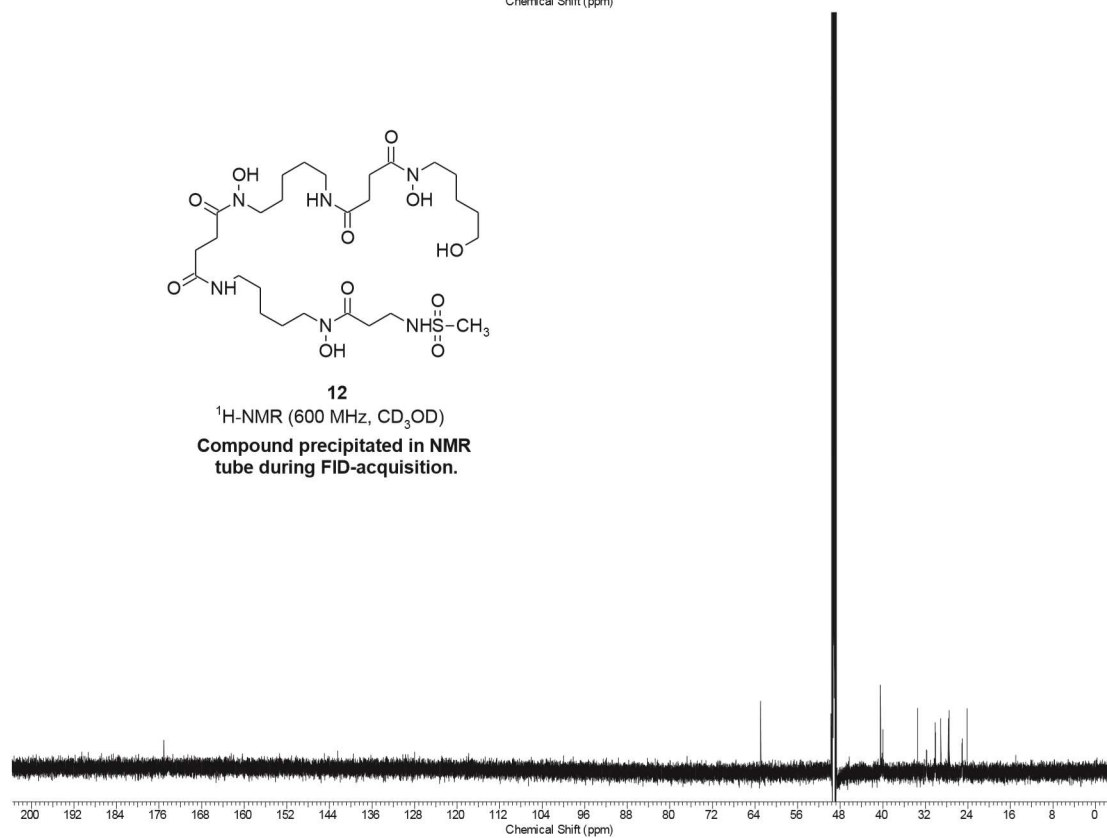
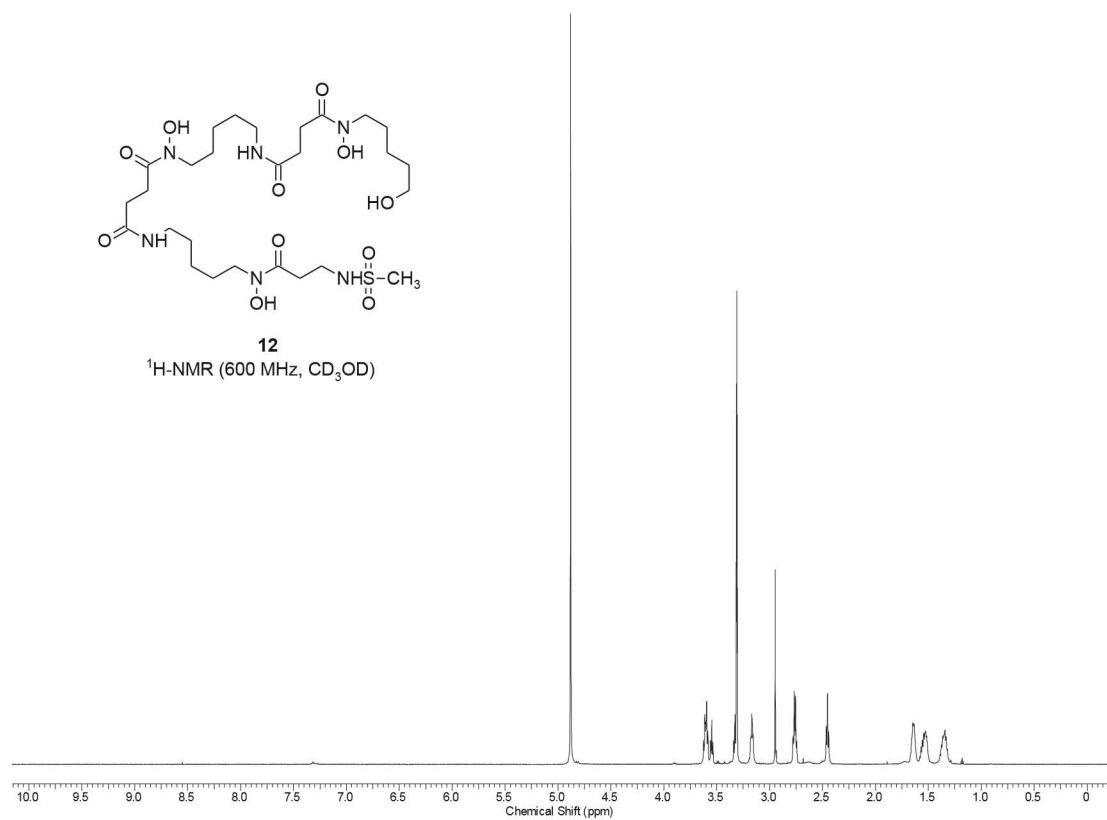
$^1\text{H-NMR}$ (600 MHz, CD_3OD)

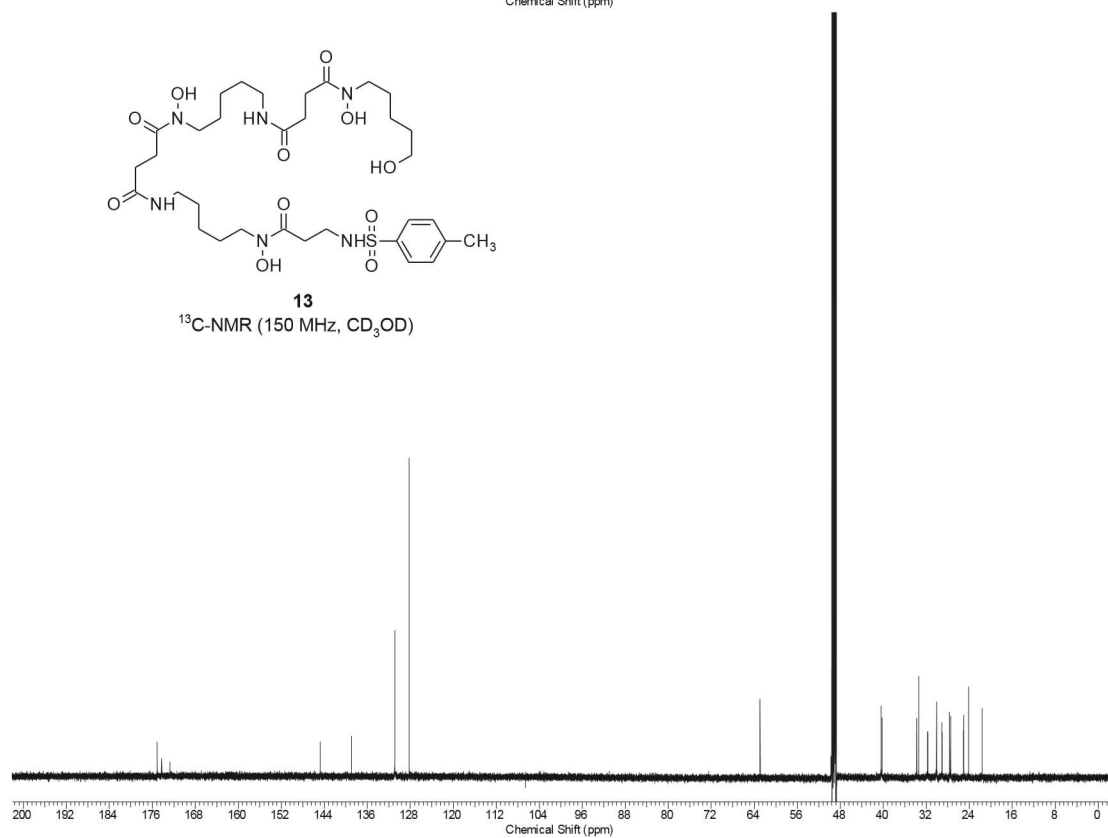
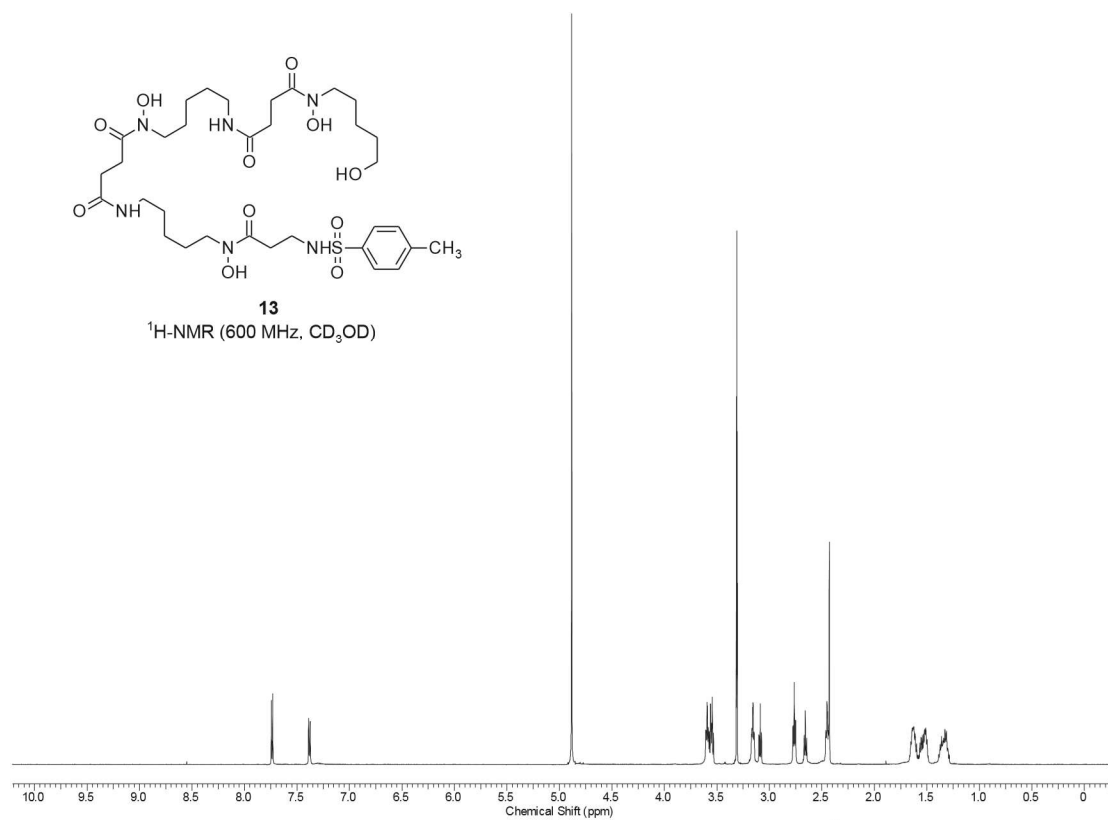


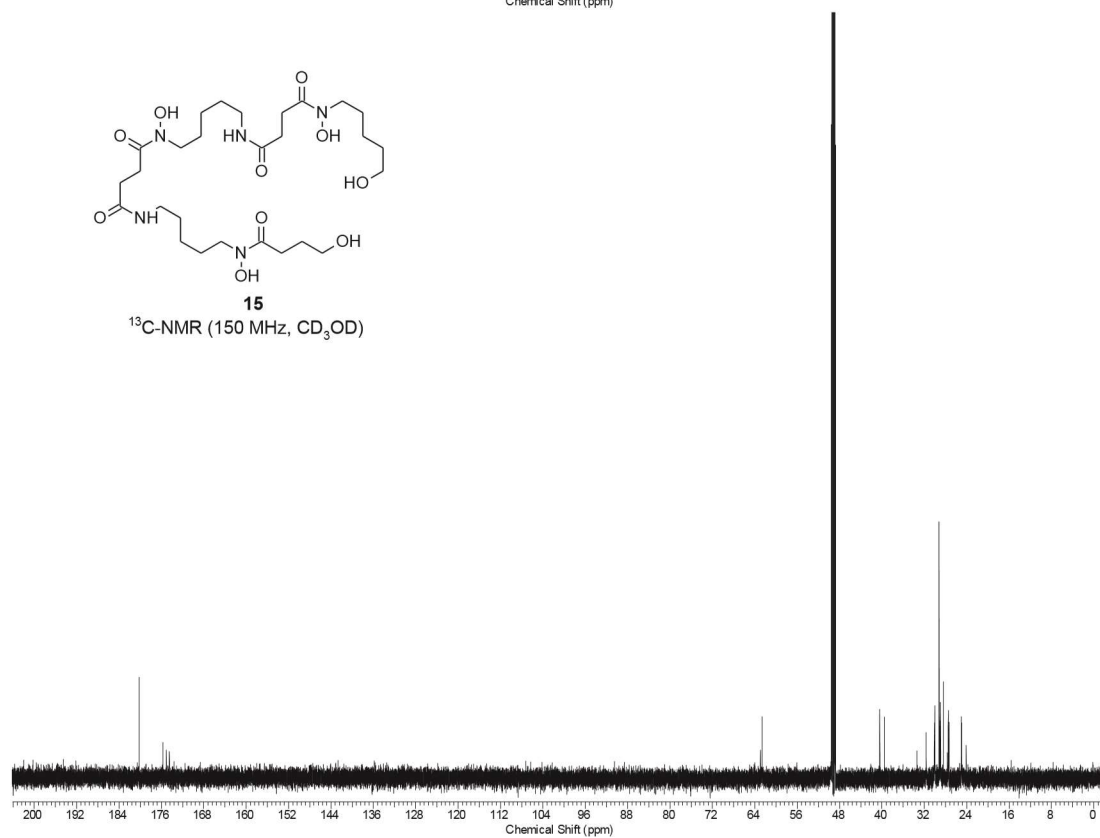
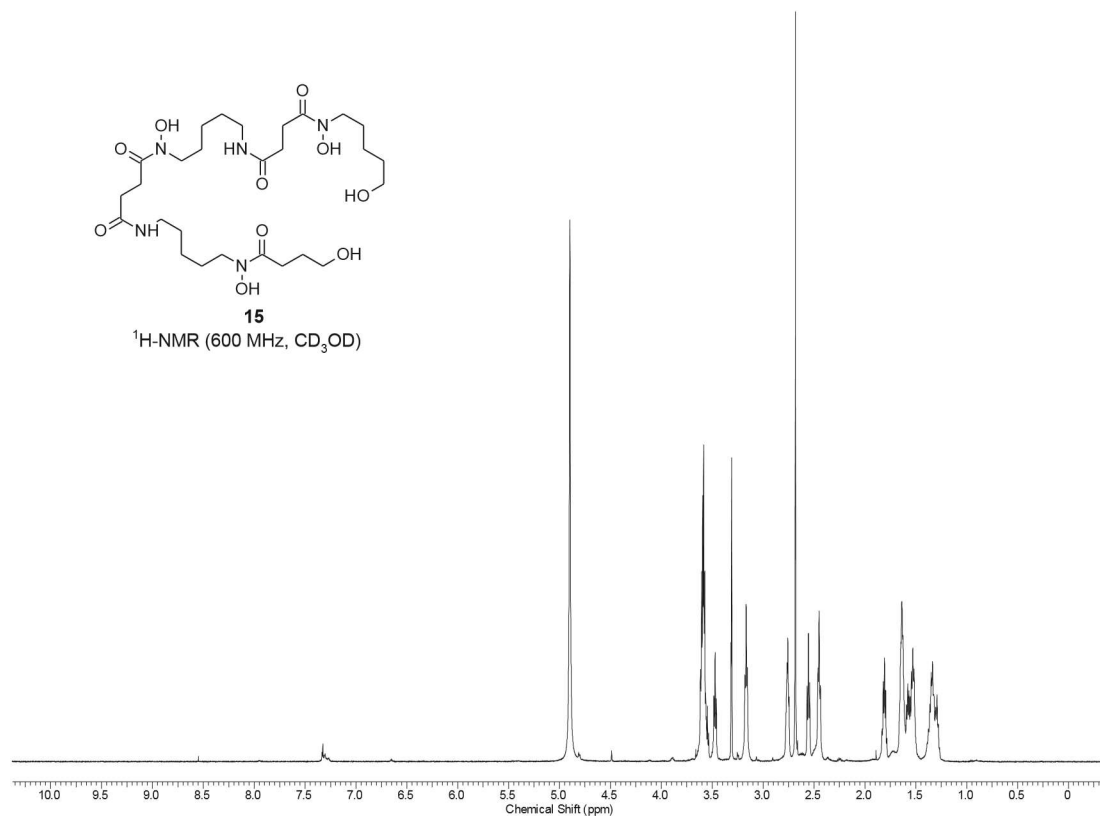
11

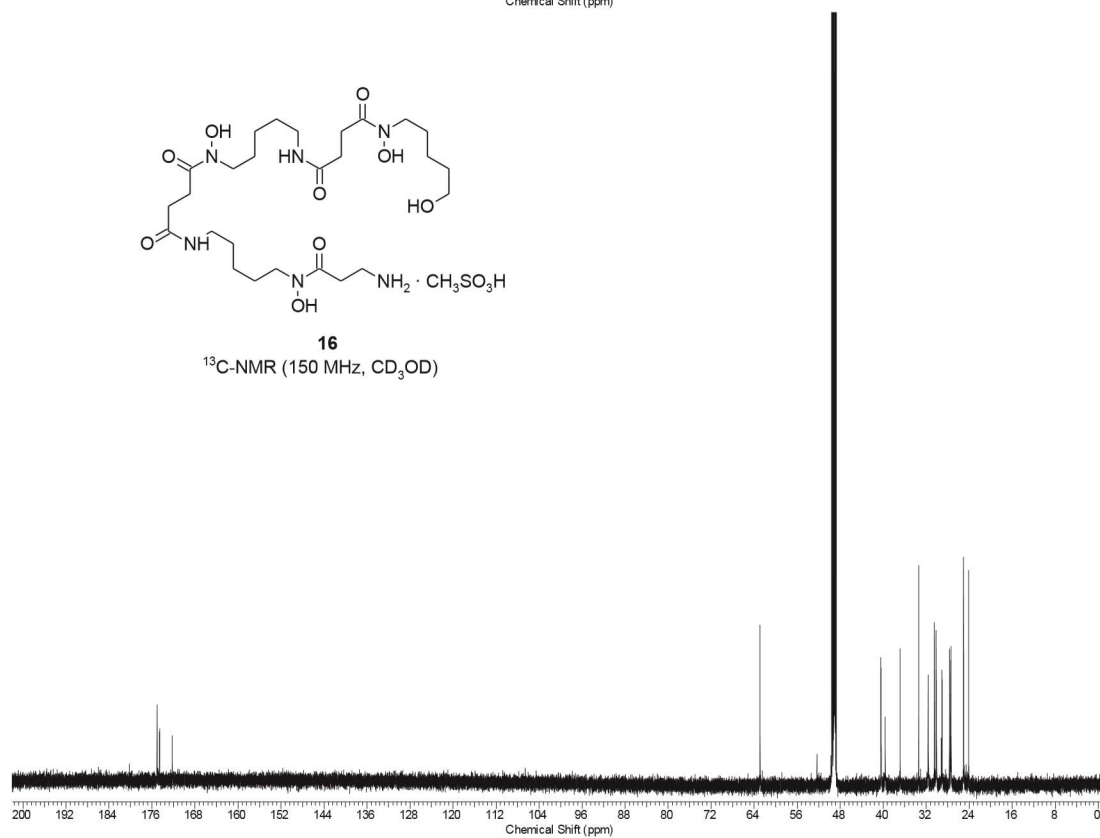
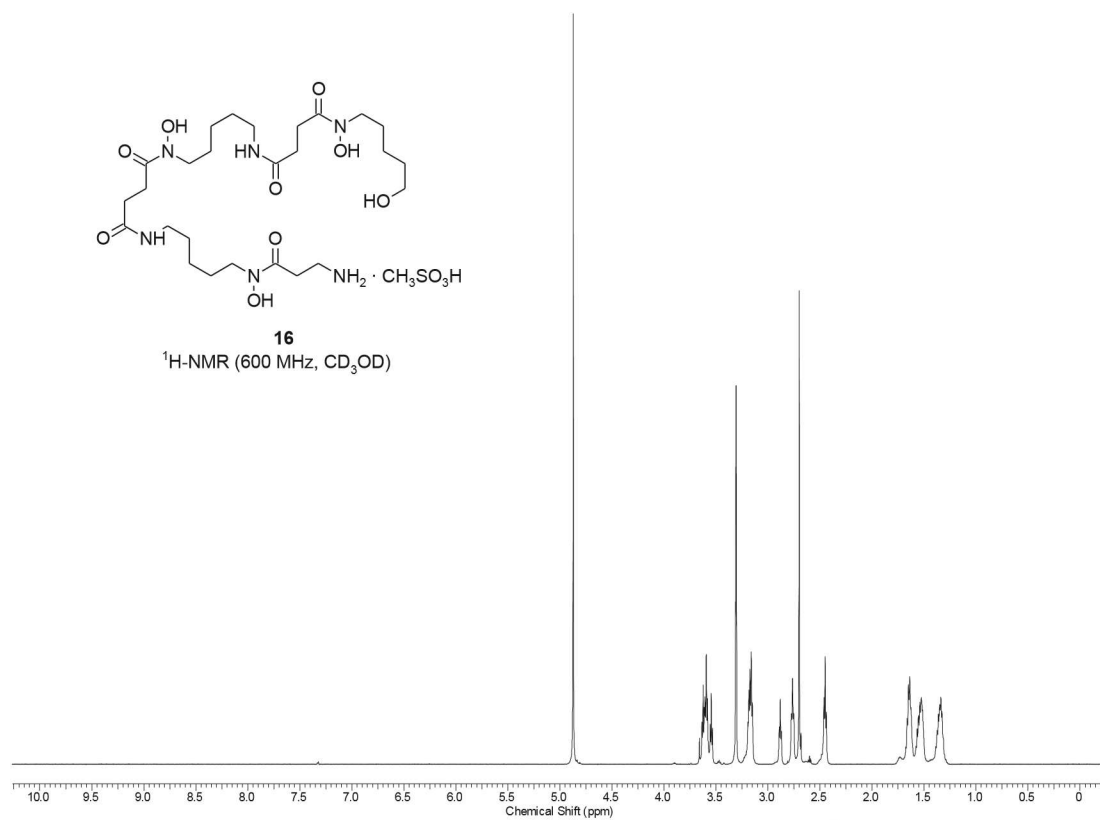
$^{13}\text{C-NMR}$ (150 MHz, CD_3OD)

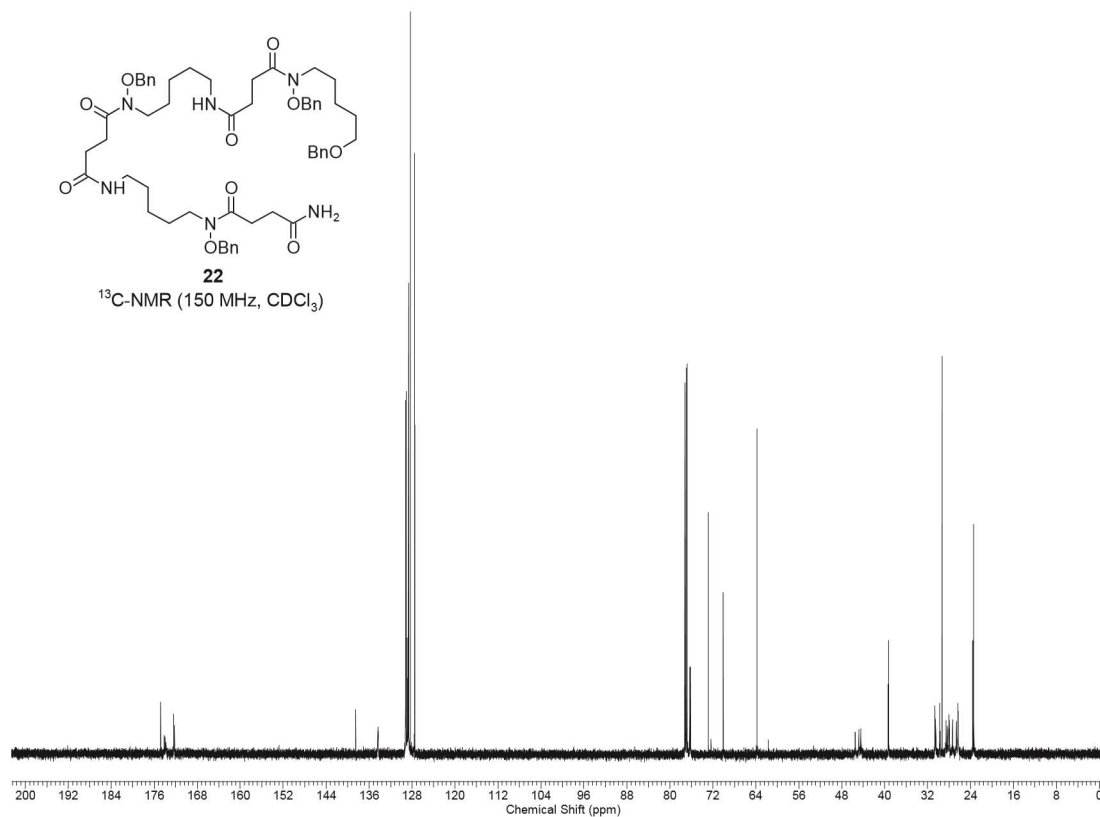
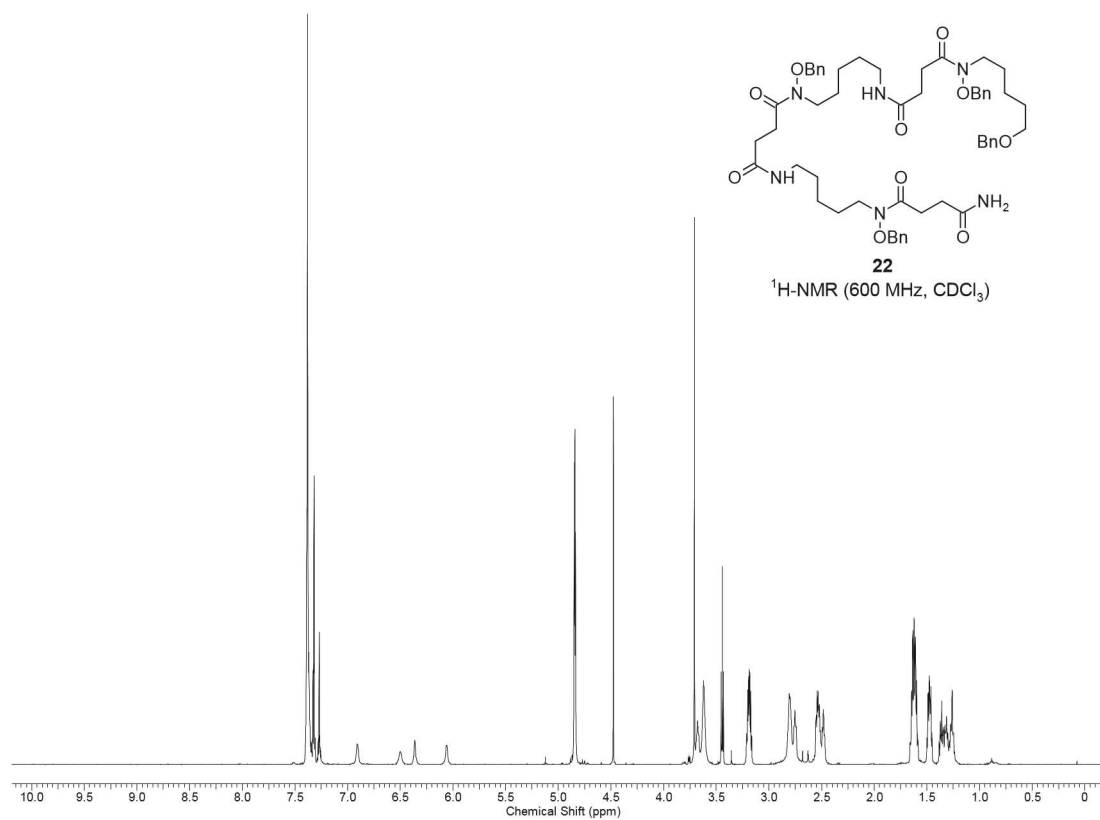


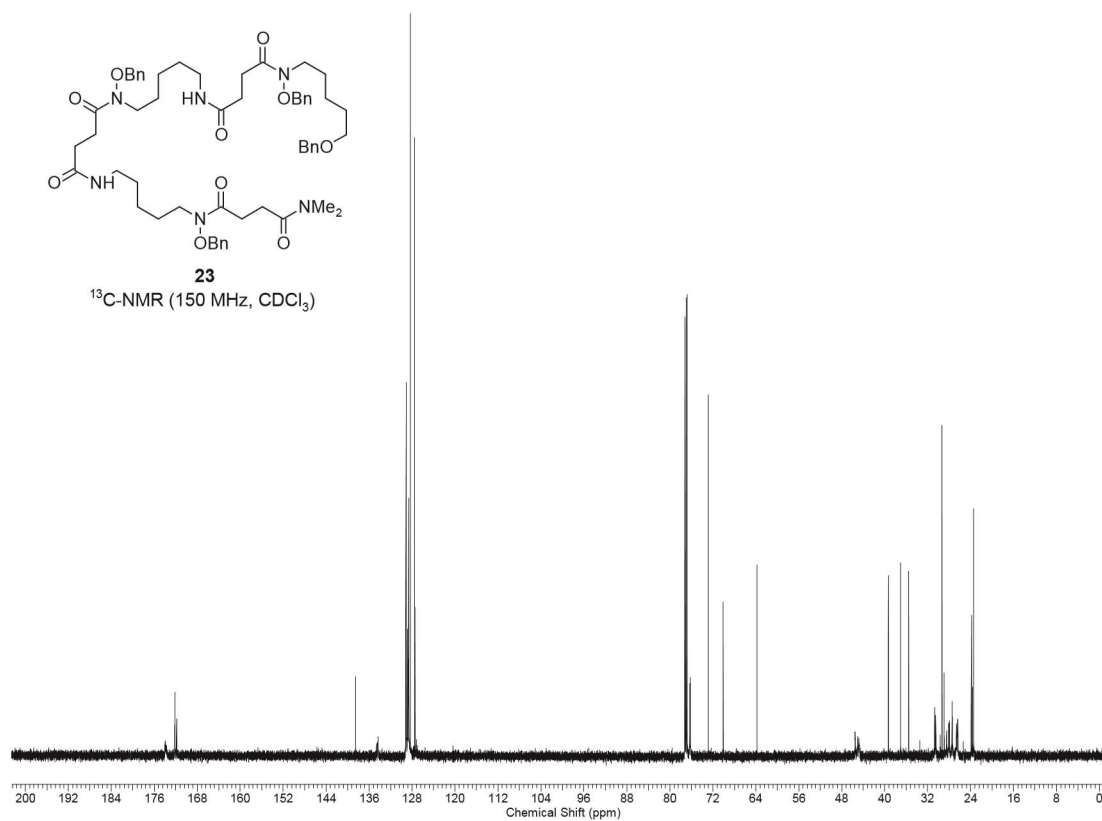
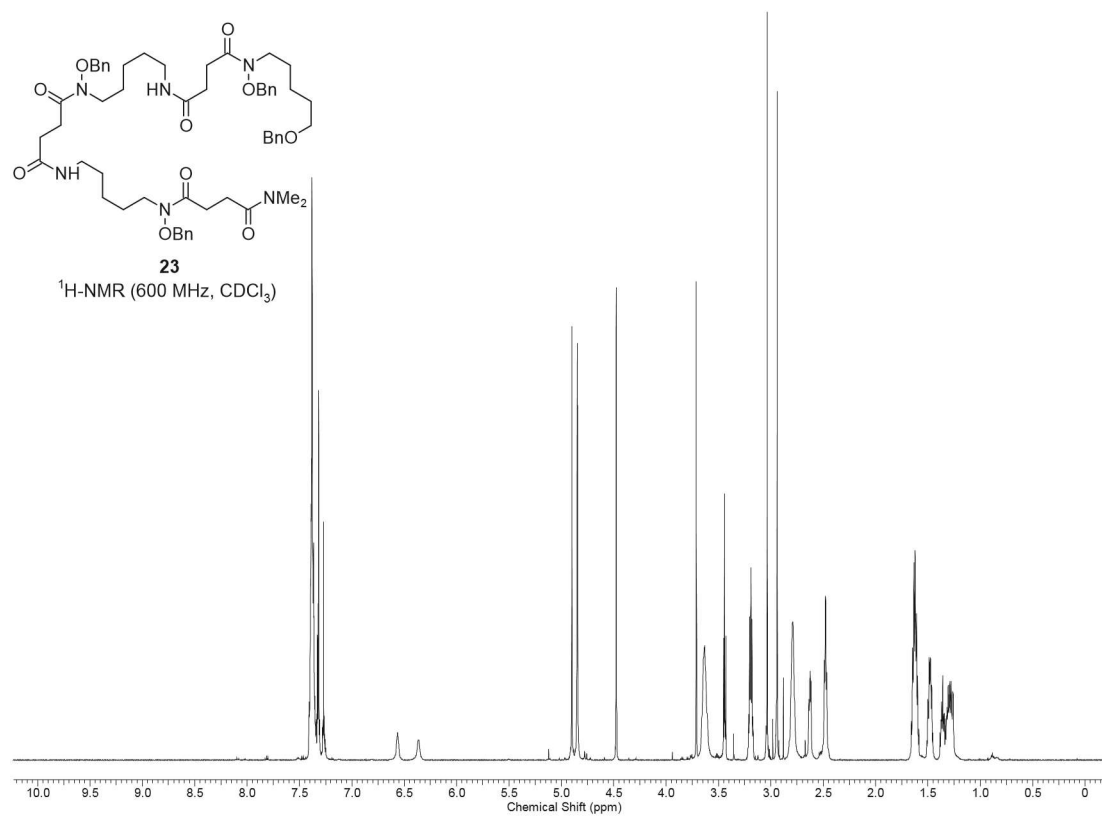


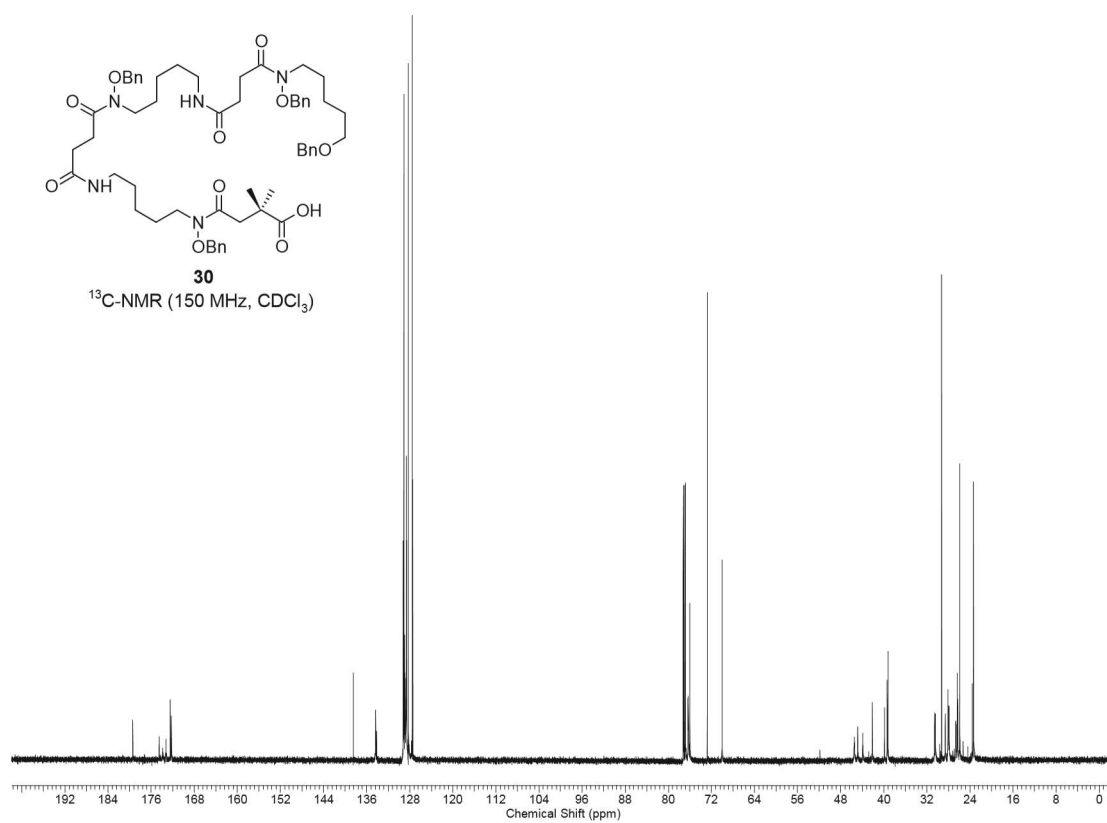
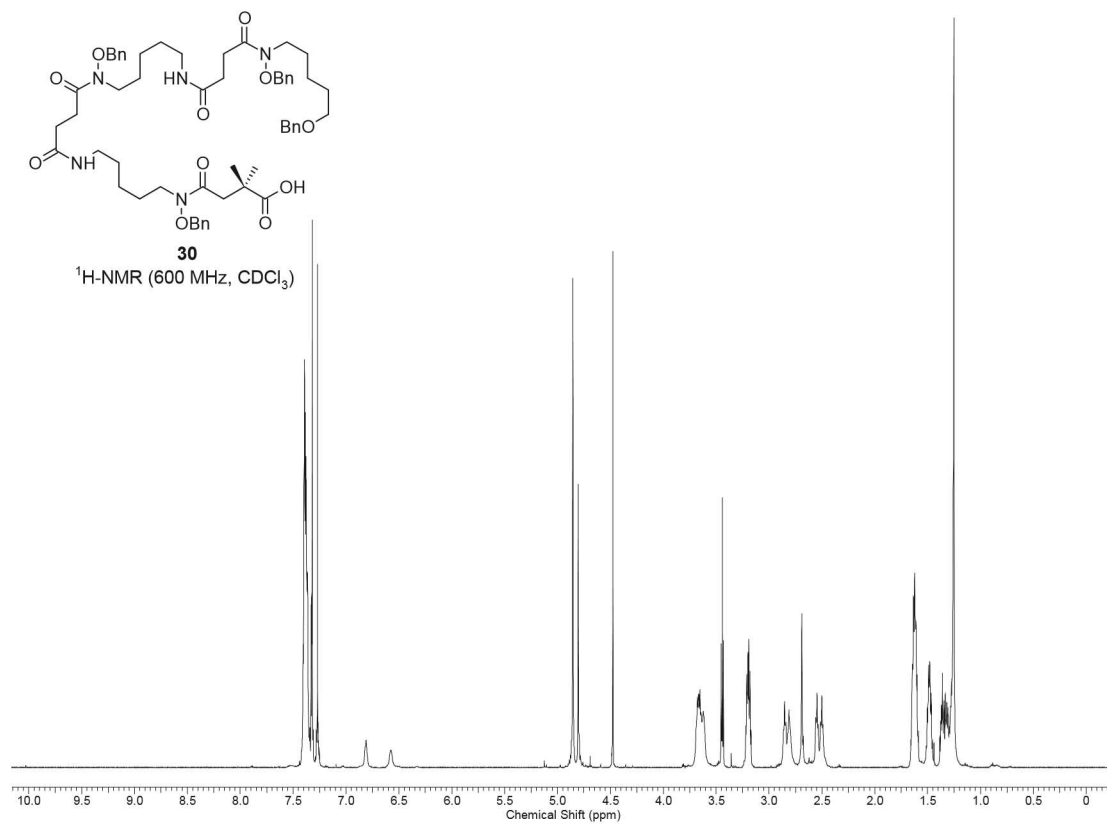


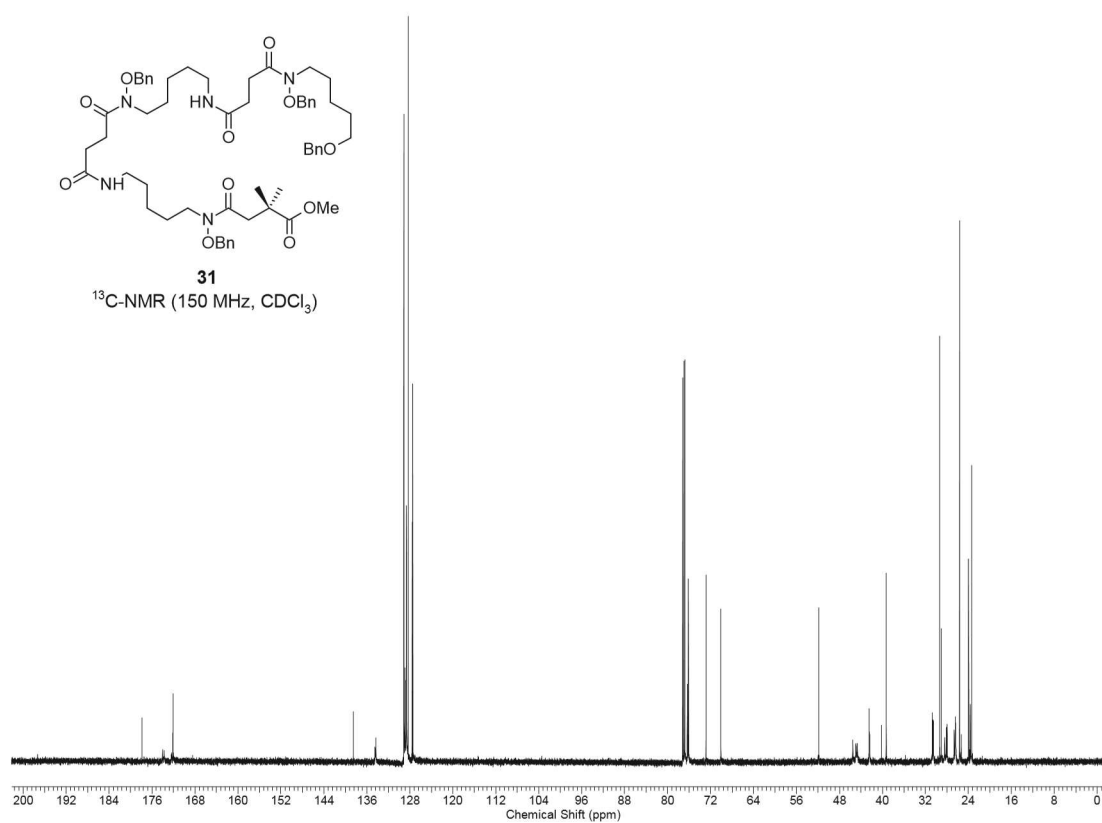
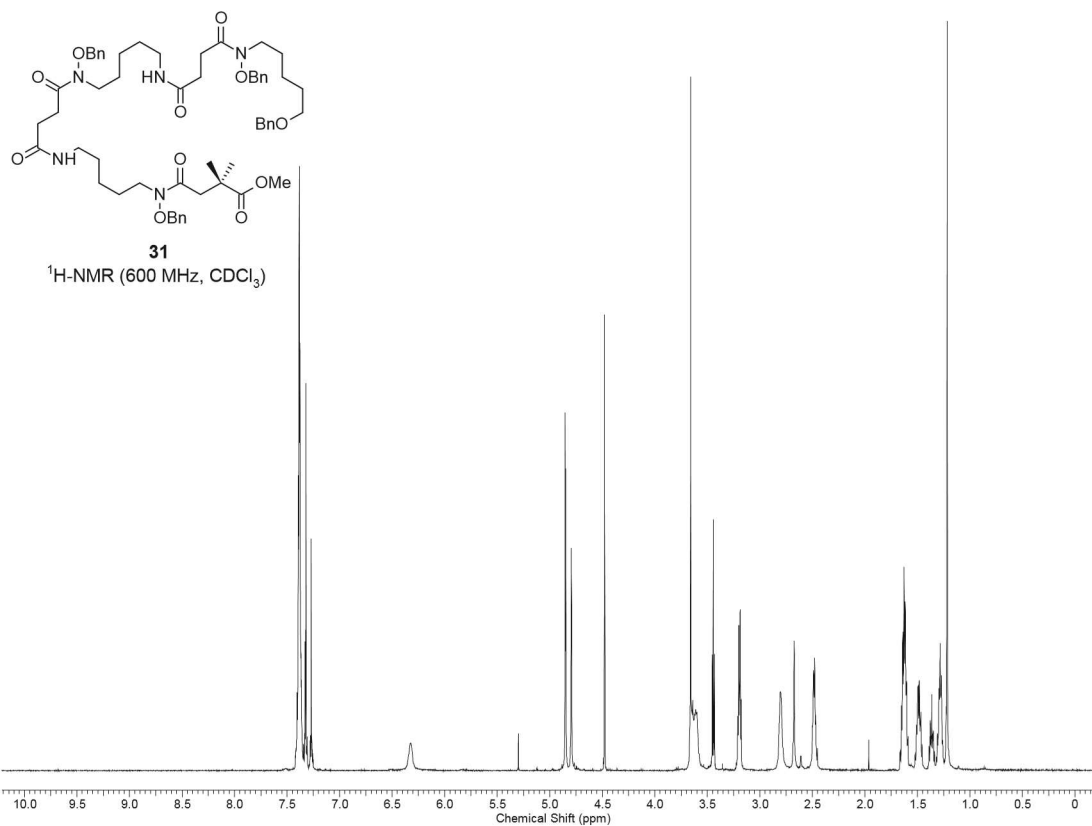


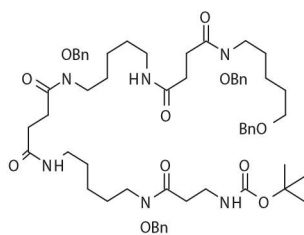






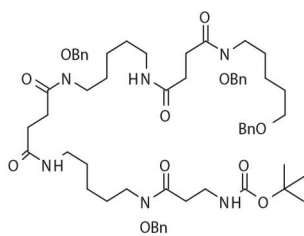
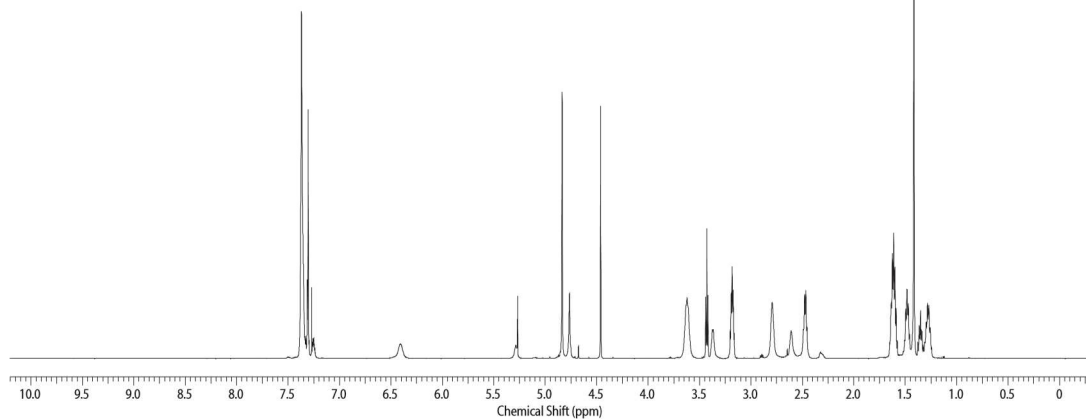






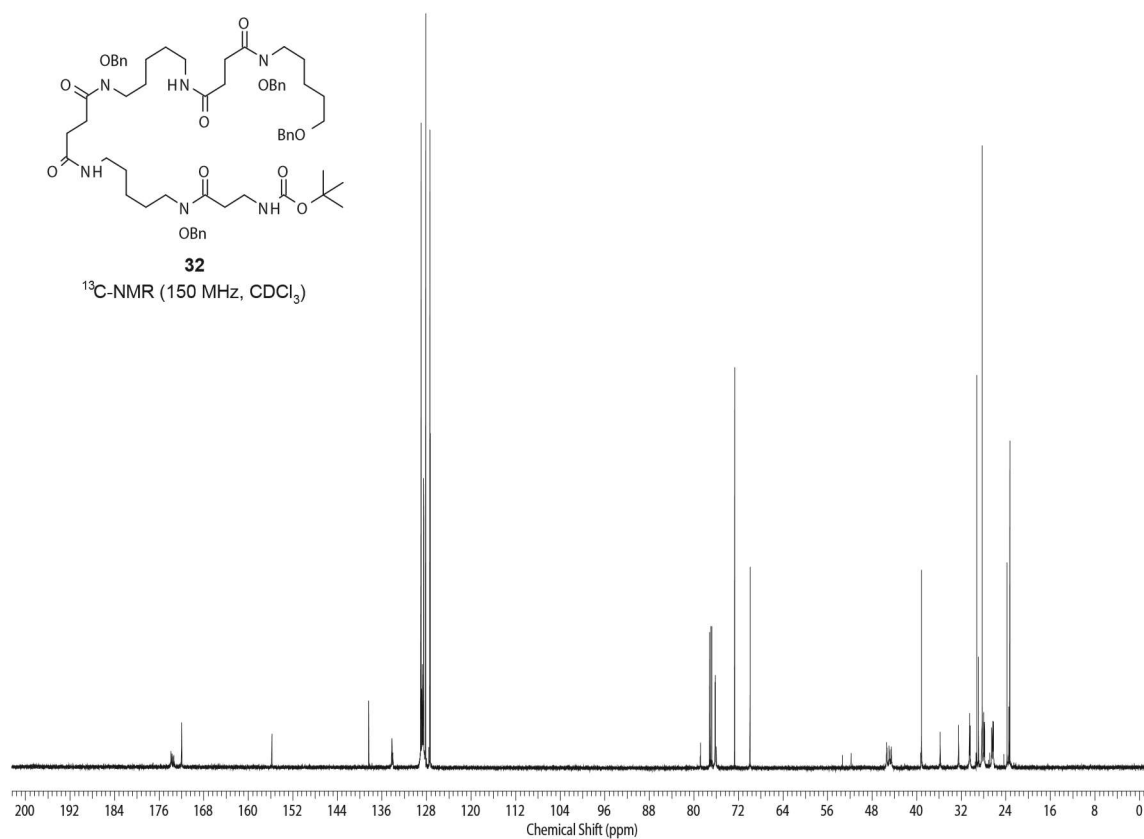
32

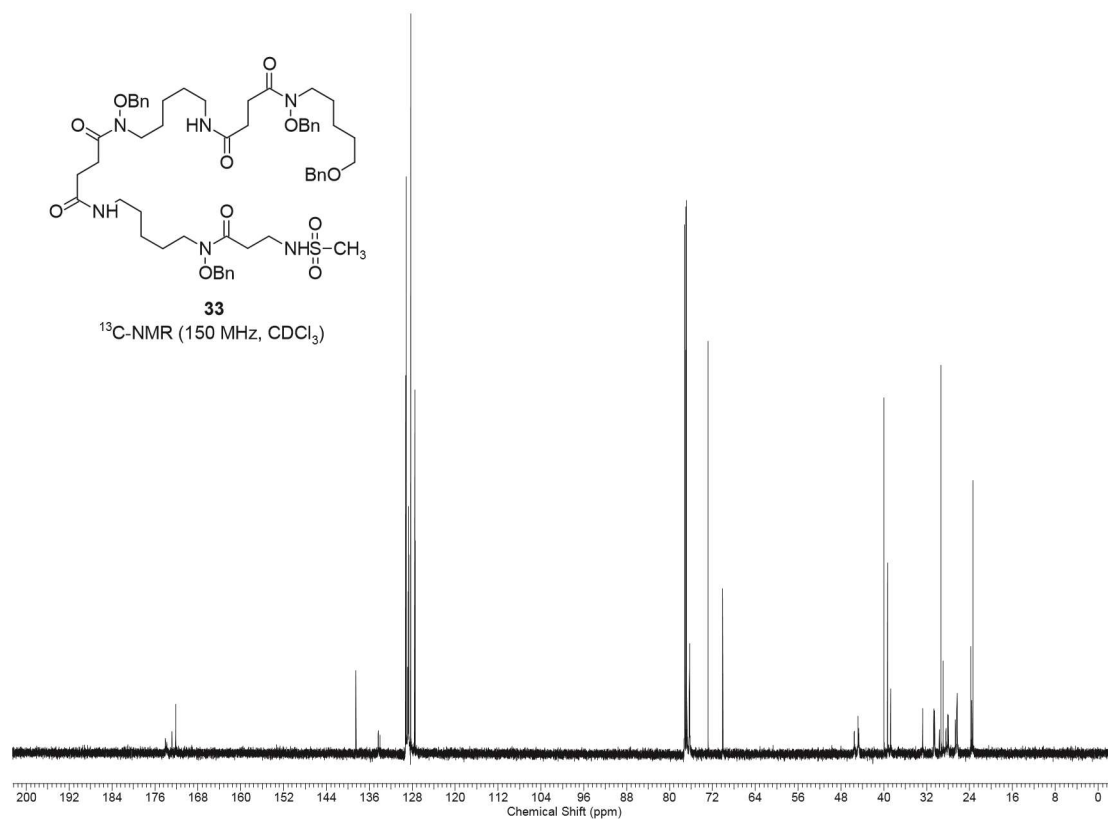
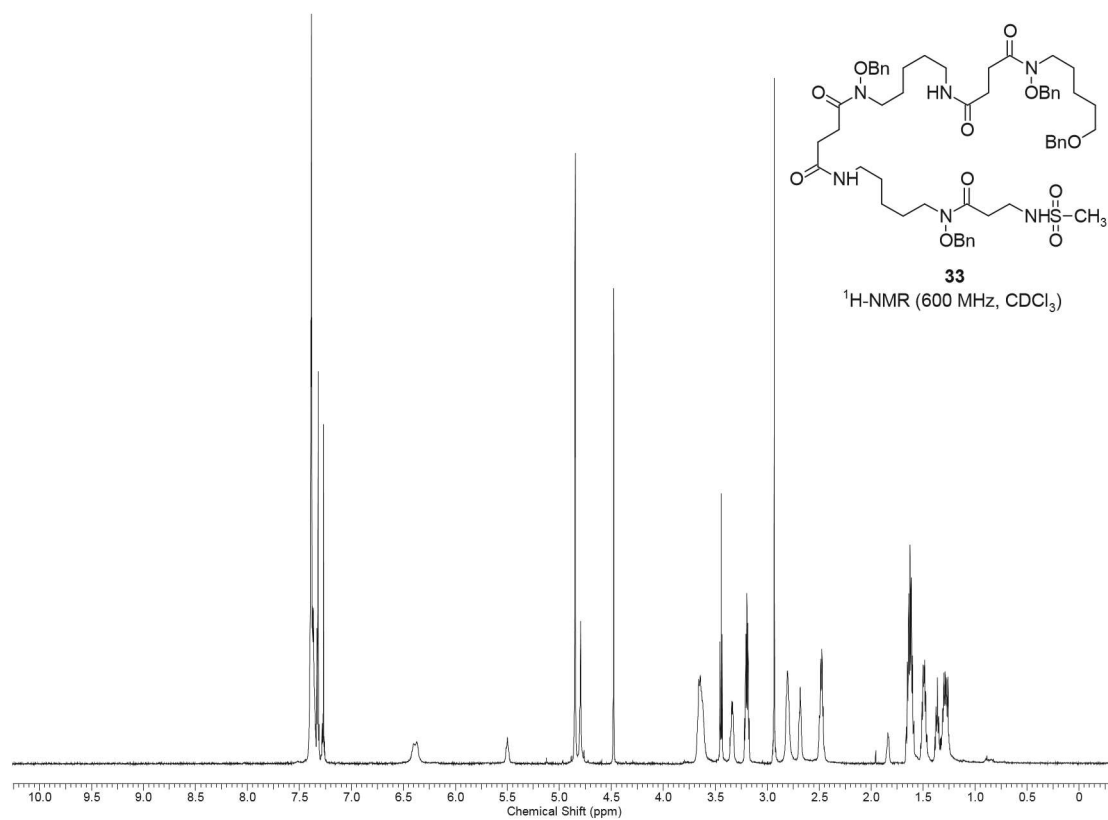
$^1\text{H-NMR}$ (600 MHz, CDCl_3)

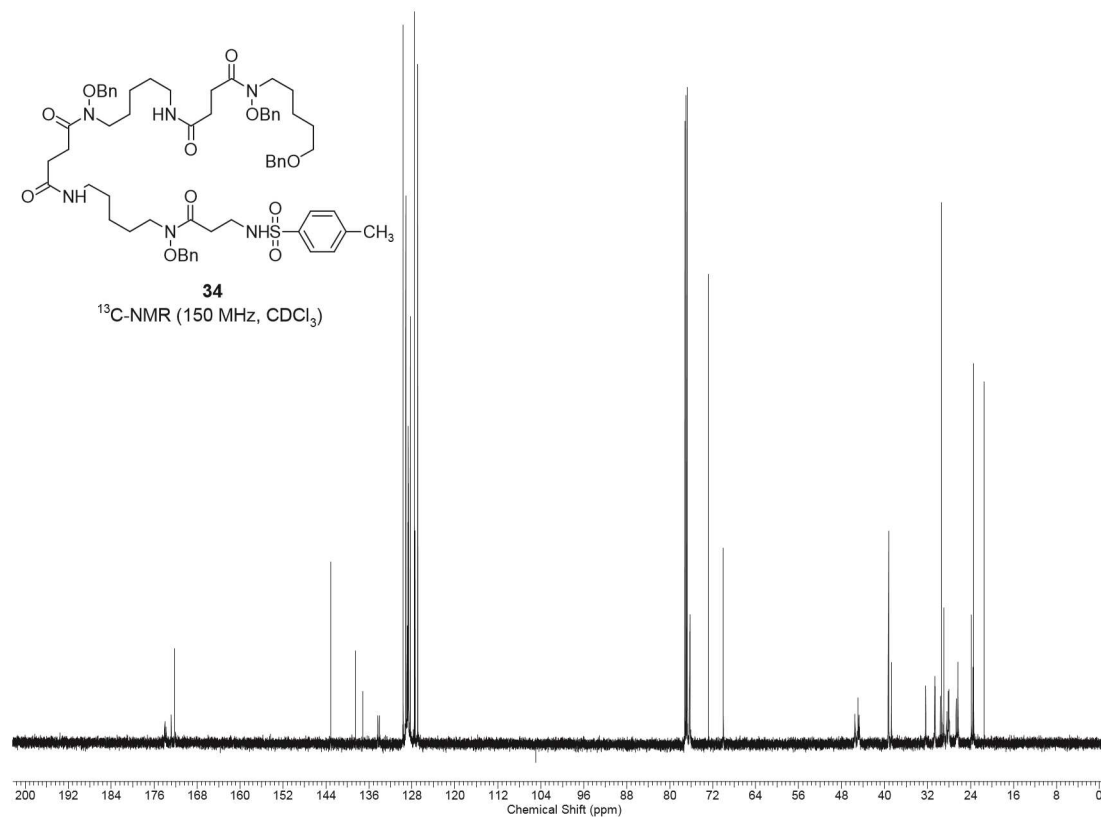
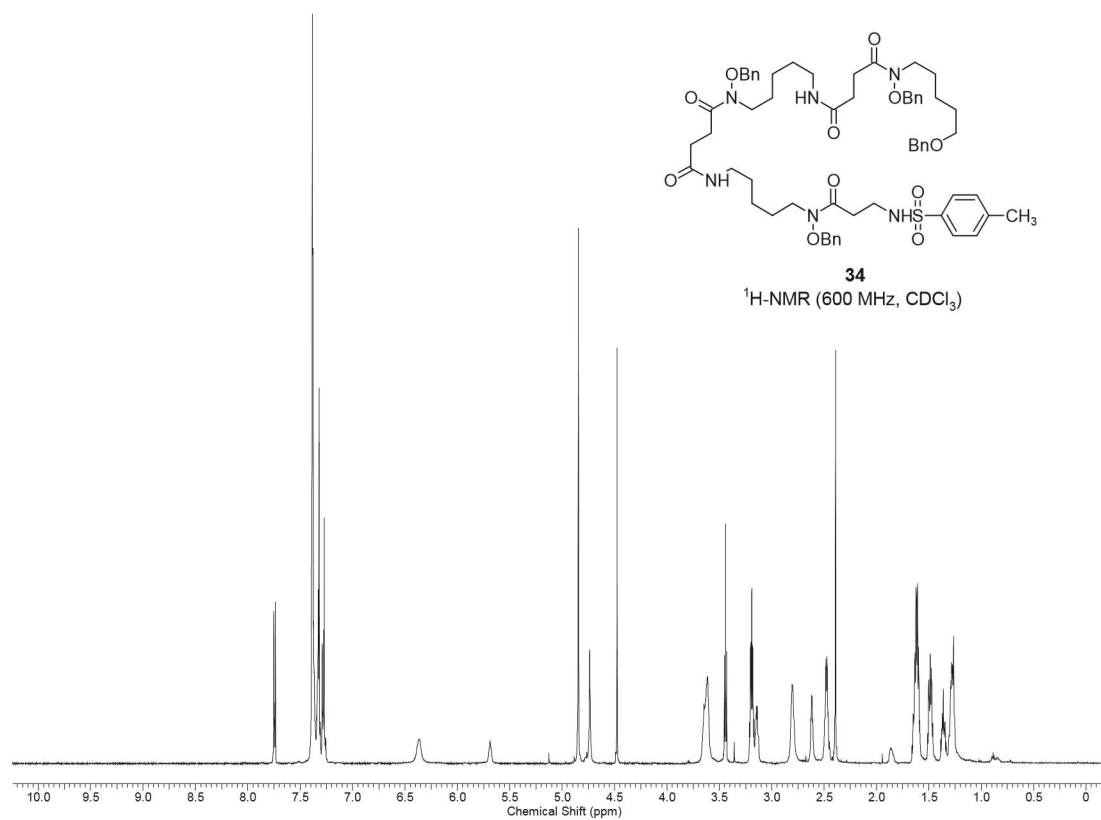


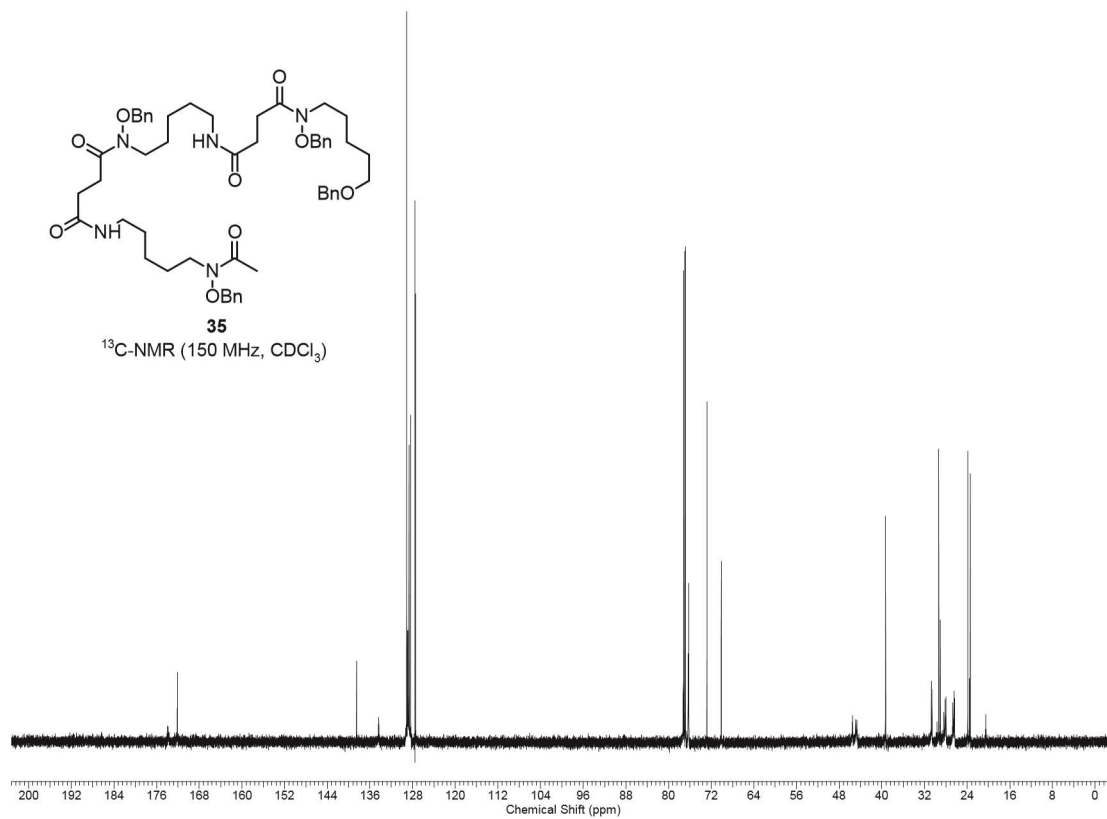
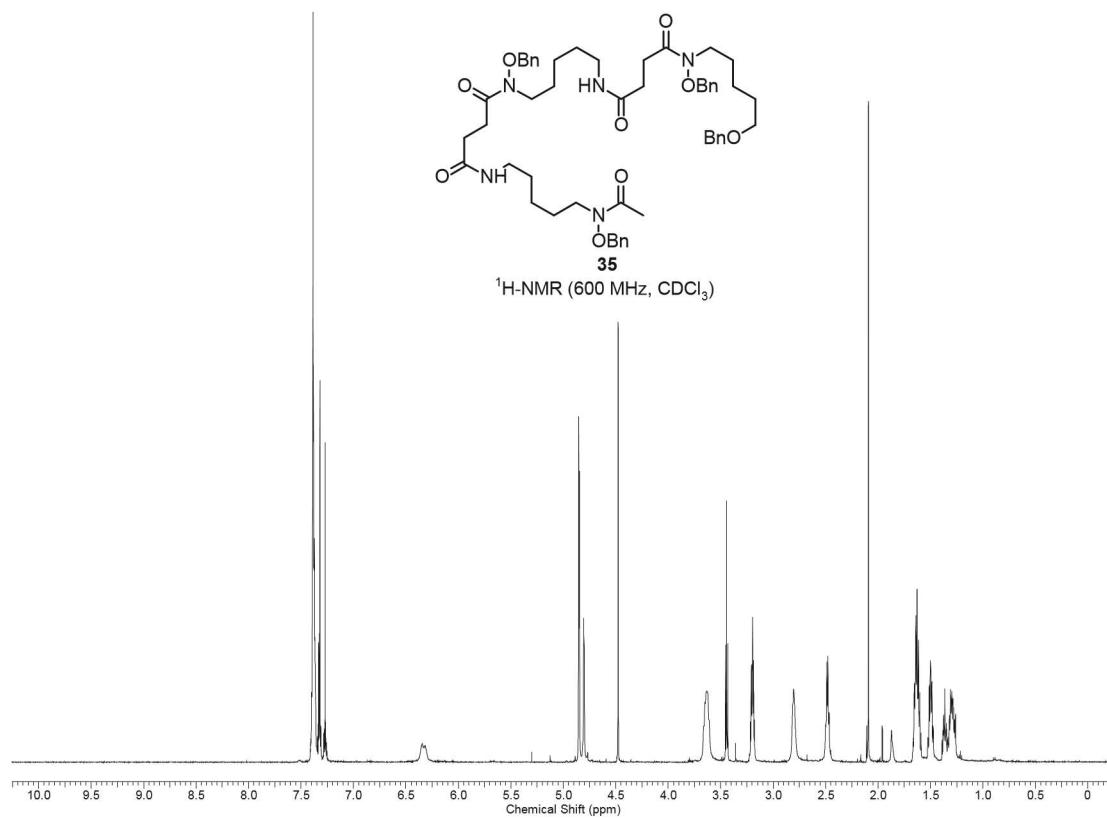
32

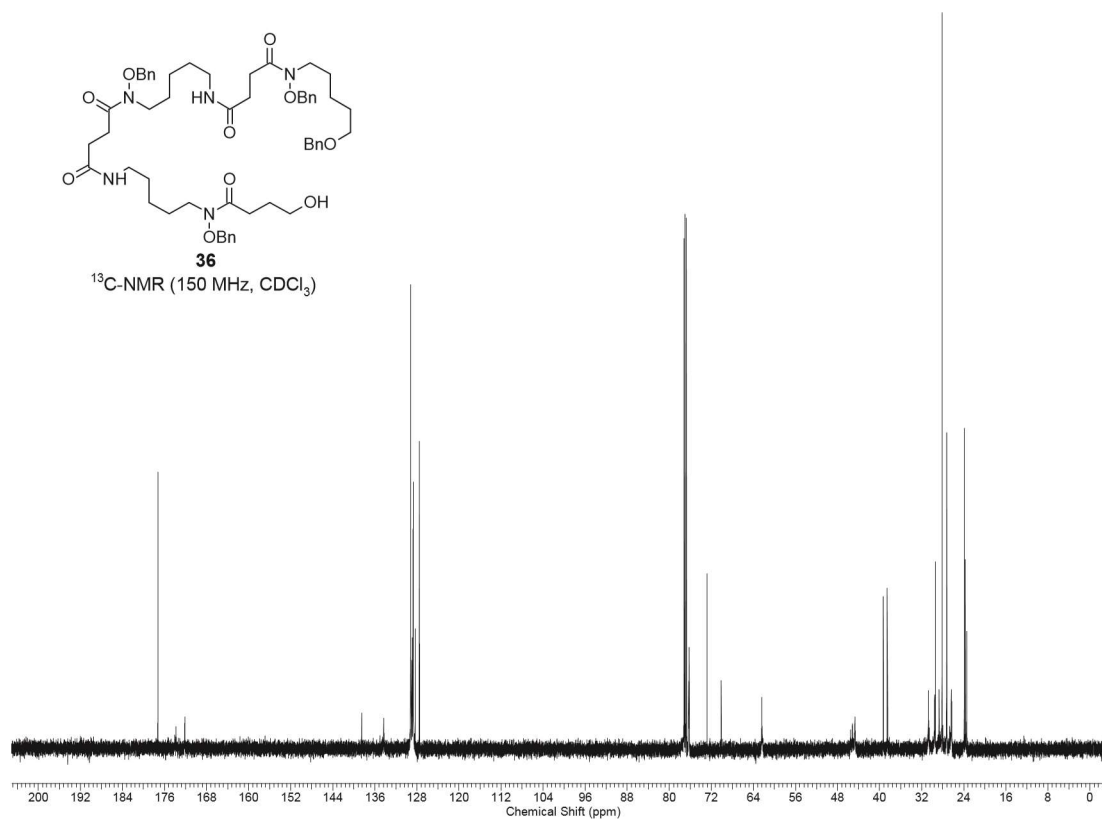
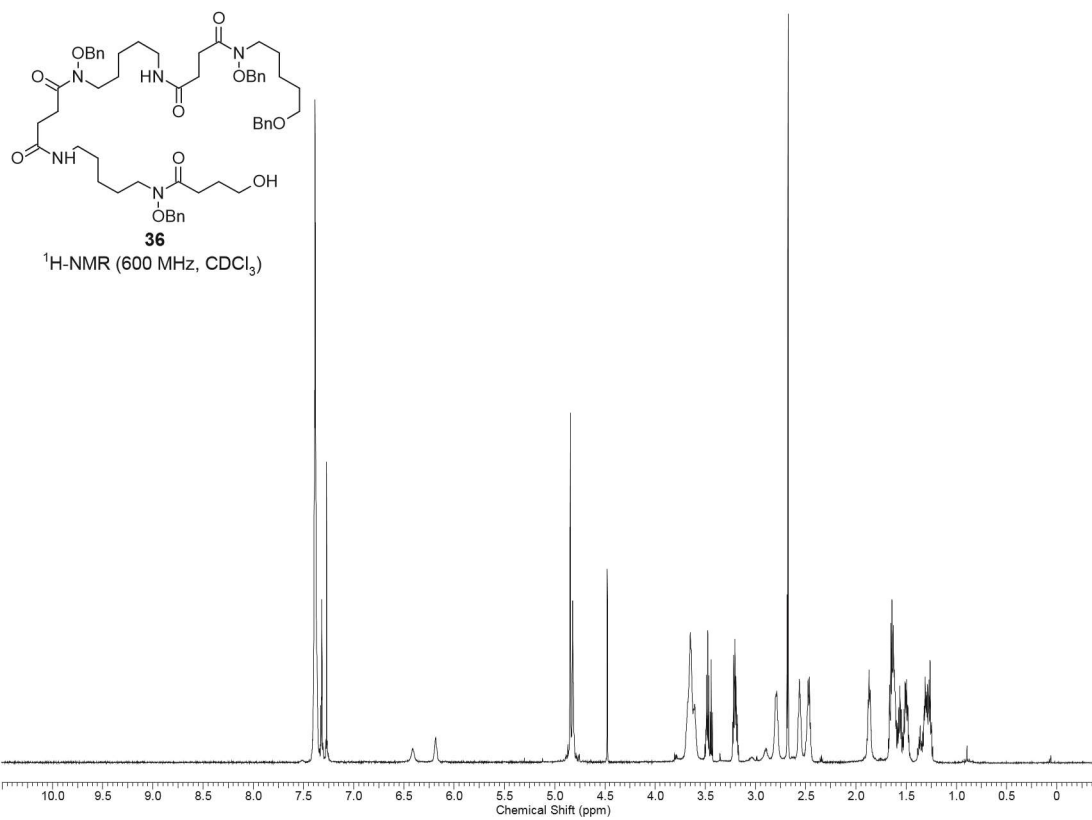
$^{13}\text{C-NMR}$ (150 MHz, CDCl_3)

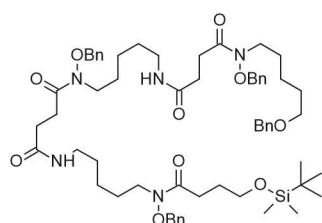




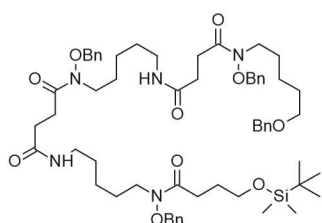
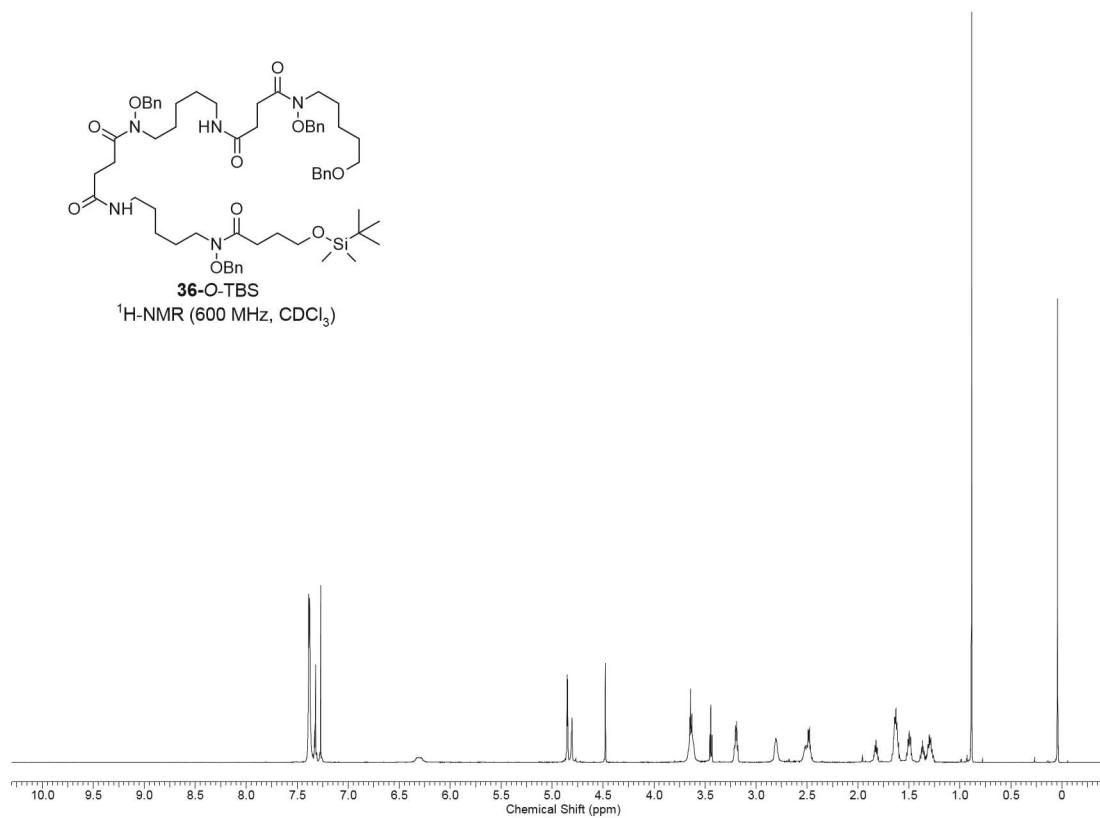




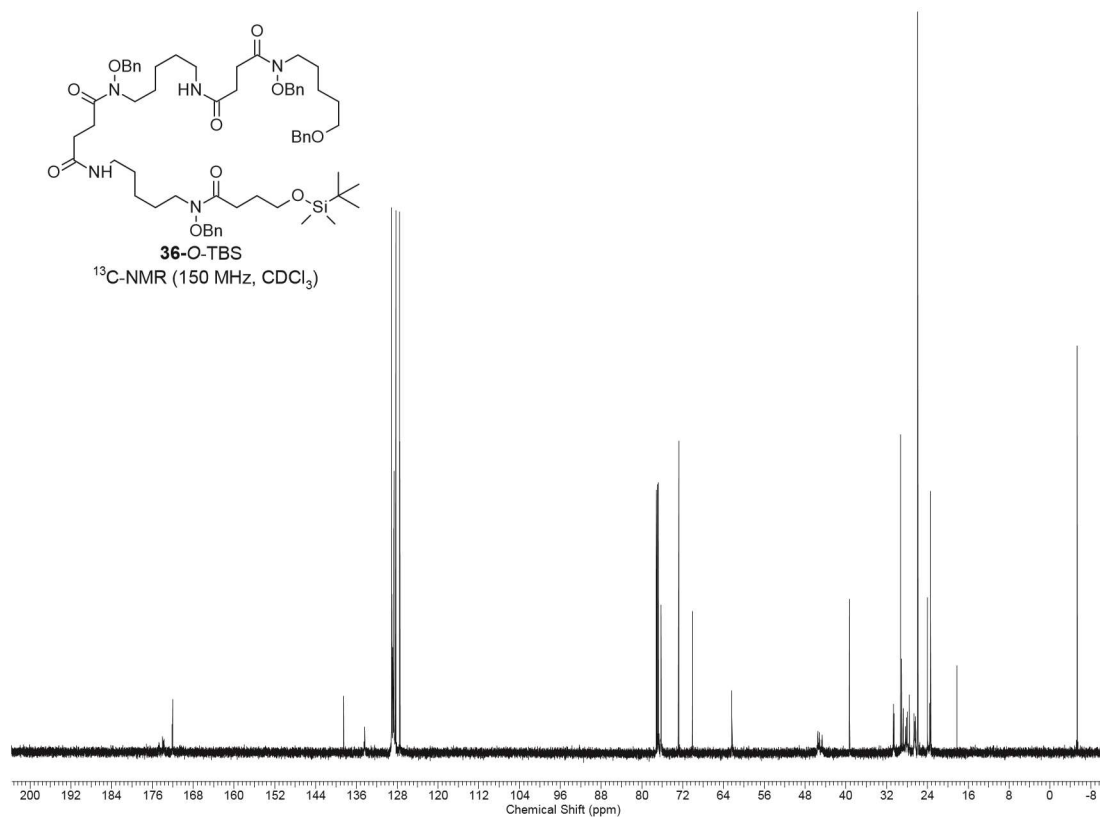


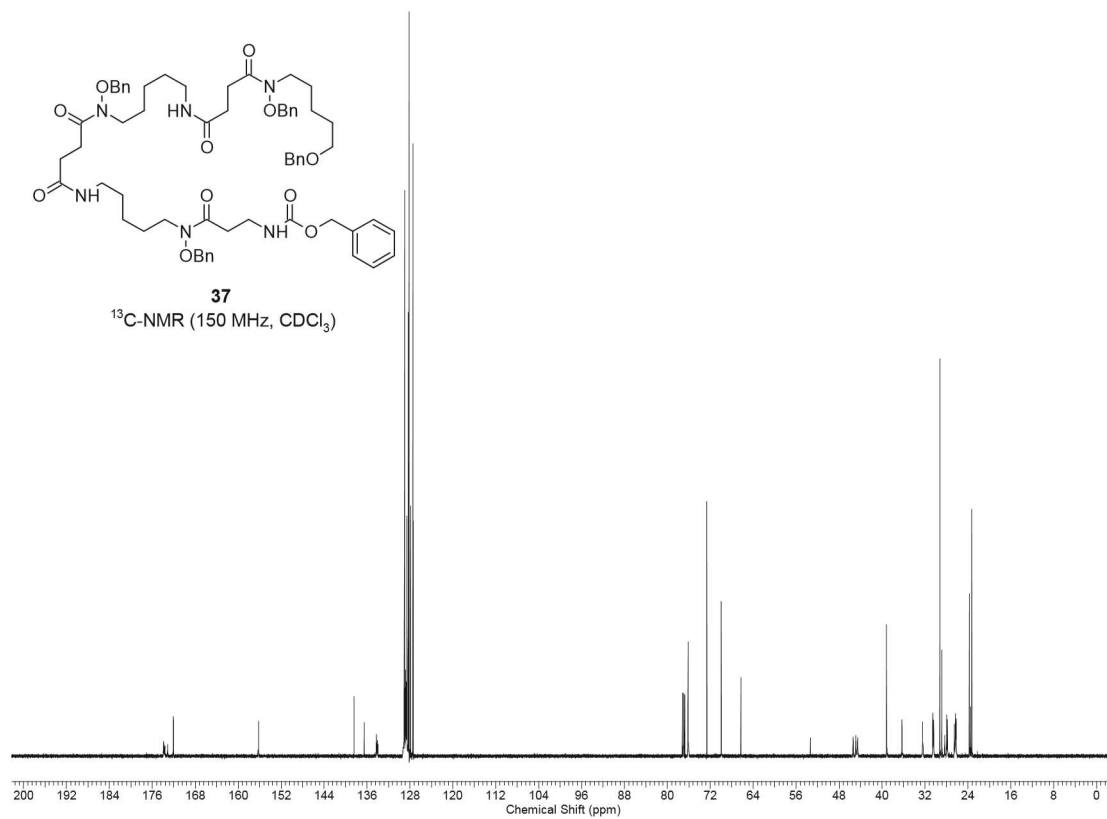
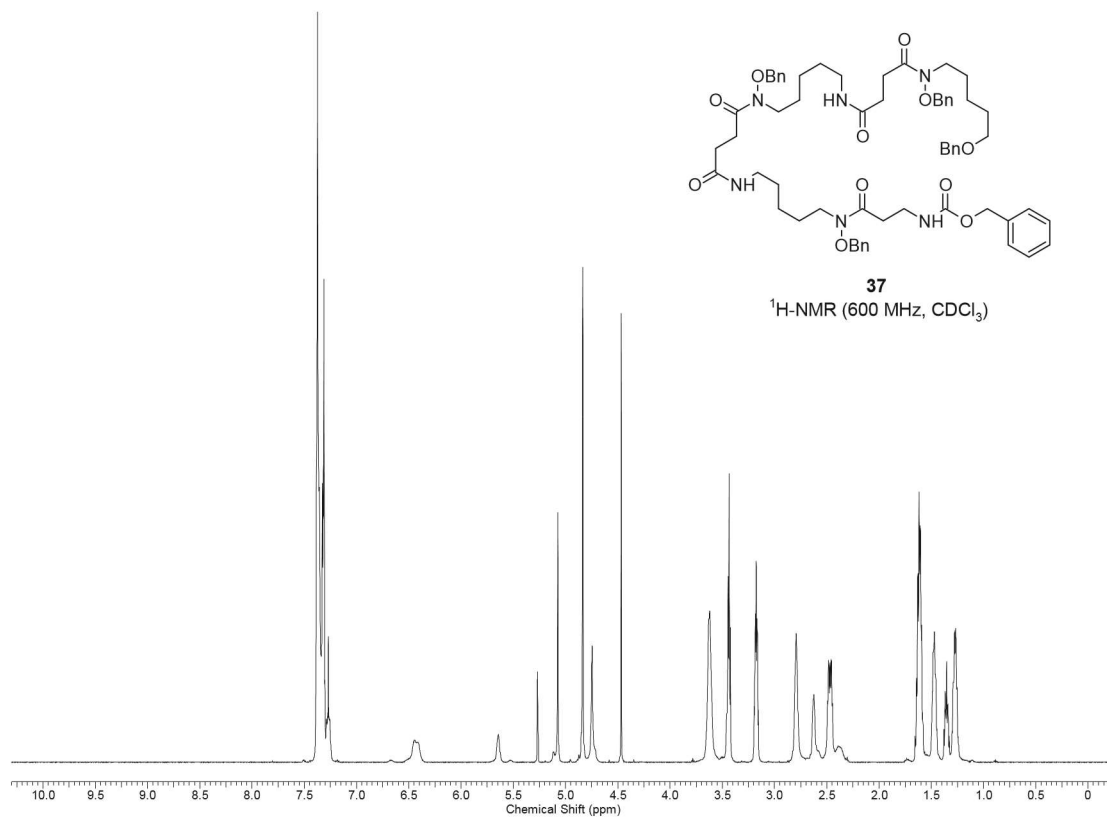


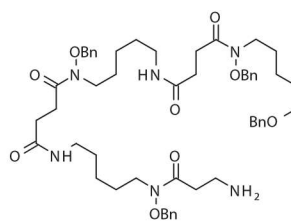
36-O-TBS
 $^1\text{H-NMR}$ (600 MHz, CDCl_3)



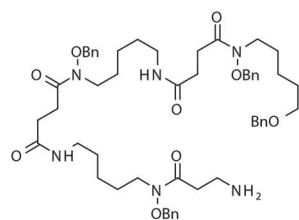
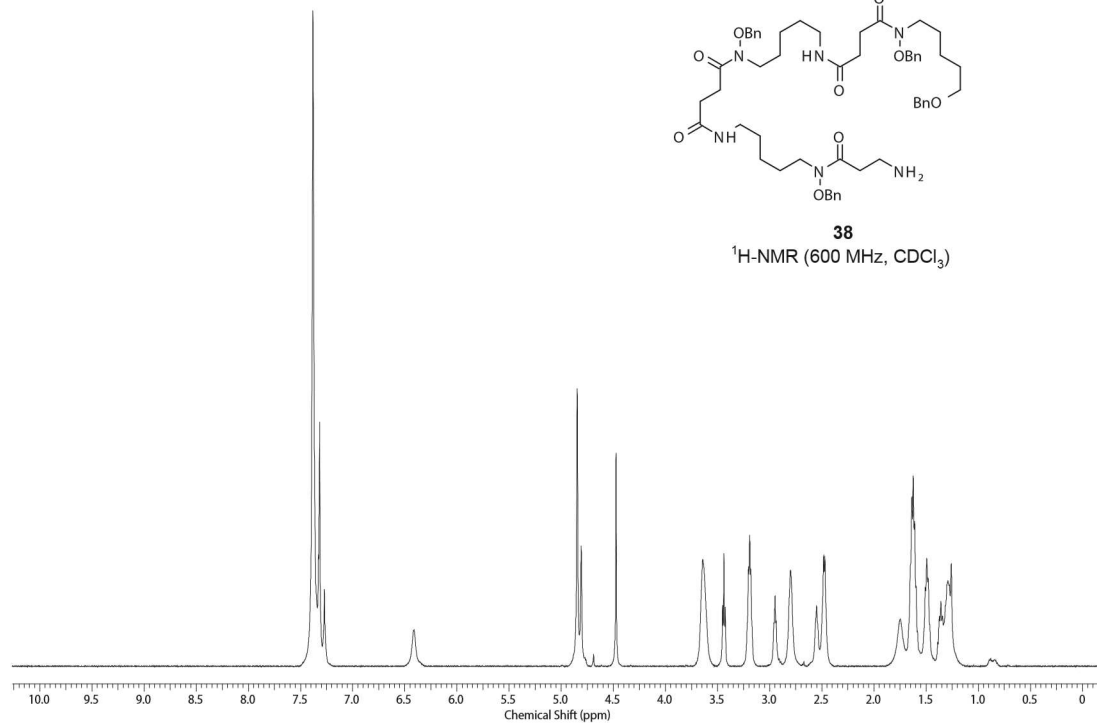
36-O-TBS
 $^{13}\text{C-NMR}$ (150 MHz, CDCl_3)



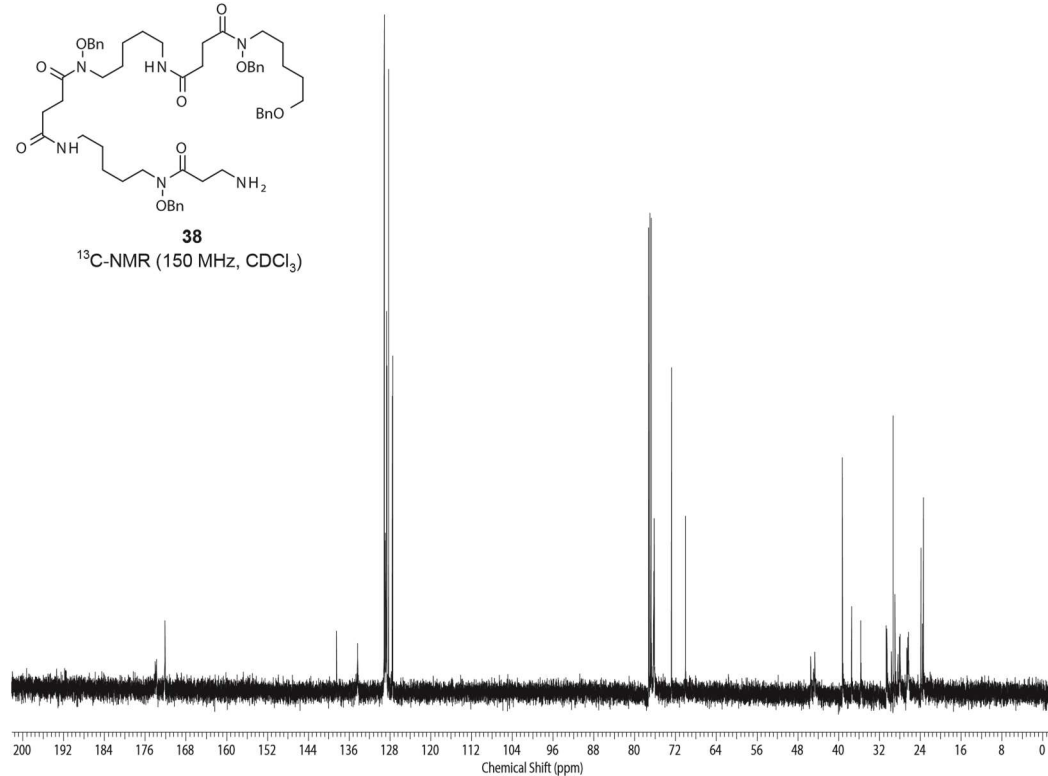




38
¹H-NMR (600 MHz, CDCl₃)



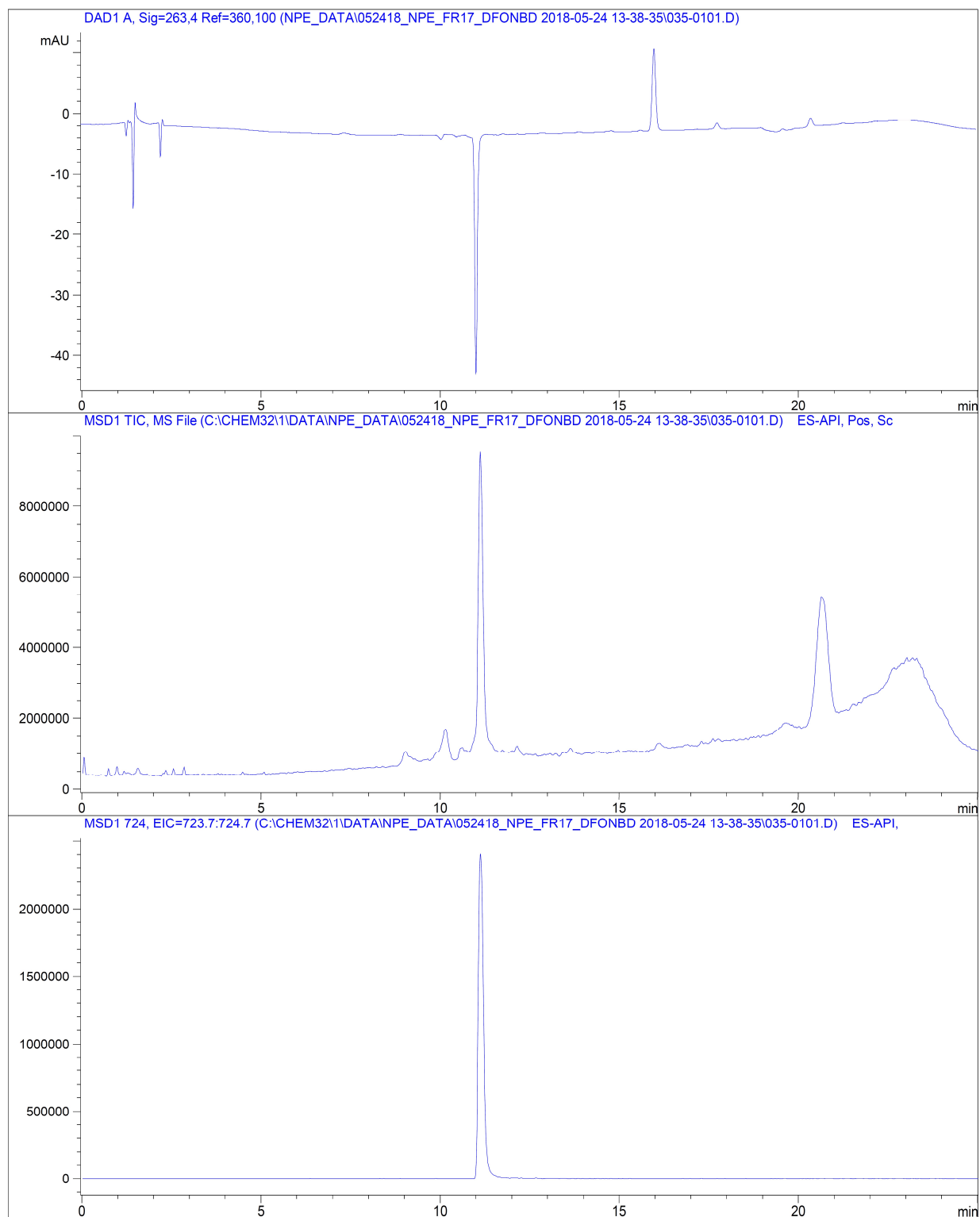
38
¹³C-NMR (150 MHz, CDCl₃)



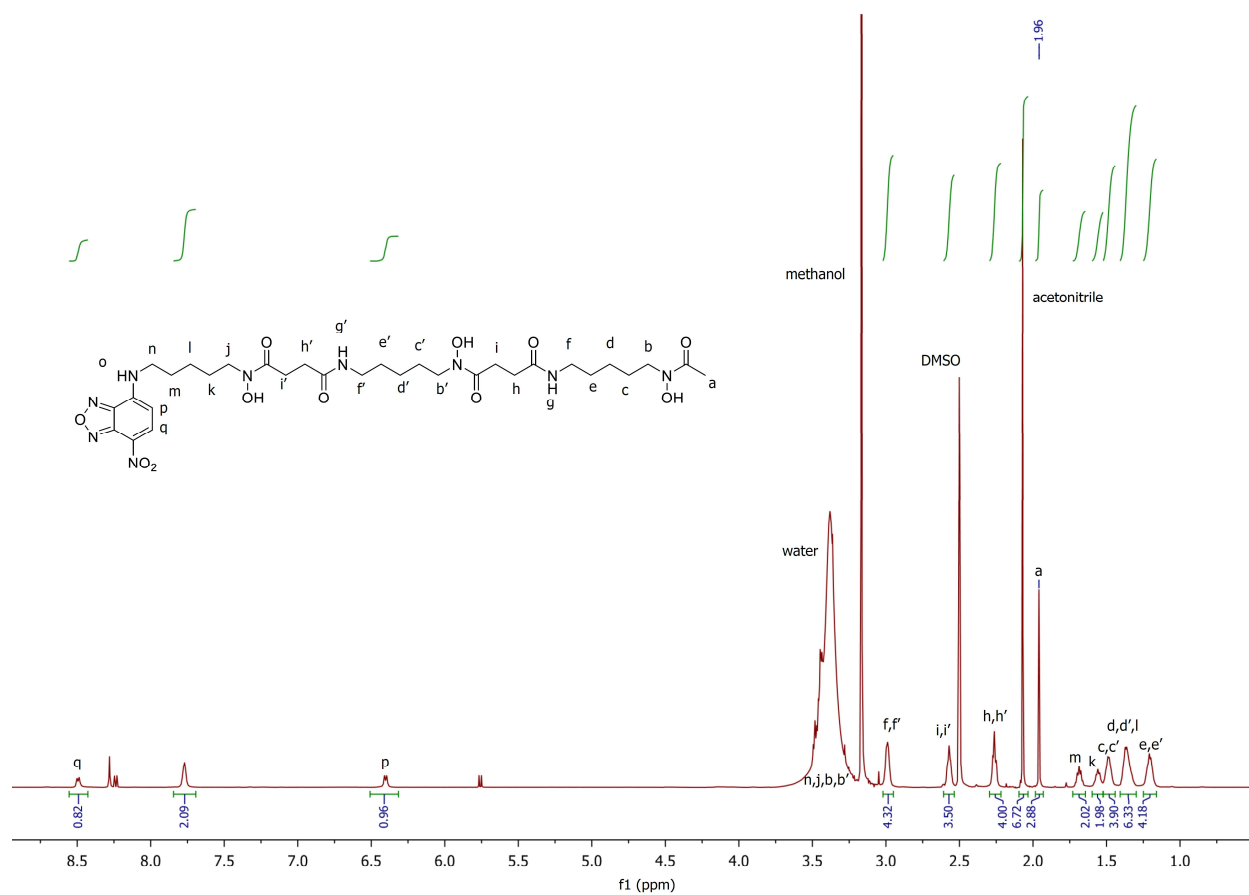
A.3 References

- [1] Hood, M. I.; Skaar, E. P. (2012) Nutritional immunity: transition metals at the pathogen–host interface. *Nat. Rev. Microbiol.* 10, 525.
- [2] Crumbliss, A. L., Aqueous solution equilibrium and kinetic studies of iron siderophore and model siderophore complexes. In *Handbook of Microbial Iron Chelates*, Winkelmann, G., Ed. CRC Press: Boca Raton, FL, 1991; pp 177-233.
- [3] Wencewicz, T. A. (2011) Development of microbe-selective antibacterial agents: From small molecules to siderophores. University of Notre Dame, Notre Dame, IN.
- [4] Roosenberg, J. M., 2nd; Miller, M. J. (2000) Total synthesis of the siderophore danoxamine. *J. Org. Chem.* 65, 4833.
- [5] Wencewicz, T. A.; Oliver, A. G.; Miller, M. J. (2012) Iron(III)-templated macrolactonization of trihydroxamate siderophores. *Org. Lett.* 14, 4390.
- [6] Wencewicz, T. A.; Long, T. E.; Mollmann, U.; Miller, M. J. (2013) Trihydroxamate siderophore-fluoroquinolone conjugates are selective sideromycin antibiotics that target *Staphylococcus aureus*. *Bioconjugate Chem.* 24, 473.
- [7] Liu, X. S.; Patterson, L. D.; Miller, M. J.; Theil, E. C. (2007) Peptides selected for the protein nanocage pores change the rate of iron recovery from the ferritin mineral. *J. Biol. Chem.* 282, 31821.
- [8] Warren, C. K.; Weedon, B. C. L. (1958) Carotenoids and Related Compounds. VI. Some Conjugated Polyene Diones, and Their Comparison with Capsorubin. *J. Chem. Soc.* 3972.
- [9] Dionis, J. B.; Jenny, H. –B.; Peter, H. H. (1989) Synthesis and Analytical Characterization of a Major Desferrioxamine B Metabolite. *J. Org. Chem.* 54, 5623.

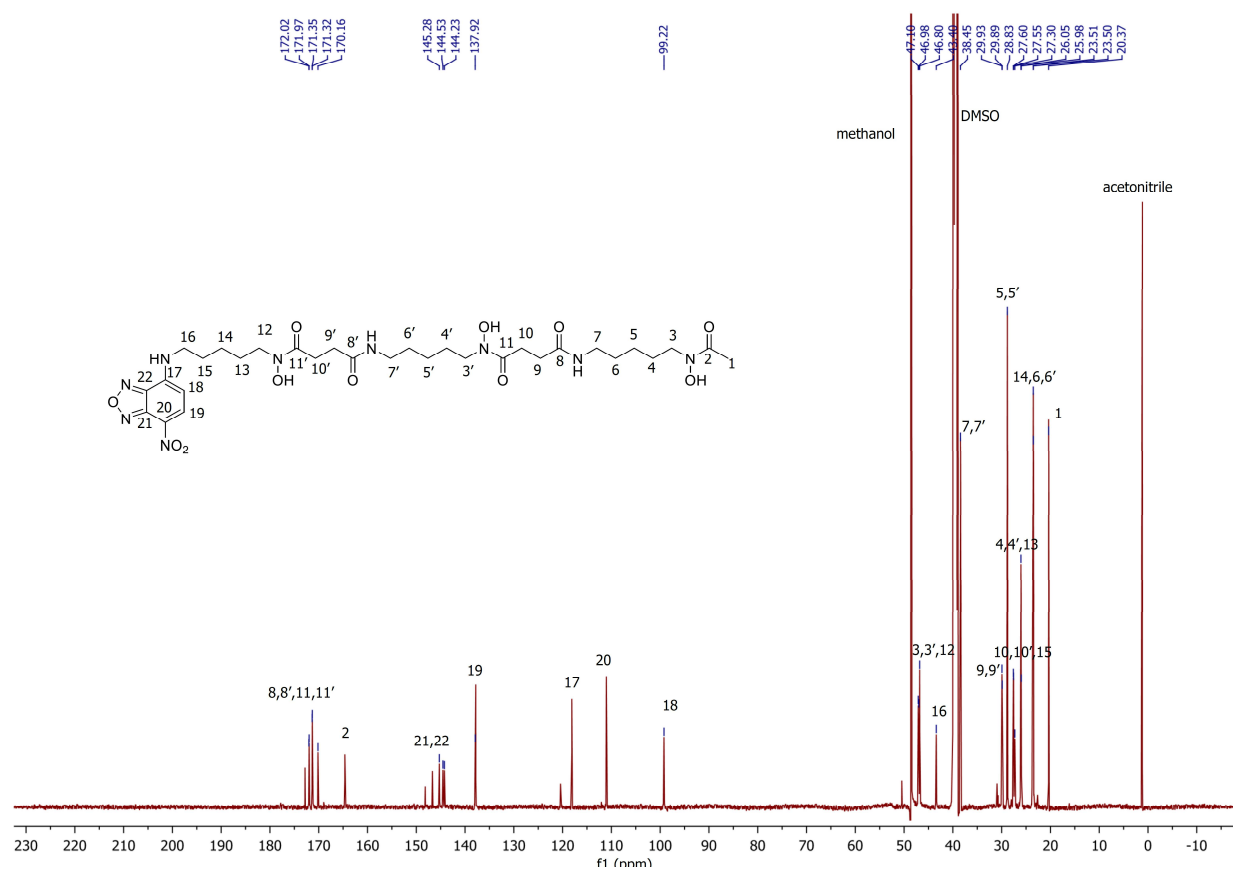
Appendix B: NMR, Raw Curves and Protein Sequences and Additional Compound Data for Chapter 3



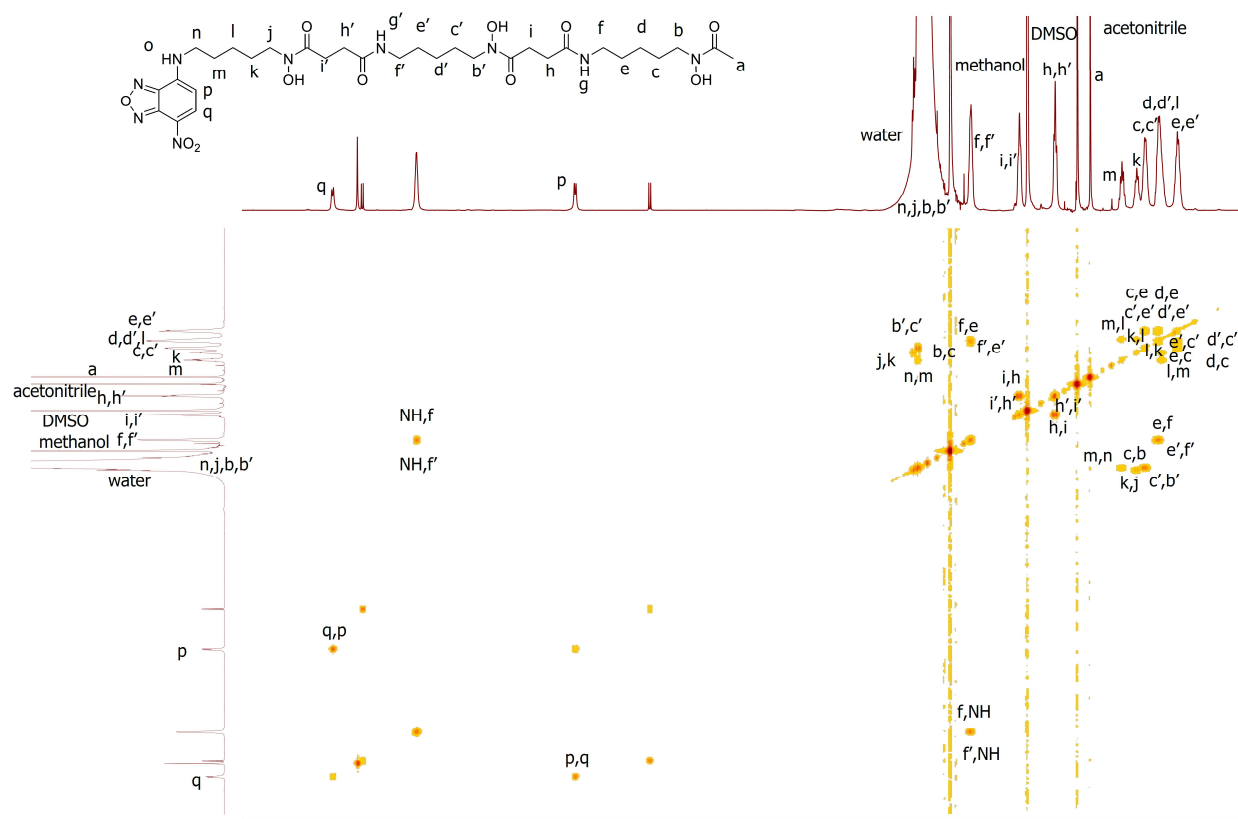
¹H



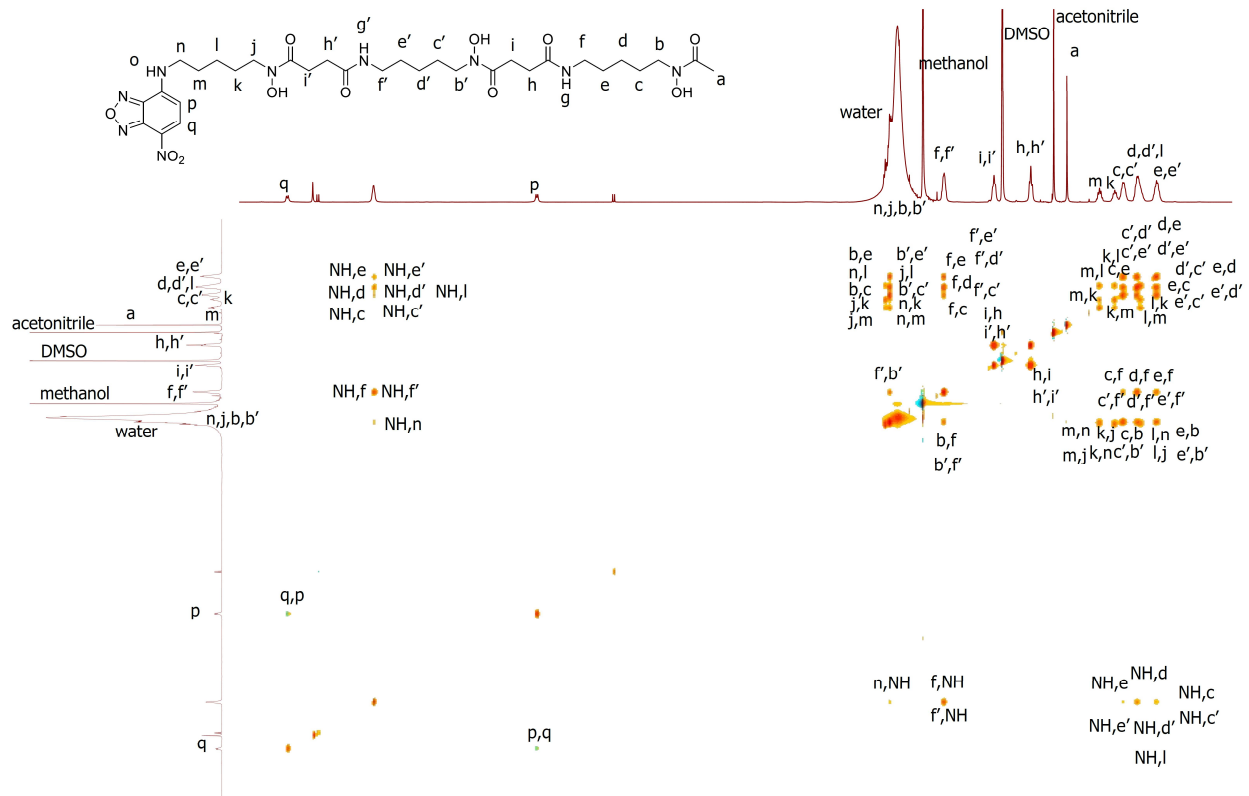
¹³C



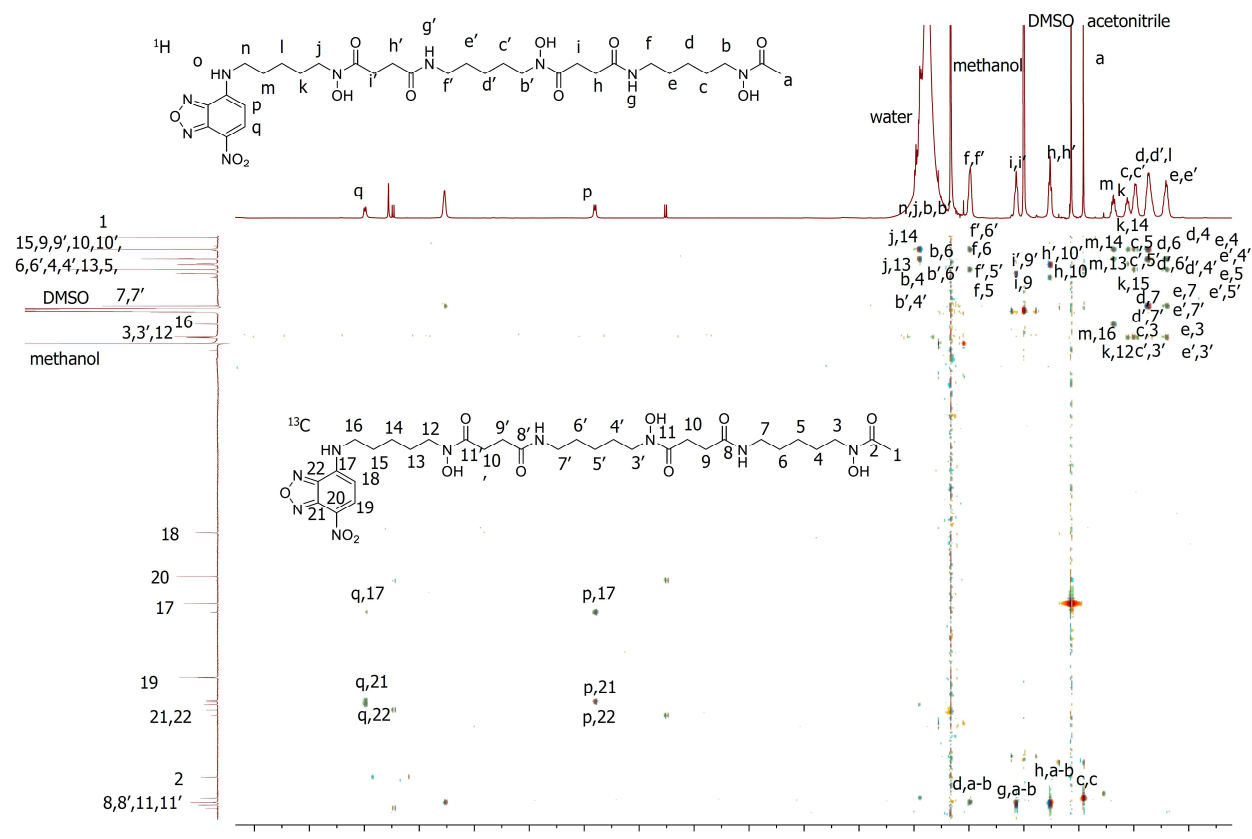
GCOSY



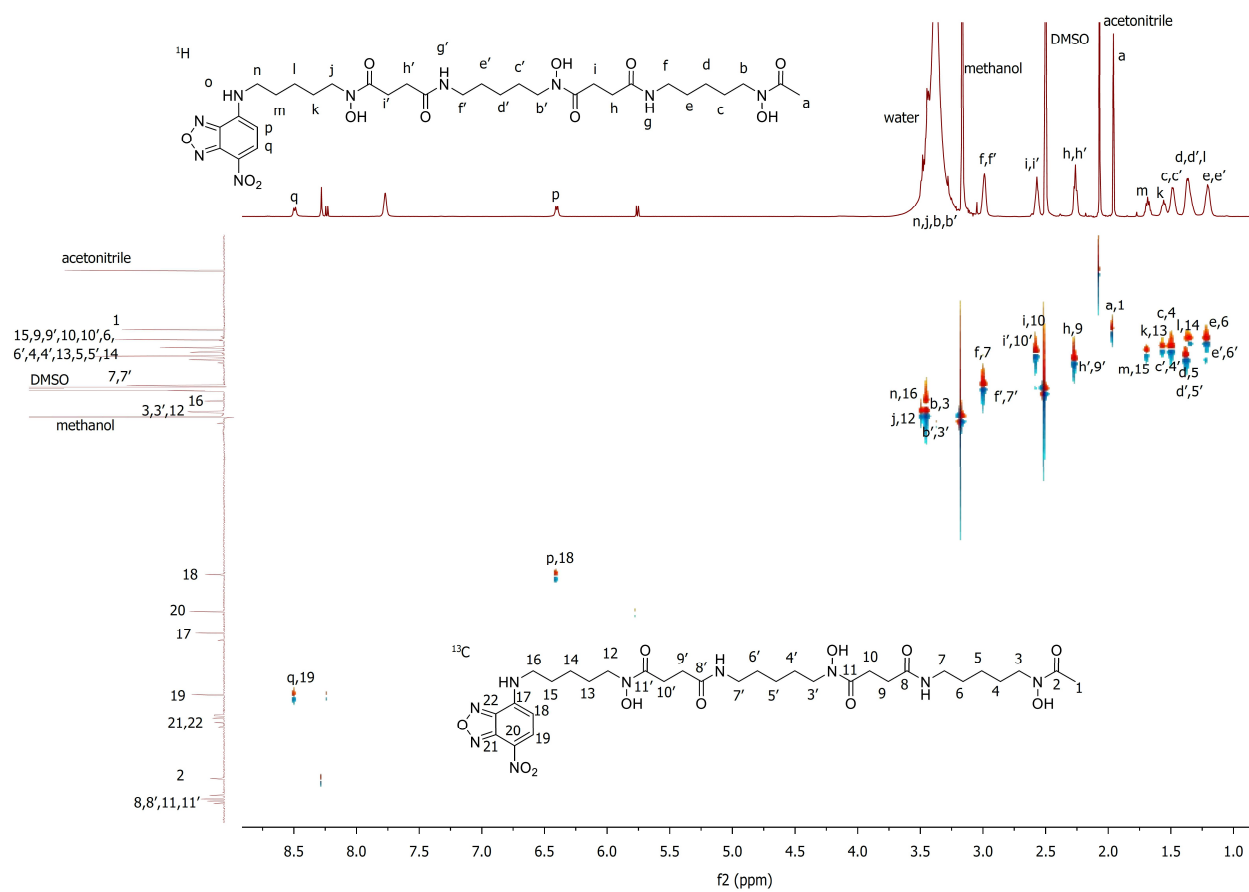
TOC

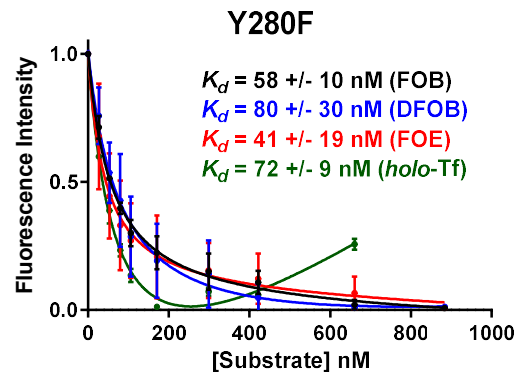
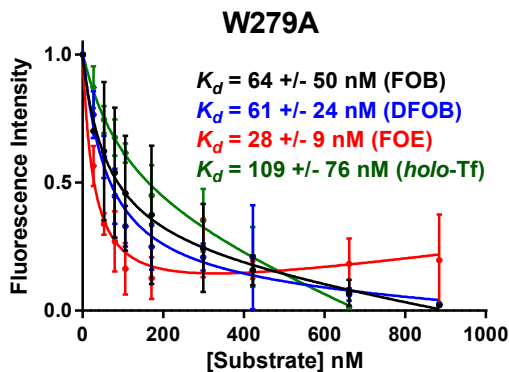
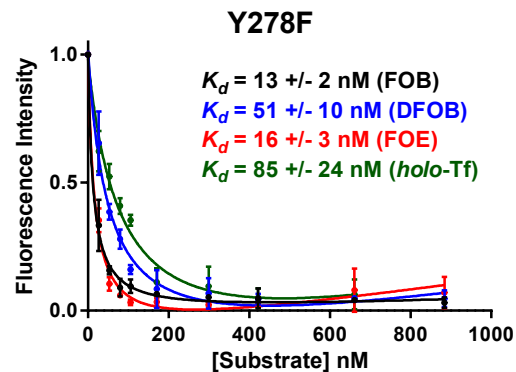
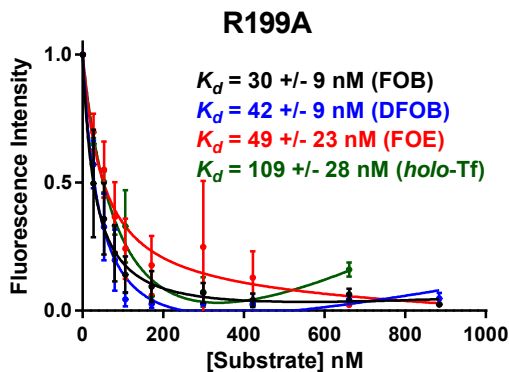
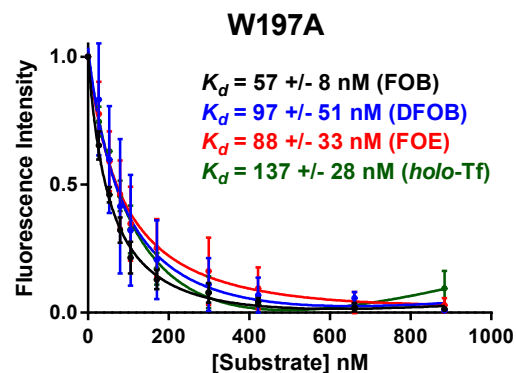
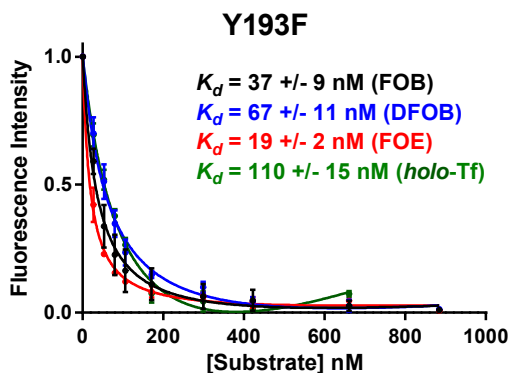
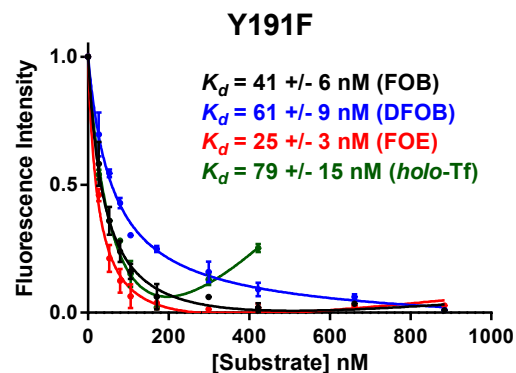
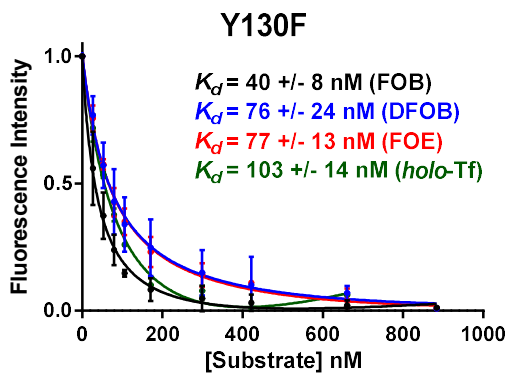


GHMBC

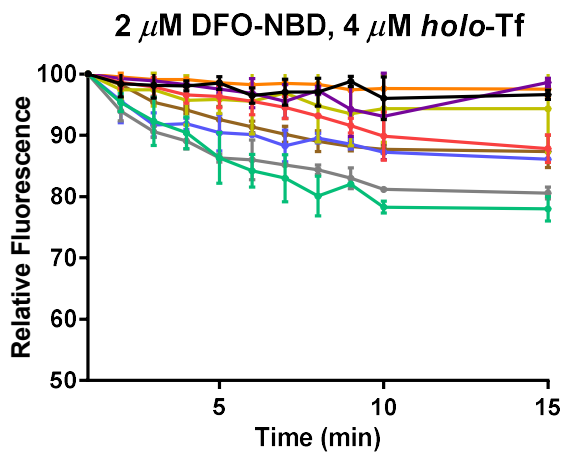
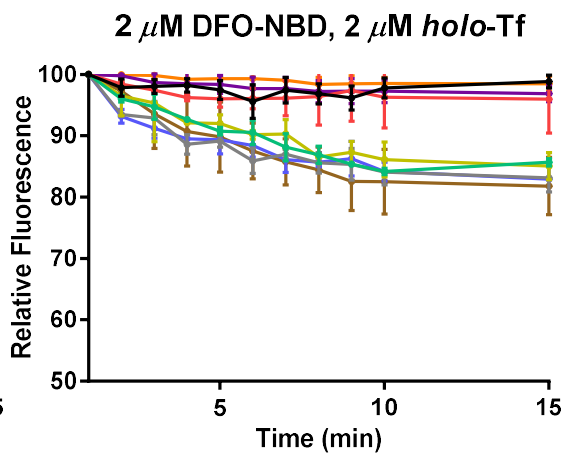
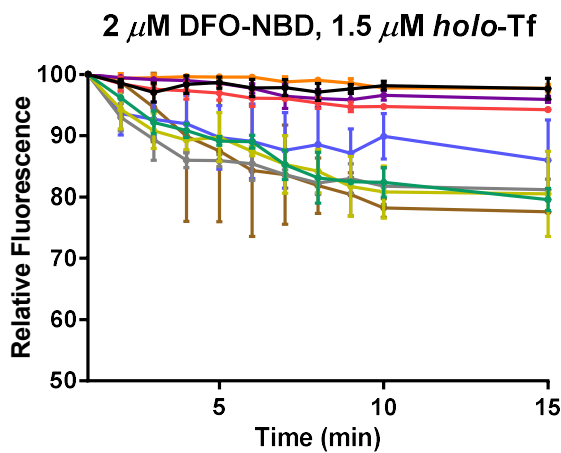
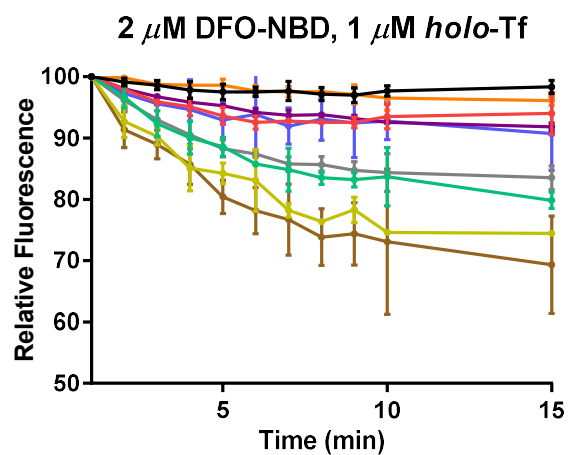
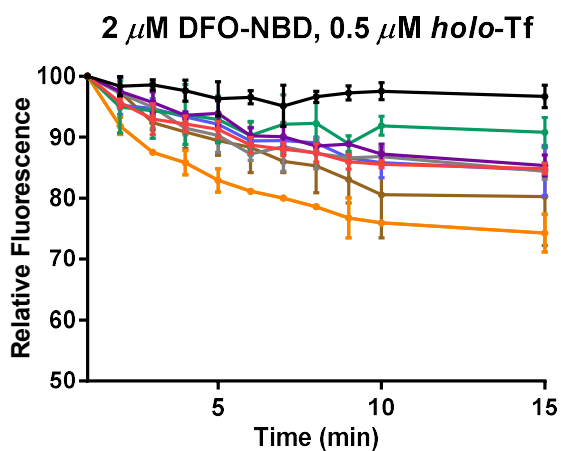


GHSQC





Fluorescence quenching of wild-type and mutant variants of *N*-His₆-FhuD2 by siderophores and human *holo*-transferrin. Graphs depict intrinsic tryptophan fluorescence quenching ($\lambda_{\text{excitation}} = 280 \text{ nm}$; $\lambda_{\text{emission}} = 340 \text{ nm}$) of the SBPs and shows dose-dependent binding to siderophore ligands. Apparent K_d values were calculated using a single-binding mode model in GraphPad Prism version 7.0b.



0 nM SBP
100 nM Y193F
100 nM Y130F
100 nM Y191F
100 nM W197A
100 nM R199A
100 nM Y278F
100 nM W279A
100 nM Y280F

Fluorescence quenching ($\lambda_{\text{excitation}} = 475 \text{ nm}$; $\lambda_{\text{emission}} = 560 \text{ nm}$) of DFO-NBD by holo-Tf with and without mutant FhuD2.

Primary protein sequences of wild type SBPs and the truncated *N*-His₆-tagged SBPs used in fluorescence quenching assays.

FhuD2-WT ^a from <i>S. aureus</i> (GenBank Accession # AAK92086.1):
MKKLLLPLIIMLLVLAACGNQGEKNNKAETKSYKMDDGKTVDIPKDPKRIAVVAPTYAGGLK KLGANIVAVNQVDQSKVLKDKFKGVTKIGDGDVEKVAKEKPDLIIVYSTDKDIKKYQKVAP TVVVDYNKHKYLEQQEMLGKIVGKEDKVKAWKKDWEETTAKDGEIKKAIGQDATVSLFD EFDKKLYTYGDNWGRGGEVLYQAFGLKMQPEQQKLTAKAGWAEVKQEEIEKYAGDYIVSTS EGKPTPGYESTNMWKNLTKATKEGHIVKVDAGTYWYNDPYTLDFMRKDLKEKLIKAAK
<i>N</i> -His ₆ -FhuD2 ^b used in this work:
MGSSHHHHHHSSGLVPRGSHMNNKAETKSYKMDDGKTVDIPKDPKRIAVVAPTYAGGLKKL GANIVAVNQVDQSKVLKDKFKGVTKIGDGDVEKVAKEKPDLIIVYSTDKDIKKYQKVAPT VVDYNKHKYLEQQEMLGKIVGKEDKVKAWKKDWEETTAKDGEIKKAIGQDATVSLFDEF DKKLYTYGDNWGRGGEVLYQAFGLKMQPEQQKLTAKAGWAEVKQEEIEKYAGDYIVSTSE GKPTPGYESTNMWKNLTKATKEGHIVKVDAGTYWYNDPYTLDFMRKDLKEKLIKAAK
YxeB-WT ^a from <i>B. cereus</i> (NCBI Reference Sequence # WP_000732596.1):
MKKLFISLTVLFLVMSACSNSSTDKKNDAGSKSETITYQSEDGKKVEVPANPKRVVVLSSF AGNVMSLGVNLVGVDSWSKQNPFRDSKLKDVAEVS DENVEKIAELNPDLIIGLSNIKNVDKL KKIAPTVTYTYGKVDYLTQHLEIGKLLNKEKEAKTWVDDFKKRAQEAGKEIKAKIGEDATVS VVENFNKQLYVYGENWGRGTEILYQEMKLMPEKVKEKALKEGYALSTEVLP EFAGDYLI VSKNKDTDNSFQETESYKNIPAVKNNRVYEANMMEFYFNDPLTLDFQLDFFKKSFLGK
<i>N</i> -His ₆ -YxeB ^b used in this work:
MGSSHHHHHHSSGLVPRGSHMSNSSTDKKNDAGSKSETITYQSEDGKKVEVPANPKRVVVL SSFAGNVMSLGVNLVGVDSWSKQNPFRDSKLKDVAEVS DENVEKIAELNPDLIIGLSNVKNV DKLKKIAPTVTYTYGKVDYLTQHLEIGKLLNKEKEAKTWVDDFKKRAQEAGKEIKAKIGEDA TVSVVENFNKQLYVYGENWGRGTEILYQEMKLMPEKVKEKALKEGYALSTEVLP EFAGD YLIVSKNKDTDNSFQETESYKNIPAVKNNRVYEANMMEFYFNDPLTLDFQLDFFKKSFLGK

^aPrelipoprotein signal sequence highlighted in magenta predicted using SignalIP-5.0.^{REF} Soluble siderophore-binding domain highlighted in teal. ^bHexahistidine motif with thrombin cleavage site highlighted in yellow. Soluble siderophore-binding domain highlighted in teal.

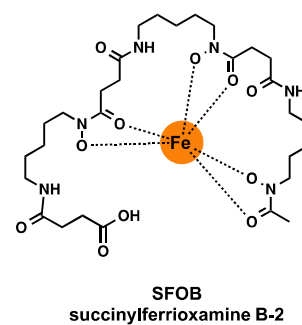
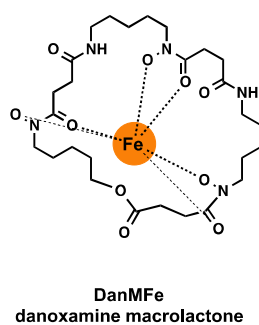
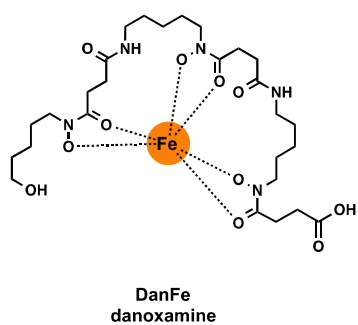
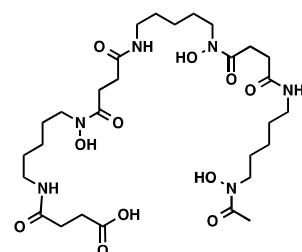
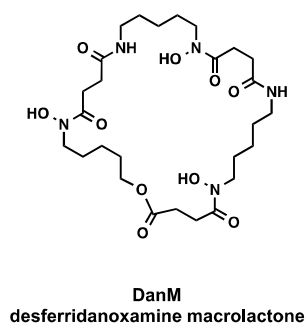
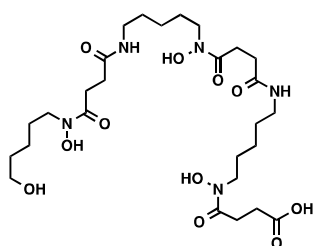
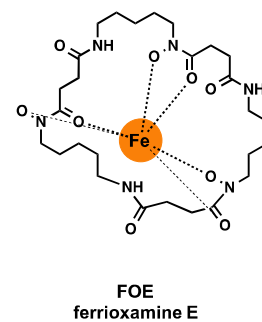
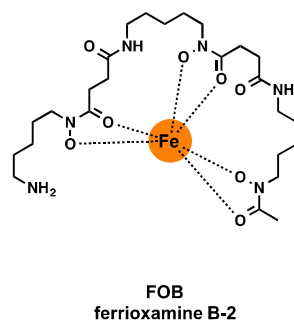
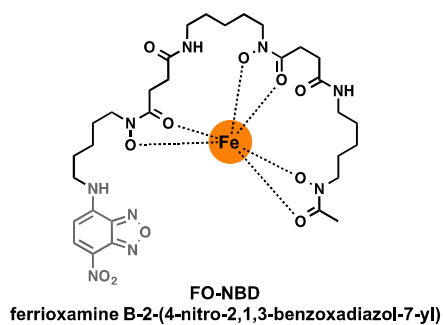
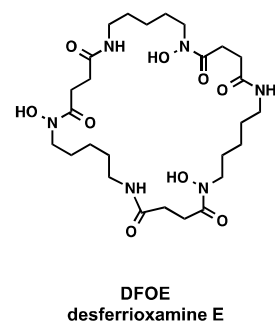
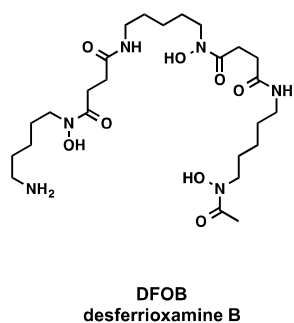
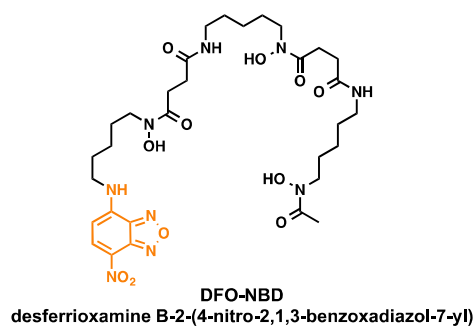
Supplementary Table 4. Codon optimized nucleotide sequences of truncated *fhuD2* and *yxeB*. Genes were cloned into a pET-28(+) vector at the NdeI-HindIII sites.

Gene encoding FhuD2 used in this work:

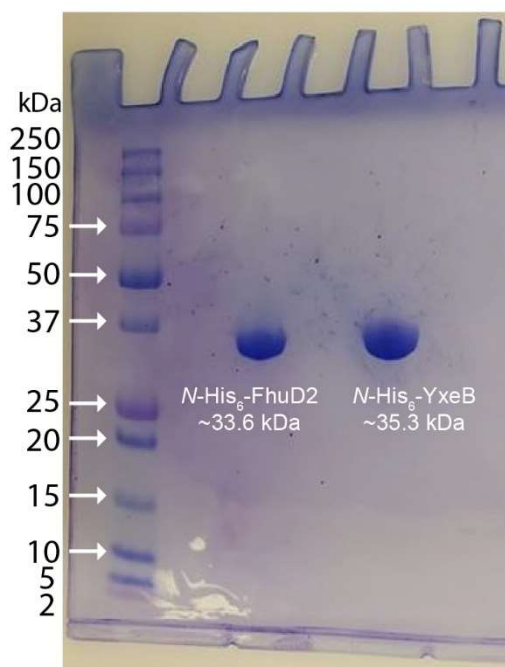
ATGAACAACAAGGCGGAGACCAAAAAGCTACAAGATGGACGATGGTAAAACCGTTGACAT
CCCGAAAGATCCGAAGCGTATTGCGGTGGTTGCGCCGACCTATGCGGGTGGCCTGAAGAA
ACTGGGTGCGAACATCGTTGCGGTGAACCAGCAAGTTGATCAGAGCAAGGTGCTGAAGGA
CAAATTCAAGGGCGTGACCAAGATTGGTGACGGCGATGTTGAGAAAGTGGCGAAAGAAA
AGCCGGACCTGATCATTGTTTACAGCACCGACAAGGATATCAAGAAATATCAAAAAGTGG
CGCCGACCGTGGTTGTGGATTACAACAAACACAAGTATCTGGAGCAGCAAGAAATGCTGG
GCAAGATTGTTGGCAAAGAAGATAAAGTGAAGGCGTGGAAGAAAGACTGGGAGGAAACC
ACCGCGAAAGATGGCAAGGAGATCAAGAAAGCGATTGGCCAGGACGCGACCGTTAGCCT
GTTTCGACGAATTTGATAAGAACTGTACACCTATGGTGATAACTGGGGTCGTGGTGGCGA
GGTGCTGTACCAGGCGTTCGGTCTGAAGATGCAACCGGAACAGCAAAAAGCTGACCGCGAA
AGCGGGTTGGGCGGAAGTGAAGCAAGAGGAAATCGAAAAATACGCGGGCGACTATATTG
TGAGCACCAGCGAGGGTAAACCGACCCCGGGCTACGAAAGCACCAACATGTGGAAAAAC
CTGAAGGCGACCAAAGAGGGTCACATCGTTAAGGTGGATGCGGGCACCTACTGGTATAAC
GACCCGTATACCCTGGATTTTATGCGTAAAGACCTGAAAGAAAAGCTGATTAAGGCGGCG
AAATAA

Gene encoding YxeB used in this work:

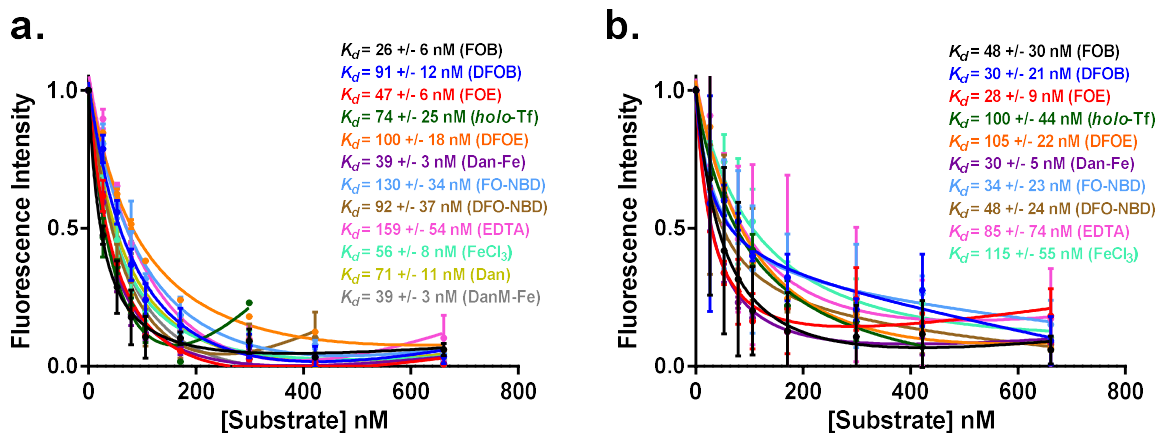
ATGAGCAACAGCAGCACCGACAAGAAAAACGATGCGAAAGGTAGCAAGAGCGAGACCAT
CACCTATCAGAGCGAGGATGGCAAGAAAGTTGAAGTGCCGGCGAACCCGAAACGTGTGG
TTGTGCTGAGCAGCTTCGCGGGTAACGTTATGAGCCTGGGTGTGAACCTGGTTGGCGTGG
ACAGCTGGAGCAAACAAAACCCGCGTTTTGACAGCAAGCTGAAAGATGTTGCGGAAGTG
AGCGACGAGAACGTTGAAAAGATTGCGGAACTGAACCCGGATCTGATCATTGGCCTGAGC
AACGTTAAAAACGTGGACAAGCTGAAGAAAATCGCGCCGACCGTTACCTACACCTATGGT
AAAGTGGATTACCTGACCCAGCACCTGGAAATTGGCAAACCTGCTGAACAAGGAGAAAGA
AGCGAAGACCTGGGTGGACGATTTCAAGAAACGTGCGCAAGAGGCGGGTAAAGAAATCA
AGGCGAAAATTGGCGAGGACGCGACCGTTAGCGTTGTGGAAAACTTTAAACAAGCAGCTGT
ACGTGTATGGCGAGAACTGGGGTCGTGGCACCGAGATCCTGTATCAAGAAATGAAGCTGA
AAATGCCGGAAGGTTAAAGAAAAGGCGCTGAAAGAAGGTTACTATGCGCTGAGCACC
GAGGTTCTGCCGGAATTCGCGGGCGATTACCTGATCGTGAGCAAAAACAAGGACACCGAT
AACAGCTTTTCAGGAGACCGAAAGCTATAAAAACATTCCGGCGGTTAAGAACAACCGTGTG
TACGAGGCGAACATGATGGAATTCTATTTTAAACGACCCGCTGACCCTGGACTTCCAACCTGG
ATTTCTTTAAGAAGAGCTTCCTGGGCAAGTAA



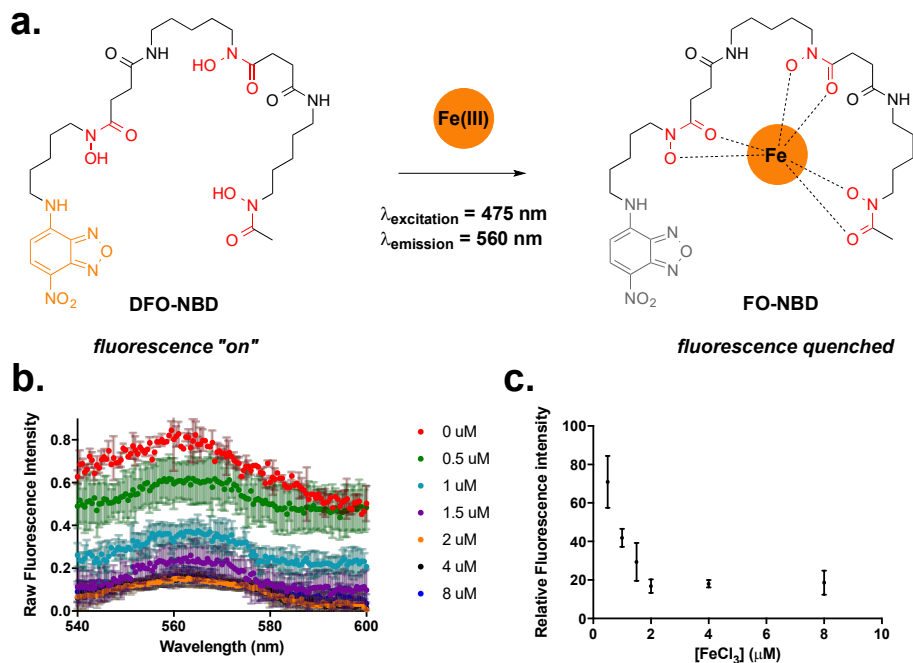
Structures and abbreviations for siderophores used in this study.



SDS-PAGE analysis of *N*-His₆-FhuD2 (~33.6 kDa) and *N*-His₆-YxeB (~35.3 kDa) purified by Ni-NTA affinity chromatography after heterologous expression in *E. coli* BL21(DE3) cells. Leftmost lane depicts ThermoFisher PageRuler Prestained Protein Ladder.



Fluorescence quenching of (a) wild-type *N*-His₆-FhuD2 and (b) wild-type *N*-His₆-YxeB by siderophores, human *holo*-transferrin, FeCl_3 , and ferric EDTA. Graphs depict intrinsic tryptophan fluorescence quenching ($\lambda_{\text{excitation}} = 280$ nm; $\lambda_{\text{emission}} = 340$ nm) of the SBPs and shows dose-dependent binding to siderophore ligands. Apparent K_d values were calculated using a single-binding mode model in GraphPad Prism version 7.0b. *N*-His₆-FhuD2 plots for DFO, Dan-Fe, Dan, and DanM-Fe were reported previously.¹ There was enough material for complete *N*-His₆-YxeB binding studies.



Desferrioxamine B-2-(4-nitro-2,1,3-benzoxadiazol-7-yl) conjugate (DFO-NBD) is a “turn off” fluorescent probe triggered by chelation of iron(III). **(a)** Structure of DFO-NBD (fluorescence “on”) and FO-NBD (fluorescence quenched). **(b)** Fluorescence emission spectra ($\lambda_{\text{excitation}} = 475 \text{ nm}$; $\lambda_{\text{emission}} = 540\text{--}600 \text{ nm}$) of $2 \mu\text{M}$ DFO-NBD with a wavelength of maximum fluorescence at $\sim 565 \text{ nm}$ after 60 min incubation with variable concentrations of FeCl_3 ($0 - 8 \mu\text{M}$). **(c)** Graph of FeCl_3 concentration versus relative fluorescence intensity of DFO-NBD at $2 \mu\text{M}$ shows a 1:1 stoichiometry for the formation of FO-NBD. Error bars in panels b and c represent standard deviation for two independent trials.